



1-1-2020

A New Approach To Measure Unique Spectral Response Characteristics For Irregularly Shaped Photovoltaic Arrays

Anthony Rafael Peters

Follow this and additional works at: <https://commons.und.edu/theses>

Recommended Citation

Peters, Anthony Rafael, "A New Approach To Measure Unique Spectral Response Characteristics For Irregularly Shaped Photovoltaic Arrays" (2020). *Theses and Dissertations*. 3116.
<https://commons.und.edu/theses/3116>

This Dissertation is brought to you for free and open access by the Theses, Dissertations, and Senior Projects at UND Scholarly Commons. It has been accepted for inclusion in Theses and Dissertations by an authorized administrator of UND Scholarly Commons. For more information, please contact und.common@library.und.edu.

A NEW APPROACH TO MEASURE UNIQUE SPECTRAL RESPONSE
CHARACTERISTICS FOR IRREGULARLY SHAPED PHOTOVOLTAIC ARRAYS

by

Anthony Rafael Peters

Bachelor of Science in Electrical Engineering Technology, Drexel University, 2010

Master of Science in Aeronautics, Embry Riddle Aeronautical University, 2017

Master of Science in Electrical Engineering, University of North Dakota, 2019

A Dissertation

Submitted to the Graduate Faculty

of the

University of North Dakota

in partial fulfillment of the requirements

for the degree of

Doctor of Philosophy

Grand Forks, North Dakota

May
2020

Copyright 2020 Anthony Peters

This dissertation, submitted by Anthony Rafael Peters in partial fulfillment of the requirements for the Degree of Doctor of Philosophy from the University of North Dakota, has been read by the Faculty Advisory Committee under whom the work has been done and is hereby approved.

Hossein Salehfar

Dr. Hossein Salehfar, Chair

Michael D. Mann

Dr. Michael Mann, Co-Chair

Forrest E. Ames

Dr. Forrest Ames, Committee Member

William Semke

Dr. William Semke, Committee Member

Prakash Ranganathan

Dr. Prakash Ranganathan, Member at Large

This dissertation is being submitted by the appointed advisory committee as having met all of the requirements of the School of Graduate Studies at the University of North Dakota and is hereby approved.

DocuSigned by:

Chris Nelson

Chris Nelson

Dean of the School of Graduate Studies

5/5/2020

Date

PERMISSION

Title A New Approach to Measure Unique Spectral Response Characteristics for Irregularly Shaped Photovoltaic Arrays

Department College of Engineering and Mines, Energy Engineering

Degree Doctor of Philosophy

In presenting this dissertation in partial fulfillment of the requirements for a graduate degree from the University of North Dakota, I agree that the library of this University shall make it freely available for inspection. I further agree that permission for extensive copying for scholarly purposes may be granted by the professor who supervised my dissertation work or, in his absence, by the Chairperson of the department or the dean of the School of Graduate Studies. It is understood that any copying or publication or other use of this dissertation or part thereof for financial gain shall not be allowed without my written permission. It is also understood that due recognition shall be given to me and to the University of North Dakota in any scholarly use which may be made of any material in my dissertation.

Anthony Rafael Peters
April 22, 2020

TABLE OF CONTENTS

LIST OF FIGURES	xi
LIST OF TABLES	xv
ABBREVIATIONS	xvi
ACKNOWLEDGMENTS	xvii
ABSTRACT.....	xix
CHAPTER 1 Introduction.....	1
1.1 Executive Summary	1
1.1.1 Overview of the Dissertation	2
1.2 Research Motivation and Objectives	4
1.2.1 Perceived Need	5
1.3 Design Constraints, Requirements, and Challenges	6
1.4 Literature Review.....	7
1.4.1 Impacts to Photovoltaics based on Orbital Characteristics.....	7
1.4.2 Using Solar Irradiance Data to Improve Solar Cell Performance.....	8
1.4.3 Color Filter Impacts on Solar Absorption Qualities for PV	9
1.4.4 Temperature Impacts to PV Chemical Composition	10
1.4.5 Power over the Life Cycle of a Vehicle.....	10
1.4.6 Thermal Impacts to Solar Cell Performance.....	11
1.4.7 New Solar Cell Designs	13
1.4.8 Solar Cell Manufacturing Changes	13
CHAPTER 2 Photovoltaic Performance Characteristics.....	15
2.1 Introduction.....	15

2.1.1 Solar Cell Testing Standardization	16
2.2 Photovoltaic Systems Theory and Background	17
2.2.1 Blackbody Radiation.....	18
2.2.2 External Factors for Photovoltaic Performance	21
2.2.3 Photovoltaics as a Semiconductor	22
2.3 Photovoltaic System Performance Modeling.....	23
2.3.1 Atmospheric Modeling	26
2.3.1.1 Relative Earth-Sun Geometry Calculations	26
2.3.1.2 Relative Earth-Sun Energy Calculations	29
2.3.1.3 ASHRAE Clear-Sky Radiation Modeling	32
2.3.1.4 Average Daily Insolation Calculations	33
2.4 Existing Photovoltaic Test Methods	35
2.4.1 Individual Solar Cell Performance Testing.....	36
2.5 Solar Cell Electrical Properties under Illumination	36
2.5.1 Electrical Characteristics	37
2.5.1.1 Equivalent Circuit	37
2.5.1.2 Short Circuit Current Density	43
2.5.1.3 Open Circuit Voltage	45
2.5.1.4 Fill Factor	45
2.5.1.5 Conversion Efficiency	46
2.5.1.6 Bandgap Energy	47
2.5.1.7 Electrical Energy and Light Current	49
2.5.1.8 Determination of Maximum Power	52

2.5.2 Illuminance Measurement and Solar Cell Optical Losses	52
2.5.2.1 Extrapolating Irradiance from Illuminance Measurements	56
2.5.2.2 Luminous Flux and Illuminance	58
2.5.2.3 Solar Cell Losses due to Reflectance	58
2.5.2.4 Other Solar Cell Losses	60
CHAPTER 3 Blackbody Radiation Simulator and Test Equipment Design	63
3.1 Introduction	63
3.2 Background and Perceived Need	63
3.2.1 BBRS Capabilities and Requirements	65
3.3 BBRS Topology and Materials	65
3.3.1 Standard Simulator Components	67
3.3.1.1 Inter-Integration Circuit Communication Protocol	72
3.3.2 BBRS Subsystem Design	74
3.3.2.1 Environmental Control and Monitoring Subsystem Design	74
3.3.2.2 Artificial Sun Module Subsystem Design	80
3.3.2.2.1 Solar Test Array Layer 1 Subsystem Design	81
3.3.2.2.2 Solar Test Array Layer 2 Subsystem Design	83
3.3.2.3 Beta Angle Position and Control Subsystem Design	87
3.3.2.4 Spectrum Calibration and Response Subsystem Design	90
3.3.2.5 Photocurrent Measurement Subsystem Design	92
3.3.2.6 Specialized Test Equipment Bill of Materials (BOM)	96
3.4 Design of the Experimental Photovoltaic-Embedded Airfoil	96
3.4.1 Background	97

3.4.2 Experimental Airfoil Topology and Materials.....	97
3.4.3 Technology Limitations	98
3.4.3.1 Solar Cell Considerations	98
3.4.3.2 Experimental Airfoil Fabrication.....	99
3.4.3.3 Airfoil Dimension Mapping.....	99
3.4.3.4 Integration of PV Performance Measurement Devices	101
CHAPTER 4 Test Methodology and Results	102
4.1 Introduction.....	102
4.2 Test Methodology using the BBRS	103
4.2.1 Initial BBRS Test Procedures	104
4.2.2 Energy Flux Initial Test	106
4.2.3 PV Array Beta Angle Spectral Response Experiment.....	108
4.2.3.1 Flat Cell Configuration Testing	108
4.2.3.2 Airfoil Cell Configuration Testing	109
4.2.4 Thermal Stress Experiment.....	110
4.3 Statistical Test Methodology	112
4.3.1 Choosing the Appropriate Statistical Test	113
4.3.2 Statistical Hypothesis.....	113
4.3.2.1 Determination of <i>a priori</i> and Statistical Power.....	114
4.4 Results.....	115
4.4.1 Energy Flux Initial Test	116
4.4.2 PV Array Beta Angle Spectral Response Experiment.....	119
4.4.3 Thermal Stress Experiment.....	125

4.4.4 ANOVA Test Results	127
4.5 Data Collection and Analysis Procedures	130
4.6 Solar Cell Correction Factor for Irregularly Shaped Arrays.....	131
4.6.1 Mathematical Framework and Rationale	132
4.6.1.1 Initial Calculations	132
4.6.1.2 Corrections for a Curved Airfoil Array	135
4.6.2 Proposed Performance Correction Factor	137
4.7 Validity and Triangulation Concerns.....	139
4.8 Ethical Issues and IRB Considerations	139
4.9 Reliability and Reproducibility.....	140
CHAPTER 5 Conclusions, Contributions, and Future Work	141
5.1 Research Conclusions	138
5.1.1 Subsystem Design Challenges	138
5.1.2 Limitations	139
5.1.3 Comparison of Flat Panel to Airfoil Panel Performance	140
5.1.4 Significance of the Study	144
5.1.4.1 Contributions	144
5.2 Future Work	145
5.2.1 Different Airfoil Configurations	145
5.2.2 Spectrum Emitter Sources.....	146
5.2.2.1 Quality Control Methods	146
5.2.3 Emissivity Impacts.....	148
5.2.4 GaN Comparison to Si PV Technologies	148

5.2.5 Vibration Testing	151
5.2.6 Other Design Improvements and Research Efforts	153
5.3 Conclusion Statement	155
References.....	158
Appendix A.....	166
Appendix B.1	167
Appendix B.2	171
Appendix C.1	172
Appendix C.2	178
Appendix D.1	179
Appendix D.2.....	188
Appendix E.1	189
Appendix E.2	192
Appendix F.1.....	193
Appendix F.2.....	197
Appendix G.1	198
Appendix G.2.....	205
Appendix H.....	206
Appendix I	207
Appendix J	210

LIST OF FIGURES

Fig. 2.1. Solar radiation spectrum graph illustrating the solar absorption qualities that are apparent for photovoltaics to generate photocurrent.	16
Fig. 2.2. Electro-optical characteristic curve for red chip LED, part number LL-S150VC-V1-2B.	19
Fig. 2.3. Illustration of air mass ratio geometries for an Earth-Sun orbit.	21
Fig. 2.4. A p–n junction diode.	22
Fig. 2.5. Current version of LabView18 solar cell calculator v.2.2.3.	25
Fig. 2.6. Solar power generation calculator using LabView19.	25
Fig. 2.7. Illustration of beam radiations in different configurations.	30
Fig. 2.8. Different solar radiation geometries.	31
Fig. 2.9. ASHRAE clear sky radiation modeling tool formulated using Microsoft Excel.	33
Fig. 2.10. Matlab-generated graphs for an average daily insolation.	34
Fig. 2.11. Equivalent circuit for a simple PV device with a connected load.	37
Fig. 2.12. A simple equivalent circuit for a photovoltaic cell.	38
Fig. 2.13. Another simplified equivalent circuit for a photovoltaic cell.	38
Fig. 2.14. Equivalent circuit for a simple PV device with a connected load and parallel resistance.	39
Fig. 2.15. Equivalent circuit for a simple PV device with a connected load.	39
Fig. 2.16. A sun path diagram showing solar altitude and azimuth angles for 40 degrees latitude.	40
Fig. 2.17. A more complex equivalent circuit for a PV cell includes both parallel and series resistances.	41
Fig. 2.18. PV circuit resistances in series and parallel.	42
Fig. 2.19. PV modules in series and in parallel.	42
Fig. 2.20. Effect of shading one cell in an n -cell module or array.	43
Fig. 2.21. The fill factor (FF) as a function of open circuit voltage (V_{oc}) for a solar cell that is represented by an ideal diode.	46
Fig. 2.22. Maximum efficiencies of photovoltaics as a function of their bandgap over different air masses.	48
Fig. 2.23. Distribution for frequency of photons, plotted as a function of energy.	49
Fig. 2.24. Microsoft Excel program formulated to execute the light current function.	51

Fig. 2.25. Non-normalized values of the scotopic and photopic curves of spectral luminous efficacy.	54
Fig. 2.26. Matlab/Simulink model for a PV exact power system.	60
Fig. 2.27. Matlab/Simulink graphical model for a PV exact model power system.	61
Fig. 2.28. PTC heating element embedded on a sample PV-embedded test airfoil.	62
Fig. 3.1. General PV electrical performance characteristics.	64
Fig. 3.2. Overall concept for the solar cell simulator programmable interfaces.	66
Fig. 3.3. Front image of the BBRS enclosure.	68
Fig. 3.4. Stacked microcontrollers.	69
Fig. 3.5. Arduino Uno R3 microcontroller.	70
Fig. 3.6. ATMEGA328 microcontroller board.	70
Fig. 3.7. Adafruit METRO Mini 328 microcontroller board.	71
Fig. 3.8. HD44780 LCD display.	72
Fig. 3.9. Inter-integrated circuit communication protocol.	73
Fig. 3.10. Basic internal structure of an SDA/SCL line.	74
Fig. 3.11. Startup menu for a sample version of the ECMS.	75
Fig. 3.12. BMP280 sensor.	76
Fig. 3.13. DHT22 wired temperature and humidity sensor.	76
Fig. 3.14. SRD-05VDC-SL-C assembled serial relay driver.	77
Fig. 3.15. Serial relay driver conceptualized circuit.	78
Fig. 3.16. ECMS module thermal baseplate.	78
Fig. 3.17. W1209 temperature controller.	79
Fig. 3.18. Bayite 12V/10A temperature controller.	80
Fig. 3.19. ASMS solar test array layer 1 and 2.	81
Fig. 3.20. LED sequins used for the artificial sun to stimulate the solar cells.	82
Fig. 3.21. ASMS STAR1 completed LED array shield module.	82
Fig. 3.22. VL6180X TOF and lux sensor.	83
Fig. 3.23. TSL2561 lux sensor.	84
Fig. 3.24. ML8511 UV sensor.	85
Fig. 3.25. ML8511 UV sensor output voltage versus ultraviolet intensity graph.	86
Fig. 3.26. TMP007 contactless temperature sensor.	86
Fig. 3.27. 4x4 membrane-type keypad circuit diagram.	87
Fig. 3.28. BAPCS A3967 stepper driver.	88

Fig. 3.29. NEMA17 series stepper motor.	89
Fig. 3.30. Beta angle position and control subsystem (BAPCS) module.	89
Fig. 3.31. SCARS TSL2591 lux sensor.	91
Fig. 3.32. Spectral responsivity for a channel 1 and channel 0 photodiode.	91
Fig. 3.33. SCARS VEML6075 UVA/UVB sensor.....	92
Fig. 3.34. PCMS INA219 board.	93
Fig. 3.35. PCMS INA169 board.	94
Fig. 3.36. PCMS datalogger.	95
Fig. 3.37. PCMS main circuit build stackup.	95
Fig. 3.38. A portable silicon-based 6V/1W solar cell.	97
Fig. 3.39. Airfoil plotter toolkit mapping process.	100
Fig. 3.40. JGAurora A5S 3D Printer used for experimental PV airfoils.	100
Fig. 3.41. Final version of the experimental PV-embedded NACA0024 airfoil.	101
Fig. 4.1. Inside of the BBRS using the calibration laser.	107
Fig. 4.2. Measured temperature increase over time.	112
Fig. 4.3. GPower-generated <i>a priori</i> metrics for the ANOVA statistical test.	115
Fig. 4.4a. Total energy gathered from the energy flux initial test in the red EMS region (624 nm) using the SCARS.	116
Fig. 4.4b. Total energy gathered from the energy flux initial test in the green EMS region (520 nm) using the SCARS.....	117
Fig. 4.4c. Total energy gathered from the energy flux initial test in the blue EMS region (468 nm) using the SCARS.....	117
Fig. 4.4d. Total energy gathered from the energy flux initial test in the white EMS region (480 nm) using the SCARS.....	118
Fig. 4.4e. Total energy gathered from the energy flux initial test in the UV EMS region (365 nm) using the SCARS.	118
Fig. 4.4f. Total energy gathered from the energy flux initial test in the IR EMS region (925 nm) using the SCARS.	119
Fig. 4.5. Voltage profile for different wavelengths of light for both flat and airfoil (curved) configured PV arrays.	120
Fig. 4.6. Total power generated using different wavelengths of light for both flat (left) and airfoil (right) configured PV arrays.	123
Fig. 4.7. Average total power generated accounting for multiple wavelengths of light for both flat and airfoil configured PV arrays as a function of angle of incidence.	123
Fig. 4.8. Average total power generated accounting for multiple wavelengths of light for both flat and airfoil configured PV arrays as a function of angle of incidence.	124

Fig. 4.9. Temperature impacts to flat and PV airfoil configured arrays broken down by spectral response for current and voltage.	126
Fig. 4.10. Analysis of variance (ANOVA) sample of inputs to MiniTab software for average power yielded from flat and airfoil configuration PV arrays.	128
Fig. 4.11. Minitab analysis of variance for the BBRS test data comparing the flat panel and PV-embedded airfoil (curved) panel configuration.	129
Fig. 4.12. Geometric relationship between the solar irradiance source and PV panel.	135
Fig. 4.13. The photovoltaic array performance correction factor for the NACA0024 airfoil. ...	138
Fig. 5.1. Flexible PV cell after thermal stress experiment for both airfoil and flat cell configuration.	143
Fig. 5.2. Electromagnetic spectrum energies for a blackbody broken down by ultraviolet, visible, and infrared spectrums.	147
Fig. 5.3. Direct (left) and indirect (right) bandgap processes for a theoretically ideal semiconductor.	149
Fig. 5.4. A comparison of Si, GaN, and GaAs semiconductor materials by resultant photon energy as a function of incident photon wavelength (left) and electron frequency as a function of incident photon wavelength (right).	151
Fig. 5.5. SW-420NC vibration sensor.	152
Fig. 5.6. GY-521 3-axis accelerometer.	152
Fig. 5.7. Vibration simulation subsystem.	152

LIST OF TABLES

Table 1. Energy flux based on wavelength of light.	20
Table 2. Photopic and scotopic luminous efficiency and conversion values used for lux conversion and correction to luminous flux density.	55
Table 3. Cumulative voltage gains for 180-degree ASMS swings over 20 different tests. based on wavelength of light.	119
Table 4. Type and energy for some common semiconductor materials.	146

ABBREVIATIONS

AM	Air Mass Coefficient
ASMS	Artificial Sun Module Subsystem
BAMS	Broad Area Maritime Surveillance
BAPCS	Beta Angle Position and Control Subsystem
BBRS	Blackbody Radiation Simulator
BOL	Beginning of Life
CONOPS	Concept of Operations
CNC	Computer Numerical Control
ECMS	Environmental Control and Monitoring Subsystem
EMS	Electromagnetic Spectrum
EOL	End of Life
FOD	Foreign Object Debris
HALE	High Altitude Long Endurance
IDE	Integrated Development Environment
IR	Infrared
I2C	Inter-Integrated Circuit
LCD	Liquid Crystal Display
MTTF	Mean Time to Failure
Op-Amp	Operational Amplifier
PAPCF	Photovoltaic Array Performance Correction Factor
PCMS	Photocurrent Measurement Subsystem
PTC	Positive Temperature Coefficient
PV	Photovoltaic
SCARS	Spectrum Calibration and Response Subsystem
SCL	Serial Clock Digital Input
SDA	Serial Data Digital Input
STC	Standard Test Conditions
STE	Specialized Test Equipment
UAV	Unmanned Aerial Vehicle
UAS	Unmanned Aerospace/Aerial System
UV	Ultraviolet
UVI	Ultraviolet Index
sUAS	Small Unmanned Aerospace/Aerial System
WCA	Worst Case Analysis

ACKNOWLEDGMENTS

I wish to express my sincere appreciation to the members of my advisory Committee for their guidance and support during my time in the doctoral program at the University of North Dakota. More specifically, I would like to take the opportunity to personally thank my dissertation committee chairs Dr. Michael Mann and Dr. Hossein Salehfar for their technical support, sage advice, and encouragement to pursue research in renewable energy integration during my time as a PhD student at the University of North Dakota. I would also like to thank Paul Votaw and Timothy Alsrue for all the extra time they spent mentoring me to be a better engineer, the willingness to spread their wisdom, and their friendship.

To my wife, Lola.

ABSTRACT

Current photovoltaic (PV) panel test methods do not provide efficient and repeatable standardization, which can result in inconsistent results. Test requirements for individual PV cells are promulgated by standard test conditions (STC), but do not directly translate to new array or panel designs, particularly for panels that are irregularly shaped and used for different applications. Optimal angles that yield the most power delivery from the PV device when integrated into a panel are achieved by manipulating the panel's orientation via single or dual axis tracking (e.g., maximum power point tracking). In applications where PV is intended to be integrated into a flying object, such as an unmanned aerial vehicle (UAV), maximum power point tracking (MPPT) is not an option due to aerodynamic constraints resulting from airfoil and control surface design. In these instances, it is pertinent to develop a system that can consistently measure responses of a PV-embedded airfoil in a controlled environment that is also cost-efficient and readily available for researchers to use. Additionally, the system must also be scalable to meet the needs of larger experimental setups for future UAV development. The intent of this dissertation was to propose a new method for capturing the PV-embedded airfoil performance as it compares to a conventional flat panel in terms of efficiencies. As a result, a user has the ability to analyze the collected experimental data and subsequently develop a performance correction factor that is specific to the airfoil used. Recommendations to further enhance analysis of UAV integrated PV efficiency factors, such as vibration impacts on performance, will also be discussed. From an analysis of experimental data, unmanned aerial systems (UAS) engineers can be able to integrate renewable energy systems more effectively and therefore increase vehicle energy efficiency.

CHAPTER 1

INTRODUCTION

1.1 Executive Summary

Understanding the factors that negatively impact solar cell efficiency and how they influence overall unmanned aerial systems (UAS) performance can change how an unmanned aerial vehicle (UAV) is designed. Ensuring adequate power margins in photovoltaic (PV) array design by accounting for these variables enables engineers to construct a more reliable power system. Considerations such as thermal cycling and intensity, specific wavelength of light, and solar angle of incidence are a few important performance factors to predict maximum theoretical PV system power output. The impact of these variables was studied in the case of non-uniformly shaped PV arrays intended to be used in combination with large-scale high-altitude long endurance (HALE) UAV airfoils, such as those used by the MQ-4C Triton. Through the special fabrication of a scalable Blackbody Radiation Simulator (BBRS), the variables of wavelength of light and angle of incidence represented by beta angle were studied as to how they influence solar array performance over extensive use on terrestrial UAS platforms over the course of a solar day. Through observed data collected from the BBRS under solar cell standard test conditions (STC), a comparison of voltage output between a flat cell and a custom PV-embedded airfoil with identical surface areas was conducted. Each design was subjected to different beta angles, as well as different wavelengths of light. Using observed data deltas from both tests, a correction factor was obtained to adequately predict any deviations in PV panel output from a flat panel design to one using an irregularly shaped panel. The experimental test procedure was divided into phases with each PV performance factor of wavelength and beta angle subjected to each PV array type, with measured voltage data logged for later analysis. It was originally

anticipated that the amount of total energy during the course of a solar day was approximately equal in the two designs, however the distribution of power output was skewed due to the curved panel design. The correction factor for calculated performance predictions, coupled with the spectrum response characteristic derived from the solar day profile will assist UAS design engineers develop worst case analyses (WCAs) for in-flight performance as well as analyze for cosine losses and thermal stresses in different PV array designs, thus influencing total UAV design. This dissertation focuses on the fabrication of the BBRS and highlights the ability to analyze experimental data collected from the system to generate a specific performance correction factor based on the desired airfoil design. Future testing for the BBRS includes vibration impacts for flat array and irregularly shaped arrays.

The effects of temperature can vary as a function of altitude, as well as time of year, while solar incidence angle varies as a function of time of day and time of year. Temperature concerns due to repeated cycling and constant exposure can ultimately influence how much heat dissipative capacity a vehicle needs to have in order to adequately radiate heat. Specular reflections from other portions of the vehicle may also serve as additional forms of heat damage to a solar array, thus negatively impacting the end of life (EOL) performance. Cosine power losses due to obstruction in optimal incidence angles is another factor considered for future analysis, as photovoltaic embedded airfoils lack the ability for normalized solar tracking due to aerodynamic concerns (i.e., disturbance of airflow over the leading edge and altering the critical angle of attack for the airfoil).

1.1.1 Overview of the Dissertation. This dissertation was intended to propose a new method for quantifying and measuring the spectral response characteristic of photovoltaic devices that are irregularly shaped. Conventional PV modules and arrays, which are made up of

multiple cells, are tested to comply with specific safety and quality requirements. The general tests comprise of subjecting an array, module, or individual cell to various load conditions, under standard test conditions (STC) comprised of air mass coefficient of 1.5 (i.e., AM1.5, or air mass ratio 1.5), solar radiation of $1000/\text{Wm}^2$, and a module temperature of 25 degrees Celsius ($^{\circ}\text{C}$) as promulgated from the International Electrotechnical Commission (IEC) [23]. Specifically, under test certificate IEC61215, these tests are conducted for monocrystalline, polycrystalline and thin film solar devices. Other test methods from entities such as the National Renewable Energy Laboratory (NREL) exist for multiple cell designs and chemical architectures such as Gallium Arsenide (GaAs), and include accelerated life testing, thermal cycling, UV exposure, electroluminescence, and dynamic mechanical loads [21]. However, the conventional tests do not include other various influences on PV performance, such as wavelength of light and angle of incidence. Tests to study the angle of incidence impacts for cell and PV module designs can yield inconsistent results when repeated, simulations to predict system performance are subject to numerous variables and are difficult to verify [13]. Additionally, the analog-to-digital measurement tools used to measure and log dynamic data for a myriad of solar cell performance factors can be expensive and require advanced software packages not commonly available to renewable energy researchers.

The design and intent of the BBRS focuses on the advancement of PV testing by addressing the shortfalls in the aforementioned test methods and standards. This never before utilized system presents a unique approach to systematically evaluate wavelength of light and angle of incidence impacts on PV devices in various configurations and shapes and is proposed for future standardization of PV test procedures. The BBRS uses components that are smaller, more efficient, at lower costs by using commercially available microcontrollers, as well as

providing the ability to be scaled to meet the requirements of larger loads and modules. More importantly, the proposed method presents a more controlled and repeatable test environment that is more conducive to yielding consistent and reliable data for further analysis. The BBRS design coupled with proposed correction factors generation methods to predict PV performance is both new and innovative and hopes to yield a level of higher reliability and confidence in design for renewable energy users and researchers worldwide. The ability to obtain important experimental results from critical PV performance-related data using the BBRS will allow system designers to formulate a more detailed analysis of experimental results using other airfoil designs.

1.2 Research Motivation and Objectives

The objective of this research is to propose an appropriate test method that accurately measures photovoltaic responses for different solar cell types, solar array shapes, and architectures. This was achieved using existing commercially developed standardized test conditions (STC) for solar cell testing; particularly the STCs of interest were to consider all test cell temperatures to be no greater than 25°C, and at AM1.5 illumination. The exception to this STC was during the execution of the temperature impacts study where the temperature of the PV array was increased to the point a physical failure was noted from the PV device. To successfully accomplish the objective, the fabrication of experimental and specialized test equipment was required. The experimental BBRS subjected the PV device and/or array under specific environmental conditions simulating a controlled solar illumination source, while varying the beta angle (e.g., angle of incidence) and collecting PV performance data to measure the photovoltaic response. This response was tabulated and graphed in order to present a new way of evaluating solar cell performance that is not exclusive to maximum power points, and instead

presents a unique spectral response characteristic curve that provides power data for a particular PV cell/array tailored for a defined mission.

The main problem for the research proposal is that solar cell performance depends greatly on normalized solar tracking to optimize power generation, and integration for HALE UAS operations has profound aerodynamic implications. Subproblems for this effort involve evaluating the specific effects on solar cells in a HALE mission profile due to: (1) varying solar angles of incidence, and how cosine losses due to hour angle and vehicle structure obscurations impact photocurrent generation, and (2) thermal stresses [14, 40]. Using the lessons learned from solar cell technological enhancements, potential for reduced development and integration costs, and applications in space, it may become possible to increase system confidence/viability for solar applications in certain fossil-fuel dependent UAS [5]. Another objective of this dissertation was to build a product that could be used to either supplement or replace existing test methods for solar devices using low-cost methods. Other studies have shown that using Arduino microcontrollers and Excel can prove incredibly effective attaining reliable and accurate data when compared to traditional instrumentation [13].

1.2.1 Perceived Need. The utilization of photovoltaics (PV) is a critical renewable energy research area and has direct applications to the aviation and aerospace industry. Specifically, solar cells are used for satellites in orbital profiles with varying degrees of thermal intensity, such as low elliptical earth orbit (LEO), and are subject to rapid periods due to their low apogee and perigee [24]. Ensuring a survivable thermal-resilient design are optimal user requirements for the solar cells that will be delivering power to space vehicles on orbit or in a terrestrial environment. Ensuring that the vehicle in question will also attain adequate power margins at beginning of life (BOL) and end of life (EOL) to meet mission life requirements is

important to maintaining duty cycles for essential payloads and total spacecraft functionality [24]. Analyzing variables that effect solar cell performance, such as wavelength of light (i.e. red, green, blue) with respective voltage impacts, are important to study in order to broaden the understanding of the predicted performance a cell type will have [61]. Additionally, new and innovative renewable energy solutions for the aviation industry is pertinent due to diminishing fossil fuels is a national priority and understanding viable solutions through optimizing solar cell efficiency is key in assuring future energy solutions [3].

1.3 Design Constraints, Requirements, and Challenges

Some of the challenges presented in this study are addressed from a series of technical assumptions to establish the theoretical framework in which the study was executed. For the research project, an ideal geographic region that is exposed to a 12-hour solar day was used as the base collection point for qualitative data regarding renewable energy. Thermal assumptions were based on atmospheric standard day incorporated from the Federal Aviation Administration Handbook of Aeronautical Knowledge [15]. It is assumed that the solar cell fabrication process has quality assurance measures in place to ensure uniformity of the metallization process (i.e. equal sizes for all electrical diodes), and that [if used in the cell design] the cell interconnect coverglass and top layer is free of cracks or imperfections [56]. It is also assumed that the initial cell design was a silicon-based design, with a bandgap energy of approximately 1.12 electron volts (eV). The surface area will vary among cell types, but the main solar test cell was a rectangular shape to most efficiently cover the PV test airfoil and is approximately 4.071 mm² per cell.

In terms of incidence angle, the cell was exposed to a simulated standard solar day where the point from sunrise to sunset allowed a cell to gather a pre-calculated amount of solar energy.

This amount of energy captured at the cell varied primarily as a function of the angle at which solar energy is received relative to the panel orientation [52]. Developing a system that consistently subjects a PV array to the same light intensities as a function of beta angle per unit time regardless of PV orientation or configuration was critical. This design challenge was accomplished by the beta angle spectrum analysis experiment which addresses subproblem 1. Other technical limitations are presented as thermal limitations due to temperature regulation when addressing subproblem 2, where the research plan utilized a contactless temperature sensing method to identify temperature fluctuations as induced by heating elements, and their resultant impact to photocurrent output. For different configurations of the initial solar cell in series and parallel modes, thermal stresses would possibly be indicated by a shunted cell, or a more accelerated deterioration in photocurrent over each cycle period as presented in the thermal stresses experiment [10].

1.4 Literature Review

There have been multiple research efforts surrounding the topic of renewable energy, and improving solar cell technology, however the ultimate goal of the literature review was to obtain sources that focus specifically on impacts on PV performance factors and efficiency.

Additionally, the objective was to highlight potential research areas for future work and identify methods for optimizing individual cell performance under terrestrial conditions. The following literature review encompassed both quantitative and qualitative research studies, where the themes of renewable energy are discussed in the following subsections below.

1.4.1 Impacts on Photovoltaics based on Orbital Characteristics. In a 2003 article published by Imamura and Khoshaim [24], space-based applications for photovoltaics were addressed, and highlighted solar power as the “principle source of electrical power for a vast

majority of future spacecraft missions”. Having the perceived need for continued solar cell research clearly defined for such high-profile applications aids in validating future studies surrounding this topic. The authors provide analysis of silicon-based solar cells that are required to perform high rate energy collection during orbital regimes to meet the continuous power supply demands of the spacecraft bus system. Accounting for variables such as the eclipse duration, orbital plane characteristics (i.e. apogee, perigee, differing beta solar angles, rotational velocity and inclination), and rotations an orbital average power (OAP) can be calculated and compared to system requirements. While this article applies to a spacecraft power system, the same assumptions regarding incidence angles and cosine losses can be applied for a terrestrial system. If a cell string does not yield enough power during illuminated rotations, then the batteries which hold those stored charges may not have enough power to maintain continuous energy to the spacecraft during eclipse [24]. For a mirrored terrestrial HALE UAS application, this directly applies to a scenario where an optimized flight pattern would need to be developed to maximize solar output and minimize losses [14]. Understanding the implications of a load power profile, and direct energy transfer configurations as it pertains to solar cell performance is critical to keeping a satellite that experiences more frequent light and temperature oscillations operational. This paper was important to the research effort in that it shows a clear relationship between duration of exposed solar energy to overall power output and highlights the requirement to evaluate solar cell efficiency based on mission and environment.

1.4.2 Using Solar Irradiance Data to Improve Solar Cell Performance.

Meteorological satellite constellations (METEOSAT) images taken from space have proven useful to determine levels of solar irradiance in certain geographic areas of the world. The study conducted by Muselli et al. [39] is pertinent to improving terrestrial-based stand-alone solar cell

collection areas where determination of hourly solar energy is measured and predicted based on tilted and flat inclinations. This information is useful to researchers to determine an estimate of how much solar radiation a cell can experience in a given period based on relative azimuth to the sun (i.e. beta angle). The photovoltaic module surface and the load energy during solar stimulation allows researchers to quantify/predict voltage output based on exposure periods and adjust cell density and size to best suit an area's energy needs [39]. This study is relevant to the research effort because understanding solar irradiance principles and the stimulation periods for silicon-based solar cells allows energy engineers to establish an initial annual solar exposure in different areas of the world and alter the PV epitaxial growth process to maximize solar absorption properties [39].

1.4.3 Color Filter Impacts on Solar Absorption Qualities for PV. To specifically address the studies involving individual wavelengths in the electromagnetic (EM) spectrum and the impacts on photovoltaics, the study executed by Sudhakar et al. [61] aids in understanding the predicted electrical energy outputs for silicon triple-junction solar cells when exposed to the visible light spectrum. For the EM spectrum band of 400-780 nm, which is described as the approximate visible spectrum, a solar cell will exude certain electrical output profiles based on short, medium, and long wave penetrations of each wavelength internal to the cell [61]. It is shown in this study that as the spectrum frequency increases, the more penetration will occur inside a cell and allow for greater photon absorption; in this case the color red has the most penetration in long wave. The considerations presented, such as light filtering, wavelength profile, and light intensity helped shape the BBR test procedure for measuring photocurrent, as well as aid in the photocurrent measurement subsystem (PCMS) component selection. However, instead of applying a color filter and measuring PV electrical output, the research effort involves

the use of direct wave exposure using light emitting diodes to simulate solar energy collection. Using the Sudhakar et al. study [61] as a reference, it was extremely helpful in drawing some assumptions from the test, and what to anticipate based on what is described about solar stimulation on silicon crystalline solar cells.

1.4.4 Temperature Impacts on PV Chemical Composition and Resultant Output. To fully grasp the cell growth process, chemical combinations, and junction architecture, the paper from Yurong et al. [57] was helpful in attaining information about Gallium-arsenide based solar cells. In most terrestrial applications, strictly silicon-based PV technology is commonly found, however it is good to gain information on different chemical compounds that have unique characteristics to allow for greater photocurrent generation with higher temperature tolerances [57]. This paper was helpful in understanding how a gallium arsenide cell with a silicon-germanium substrate behaves under different temperature regimes that resemble an on-orbit high temperature condition. The paper highlights the higher photocurrent yields a cell with different chemical makeups can perform under higher epitaxial growth temperatures as opposed to the conventional silicon triple junction cell [57]. Considering how these cells perform, it would be beneficial to incorporate additional variables such as chemical composition and temperature to future iterations of the research effort. As new PV cell chemical structures and processes improve, it is pertinent to continuously evolve the proposed BBRS approach to account for these new cells and analyze for those that meet the PV-embedded airfoil architectures.

1.4.5 Power over the Life Cycle of a Vehicle. The 2015 technical publication from Hausgen and Carpenter [19] not only emphasizes the costs that coincide with development and integration for solar cell technology, but also lists some of the factors associated with overall electrical power performance. Correlating values such as total solar array cost to the total mass,

deployed surface area, mission power, and solar cell efficiency are key values for programmatic decision makers to decide on the technology readiness level for any new aerospace vehicle.

Through evaluating the specific power required for satellites in different orbits, Hausgen and Carpenter are able to conclude that vehicles at lower altitudes have less accelerated deterioration from BOL to EOL based on mass as a function of specific power for fixed mission power [19]. Relating these findings to the requirements for a smaller array surface area is important, as a more efficient cell design will yield less total mass for the array and minimize costs incurred for a PV-embedded HALE UAS structure. Intuitively this makes sense as the surface area of the UAS must be considered precious real estate, and if any adjunct payload is to accompany the vehicle it should be advantageous for the system [14, 40]. This aids in the research effort in that there is not only a need for smaller array designs and more efficient cells, but there is a desire to minimize program development and integration costs by evaluating power requirements at EOL for each UAS mission on a case-by-case basis. Research, development, test, and evaluation (RDT&E) costs can precipitously propagate in the engineering life cycle and formulating an alternative and cost-effective PV test solution early on is paramount.

1.4.6 Thermal Impacts on Solar Cell Performance. As a critical supporting document to subproblem 2 pertaining to thermal stress impacts on photocurrent yield, knowing that there is a relationship between thermal distortions to the solar cell based on environmental characteristics is important for future research efforts to optimize cell efficiency. In the 2010 paper from Kim & Han [30], they emphasize that since the solar array is thermally isolated from the UAS bus, that they are able to conduct a thermal analysis of the array alone. Knowing that the level of effort required for a thermal evaluation allows for independent testing of an individual component can save time, resources, and keep costs low for a program looking to enhance solar panel

technologies. Specular reflections and a worst-case analysis (i.e. hottest day with maximum solar intensity focused on the arrays) are evaluated in the test, which indicate that total array absorptance and emissivity contribute to the panel's ability to dissipate heat. Moreover, the team uses ground testing and modeling to validate their findings, which indicates that a test limitation was present in their study to preclude on-orbit data and still find test significance. This aids in the research proposal to show that use of thermal modeling can be useful to draw conclusions on thermal impacts on cell performance and methods to reducing heat over the array. Additionally, showing that a solar array built with the appropriate reflective material and coverglass can withstand the thermal fluctuations expected in a HALE environment. Furthermore, the heat dissipation requirements for continuous optimized cell performance presents strong evidence that the same dissipation measures need to be taken for smaller panel sizes.

Building on the foundations of the paper presented by Kim & Han, the 2014 research publication from Wang et al. [56] focuses specifically on the panel structure and impacts of thermally induced vibrations. Vibrations and acoustic shock have been shown to place additional stresses on cell strings and can even cause cracking of the cell coverglass; this can accelerate individual cell deterioration due to more direct exposure of a thermally undulating environment. For most solar arrays, rigid honeycomb panels are used as the primary mounting assembly, and different moments within the flight path can subject the panel to sustained levels of increased heat or cold. These oscillations can impact the magnitude of vibrations occurring within the panel, where high frequency levels have been shown to impact cell structural integrity. Understanding that this phenomenon can be accounted for and predicted through modeling Fourier's law of heat conduction and the penumbra (period where the panel is first exposed to sunlight after eclipse cycle) is important to factoring in another variable that can impact solar

power performance at the structural level for the entire array. From this information, using flexible solar cells became the standard for this research effort, where the freedom to minimize rigidity and fragility concerns for the cells outweighs the losses in efficiencies and PV output of many more efficient designs. While the other architectures may yield more output, they are fragile and mounting them to a large vibrating UAS platform would require a robust anti-vibration system setup and several protective layers.

1.4.7 New Solar Cell Designs. As renewable energy technology progresses, new solar cells are being developed using innovative techniques to change the way each junction/layer within a cell can change solar energy into electrical power. In the 2015 paper from Miyashita, Ahsan & Okada [38] the dilute nitride formation solar cell grown by molecular beam epitaxy is discussed. As with many new technologies, the eventual integration phase poses many risks, as these new designs have not been flight proven yet and meeting mission or program specific requirements have not been met. However, considering the dilute nitride architecture houses a four-junction material and has higher resiliency to heat, radiation and yields much higher efficiencies and photocurrent than triple junction cells, considering this as a future risk mitigation opportunity is good to mention. From a programmatic perspective, having an opportunity to qualify a cell for flight in future applications presents risk in and of itself, but can pay dividends down the line when conventional GaAs cells grown using a process called metal oxide chemical vapor deposition (MOCVD) will have stagnating efficiency levels and cannot meet electrical power requirements. This is important to the research effort to account for other cell types currently in development, consider there is a potential for GaAs cell efficiency to plateau, and recognize that there is a need for completely new flexible cell designs to be researched.

1.4.8 Solar Cell Manufacturing Changes. There are changes that can be made to the solar cell fabrication process that allow for a higher yield in photocurrent by altering the bandgap energy differential in cell layering. One such process is discussed in 2015 by Zhang et al. [58] by using the chemical vapor deposition phase to synthesize a graphene-silicon layer that can allow for greater potential and energy production in a solar cell. Comparing the test results between a layer using silicon, graphite, and silicon-graphene (SiG), the binding energy for SiG was significantly higher. This presents evidence that there are multiple growth process changes that can be made to increase cell efficiency. However, this testing was done at atmosphere one point five, or air mass ratio 1.5 (AM1.5), and in order to qualify space solar cells the testing must be proven at atmosphere zero, or air mass ratio 0 (AM0). The intended HALE UAS environment would likely be an environment between AM0 and AM1. An additional consideration for this is that once a chemical process changes in the certified solar cell synthesis, a requalification may be required as per the American Institute of Aeronautics and Astronautics S111 guidance. While this change may be beneficial, it is important to evaluate for the research proposal in that it highlights another risk area for future research and including program experts into this arguably proprietary process may prove time consuming and costly. Nevertheless, any process improvements that yield higher photocurrent and photovoltaic efficiencies are critical to evaluate.

CHAPTER 2

PHOTOVOLTAIC PERFORMANCE CHARACTERISTICS

2.1 Introduction

Solar cells are inherently designed to operate efficiently at different wavelengths and depend greatly on the materials used to manufacture them and understanding how to develop cells that exude certain desirable characteristics. Such characteristics of benefit to an unmanned aerospace system (UAS) would be sustainable voltage and power outputs under different conditions, which enables aerospace engineers the ability to predict photovoltaic responses more accurately [61]. The most fundamental and widely discussed characteristic for a solar cell is the electrical efficiency. Enabling scientists to better understand these characteristics and optimum performance conditions will allow for future research efforts to “create cells that will respond under a wide range of wavelengths in the electromagnetic spectrum” [61]. Fig. 2.1 illustrates the solar radiation spectrum, where a majority of the absorption that occurs for a solar cell is within the 400-780 nanometer (nm) spectrum. This spectrum range is where most of the photocurrent generated from a solar cell gains energy and is analyzed in this research work to determine how much short, medium or long wave energy penetrates into the junction material of a cell.

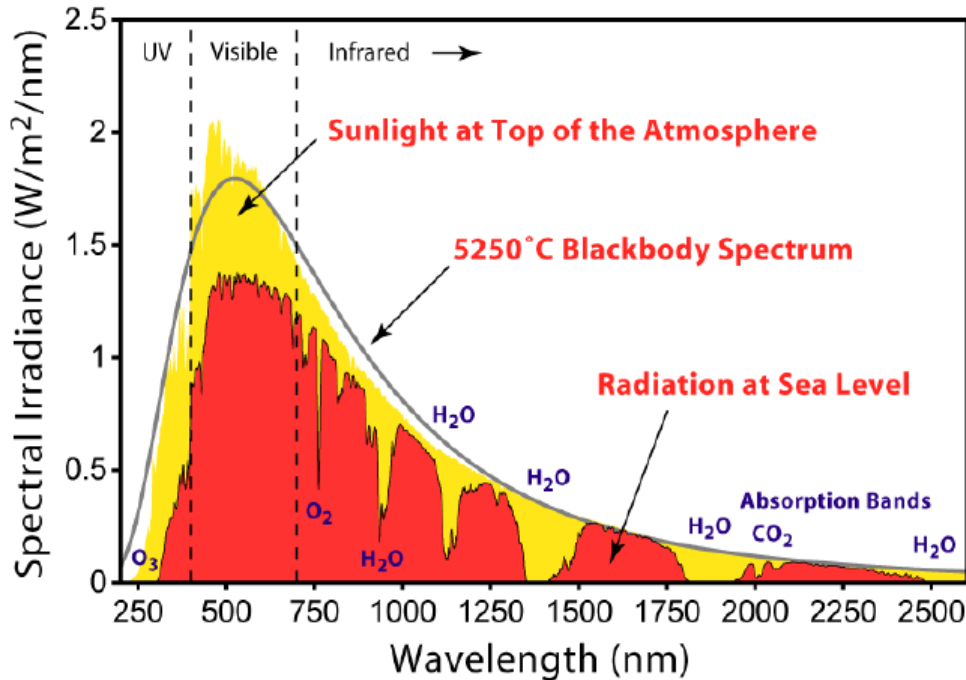


Fig. 2.1. Solar radiation spectrum graph illustrating the solar absorption qualities that are apparent for photovoltaics to generate photocurrent. For more details, the reader is referred to [61, Fig. 2].

There are established industry standards, set forth by such entities as the American Society for Testing and Materials (ASTM), where testing conditions such as regulated temperature and humidity are defined. However, fabricating a system that replicates an ideal simulated environment is expensive and problematic. Some of the specific standards this work addresses are described in detail.

2.1.1 Solar Cell Testing Standardization. Air mass with a spectrum of 1.5 (e.g., AM 1.5), is defined as the standard for solar cell testing as per ASTM G-173-03 (2012) in the “Standard Tables for Reference Solar Spectral Irradiances: Direct Normal and Hemispherical on 37° Tilted Surface”; this table denotes the specific conditions for achieving AM1.5 [45]. “The uncertainty in using AM 1.5 spectra to predict field performance depends on the particular PV device design and climate. The wavelength distribution of photon flux varies with respect to conditions such as water vapor and air mass, and this in turn influences current densities in PV

devices, depending on such device characteristics as bandgap(s). Therefore, PV device design (e.g. optimization) should be based on a range of spectra representing various atmospheric conditions and air masses” [45].

The one-sun illumination intensity of $100 \text{ mW}/\text{m}^2$ is achieved in a test environment most commonly through the utilization of an artificial light source, which was accomplished by a wavelength spectrum simulator using light emitting diodes (LEDs), and ideally the illumination source would have specific associated properties. These include a spatial non-uniformity of less than 1%, a variation in total irradiance with time of less than 1% and filtered for a given reference spectrum to have a spectral mismatch error of less than 1%. These requirements are essential in obtaining an accuracy of better than 2% [14]. Additionally, a constant cell baseplate temperature of 25°C was used, and photocurrent measurements were taken using a set of standard alligator clip connectors attached to a custom harness which is subsequently connected via a quick disconnect fitting to the photocurrent measurement control subsystem.

2.2 Photovoltaic Systems Theory and Background

In order to have a basic understanding of cell terminology, the following terms have been selected for further explanation as they are commonly used when discussing solar cell growth, power generation, and relative performance. Solar cells are commonly known as photovoltaics, with the typical electrical output represented in amperes (A) or milliamperes (mA) for the resultant photocurrent. Many terrestrial solar cells are silicon-based, whereas space cells have what is known as a Gallium Arsenide (GaAs) chemical composition for each layer and are grown on a Germanium (Ge) substrate [1, 58]. The “substrate” essentially acts as the foundation layer in which all the other layers are grown via MOCVD [38, 58]. For external factors, temperature exposures are typically expressed in degrees Celsius ($^\circ\text{C}$), with blackbody radiation in degrees

Kelvin (K), where qualification for cell designs in a terrestrial environment assume a standard of 25°C [37]. Solar energy is measured in terms of radiance and is represented in power densities of kilowatts per square meter (kW/m^2).

To best determine the amount of energy a solar cell can produce at a given moment or over a specified time interval, it is essential to first quantify several conditions numerically. Such conditions involve the quantification of solar illumination, or available energy from the sun, during specified time period(s) and geographic locations. Additionally, atmospheric interference needs to be accounted for since solar rays penetrate differently through the Earth's atmosphere and impact the total available luminous flux density available for photovoltaic (PV) devices. Prior to quantifying the energy flux present in the form of a blackbody, certain considerations need to be accounted for at the PV-level. Specifically, these considerations include: the chemical architecture and success of p-n channeling (i.e., PV cell conversion efficiencies), PV orientation, PV panel electrical architecture (e.g., solar cells mounted in series or parallel), and presence of losses within the cell due to temperature and cell design impacts.

2.2.1 Blackbody Radiation. The control of particular solar cell test variables such as temperature is important since every object emits radiant energy in an amount that is a function of its temperature [10]. The blackbody itself is described as a perfect emitter and perfect absorber where radiation is neither reflected nor transmitted through it. The two primary variables that are accounted for in the quantification of energy flux are largely temperature and the wavelength of light [55]. Accurately predicting the temperature for blackbody radiation at a given point is shown by (1) [55].

$$F_{BB} = \sigma T^4 \tag{1}$$

Where σ is the Stefan-Boltzmann constant, T is the temperature at the given point, which in the instance of this experiment the ideal temperature would be 25°C, or 298.15 K. Since the ideal test temperature is already determined, the energy flux based on the wavelength of light needs to be calculated using (2) [55].

$$F_{BB}(\lambda) = \frac{C_1(\lambda \times 10^6)^{-5}}{\left[\exp\left(\frac{C_2}{(\lambda \times 10^6)T}\right) - 1\right]} \quad (2)$$

Where C_1 and C_2 are flux equation constants and represented by $3.742 \times 10^8 \text{ Wm}^3/\text{K}$ and $1.439 \times 10^4 \text{ m/K}$, respectively. Substituting a wavelength value for λ is representative of the manufacturer's wavelength measurement as shown in Fig. 2.2 for a 1.10mm red chip LED with part number LL-S150VC-V1-2B.

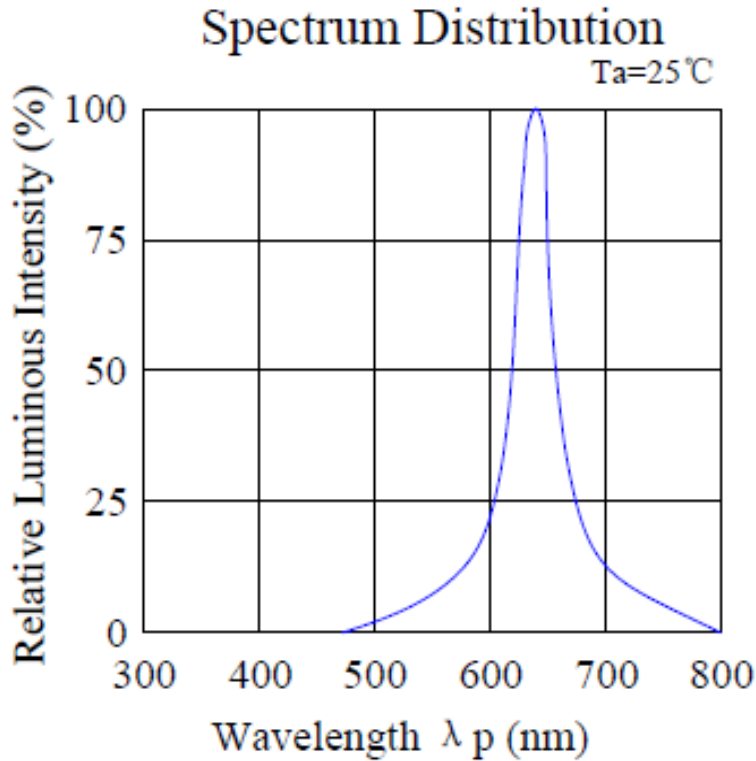


Fig. 2.2. Electro-optical characteristic curve for red chip LED, part number LL-S150VC-V1-2B. The graph shows an approximate wavelength of 620 nm based on a relative luminous intensity of 100%. For more information, the reader is referred to [34, Fig. 18].

The dominant wavelength (λ_D) was used for the experimental standard for each LED, where λ_D is the single wavelength which defines the color of the device. Given the dominant wavelength of 624 nm for the red LED, at a temperature of 25 C/298.15 K, and substituting into (1) and (2) yields an energy flux of 1.030×10^{-24} W/m². Using a similar product from the same manufacturer to simulate blue and green colors and wavelengths based on their respective electro-optical characteristic curve under the same conditions is shown in Table 1.

TABLE 1
ENERGY FLUX BASED ON WAVELENGTH OF LIGHT

<i>Part No.</i>	<i>Color</i>	<i>Dominant Wavelength (nm)</i>	<i>Peak Emission Wavelength (nm)</i>	<i>Flux (W/m²)</i>
LL-S150VC-V1-2B	Red	624	620	1.030×10^{-24}
S-150PGC-G5-1B	Green	525	520	1.135×10^{-30}
LL-S150BC-B4-1B	Blue	470	468	4.209×10^{-35}

Note. Calculated energy flux based on the specific wavelength of light from a light emitting diode using (2); calculations assume 298.15 K, and 100% relative luminous intensity

To minimize wavelength deviations outside the center of the bell curve in Fig. 2.2, the lux intensity was measured with a lux detector, where the total luminosity was taken over the tested surface area. The lux is an SI unit for light intensity/illuminance per unit surface area, shown by the irradiance source exposure value ($E_{V(lux)}$), and the relationship between lux and lumens is shown by (3).

$$\Phi_{V(lumens)} = E_{V(lux)} \times PV \text{ Area } [m^2] \quad (3)$$

Similar to (2), the emissive power per unit area of a blackbody (in W/m² um) can be expressed through Planck's law, shown in (4) [36] below.

$$E_{\lambda} = \frac{3.74 \times 10^8}{\lambda^5 \left[\exp\left(\frac{14400}{\lambda T}\right) - 1 \right]} \quad (4)$$

Where E_λ is the blackbody emissive power per unit area, T is the blackbody absolute temperature (K) and λ is the wavelength (μm). Since the objective of this section is to describe blackbody radiation and the resultant power per unit area, it is important to consider different quantitative approaches as the determination of available energy for solar to electric energy conversion is a critical first step.

2.2.2 External Factors for Photovoltaic Performance. Another critical step in determination of available energy for solar to electric energy conversion is the impact of the Earth's atmosphere. The air mass ratio is a measure of the amount of atmosphere the sun's rays must pass through to reach the Earth's surface; this ratio is expressed by m , and for a scenario where the sun is directly overhead, $m = 1$ [36]. Aside from more complex model considerations discussed in section 2.3.1, Fig. 2.3 below can be helpful to determine the basic air mass ratio for a solar problem.

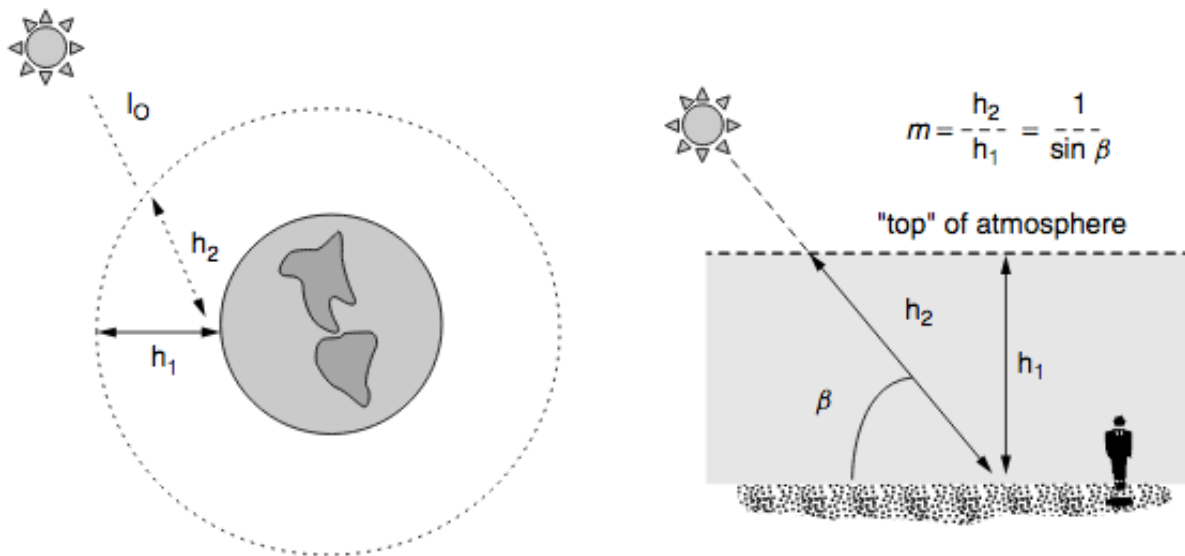


Fig. 2.3. Illustration of air mass ratio geometries for an Earth-Sun orbit (left), with ground-based geometry and resultant equation shown (right). For more details, the reader is referred to [36, Fig. 2].

The air mass ratio can be calculated simply by use of (5) below, where h_1 is the path height through the atmosphere when the sun is directly overhead, h_2 is the path height through the atmosphere to reach a spot on the surface, and β is the solar altitude angle [36].

$$m = \frac{h_2}{h_1} = \frac{1}{\sin \beta} \quad (5)$$

This discussion is relevant in that the air mass ratios are discussed heavily in solar cell standardized testing. By convention, an air mass ratio of 1 is represented by AM1, with AM1.5 assumed for an average solar spectrum at the Earth's surface. Under this assumption, approximately 2% of the incoming solar energy is in the UV spectrum, 54% in the visible spectrum, and 44% in the IR spectrum.

2.2.3 Photovoltaics as a Semiconductor. When describing a PV device as a semiconductor, it is pertinent to also describe the characteristics of a diode and how current flows across a p-n channel or junction. Fig. 2.4 below illustrates the diode junction and characteristic curve as a function of voltage and current.

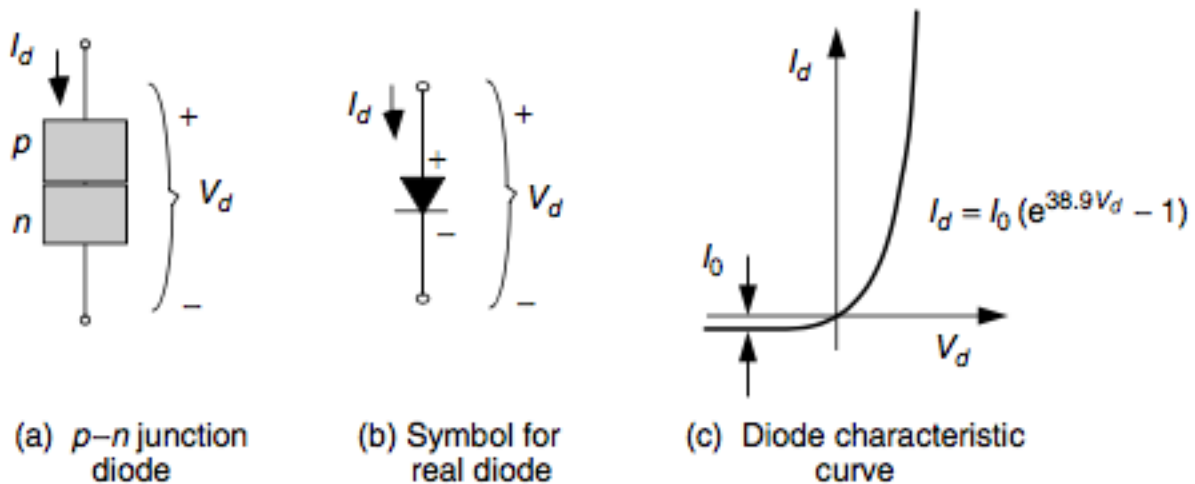


Fig. 2.4. A p-n junction diode allows current to flow easily from the p-side to the n-side, but not in reverse. (a) p-n junction; (b) its symbol; (c) its characteristic curve. For more details, the reader is referred to [28, Fig. 15].

It is pertinent to note that the diode in Fig. 2.4 is tested under standardized test conditions (i.e., 25C, and AM1.5) and is considered an “ideal diode”. Therefore, the use of the Shockley diode equation as shown in (6.1) is assumed, where its corresponding treatment is shown below in (6.2) to yield the simplified form in (6.3).

$$I_d = I_0 \left(e^{\frac{qV_d}{kT}} - 1 \right) \quad (6.1)$$

$$\frac{qV_d}{kT} (\text{at } 25^\circ\text{C}) = \frac{1.602 \times 10^{-19}}{1.381 \times 10^{-23}} \left(\frac{V_d}{T} \right) = 11600 \left(\frac{V_d}{298.15 \text{ K}} \right) \quad (6.2)$$

$$\therefore I_d = I_0 (e^{38.907V_d} - 1) \quad (6.3)$$

This is an important equation and relationship for PV devices, as other electrical characteristics such as the reverse saturation current, diode current, and diode voltage can be calculated. Semiconductor material is also a vital part of the consideration process for solar cell technology, where efficiencies can be improved through utilization of different materials. More specifically, current PV technology commercially available primarily employs pure crystalline silicon as the primary semiconductor material, where at absolute zero, silicon is a perfect electrical insulator [36]. Since PV technology has a clearly defined relationship with temperature in terms of electrical output, it is important to note that as temperature increases, the more electrons will free themselves from their nuclei and thus increase the free electrons to flow as electric current [25]. An important performance variable as part of the semiconductor material discussion is to explore the differences in bandgap energy between silicon and other materials such as Gallium Nitride (GaN); this discussion is continued in section 2.5.1.6.

2.3 Photovoltaic System Performance Modeling

A comprehensive approach to estimating PV system output should account for each cell output impacted by several factors, including: (1) temperature, (2) insolation flux density, (3) suboptimal panel slope, and (4) local solar climate characteristics as they vary throughout the year [55]. The first step in this approach is to approximate the average daily panel output (E) based on insolation summed over the month, as shown by (7) below.

$$E_{month}[kWh] = \frac{A \Sigma_{month} \eta_i I_i}{N} \quad (7)$$

Where E is the monthly averaged energy output, A is the panel area (m^2), η_i is the average hourly panel efficiency, I_i is the integrated insolation for the hour (kWh/m^2), N is the number of days in the integration period, and Sigma is the daylight monthly hours sum.

Subsequently, per (8) [55] below is representative of the average panel efficiency.

$$\eta_i = \eta_{rated} [1 - \beta(T_{c,i} - T_{rated}) + \gamma \log_{10}(I_i)] \quad (8)$$

Where η_i is the hourly cell efficiency as a function of cell and array design, temperature, and insolation density, β is the temperature efficiency coefficient, $T_{c,i}$ is the average hourly cell temperature, T_{rated} is the cell efficiency temperature rating, and gamma is in the cell efficiency insolation flux density coefficient [55]. Aside from using tedious calculations to forecast PV power outputs over the course of a solar day, a computation and subsequent visual can be provided from a custom-made program using the LabView19 software package, as shown in Fig. 2.5 and Fig. 2.6 below.

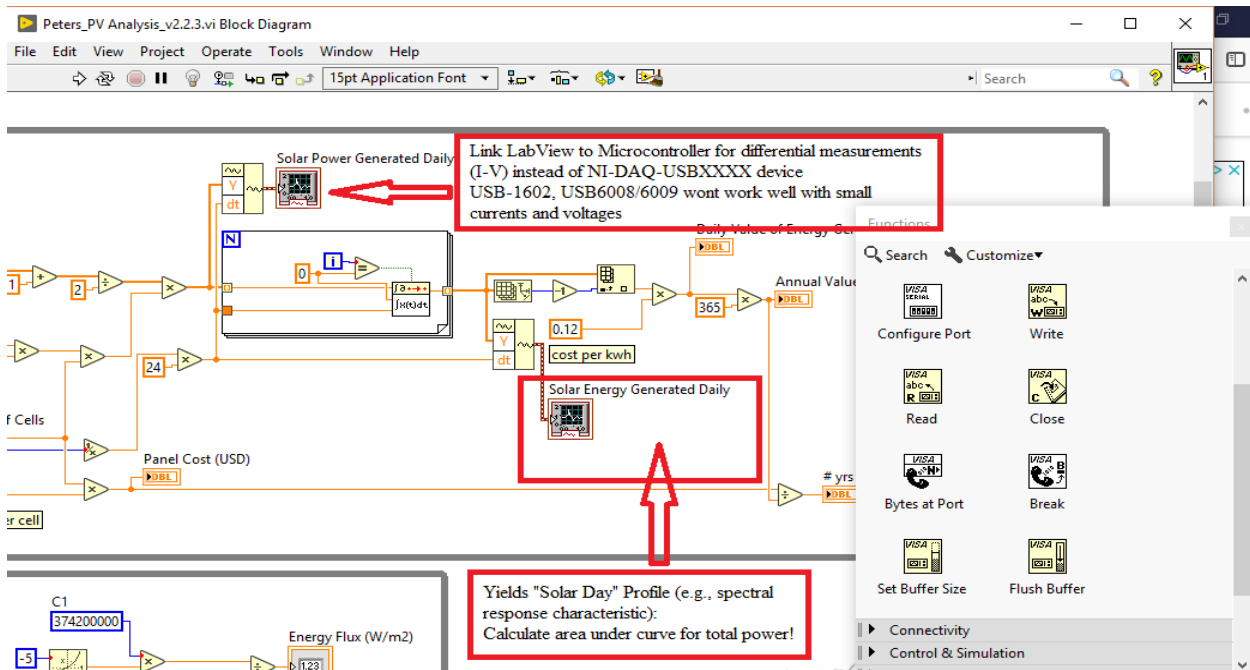


Fig. 2.5. Current version of LabVIEW19 solar cell calculator v.2.2.3. The arrow illustrates a potential future version intended to sync up measurement device(s) to LabVIEW directly. From the spec sheets, the NI USB-6008/6009 devices might not be able to pick up small currents and voltages generated by the solar cell under different wavelengths. Therefore, the use of the voltage divider circuit (validated with multimeter) has been used to generate I-V data. Subsystems can be linked directly to LabVIEW using command structure within the SS code to send serial data to LabVIEW.

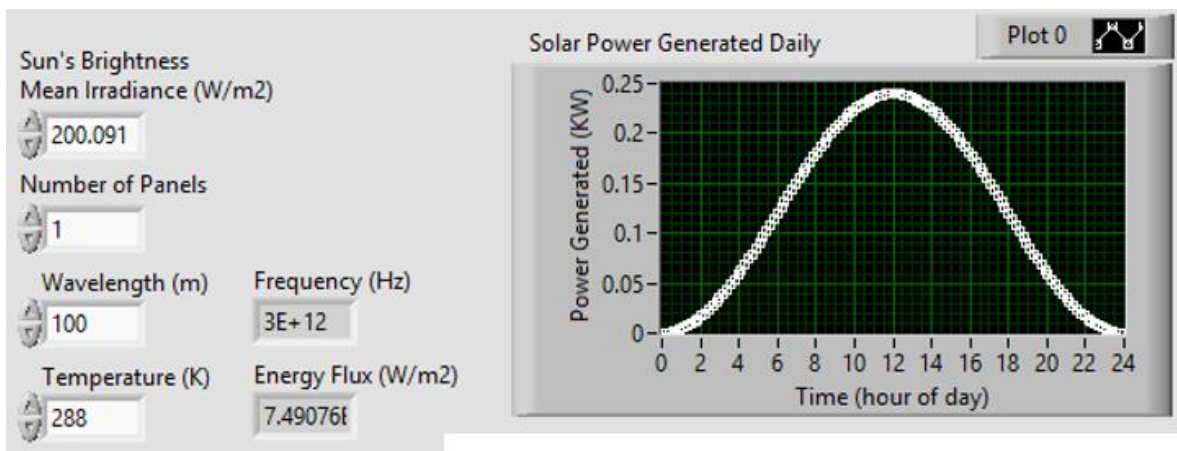


Fig. 2.6. Solar power generation calculator using LabVIEW19. This program is built using silicon solar cells with a bandgap energy of 1.12 eV, 63cm^2 surface area cells with a solar mean irradiance of 200 W/m^2 . The area under the graph to the right is depicting a simulated solar energy profile for a standard solar day and assumes a clear sky radiation index of $k = 1$.

By utilizing this software, the PV response over a specified range of values such as wavelength and energy flux of incoming light can be measured, yielding a normal distribution shown in Fig. 2.6 above. This distribution establishes the standard for what is expected for the experimental PV design resulting from stimulation in each wavelength of light. It was expected that this normal distribution for a flat cell in terms of power output over time or beta angle would be present for each wavelength of light used in the BBRs. Deviations from this normal distribution were expected and evident from skewed distributions resulting from an irregularly shaped PV design. The differences from the flat cell and curved cell data set were evaluated and served as the basis for the spectrum response characteristic (SRC). This characteristic was used to further establish a correction factor that accounts for the SRC over a band of spectral geometries; the mathematical framework for this correction factor is provided in section 4.6.

2.3.1 Atmospheric Modeling. As mentioned previously, a basic air mass ratio can be calculated for a given solar collection problem, however there are more sophisticated atmospheric modeling and calculation efforts to discuss as part of the research effort. Although the intent of this effort is to propose an alternative approach for standardized PV-embedded systems testing, the resultant BBRs data collected can be further analyzed to meet specific geographic mission requirements that more closely resemble the operational environment.

2.3.1.1 Relative Earth-Sun Geometry Calculations. For the research effort, it should be noted that for a moving UAS intended to utilize PV devices in a fixed position, a dynamic model would need to be generated to better predict the maximum power points in terms of beam radiation arrival angles and energy flux to best predict the conditions in the planned operational environment.

Some basic calculations to assist with the concept of predicting Earth and Sun relative positioning are provided below, as this will help a researcher understand the relationship between fluctuating intensity levels of solar energy based on time of year, and geographic position on Earth. The first problem is to discuss the Earth's orbit and the variation of its distance during the year from the Sun, as increased distances can reduce optimized solar intensities. Using the calculation method below, we can calculate the minimum and maximum distances Earth will be from the Sun. Assume that the point at which the Earth is nearest the Sun, the perihelion, occurs on January 2, at which point it is a little over 147 million kilometers away. At the other extreme, the aphelion, which occurs on July 3, the Earth is about 152 million kilometers from the Sun. This variation in distance is described by (9) [36] below, where n is the number of calendar days.

$$d = 1.5 \times 10^8 \left\{ 1 + 0.017 \sin \left[\frac{360(n-93)}{365} \right] \right\} \quad (9)$$

Using (9), it is determined that the minimum and maximum distances from the Earth to the Sun will occur on January 2 at 1.47×10^8 km, and July 3 at 1.52×10^8 km respectively. Another calculation technique would be to determine the desired angle(s) for a specific orientated PV device to have it normal to the sun's rays at solar noon (e.g., achieve maximum power point angles for a fixed PV array angle). A South-facing collector at 36 degrees latitude, the desired angles can be calculated by a desired day, such as January 1, and assume that to find the angle for a solar collector using normal vectors relative to the sun's rays that the optimal tilt angle β_N is determined by (10) [36] below.

$$90^\circ - \beta_N = \text{Latitude } (L) - \text{equinox } (\delta) \quad (10)$$

Where the equation to find the equinox angle δ is given by (11) [36], and n is the number of days in the solar year, and L is 36 degrees.

$$\delta = 23.45^\circ \sin\left(\left(\frac{360^\circ}{365 \text{ days}}\right)(n - 81)\right) \quad (11)$$

Since January 1st is the first day of the calendar year, n would be equal to 1, where δ needs to first be calculated as $\delta = 23.45^\circ \sin\left(\left(\frac{360^\circ}{365 \text{ days}}\right)(n - 81)\right) \rightarrow \text{if } n = 1 \rightarrow \delta = -23.0097^\circ$. Now that the delta is computed, the optimum solar array angle can be calculated using (12) [36] below.

$$\beta_N = 90^\circ - (L + \delta) \quad (12)$$

Where the final solar array angle is computed as $\beta_N = 90^\circ - (L + \delta) = 90^\circ - (36^\circ + (-23.0097^\circ)) = 77.0097^\circ$.

Other valuable techniques involve the use of determination of solar time, which can be especially helpful for this research effort in optimizing solar collection opportunities based on a desired operating region. If the PV-powered UAS is intended to operate in a desert environment such as Iraq for reconnaissance but is mostly tested in a US region that is mostly covered with clouds, such as Seattle, then adjustments need to be made for training versus actual environments. This method can help with some of the basic geometry corrections based on latitude, to calculate solar time, and solar altitude angle. Assume that the latitude for Seattle is 47 degrees, and that the training is held mostly in the summer, where for this analytical example assume June 21st is indicative of the summer solstice. Additionally, assume that the Earth rotates around the sun at approximately 15 degrees per hour for a value of H , the azimuth angle for due west will be approximately -90 degrees, and that the solar declination (i.e., delta value) is known at 23.45 degrees. An analyst can use (13) [36] below to find the time of the day (i.e., solar time) at which the sun will be due West.

$$\cos H \geq \frac{\tan \delta}{\tan L}, \text{ then } |\phi_S| \leq 90^\circ; \text{ otherwise } |\phi_S| > 90^\circ \quad (13)$$

From this, the hour angle is solved by $H = \cos^{-1} \frac{\tan \delta}{\tan L} = \cos^{-1} \left(\frac{\tan 23.45}{\tan 47} \right) = -66.14 \rightarrow$
assuming 15° per hour $\rightarrow -\frac{66.14}{15} = -4.4093$ hours. Since the objective is to find the solar time when the sun will be due West, then the sun will be setting, and therefore it is required to subtract 4.4 hours from solar noon, where *solar time* = 12:00 – (–4.4093) = 16:24:33. The same method can be applied for a sun rising condition (e.g., solar time when the sun will be due East).

The altitude angle of the sun is calculated by (14) [36] below.

$$\sin \beta = \cos L \cos \delta \cos H + \sin L \sin \delta \quad (14)$$

Where substituting the information from the hour angle, latitude, and summer solstice delta (23.45 degrees) yields $\beta = \sin^{-1}((\cos 47)(\cos 23.45)(\cos -66.14) + (\sin 47)(\sin 23.45)) = \sin^{-1}(0.5441) = 32.965^\circ$. These calculations can also be built into a Microsoft excel file and used to run calculations quickly for any UAS operator intending to make solar predictions for the PV system based on orientation.

2.3.1.2 Relative Earth-Sun Energy Calculations. The most important result from understanding these methods is that the UAS operator can take the position information and predict available solar energy for the PV system to accomplish electrical energy conversion. Once again assuming a South-facing PV array condition at the first of the year on January 1 at solar noon, with a latitude of 40 degrees, we can determine the direct beam insolation normal to the sun's rays, the beam radiation for a tilted surface, diffuse radiation, and reflected radiation on

the PV array. The direct beam insolation (I_B) is shown in Fig. 2.7 and can be calculated using (15) [36] below.

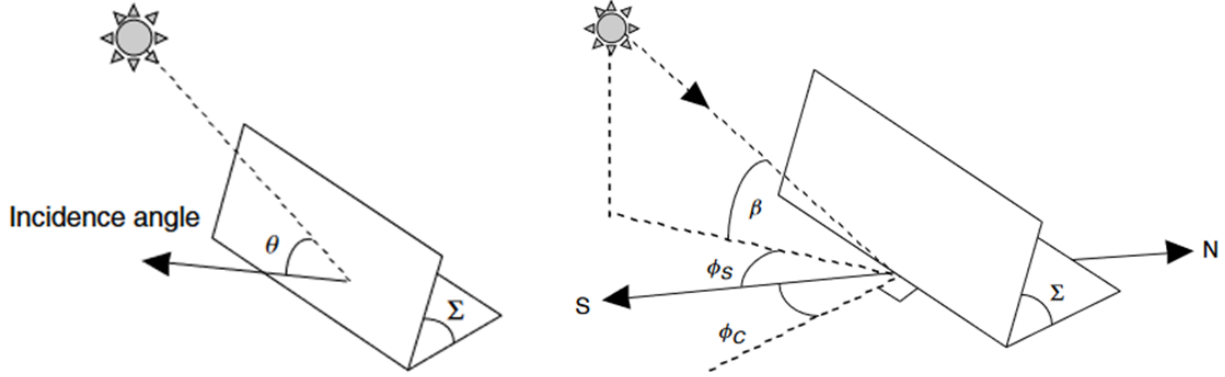


Fig. 2.7. Illustration of beam radiations in different configurations. The left image depicts the simplified direct beam radiation where θ is the angle between a vector normal to the collector face and the incoming solar beam radiation. The right image shows the collector azimuth angle ϕ_C and tilt angle along with the solar azimuth angle ϕ_S and altitude angle β . For more details, the reader is referred to [36, Fig. 20-21].

$$I_B = Ae^{-km} \quad (15)$$

Solving for A is accomplished by $A = 1160 + 75 \sin\left(\left(\frac{360}{365}\right)(n - 275)\right) \rightarrow \text{if } n = 1 \rightarrow$
 $A = 1234.99 \text{ W/m}^2$. Where the value k is solved as $k = 0.174 + 0.035 \sin\left(\left(\frac{360}{365}\right)(n -$
 $100)\right) \rightarrow \text{if } n = 1 \rightarrow k = 0.1393$. The next step is to solve for the optimal solar altitude angle,
 which reuses (11) from earlier, as $\beta_N = 90 - L + \delta = 90^\circ - (40^\circ) + \left[23.45 \sin\left(\left(\frac{360}{365}\right)(1 -$
 $81)\right)\right] = 26.99^\circ$. Using the angle, the value of m , or air mass ratio, can now be computed reusing
 (5), as $m = \frac{1}{\sin \beta_N} = \frac{1}{\sin 27} = 2.203$. Where $\therefore I_B = Ae^{-km} = (1234.99)e^{-(0.1393)(2.203)} =$
 $908.703 \frac{W}{m^2}$.

Since I_B is representative of direct beam radiation (i.e., normal to the irradiance source, or sun's rays), it must be translated to account for a striking a tilted collector face (I_{BC}) shown in Fig. 2.7 above, and can be calculated using (16) [51] below.

$$I_{BC} = I_B \cos \theta \quad (16)$$

Where θ is the angle drawn from the incoming beam radiation, and a line drawn normal to the collector face [36]. Which for this example problem is shown by $\cos \theta = \cos \beta \cos(\phi_S - \phi_C) \sin \Sigma + \sin \beta \cos \Sigma$, and is shown as: $\cos 27 \cos(0 - 0) \sin 40 + \sin 27 \cos 40 = 0.9204$. Where $\therefore I_{BC} = I_B \cos \theta = (908.703)(0.9204) = 863.396 \frac{W}{m^2}$.

The diffuse radiation is illustrated in Fig. 2.8 and can be calculated using (17) [51] below.

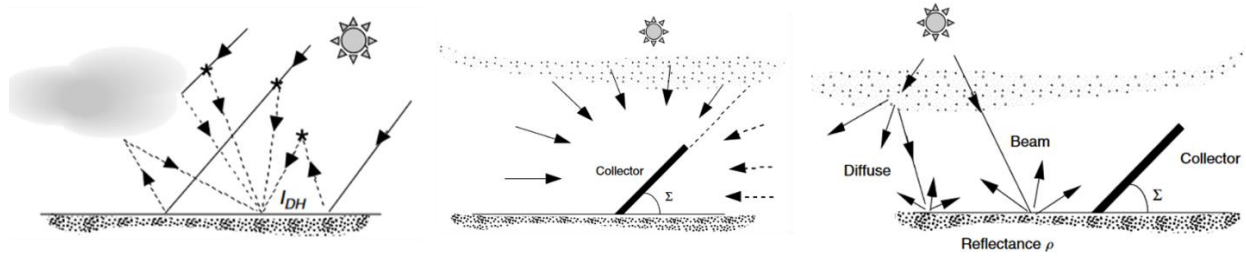


Fig. 2.8. Different solar radiation geometries. The left image depicts multiple scattering patterns for diffuse radiation, which can be scattered by atmospheric particles and moisture or reflected from clouds. The center image illustrates the diffuse radiation on a collector assumed to be proportional to the fraction of the sky that the collector “sees”. The right image shows several beams of solar radiation where the ground is assumed to reflect radiation with equal intensity in all directions. For more details, the reader is referred to [36, Fig. 22-24].

$$I_{DC} = C I_B \left(\frac{1 + \cos \Sigma}{2} \right) \quad (17)$$

However, the value of C must first be calculated assuming $n=1$, where then $C = 0.095 + 0.04 \sin \left(\left(\frac{360}{365} \right) (n - 100) \right) = 0.0554$. Where $\therefore I_{DC} = C I_B \left(\frac{1 + \cos \Sigma}{2} \right) = (0.0554)(908.703) \left(\frac{1 + \cos 40}{2} \right) = 44.42 \frac{W}{m^2}$.

For a given ground reflectance coefficient (ρ), the reflected radiation illustrated in Fig. 2.8 can be calculated using (18) [51] below.

$$I_{RC} = \rho I_B (\sin \beta + C) \left(\frac{1 - \cos \Sigma}{2} \right) \quad (18)$$

Where $I_{RC} = (0.2)(908.703)(\sin 27 + 0.05534) \left(\frac{1 - \cos 40}{2} \right) = 10.83 \frac{W}{m^2}$. Through an understanding of these computations, not only can an ideal conditions calculator be developed in Excel, Matlab, or Simulink, but they also help establish the theoretical framework for the PV system performance correction factor discussed in Chapter 4. This is also important because when the UV, visible, and IR spectrum are evaluated individually in terms of the PV system's response to these respective regions, decisions on which spectrum to utilize for future testing are made, which is discussed when addressing subproblem 2 in Chapter 4 and in the future work in Chapter 5.

2.3.1.3 ASHRAE Clear-Sky Radiation Modeling. This approach is very common when attempting to predict a PV array performance given a specific set of parameters, such as the time of year, declination, surface azimuth, surface tilt, and even reflectance values [55]. A basic model was formulated using Microsoft Excel and is shown in Fig. 2.9 as a modeling tool to evaluate the total solar radiation incident on an inclined PV array.

Atmospheric Modeling: Ashrae Clear Sky Radiation Model (allows PV performance prediction without irradiance measurement)			
Predict the amount of total solar radiation incident on an inclined PV panel or wing			
Inputs			
Variable	Symbol/Equation	Value	Unit
Month:		10	
Day:		6	
Latitude:		45	Degrees
Surface Azimuth:		0	Degrees
Surface Tilt:		90	Degrees
Ground Reflectance:		0.13	
Outputs			
Number of Days:	<i>n</i>	279	Days
Declination:		-6.18	Degrees
n-D:		273	
Intermediate Calc. for n-D:		243.00	
Sunset		83.78	Degrees
Sunrise		6.41	Hours
Sunset		17.59	Hours
Intermediate Calc. for A:		365.00	
Intermediate Calc. for B:		0.18	
Intermediate Calc. for C:		0.09	
A:		378	
B:		0.16	
C:		0.073	

Ashrae Model			
$R_{Tc} = R_{Dc} + R_{at} + R_{rt}$	(1)		
$R_{Dc} = R_b \cos \theta_s$	(2)		
$R_{at} = C R_b \left[\frac{1 + \cos \beta}{2} \right]$	(3)		
$R_{rt} = \rho R_b (\sin \gamma_s + C) \left[\frac{1 - \cos \beta}{2} \right]$	(4)		
$R_b = E \exp \left(-\frac{k}{\sin \gamma_s} \right)$	(5)		
$\delta = 23.45 \sin[360(284 + D)/365]$			
$\omega = 15(LMT - TZ - 12) + LL + ET/4$			

Inputs		Outputs											
SOLAR TIME	Solar Altitude (deg)	Solar Azimuth (deg)	Angle of Incidence (deg)	Incident Flux (BTU/hr-ft ²)				Transmitted		Intermediate Calcs		Solar Transmission and Absorption	
				IDN	ID	Id	IR	Single DSA	SHGF	BTU/Hr-ft ²	BTU/Hr-ft ²	Cos(theta)	Idv/Idh
5.0	-14.96	-96.29	96.07	0.0	0.0	0.0	0.0	0.0	0.0	-0.106	0.51	0.00	0.000
5.5	-9.67	-90.91	90.89	0.0	0.0	0.0	0.0	0.0	0.0	-0.016	0.54	0.00	0.000
6.0	-4.37	-85.62	85.63	0.0	0.0	0.0	0.0	0.0	0.0	0.076	0.59	0.19	0.051
6.5	0.89	-80.33	80.33	0.0	0.0	0.0	0.0	0.0	0.0	0.168	0.63	0.40	0.065
7.0	6.07	-74.96	75.04	83.3	21.5	4.2	1.0	16.3	17.1	0.258	0.68	0.57	0.063
7.5	11.12	-69.40	69.81	164.9	56.9	8.9	2.8	48.2	50.5	0.345	0.74	0.68	0.058
8.0	15.98	-63.59	64.68	211.4	90.4	12.3	4.8	81.9	85.6	0.428	0.79	0.76	0.056
8.5	20.60	-57.42	59.73	239.9	120.9	14.9	6.6	113.7	118.7	0.504	0.85	0.80	0.056
9.0	24.89	-50.80	55.02	258.5	148.2	17.0	8.3	142.1	148.3	0.573	0.90	0.82	0.057
9.5	28.79	-43.68	50.66	271.1	171.9	18.9	9.8	166.6	174.0	0.634	0.95	0.84	0.058
10.0	32.18	-35.97	46.77	279.9	191.7	20.4	11.0	187.1	195.4	0.685	1.00	0.85	0.058
10.5	34.98	-27.67	43.48	286.0	207.5	21.5	12.0	203.5	212.4	0.726	1.03	0.85	0.057
11.0	37.08	-18.82	40.96	289.9	218.9	22.4	12.7	215.4	224.8	0.755	1.06	0.86	0.056
11.5	38.38	-9.53	39.36	292.1	225.9	22.9	13.2	222.7	232.3	0.773	1.07	0.86	0.055
12.0	38.82	0.00	38.82	292.8	228.2	23.1	13.3	225.2	234.9	0.779	1.08	0.86	0.055
12.5	38.38	9.53	39.36	292.1	225.9	22.9	13.2	222.7	232.3	0.773	1.07	0.86	0.055
13.0	37.08	18.82	40.96	289.9	218.9	22.4	12.7	215.4	224.8	0.755	1.06	0.86	0.056
13.5	34.98	27.67	43.48	286.0	207.5	21.5	12.0	203.5	212.4	0.726	1.03	0.85	0.057
14.0	32.18	35.97	46.77	279.9	191.7	20.4	11.0	187.1	195.4	0.685	1.00	0.85	0.058
14.5	28.79	43.68	50.66	271.1	171.9	18.9	9.8	166.6	174.0	0.634	0.95	0.84	0.058
15.0	24.89	50.80	55.02	258.5	148.2	17.0	8.3	142.1	148.3	0.573	0.90	0.82	0.057
15.5	20.60	57.42	59.73	239.9	120.9	14.9	6.6	113.7	118.7	0.504	0.85	0.80	0.056
16.0	15.98	63.59	64.68	211.4	90.4	12.3	4.8	81.9	85.6	0.428	0.79	0.76	0.056
16.5	11.12	69.40	69.81	164.9	56.9	8.9	2.8	48.2	50.5	0.345	0.74	0.68	0.058
17.0	6.07	74.96	75.04	83.3	21.5	4.2	1.0	16.3	17.1	0.258	0.68	0.57	0.063
17.5	0.89	80.33	80.33	0.0	0.0	0.0	0.0	0.0	0.0	0.168	0.63	0.40	0.065
18.0	-4.37	85.62	85.63	0.0	0.0	0.0	0.0	0.0	0.0	0.076	0.59	0.19	0.051
18.5	-9.67	90.91	90.89	0.0	0.0	0.0	0.0	0.0	0.0	-0.016	0.54	0.00	0.000
19.0	-14.96	96.29	96.07	0.0	0.0	0.0	0.0	0.0	0.0	-0.106	0.51	0.00	0.000

Fig. 2.9. ASHRAE clear sky radiation modeling tool formulated using Microsoft Excel. The standard model shown assumes a time of year for October 6th, with a latitude of 45 degrees, surface azimuth of 0 degrees, surface tilt of 90 degrees, and ground reflectance values of 0.13. Outputs for the system are provided in green, with additional outputs shown in the resultant table for solar transmission and absorption [11, 27, 35, 55].

This type of calculation tool can be useful for designers to quickly determine the amount of solar radiation available for solar to electric conversion given a particular time of year and PV array tilt angle.

2.3.1.4 Average Daily Insolation Calculations. Computing the average daily insolation can be accomplished using Matlab. This is an important consideration when predicting PV system output, because it takes into account the daily insolation (i.e., thermal energy) for a

specific geographic region, the average clearness index (i.e., K-value, or ratio of solar irradiation on horizontal surfaces to solar irradiation outside the atmosphere), and the atmospheric transmittance based on air temperature. This approach is similar to the ASHRAE clear sky radiation approach but assists with further calculations for the ratio of the average insolation on a tilted surface to the corresponding average total insolation on a horizontal surface; this is represented by (19) [11, 55] below where ρ is the ground insolation reflectivity coefficient.

$$\bar{R} = \left(1 - \frac{\overline{H_d}}{\bar{H}}\right) \overline{R_{b,\beta}} + \left(\frac{\overline{H_d}}{\bar{H}}\right) \left(\frac{1 + \cos(\beta)}{2}\right) + \frac{\rho[1 - \cos(\beta)]}{2} \quad (19)$$

The code and references to the appropriate equations is shown in Appendix I, with the resultant outputs given in Fig. 2.10 below.

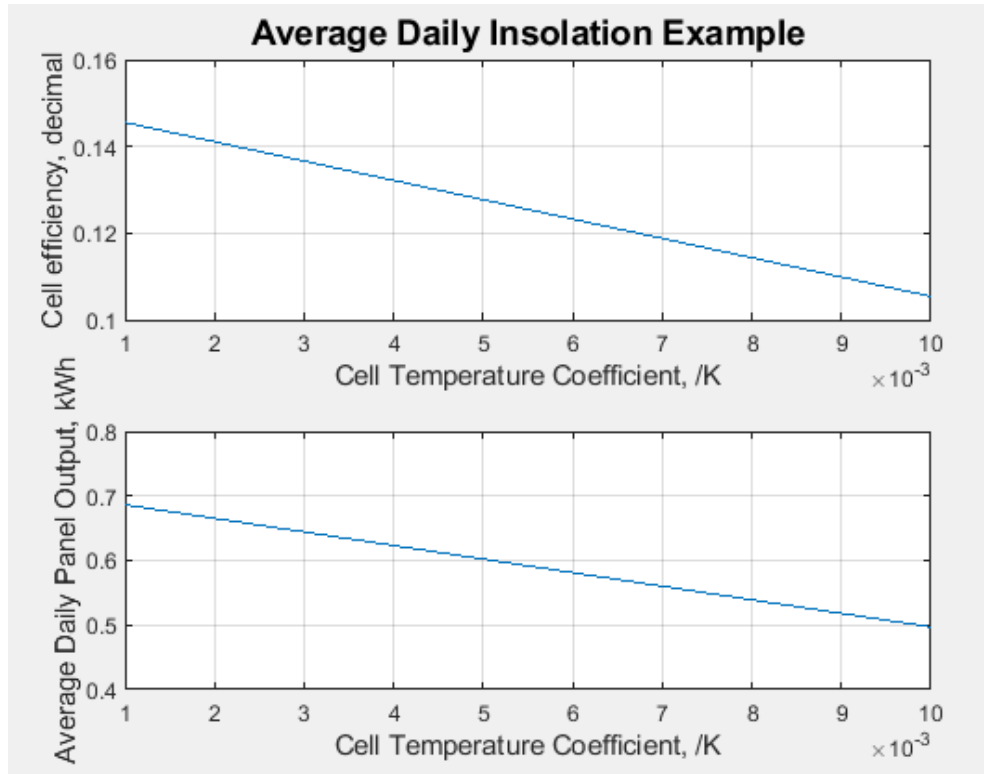


Fig. 2.10. Matlab-generated graphs for an average daily insolation example assuming a time of year for October 6th, with a latitude of 45 degrees, surface azimuth of 0 degrees, surface tilt of 90 degrees, and ground reflectance values of 0.13. For more details, the reader is referred to [55], geographical solar radiation data gathered from and available at [41, 42].

This further analysis capability gives engineers the ability to quickly predict and tabulate average daily panel output in kilowatt hours (kWh) given a specific geographic area, temperatures, and cell efficiencies. This analysis takes the basic ASHRAE radiation model a step further and can be helpful when determining possible PV system losses for PV-embedded airfoil technology operating in different operational environments and different times of the year.

2.4 Existing Photovoltaic Test Methods

Through execution of a literature review of the solar cell radiation handbook [51], it was helpful in assessing how to effectively test solar cells and panels and developing relevant technologies to enhance the understanding of photovoltaic device behaviors under illumination. The most commonly used measurement in the analysis of radiation effects (e.g., blackbody radiation) in solar cells is the current-voltage characteristic under illumination [51]. There is a strong and distinct relationship between solar cell response and optical wavelength, the light source is a major variable in the evaluation of solar cell parameter changes. To accomplish testing how the PV device behaves as a function of optical wavelength, wavelength-calibrated light emitting diodes were used as a solar illumination source with a separate subsystem (i.e., Spectrum Calibration and Response Subsystem – SCARS) measuring the emitted luminosity in lux. Maintaining a consistent illumination level will aid in providing a unique solar cell response, especially when subjecting the cell to different angles of incidence. Additionally, fabricating a subsystem with the functionality to accurately manipulate the solar illumination source at different beta angles (e.g., angles of incidence relative to the solar cell normalized orientation) would allow for different wavelength impacts as a function of illumination angle. Utilizing this beta profile, a PV system user can evaluate a device based on a desired profile for flat or irregularly shaped solar devices, such as those intended to be mounted on airfoils.

2.4.1 Individual Solar Cell Performance Testing. Specific light sources and solar simulators are used to execute solar cell testing and evaluate device performance under strict parameters. Consider that the spectral irradiance of the sun at $1.5 \times 10^{11} m$ (e.g., one astronomical unit – AU), and silicon based solar cells is generally limited to the region between 0.3 and 1.2 μm where in this range the power density is $104.4 mW/cm^2$ [51]. Although there are several different techniques for solar simulation, the most common is to use a Xenon arc lamp with filtering to remove undesired near infrared (IR) line spectra. For the blackbody radiation simulator experiment, it should be noted that wavelengths in the red and near-IR solar cell response region is most changed by irradiation [51]. An important variable to consider for this experiment is to account for the extent to which a lack of solar spectral match affects a solar measurement; this can be accomplished if the spectral response of the solar cell and light source spectral intensity are known. The light-generated current of the illuminated cell in a simulator and actual solar conditions can be represented by (20) [51].

$$I_{L,solar} \left[\frac{A}{cm^2} \right] = I_{L,simulator} \left(\frac{\int R(\lambda)E(\lambda)_{solar}d\lambda}{\int R(\lambda)E(\lambda)_{simulator}d\lambda} \right) \quad (20)$$

Where $R(\lambda)$ is the solar cell spectral response (A/W), $E(\lambda)$ is the spectral irradiance (W/cm²-um), and $d\lambda$ is an increment of wavelength (um). In this instance, it is important to further define a test cell, which is described as a primary standard cell. Primary standard cells are defined as the primary cells to be used for operational purposes on the intended platform in the designated environment, and as they are considered too valuable for research and experimentation purposes, secondary standard cells were used for simulator verification.

2.5 Solar Cell Electrical Properties under Illumination

For a radiation simulator to be effective, understanding the inner workings of how a photovoltaic device functions as an electrical device is essential. To accurately determine a PV device's capability to convert energy at a given geographic location and time, it is pertinent to calculate certain factors such as solar time, equation of time, etc. as these factors will greatly impact how a PV analysis is conducted. This will enable a PV system user to gain a better understanding in computing the energy emissions present in an environment that is available to convert into electrical energy [36].

2.5.1 Electrical Characteristics. The main parameters that are used to characterize the performance of solar cells are: (1) the peak power (P_{MAX}), the short-circuit current density (I_{SC}), the open-circuit voltage (V_{OC}), fill factor (FF), and conversion efficiency (η); these parameters can be determined from the illuminated I-V curve for that particular cell [26].

2.5.1.1 Equivalent Circuit. As the PV device is treated like a semiconductor, it is also important to demonstrate how the device interacts with an electrical system by analyzing the equivalent circuit. A simply equivalent circuit for a PV device is shown below in Fig. 2.11, with more detailed descriptive illustrations of the circuit shown in Fig. 2.12 and Fig. 2.13.

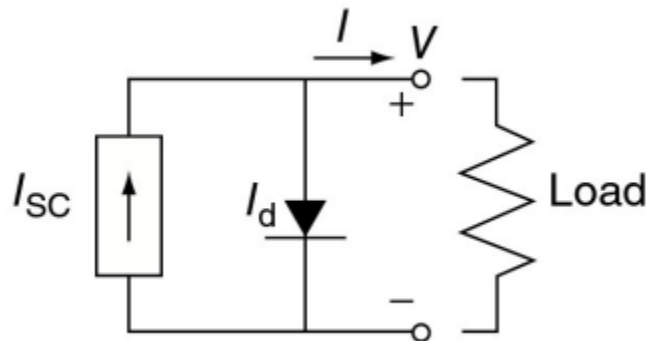


Fig. 2.11. A simplified equivalent circuit for a photovoltaic cell, which consists of a current source, indicated as short-circuit current (I_{sc}) driven by sunlight in parallel with a real diode. For more details, the reader is referred to [28, Fig. 18].

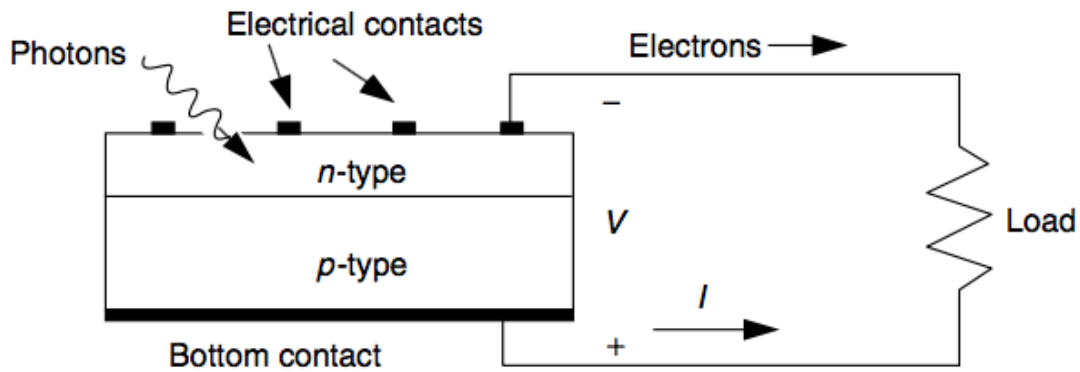


Fig. 2.12. A simple equivalent circuit for a photovoltaic cell, which consists of a current source driven by sunlight in parallel with a real diode. Electrons flow from the n-side contact, through the load, and back to the p-side where they recombine with holes. Conventional current I is in the opposite direction. For more details, the reader is referred to [28, Fig. 17].

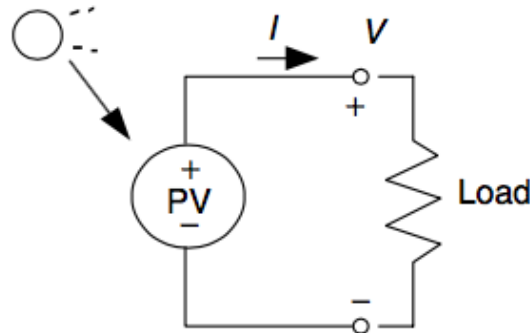


Fig. 2.13. Equivalent circuit for a simple PV device with a connected load. For more details, the reader is referred to [28, Fig. 18].

However, many PV systems are complex and involve multiple cells that comprise a much larger solar array. These arrays are designed to meet specific voltage and power requirements for payloads on various terrestrial and space based UAS [24]. Considering the research effort intends to address large arrays used for additional power generation for UAV adjunct payloads it is important to discuss system resistances, shading, and different wiring configurations. Fig. 2.14 below illustrates an equivalent circuit with a parallel resistance connected to a load, with Fig. 2.15 showing the differences graphically for two different cells.

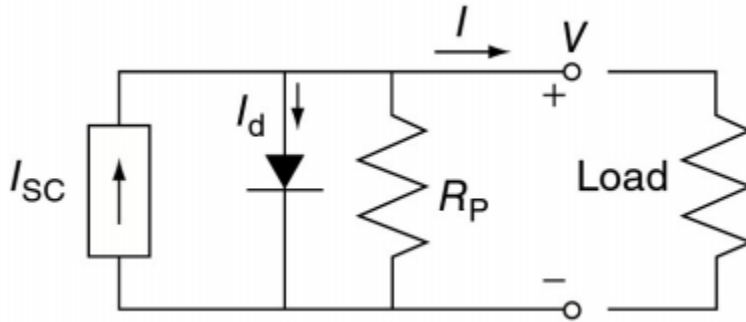


Fig. 2.14. Equivalent circuit for a simple PV device with a connected load and parallel resistance. For more details, the reader is referred to [28, Fig. 22].

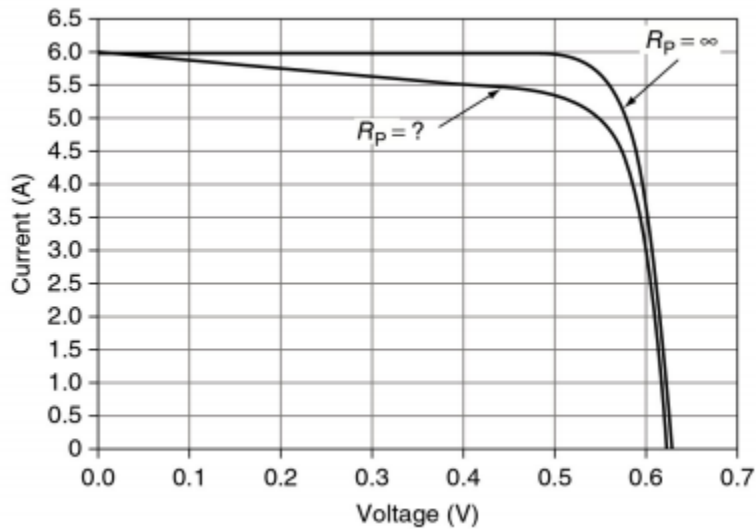


Fig. 2.15. Equivalent circuit for a simple PV device with a connected load. For more details, the reader is referred to [28, Fig. 23].

Using the graph in Fig. 2.15 as an example, when comparing two cells the point where the slope begins to drop in current for the equivalent circuit of the other cell can be estimated from $V = 0.44 \text{ V}$, where $\Delta I = 6.0 \text{ A} - 5.5 \text{ A} = 0.5 \text{ A}$. Assuming a zero series resistance, the parallel resistance in the equivalent circuit can now be solved by analyzing the relationship

between the differences in the slopes, with the change in current as shown by $R_p = \frac{V}{\Delta I} = \frac{0.44V}{0.5A} = 0.88 \Omega$.

The impacts of shading for a PV device can also negatively impact performance and desired electrical outputs. Consider a static PV array mounted at sea level on flat terrain, the impacts of shading can be effectively modeled by predicting solar intensity obstructions using a sun path diagram, which is shown in Fig. 2.16 below.

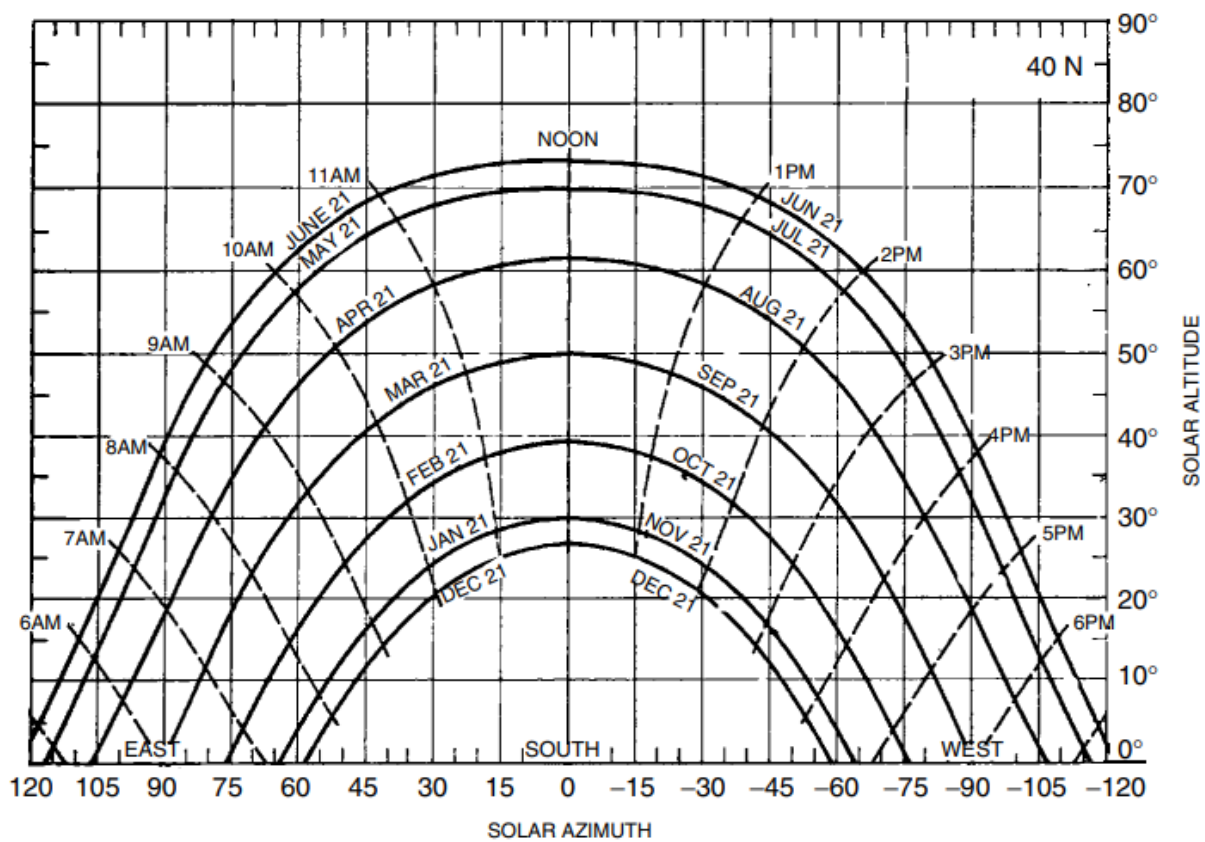


Fig. 2.16. A sun path diagram showing solar altitude and azimuth angles for 40 degrees latitude. For more details, the reader is referred to [36, Fig. 12].

Using these types of tools, coupled with clear sky radiation, beam radiation and insolation information, can allow researchers to estimate energy lost resulting from shading effects. However, when predicting energy losses for a HALE UAS, the impacts of shading are no longer dependent on ground obstacles such as trees or buildings. Instead, the obstacles can be

anything considered to directly hinder the PV's ability to capture light such as the UAS airframe structure(s) in relation to the orientation of the sun, and dense cloud layers [40]. In such a case the ASHRAE clear sky radiation models would assist with external variables negatively impacting PV performance outputs [11, 27]. However, the obstructions to solar light energy and beam radiation caused by the UAS structure itself needs to be accounted for and can be represented by an equivalent circuit analysis. Depending on the flight time, altitude, current and forecast weather conditions and geographic region in which the UAS is operating, these obstructions can vary in terms of severity and duration. Restructuring what was discussed regarding a simple cell, a more complex equivalent circuit can be explored, as shown in Fig. 2.17 below.

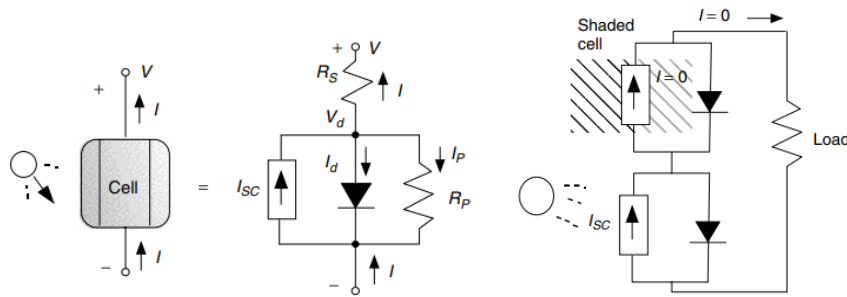


Fig. 2.17. A more complex equivalent circuit for a PV cell includes both parallel and series resistances. The shaded diode reminds us that this is a “real” diode rather than an ideal one (left). The simple equivalent circuit of a string of cells in series suggests no current can flow to the load if any cell is in the dark (shaded) (right). For more details, the reader is referred to [28, Fig. 26].

Given this information, a PV equivalent circuit that includes both series and parallel resistances can be expressed by (21.1) [13] and utilizing (6.3) to yield a simplified version in (21.2); the series and parallel resistance impact is shown in Fig. 2.18 below.

$$I = I_{SC} - I_0 \left[\exp \left(q \left(\frac{V + I * R_S}{kT} \right) - 1 \right) - \left(\frac{V + I * R_S}{R_P} \right) \right] \quad (21.1)$$

$$\therefore I = I_{SC} - I_0 \left[e^{38.9(V + I * R_S)} - 1 \right] - \frac{1}{R_P} (V + I * R_S), @T = 25^\circ C \quad (21.2)$$

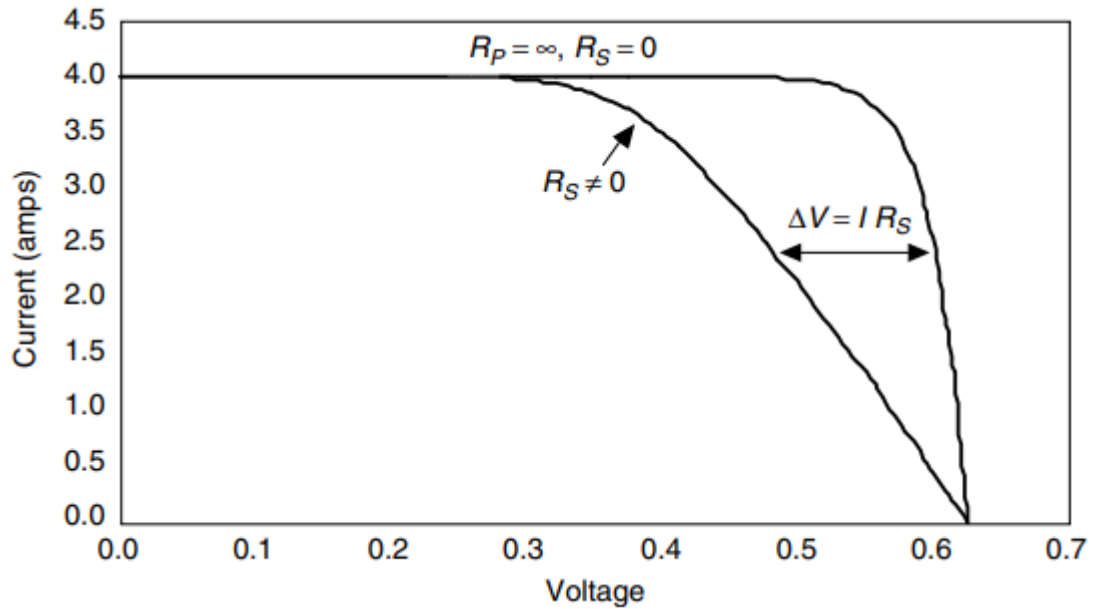


Fig. 2.18. Adding series resistance to the PV equivalent circuit causes the voltage at any given current to shift to the left by $\Delta V = I * R_S$. For more details, the reader is referred to [28, Fig. 25].

When multiple cells are connected in series and parallel configurations, it can allow a PV designer to tailor the system to the UAS power needs, which is summarized by Fig. 2.19 below.

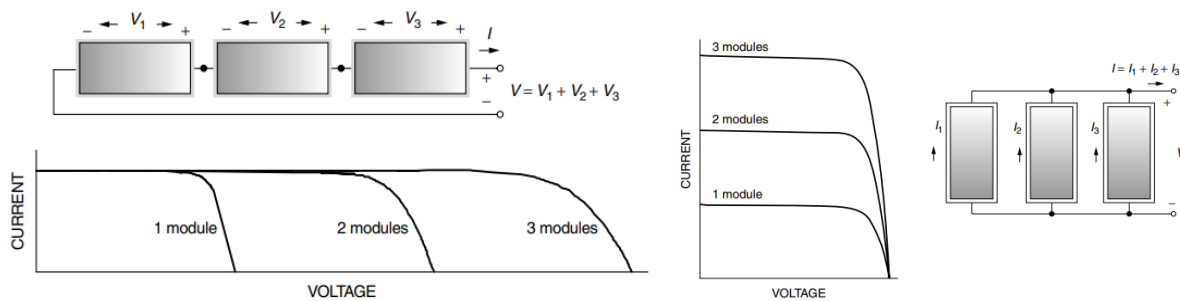


Fig. 2.19. For modules in series at any given current the voltages add (left). For modules in parallel at any given voltage the currents add (right). For more details, the reader is referred to [28, Fig. 30-32].

Once the total voltage and current for the array is designed, the effects of shading for an equivalent circuit can be graphically shown and calculated as shown in Fig. 2.20 below.

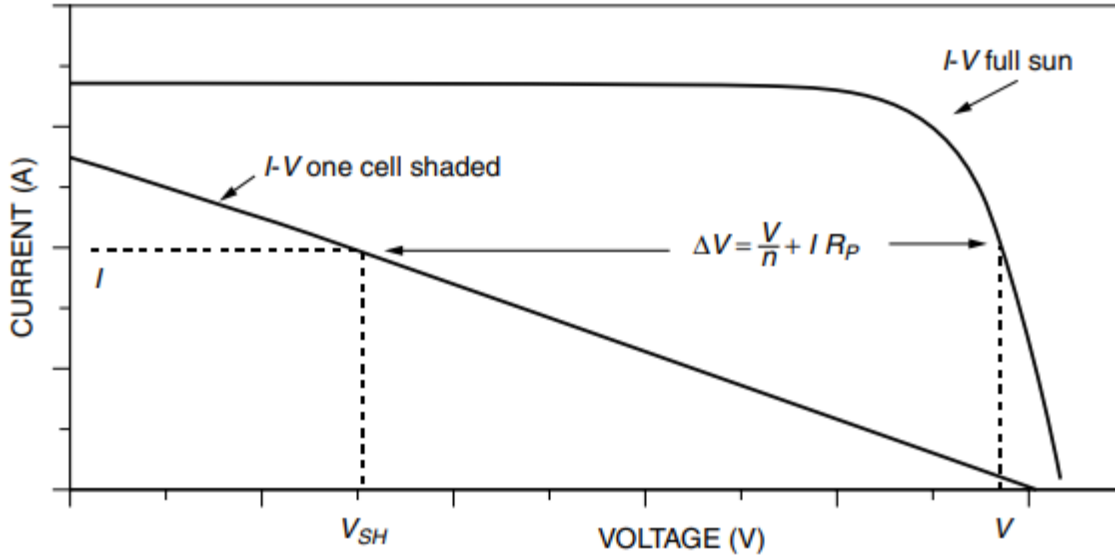


Fig. 2.20. Effect of shading one cell in an n -cell module or array, where at any given current the module's voltage drops from V to $V - \Delta V$. For more details, the reader is referred to [28, Fig. 38].

The relationship shown in (22) below is representative of the shading effects, where the PV device in series or parallel configuration acts as an element of parallel resistance, and the total drop in voltage can be computed [36].

$$\Delta V = \frac{V}{n} + I(R_P + R_S) \cong \frac{V}{n} + I * R_P \quad (22)$$

As a result of these observations of PV equivalent circuits, designing a system with high parallel resistances and low series resistances would be required to maximize cell performances [36]. As a mitigation for shading, a bypass diode would also be recommended to avoid large voltage drops across the diode during shading. Additionally, integrating the PV system into the UAS such that there are minimal obstructions caused by the airframe (e.g., place the system such that it is not blocked by other control surfaces, antennas, etc.) would be recommended.

2.5.1.2 Short Circuit Current Density. This is current that flows through the external PV equivalent circuit when the electrodes are in a short circuit configuration, and this

current magnitude is dependent on the luminous flux density magnitude, angle relative to the cell surface, and the solar cell total area. Additionally, this parameter is impacted by temperature, where as the temperature increases the I_{SC} increases, and is largely due to the fact that most bandgaps for semiconductors decrease with temperature [10]. Some assumptions pertaining to the research effort are that the maximum current density will occur when the flux source (i.e., blackbody radiation source) is approximately 90 degrees relative, or “normal” to the cell, which is otherwise stated as a beta angle of 0 degrees. It is also assumed that for experimental purposes as they pertain to the BBRs that the spectrum was standardized to a spectrum assuming AM1.5. Assume that to determine the short circuit current, an ideal case can be used in which the superposition approximation is present. That is, consider the net current flowing through the load (i.e., the sum of the photo-generation, thermal-generation, and recombination current), where the load voltage decrease is simulated by applying a forward bias voltage at the p-n junction [26]. The relationship between short circuit current (I_{SC}), the diode saturation current (I_0) (e.g., the diode leakage current density in the absence of light) and photo current (I_{ph}) is represented in (23) [51] below, and shows the behavior of the p-n junction net current during illumination.

$$I_{SC} = I_0 \left[\exp\left(\frac{eV_a}{kT}\right) - 1 \right] - I_{ph} \quad (23)$$

Where e is the absolute value of the electron charge in Joules per volt ($1.60 \times 10^{-19} \frac{J}{V}$), and V_a is the applied voltage in volts. Alternatively, the short circuit current density can be determined by (24) [51].

$$I_{SC} = qG(L_n + L_p) \quad (24)$$

Where G is the generation rate, q is the alternative form for the absolute electron charge value, and L_n and L_p are the electron and hole diffusion lengths respectively [46]. This is

additionally the point where the minimum load is interacting with the PV equivalent circuit that results in a zero-voltage condition as illustrated in the left of the x-axis of the notional I-V curve in Fig. 2.18.

2.5.1.3 Open Circuit Voltage. This is described as the voltage at which no current flows through the PV equivalent electrical circuit, and the maximum voltage that a PV device can generate [26]. Assuming an ideal diode, with no surface recombination or uniform generation, with a net current of zero, the open circuit voltage can be expressed by (25.1) [55] below.

$$V_{OC} = \frac{nkT}{q} \ln \left(\frac{I_L}{I_0} + 1 \right) \quad (25.1)$$

Where q is the electron charge, and I_L is the light-generated current. This is additionally the point where the maximum load is forced on the PV equivalent circuit that results in current at or near zero. Alternatively using (25.2), assuming an operating temperature of 25°C, the open-circuit voltage can be shown through the treatment in (25.3) to yield the simplified form in (25.4) below.

$$V_{OC} = V_T \ln \left(\frac{I_{SC}}{I_0} - 1 \right) \quad (25.2)$$

$$V_T = \frac{T}{11600} = \frac{273.15+25}{11600} = \frac{298.15}{11600} = 0.0257 \quad (25.3)$$

$$\therefore V_{OC} = 0.0257 \ln \left(\frac{I_{SC}}{I_0} - 1 \right) \quad (25.4)$$

2.5.1.4 Fill Factor. It is imperative to analyze the fill factor (FF) to evaluate the actual power at the maximum power point relative to the upper energy bound. The Fill Factor can be considered simply as a measure of quality of the solar cell. It is calculated by comparing

the maximum power to the theoretical power (P_T) that would be output at both the open circuit voltage and short circuit current together, as shown in (26) [55] below.

$$FF = \frac{I_M V_M}{I_L V_{OC}} \quad (26)$$

Where V_M is the maximum voltage, I_M is the maximum current, and I_L is the light-generated current. It should be noted that when observing the FF as a function of open circuit voltage, the FF does not change drastically with a change in open circuit voltage, as shown in Fig. 2.21 below.

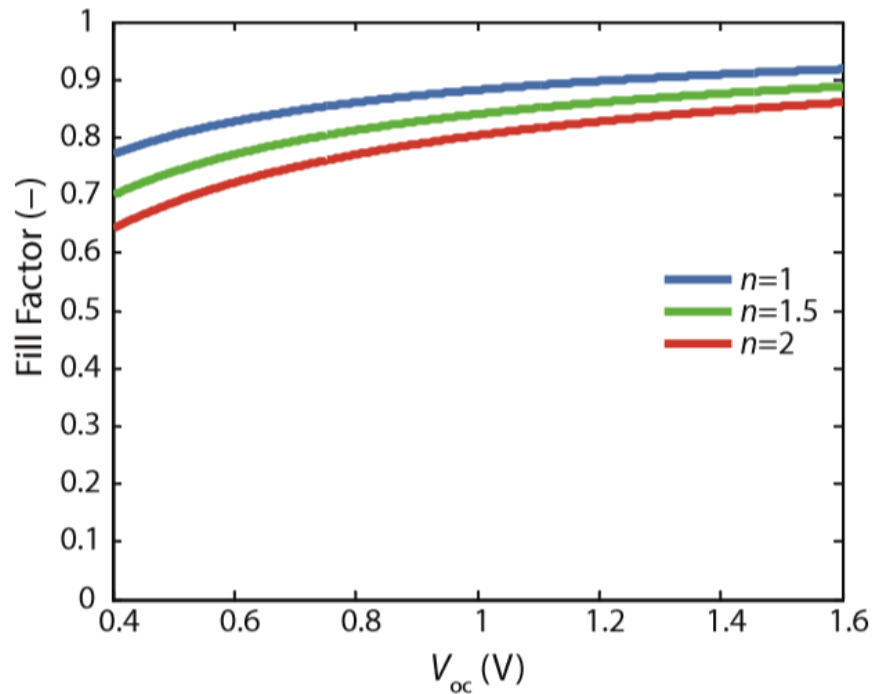


Fig. 2.21. The fill factor (FF) as a function of open circuit voltage (V_{OC}) for a solar cell that is represented by an ideal diode. The ideality factor is represented by n , which is a measure of the PV junction quality and the type of recombination. A simple recombination mechanism is assumed for this experiment, where $n = 1$. For more information, the reader is referred to [26, Fig. 1].

2.5.1.5 Conversion Efficiency. This variable is a ratio between the maximum power and incident power, where assuming a spectrum of AM1.5, a spectral irradiance value of 1000 W/m^2 is the standardized value for measuring the conversion efficiency of solar cells [26,

50]. The conversion efficiency is calculated by (27) [55] below and represented as a percentage value.

$$\eta = \frac{P_M}{P_{in}} = \frac{I_{SC}V_{oc}FF}{P_{in}} \quad (27)$$

Where P_M is the maximum power generated from the system, P_{in} is the power input to the system, I_{SC} is the short circuit current, V_{oc} is the open circuit voltage, and FF is the fill factor.

2.5.1.6 Bandgap Energy. When dealing with a PV device, the bandgap energy is a critical point of consideration when evaluating performance and maximum theoretical electrical outputs [4]. Bandgap energy is commonly referred to as the width of energy gap between the valence band and conduction band [46]. Additionally, the bandgap energy corresponds to a specific wavelength, which means that any energy in the solar spectrum with photon wavelengths longer than the corresponding wavelength cannot send an electron into the conduction band to excite a photovoltaic reaction (Master, 2004, pp. 453). Conversely, any photons below this corresponding wavelength is considered an interaction with wasted extra energy.

For PV devices with small band gap, more photons have the energy needed to excite the PV reaction in the bandgap (i.e., release an electron), but more photons will have excess energy thus yielding less voltage due to the wasted potential in high creation of hole-electron pairs. High bandgap will provide the opposite, with more voltage and less current. As a result, the “middle ground” for bandgap energies to release nominal power ranges while yielding maximum efficiencies is usually between 1.2 eV and 1.8 eV, where 1 electron volt (eV) is the energy that an electron requires when its voltage is increased by 1 volt (e.g., $1 \text{ eV} = 1.6 \times 10^{-19} \text{ J}$) [36]. This free electron can move within the semiconductor material energy bands, where namely the

most important observation is the gap between the conduction and highest filled band below it which is known as the energy band gap [36]. In the case of PV devices, an electron needs a specific amount of energy from a light photon to overcome the electrostatic force tying it to the nucleus [36]. Fig. 2.22 below graphically illustrates some efficiencies of PVs as they relate to bandgap.

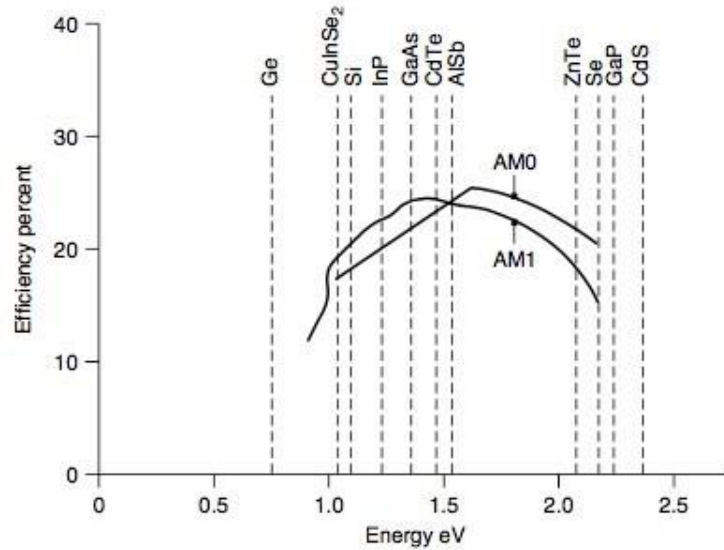


Fig. 2.22. Maximum efficiencies of photovoltaics as a function of their bandgap over different air masses. For more details, the reader is referred to [28, Fig. 11].

Based on the assumptions, the calculated relationship between the speed of light, and planks constant can be used to determine the corresponding wavelength from a bandgap energy, which for a Silicon PV device is shown by (28.1) [51] and the treatment in (28.2) to yield the answer in (28.3) below.

$$E_{g,GaAs} = \frac{ch}{\lambda} \tag{28.1}$$

$$\rightarrow \lambda = \frac{ch}{E_g} = \left(\frac{(6.626 \times 10^{-34} J*s)(3 \times 10^8 \frac{m}{s})}{1.12 eV(1.6 \times 10^{-19} \frac{J}{eV})} \right) \tag{28.2}$$

$$\therefore \lambda_{Si} = 1.109 \times 10^{-6} m \approx 1.11 \mu m \tag{28.3}$$

As a means of comparison, a Gallium Arsenide (GaAs) PV device with a bandgap energy of 1.42 eV would have a corresponding wavelength of approximately 0.87 μm . Since GaN is

currently being explored as a new semiconductor material, with a bandgap of ~ 3.4 eV it is pertinent to explore this as a potential candidate for PV-embedded airfoils in future testing.

2.5.1.7 Electrical Energy and Light Current. In order to determine the light current (I_L), there are a few assumptions that need to be stated, and for this research effort include the following: (1) a photovoltaic cell achieves a collection efficiency of η_{coll} (97%), with units as percent, for photons in a given range of energy values, represented as e_1 and e_2 , with units in Joules and in this case an energy band of 1.5×10^{-19} J (e_1) to 6.00×10^{-19} J (e_2). The variable e_1 is representative of the photonic energy range in the lower band, whilst the variable e_2 represents photon energy in the upper band. (2) The absorption coefficient is α (82%), with units in percent. (3) The same distribution for frequency of photons as a function of energy, as illustrated graphically in Fig. 2.23.

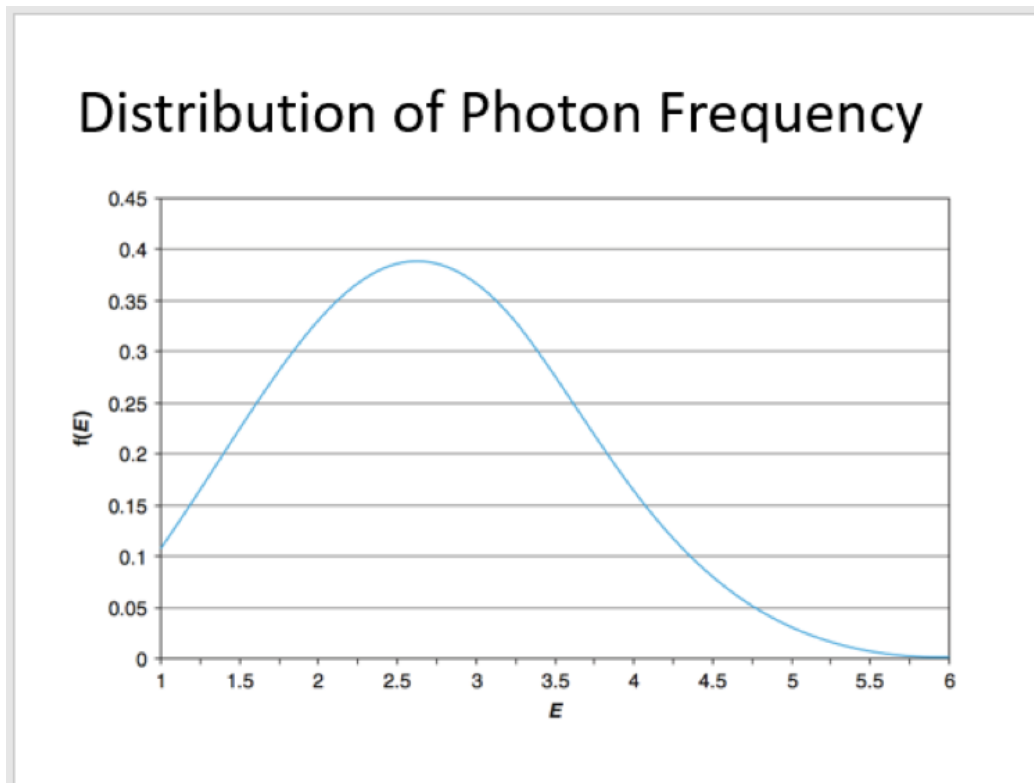


Fig. 2.23. Probability density function (PDF) showing the distribution for frequency of photons, plotted as a function of energy (W/m^2). For more details, the reader is referred to [55, Fig. 4].

(4) Assume both collection and absorption efficiency are constant, and (5) the photon arrival coefficient (S) is a constant rate and represented as $2.50 \times 10^{21} \text{ particles/s} \cdot \text{m}^2$. Based on the assumptions, the light current can be calculated by integrating across the energy range for which photovoltaic conversion takes place, represented in the (28.1) [102] below.

$$I_L = e \int_{e_1}^{e_2} \eta_{coll}(E) S(E) \alpha(E, W) dE \quad (28.1)$$

Where e is electrical energy per electron ($1.602 \times 10^{-19} \text{ J/V}$), E is the system energy (in Joules), S is the photon arrival coefficient rate, $(E)S$ is the energy (in Joules) based on the photon arrival rate, $f(E)$ is the distribution of the photon energy values, which have a predefined Weibull alpha and beta values; in this case assume that $\alpha = 3$, and $\beta = 3$, which are the scale parameter and shape parameter respectively. Since collection efficiency (η_{coll}) and absorption efficiency based on PV cell width ($\alpha(E, W)$) are constant, they can be factored out of the integral, as shown below in (28.2) and (28.3) [102].

$$I_L = e \int_{e_1}^{e_2} \eta_{coll}(E) \alpha(E, W) S * f(E) \quad (28.2)$$

$$I_L = e \eta_{coll}(E) \alpha(E, W) S \int_{e_1}^{e_2} f(E) \quad (28.3)$$

To evaluate the integral, utilize the general form of the Weibull probability distribution function (PDF) based on the designated alpha and beta values, where it is then applied to $S(E)$ [102]. Note however that to solve for the light current, the integral is converted to determine the probability that the energy (E) falls in this specified energy band range, and as a result the cumulative distribution function $F(E)$ is used as shown in (28.4).

$$F(E) = 1 - \exp[-(E/\beta)^{-\alpha}], \text{ for } x \geq 0, \alpha > 0, \beta > 0 \quad (28.4)$$

The last remaining step is to integrate $S(E)$ over the range of the noted photon energy values in the high and low band (e_2 and e_1 respectively), and substitute into (28.3), to solve for the current per area measured in amperes per square centimeter (A/cm^2) and is shown by the final light current calculation in (29) [102].

$$I_L = e \eta_{coll} \propto (2.50 \times 10^{21}) [1 - \exp[-(E/\beta)^{-\alpha}]] \frac{e_2}{e_1} \quad (29)$$

There is a distinct relationship between light current with respect to solar cell photon exposure. Generation current of a solar cell (I_L) can also be represented as function of number of photons (N) striking the photovoltaic surface, as shown in (30) [51].

$$I_L = q N A \quad (30)$$

Where the electron charge is represented by q , the number of electrons shown as N , and A representing the surface area of the cell. To assist with calculations to determine the possible cell losses given this set of parameters, a simple Microsoft Excel program was developed to execute the function to solve for light current and is shown in Fig. 2.24 below.

Electrical Properties: Light Current			
Assuming a standard distribution for frequency of photons as a function of energy (as per attached figure)			
Distribution of photon frequency as a function of energy 10^{-19} J			
Inputs		Constants	
Variable	Symbol/Equation	Value	Unit
Cell Collection Efficiency:	η_{col}	95%	Percent (%)
Absorption Coefficient:	α	80%	Percent (%)
Energy range - lower band (e1):	e_1	1.89E-19	Joules (J)
Energy range - upper band (e2):	e_2	5.68E-19	Joules (J)
Photon Arrival Coefficient:	S	2.50E+21	Particles/s-m2
Solar Constant:		S_0	1368 W/m2
Planck's Constant:		h	6.63E-34 J-s
Speed of Light:		c	3.00E+08 m/s
Unit of Charge:		e	1.60E-19 J/V
Unit conversion factor for E:			1.00E+19
Outputs			
Light Current (New Flow):	$I_L = e \int_{e_1}^{e_2} \eta_{col}(E) S(E) \alpha(E, W) dE$	236.6968	A/m2
	$I_L = e \eta_{col} \alpha \int_{e_1}^{e_2} S(E) dE$	0.236696813	mA/cm2
Spectral arrival frequency using Weibull function (CDF) $F(x) = 1 - \exp\left\{-\left[\frac{x}{\beta}\right]^\alpha\right\}$ for $x \geq 0, \alpha > 0, \beta > 0$			
Weibull Shape Parameter:	α	3	
Weibull Scale Parameter:	β	3	
Adjusted Energy range (lower band):		1.89E+00	Joules (J)
Adjusted Energy range (upper band):		5.68E+00	Joules (J)
Weibull value (lower band):		0.22123582	Joules (J)
Weibull value (upper band):		0.998871711	Joules (J)
Weibull differences:		0.777635891	Joules (J)
Cell losses		76.0000%	Percent (%)

Fig. 2.24. Microsoft Excel program formulated to execute the light current function given the parameters such as cell collection efficiency, absorption coefficient, a photon arrival coefficient and energy ranges in an upper and lower band.

2.5.1.8 Determination of Maximum Power. When describing PV devices in this research effort, the maximum theoretical power is of particular interest for engineers seeking to integrate PV into numerous systems [52]. Given the series of equations shown in (31.1) and (31.2) [55], defining a and b parameters can be done by manipulating the equations for maximum current (I_M) and maximum voltage (V_M) from their original form as shown below.

$$I_M = I_L (1 - a^{-b}) \quad (31.1)$$

$$V_M = V_{OC} \left(1 - \frac{\ln a}{a}\right) \quad (31.2)$$

When I_M and V_M are known, they can be modified and alternatively represented by (31.3) and (31.4) [55] below.

$$a = 1 + \ln \frac{I_L}{I_0} \quad (31.3)$$

$$b = \left(\frac{a}{a+1}\right) \quad (31.4)$$

As a result, the maximum power (P_M) can be determined as shown in (31.5) below.

$$P_M [mW/cm^2] = \frac{[I_M V_M] * 1000}{PV \text{ area}} \quad (31.5)$$

2.5.2 Illuminance Measurement and Solar Cell Optical Losses. Solar cells have distinct characteristic responses when exposed to a light source: (1) the energy is absorbed to turn light energy into electrical energy via P-N channeling and the photovoltaic effect (which is subsequently measured by the PCMS), where electrical losses are characterized primarily by (2) absorption of energy and subsequently radiated as heat energy (which is measured at the thermal baseplate, and contactless IR temperature sensor to analyze for a delta T), and (3) the energy is

reflected (which is known as optical losses). For the purposes of this research effort, the illumination source was provided via calibrated LEDs. To measure the maximum luminous intensity for each LED and optical losses, assume a maximum theoretical loss at beta angle 0 degrees (90 degree solar angle = normal angle to PV surface), and this maximum is based on the maximum power point angle on the bell curve (e.g., where the PV should be yielding maximum power output based on relative light source positioning).

It is assumed that the angle of solar wavelength emission (i.e., a normal solar angle relative to PV surface) yields the maximum power output, and subsequently yields the maximum optical losses. Additionally, that the optical losses follow the same “bell curve” profile when analyzing the total power output over the course of a solar day [35]. The quantification of the LED radiant flux in terms of a numerical value will initially be assigned in lux, a measure of illuminance; the reflected energy for optical losses will also be measured in lux. The devices used to measure this light intensity was the Texas Advanced Optoelectric light-to-digital conversion diode TSL2561/TSL2591 boards, which measure luminous flux, or the power of visible light (i.e., visible/luminous flux density (ϕ_v) [60]. More specifically, the photopic flux and scotopic flux densities, expressed in lumens (lux per unit area), was converted into an irradiance measurement based on a sliding scale provided in Fig. 2.25 and Table 2.

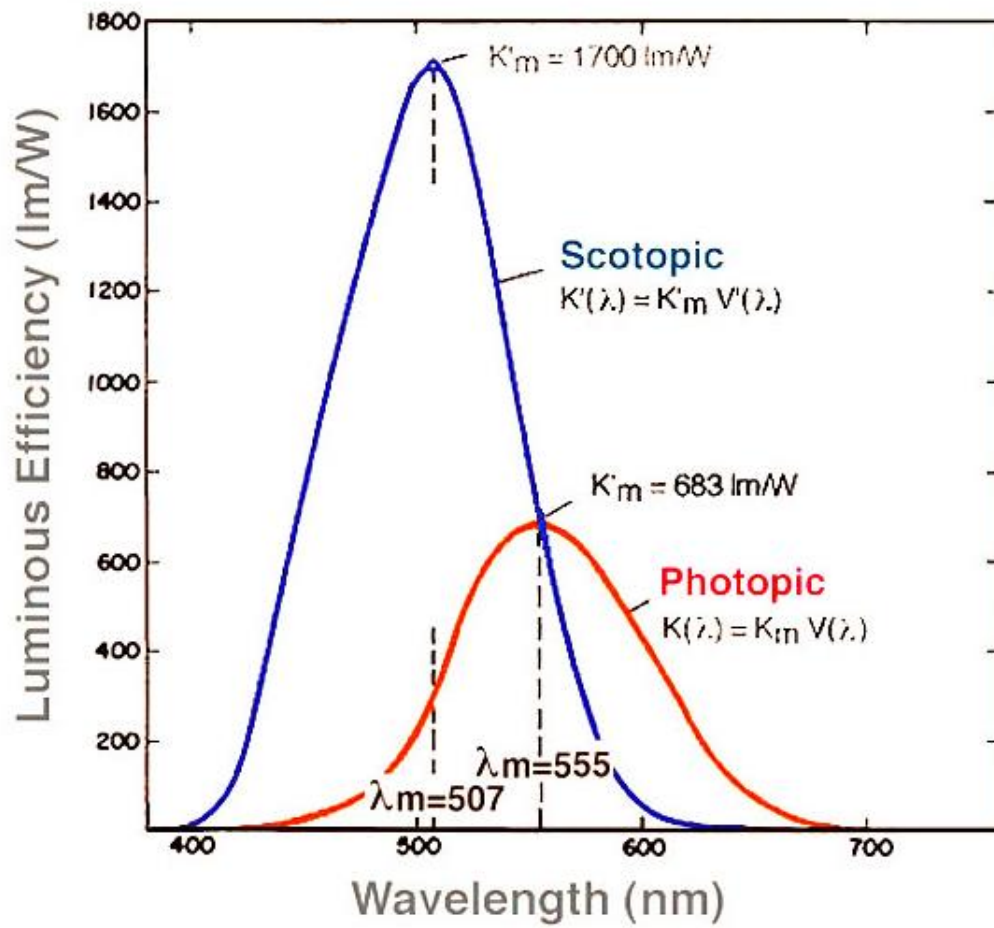


Fig. 2.25. Non-normalized values of the scotopic and photopic curves of spectral luminous efficacy. For more information, the reader is referred to [16, Fig. 3].

TABLE 2

PHOTOPIC AND SCOTOPIC LUMINOUS EFFICIENCY AND CONVERSION VALUES
USED FOR LUX CONVERSION AND CORRECTION TO LUMINOUS FLUX DENSITY

<i>Wavelength (λ) [nm]</i>	<i>Photopic Luminous Efficiency ($V_{\lambda,p}$) [%]</i>	<i>Photopic lm/W Conversion Factor [unitless]</i>	<i>Scotopic Luminous Efficiency ($V_{\lambda,s}$) [%]</i>	<i>Scotopic lm/W Conversion Factor [unitless]</i>
380	0.000039	0.027	0.000589	1.001
390	.000120	0.082	.002209	3.755
400	.000396	0.270	.009290	15.793
410	.001210	0.826	.034840	59.228
420	.004000	2.732	.096600	164.220
430	.011600	7.923	.199800	339.660
440	.023000	15.709	.328100	557.770
450	.038000	25.954	.455000	773.500
460	.060000	40.980	.567000	963.900
470	.090980	62.139	.676000	1149.200
480	.139020	94.951	.793000	1348.100
490	.208020	142.078	.904000	1536.800
500	.323000	220.609	.982000	1669.400
507	.444310	303.464	1.000000	1700.000
510	.503000	343.549	.997000	1694.900
520	.710000	484.930	.935000	1589.500
530	.862000	588.746	.811000	1378.700
540	.954000	651.582	.650000	1105.000
550	.994950	679.551	.481000	817.700
555	1.000000	683.000	.402000	683.000
560	.995000	679.585	.328800	558.960
570	.952000	650.216	.207600	352.920
580	.870000	594.210	.121200	206.040
590	.757000	517.031	.065500	111.350
600	.631000	430.973	.033150	56.355
610	.503000	343.549	.015930	27.081

620	.381000	260.223	.007370	12.529
630	.265000	180.995	.003335	5.670
640	.175000	119.525	.001497	2.545
650	.107000	73.081	.000677	1.151
660	.061000	41.663	.000313	0.532
670	.032000	21.856	.000148	0.252
680	.017000	11.611	.000072	0.122
690	.008210	5.607	.000035	.060
700	.004102	2.802	.000018	.030
710	.002091	1.428	.000009	.016
720	.001047	0.715	.000005	.008
730	.000520	0.355	.000003	.004
740	.000249	0.170	.000001	.002
750	.000120	0.082	0.000001	0.001
760	.000060	0.041	0	0
770	0.00003	0.02	0	0

Note. Data reprinted from [29, 47].

The photopic flux is weighted to match the responsivity of the human eye, which is most sensitive to yellow-green, and the scotopic flux is weighted to the sensitivity of the human eye in the dark-adapted state [47]. For the purposes of this research effort, the photopic flux was the only type taken into consideration with information from Table 2 above to generate the SCARS algorithm coded into the microcontroller. The reason for not accounting scotopic flux is to minimize variability in the resultant outputs from the SCARS, as the sensor would need to rapidly adjust its gain due to being quickly activated upon stimulation from an irradiance source from a dark-adapted state [29].

2.5.2.1 Extrapolating Irradiance from Illuminance Measurements. This particular portion of the research will contain irradiance and illuminance relationships based on the wavelength of light emitted. Based on the information provided in Table 2, the photopic and

scotopic luminous flux density can be determined ex post facto from the results of the experiment. Since the visible light spectrum detected by the TSL2561/2591 sensors are measured in lux, the corresponding photopic luminous efficiency (V_λ) and lumen-to-Watt conversion ($Z_{c,\lambda}$) for a specific wavelength of light used (λ) in the experiment (e.g., the dominant wavelengths for the red, green, and blue LEDs used) was corrected assuming 90 lumens per watt [26].

Assuming a photometric flux per unit area (i.e., illuminance) standard of 1 lux = 1 lumen/m², the values of lux can be used in the lumen-to-Watt conversion, where at 555nm: 1 lux = 683.000 W/m² [47]. From here, a photopic luminous flux density conversion equation can be generated and shown in (32.1) below.

$$E_{e,dir} = \frac{\phi_V}{Z_\lambda} \rightarrow E_e = \frac{E_V}{Z_{c,\lambda}} \quad (32.1)$$

Where $E_{e,dir}$ is the direct solar radiant flux, and is assumed to be equivalent to E_e , the radiant flux (ϕ_e) received by a surface per unit area (e.g., the direct solar radiant flux will mirror the function of the radiant flux for a given LED in the experiment, where the irradiance was calculated based on measured illuminance). As an example, the corrected irradiance value for a red LED at 620nm would have a maximum theoretical photopic luminous efficiency of 38.1%, and based on the values in the table, the Photopic conversion (lm/W) is obtained by multiplying V_λ by 683 and the Scotopic conversion is obtained by multiplying V'_λ by 1700 [16]. Therefore, the irradiance flux density equation from (32.1) is now transformed into (32.2).

$$E_e = \frac{E_V}{(V_{\lambda,p})Z_{c,\lambda}} \quad (32.2)$$

However, due to the nature of the experimental setup, the measured illuminance may not be the true illuminance. This is applicable in Chapter 3 which discusses the BBRS fabrication, specifically where the TSL2561 is mounted behind the first layer of the solar test array (i.e.,

STAR1). Therefore, a base measurement was taken to determine the ambient lux detected by the sensor without the presence of a reflected material (i.e., a PV cell). This resultant measurement was considered “noise” in the sensor analog signal and subtracted from the total true illuminance value. This was noted as the ambient measured illuminance ($E_{V,a}$) and was reestablished prior to each experimental run that uses a different height measurement (e.g., any time the beta angle position and control subsystem (BAPCS) arm changes height configuration, another ambient illuminance base measurement must be recorded). Therefore, the photopic irradiance flux density equation is represented by (32.3) and its corresponding explanation below.

$$E_e = \frac{E_V - E_{V,a}}{(V_{\lambda,p})_{Z_c,\lambda}} \rightarrow \text{irradiance flux density } (W/m^2) =$$

$$\frac{\text{measured illuminance (lux)} - \text{ambient illuminance (lux)}}{\text{photopic efficiency} * \text{correction factor based on } \lambda \left(\frac{\text{lux}}{W/m^2}\right)} \quad (32.3)$$

2.5.2.2 Luminous Flux and Illuminance. Luminous flux is the specification of the total quantity of light emitted from a source and is represented by (33) [29] below.

$$F = K_m \int F_e(\lambda) V(\lambda) d\lambda \quad (\text{lumens}) \quad (33)$$

Where K_m is the maximum spectral luminous efficacy, and $F_e(\lambda)$ is the radial flux at specific wavelength, with the illuminance equation represented by (34) [29] below.

$$E = \frac{\delta F}{\delta A_r} \quad (34)$$

Where E is in lumens/m^2 , or lux, δA_r is the surface area of the receiving element relative to the incident light source angle, and δF is luminous flux based on the light emitted from the incident light source.

2.5.2.3 Solar Cell Losses due to Reflectance. Luminance is the specification of the amount of light emitted or reflected from an extended source in a given direction, measured

in candela per meters squared $\left(\frac{cd}{m^2}\right)$, where $1 \text{ lux} = 1 \text{ cd} * \left(\frac{sr}{m^2}\right)$, and “sr” is an abbreviation for seridian. Assume a perfectly diffuse reflector (i.e., a Lambertian reflector); in the case of the experimental setup, a luminance measurement for optical losses due to reflections is taken at 90 degrees solar angle and beta angle zero degrees. The solar cell is assumed to have reflective properties where the apparent brightness of the surface to the observer is the same regardless of the viewing angle (e.g., the PV surface is assumed to be isotropic), therefore the relationship between illuminance and luminance would and as per Lambert’s cosine law and is shown by (35) [47].

$$L_V = \frac{E_V R}{\pi} \quad (35)$$

Where R is the reflectance of the PV surface, where the [directional] reflectance is further expressed in (36) [47] below as the radiance reflected by the PV surface divided by the radiance received by the surface.

$$R_{\Omega} = \frac{L_{e,\Omega}^r}{L_{e,\Omega}^i} \quad (36)$$

From this overview it is evident that there are inherent optical losses that can occur for a PV device that result reflected energy due to PV design constraints. These constraints may be the product of a thicker coverglass or certain glass cover material that is intended to shield the PV cell or array from the elements, or from deep space radiation. Regardless, there is a distinct tradeoff that occurs where beginning of life (BOL) performance is sacrificed in the form of power output and cell efficiencies to accommodate for end of life (EOL) performance due to radiation or environmental degradation of the PV surface.

2.5.2.4 Other Solar Cell Losses. As mentioned previously, there are a few ways that a solar device behaves when stimulated by a light source. If it absorbs the light energy and converts it to electrical energy, then there are potential losses due to the conversion process internal to the cell or during electrical energy conversion, storage, and/or transmission. Although there are many different internally and externally influenced losses that can occur with regard to PV performance, this dissertation will focus on spectral response as a function of angle of incidence, and thermal stresses. However, some internal PV array considerations need to be discussed, such as series and parallel resistances, which can be modeled using Matlab/Simulink software and assist with PV analyses using basic and exact models. The Matlab/Simulink PV model is shown in Fig. 2.26, with results of sample series and parallel resistances shown in Fig. 2.27.

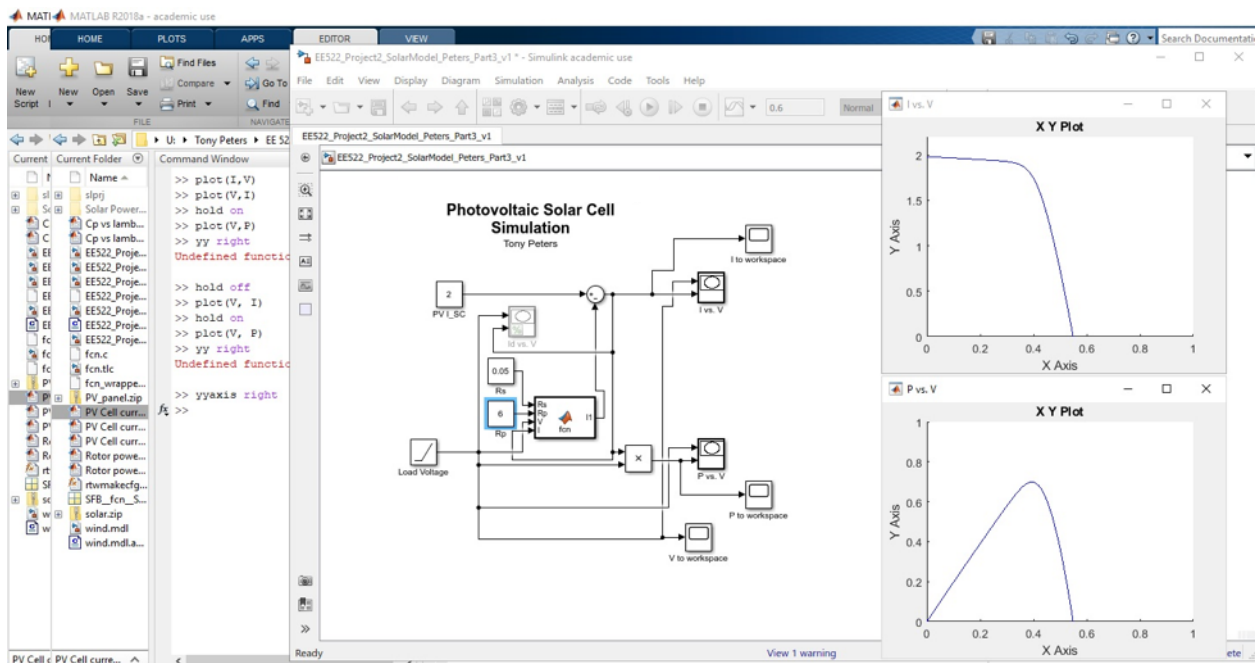


Fig. 2.26. Matlab/Simulink model for a PV exact power system, with current as a function of voltage, and power as a function of voltage XY graphs located on the right. This is an updated model to reflect series resistance of 0.05 ohms, and a parallel resistance of 6 ohms.

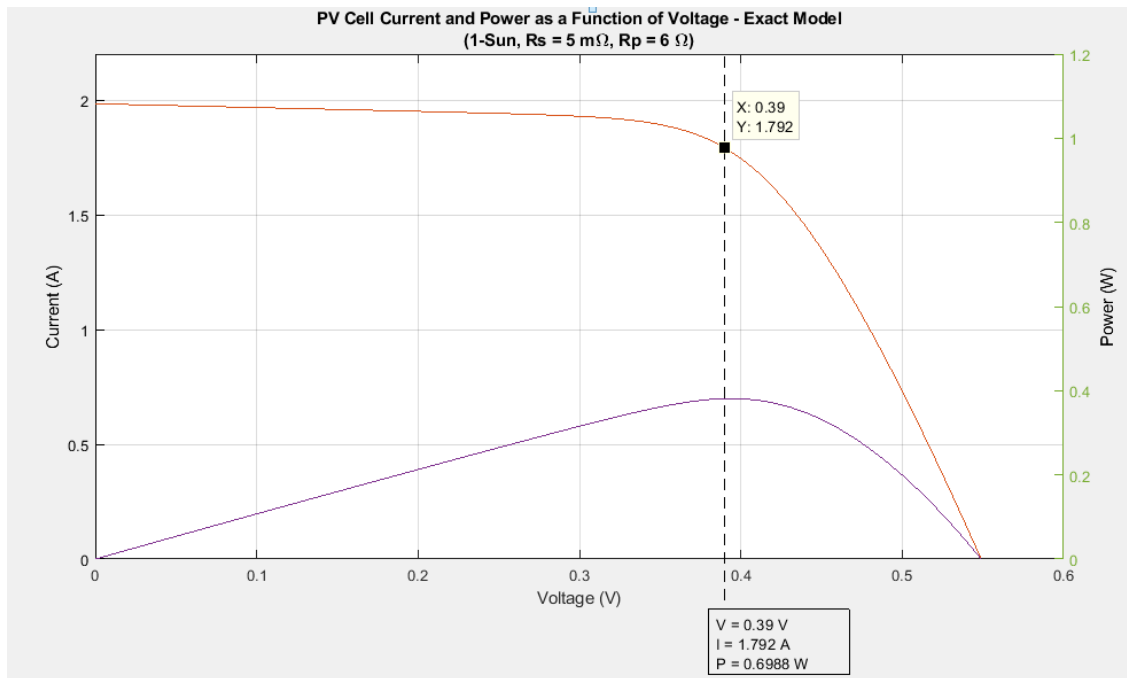


Fig. 2.27. Matlab/Simulink graphical model for a PV exact model power system, with current as a function of voltage indicated in red, and power as a function of voltage in purple. Maximum power occurs at approximately 0.39 V, 1.792 A, and yielding ~ 0.6988 W.

Other losses that may occur using the BBRs for PV testing could come in the form of variable load and resistance setting during testing. Considering this, the variable load metric is not used in the standard experiment and is thus recommended for future testing. The variable resistance in this experiment is accomplished using a $10\text{ k}\Omega$ potentiometer [89], and from measured conditions was able to create an artificial resistance ranging from $9.125\ \Omega$ to $99.325\ \text{k}\Omega$. For the data collection, the potentiometer setting was put on its minimal resistance value to avoid heavy losses in the system.

Solar cell electrical losses due to increased temperature is a widely researched topic, and quantitatively proven to reduce PV electrical energy output efficiencies as heat in the system increases [10]. For this research effort, the use of positive temperature coefficient (PTC) heaters in analysis will aid in evaluating different heat areas on the experimental PV airfoil. This was accomplished using independently controlled thermal regulators, with PTC heaters [94]

embedded onto the airfoil surface as shown in Fig. 2.28 below. Measurements will then be taken using the Adafruit Industries BMP280 sensor that measures the baseplate temperature, two thermistors embedded onto the PV airfoil, and the TMP007 sensor on the artificial sun module subsystem (ASMS) solar test array layer 2 (STAR2).

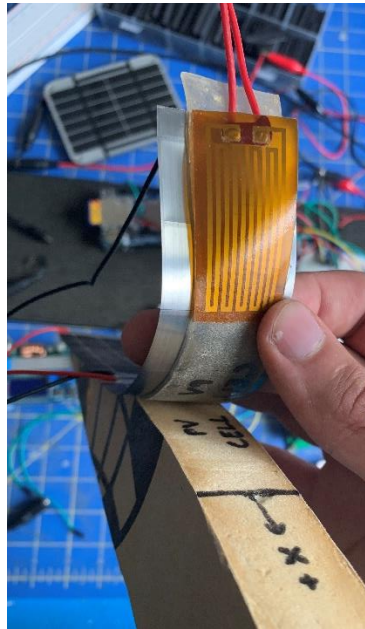


Fig. 2.28. PTC heating element embedded on a sample PV-embedded test airfoil. For more details, the reader is referred to [94].

Using temperature as another test condition in this research effort can be used to determine a worst-case analysis (WCA) for PV maximum outputs. More specifically, if there is an area of concentrated heat over the PV airfoil, the areas where the highest fluctuations are present in terms of degraded performance can be observed (i.e., trailing edge, top of airfoil, etc.). Additionally, as the PV device is intended to be used on an aerial platform there may be losses due to vibrations that were not quantified through experimentation at this time. This topic will be discussed further in the future work section.

CHAPTER 3

BLACKBODY RADIATION SIMULATOR AND TEST EQUIPMENT DESIGN

3.1 Introduction

To ensure that all the analysis factors, variables, and elements of photovoltaic system output are addressed, each of the key drivers for cell performance will need to be discussed and subsequently accounted for. The BBRS is inherently designed to accommodate many of the factors that impact cell performance, specifically addressing key drivers including (but not limited to): temperature, humidity, light wavelength, luminous flux density, optical losses, illumination angle and even vibrations. This chapter will focus on the specifics of how the BBRS was fabricated, subsystem requirements, why certain parts were selected, and notable design limitations and obstacles incurred during the design and fabrication process.

3.2 Background and Perceived Need

A new PV test method to measure the unique spectral response characteristics for different arrays could be beneficial for several different application areas where determination of a specific cell design is of great importance. More specifically, this new method can be beneficial for UAS design engineers when a desire is present to incorporate PV technology into the vehicle's wings, fuselage or other available flight surface areas where the overall shape can be characterized as "irregular". These areas of irregularity are intended to maximize aerodynamic performance, and the addition of PV cells and arrays should not decrease aerodynamic efficiencies; thus, the PV design is considered secondary to aerodynamic performance. Aside from strictly terrestrial environments, this new test method can be considered for use in space vehicle development, where the irregularity of PV array structures may be dependent on other environmental or operational driving factors. These design

considerations can range from vibrations during launch, and deconflictions with externally mounted radiators, payload antennas or sensors during operations or initial deployment. Having a single standardized method that is low cost and repeatable may allow system designers for both terrestrial and space based UAS to explore other PV options for their system.

Conventional PV test methods yield the maximum peak voltage and current in the form of a current vs. voltage (I-V) and/or power vs. voltage (P-V) curve, which is provided from each manufacturer for their respective design, as shown in Fig. 3.1 below.

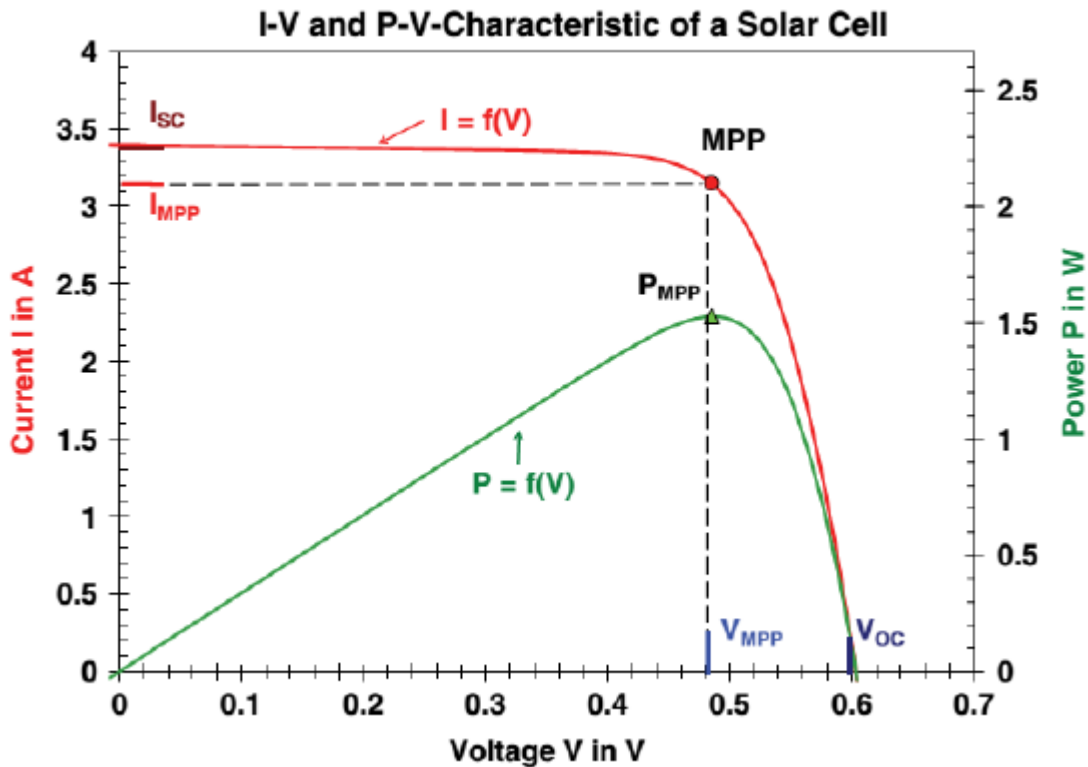


Fig. 3.1. General graphical information representing PV electrical performance characteristics that are considered prior to power system integration. The red line on the top shows the I-V curve for a nameplate cell in terms of varying temperature and irradiance respectively. Where the green line on the bottom illustrates the maximum power point relative to the power curve for a given solar cell. This graph shows the characteristic I-V and P-V curves for a mono-crystalline silicon solar cell with a cell area of 102 cm². For more information, the reader is referred to [17, Fig. 1], [44].

However, due to changing beta angles and decreases in solar intensity, it might benefit PV users to determine the point of diminishing returns in the form of a beta angle with resultant bell curves. More specifically, it is more pertinent for PV applications to show the spectral response as a function of beta angle with resultant power output metrics then simply indicating maximum theoretical power and maximum power as tested.

3.2.1 BBRS Capabilities and Requirements. A proposed piece of specialized test equipment (STE) known as a blackbody radiation simulator can accurately indicate current, voltage and power output profiles for a given PV design under specific conditions (e.g., varying PV surface temperature, luminous flux density, irradiance, as a function of varying beta angles). This new STE can be used with UAS applications where the solar angle of incidence plays a major role in optimized PV output, and additionally is scalable to be used for analysis of non-planar arrays with unique shapes that are dictated to meet irregularly shaped PV arrays. Since the PV array is exposed to varying solar intensities as its orientation varies relative to the sun during aerial flight, it is important to model other behaviors of the PV array in terms of other degrading factors (i.e., temperature) especially when non-standard array dimensions are utilized. To aid in standardizing the testing for non-standard PV array dimensions and shapes, the use of the BBRS is utilized to demonstrate the spectral response characteristic for a particular cell. For the purposes of this dissertation, it is proposed that incorporating a scaled system that specializes in testing irregularly shaped PV-embedded airfoils and/or PV arrays may be of use in determining solar collection capabilities for different designs by capturing an array-unique spectral response characteristic curve.

3.3 BBRS Topology and Materials

Prior to any fabrication, it was pertinent to identify initially how the system would connect multiple electronic components and sensors to both stimulate and measure the response from a given test apparatus. It was important that each of these subsystems illustrated and datalogged their respective output metrics during testing, and act as one continuously operating cohesive unit. Fig. 3.2 below illustrates the initial system concept.

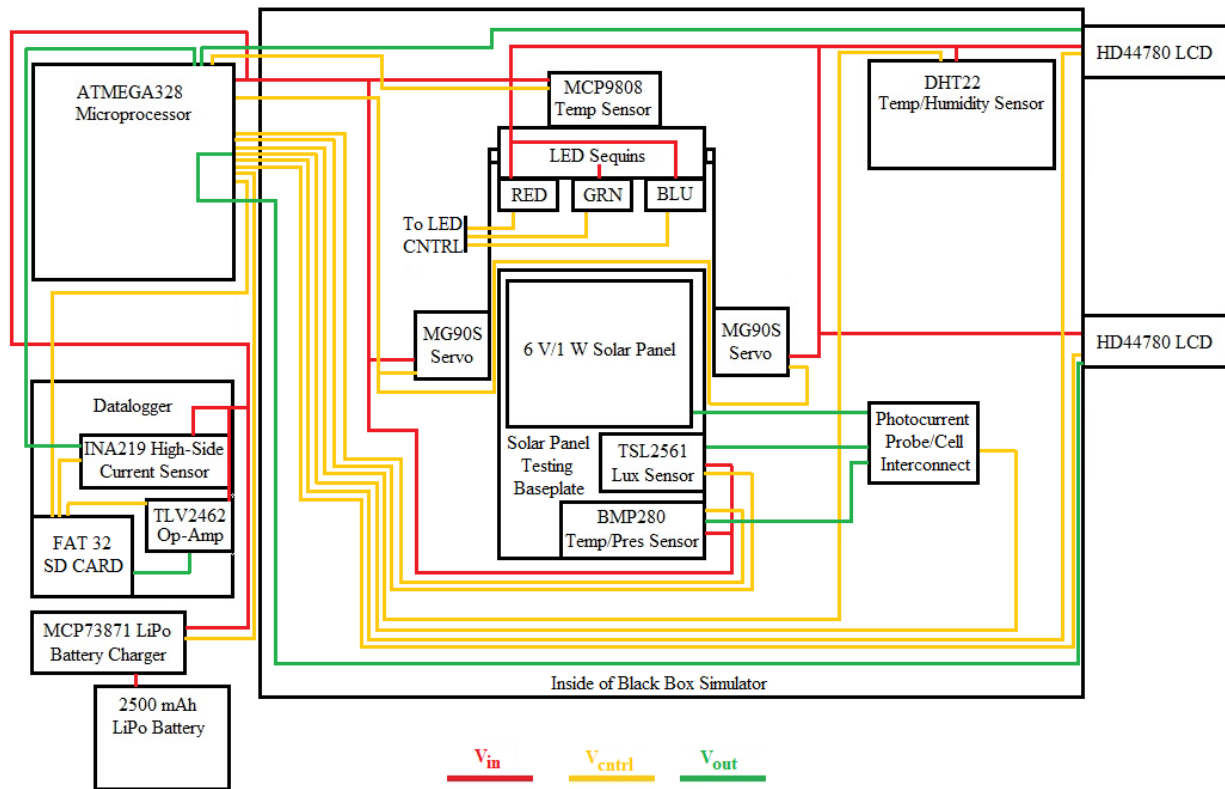


Fig. 3.2. Overall concept for the solar cell simulator programmable interfaces with major electrical components. Circuit is broken down into input, output, and control voltages ranging from 3.3 to 5 V.

As observed from Fig. 3.2, the initial concept only had one microprocessor controlling and measuring the analog data from multiple sensors. More importantly, since this design was created early in the project, many other sensor suites had not been explored and the design has since evolved to a more robust and complex system. To minimize development schedule extensions resulting from continuously updating the system with new technology as it became commercially available, an initial capabilities document was drafted. This document would serve

as the baseline for (1) system design requirements, including capabilities, limitations, (2) how the system would be electrically connected (e.g., formulation of a circuit schematic to test with software and use as a guide in fabrication), and (3) identify major system components. It should be noted that much of the process for initial fabrication came from an ad-hoc engineering approach, where electrical designs were made using PSIM and EasyEDA circuit simulation software.

3.3.1 Standard Simulator Components. The largest material constraint was that the BBRS required a central housing to minimize ambient light coming into the test fixture to maximize light intensity readings for PV standardization and subsequent irradiance testing. Even though this STE was designed to be scalable, it was important to keep the physical structure small enough to test PV cells and not take up too much bench space in the laboratory, but also large enough to cover most of the test variables discussed in Chapter 2. This large piece of material was not selected until towards the end of the BBRS design, where all the subsystems were finalized as a compact design to fit inside a designated enclosure. As COTS source selection was the most time and cost-effective method, a computer server metallic box was to serve as the main BBRS enclosure. Specifically, a Makom 9U server data cabinet, model #: 048-GM-48360 was selected and modified to be the primary BBRS enclosure [91]. The cabinet interior was coated with black non-reflective material, and custom 3D printer rails used for mounting BAPCS and ECMS modules with each module capable of being laser leveled. The modified BBRS enclosure is shown in Fig. 3.3 below with the side panel doors removed to demonstrate the ability to modify the test module positions along the bracket system.

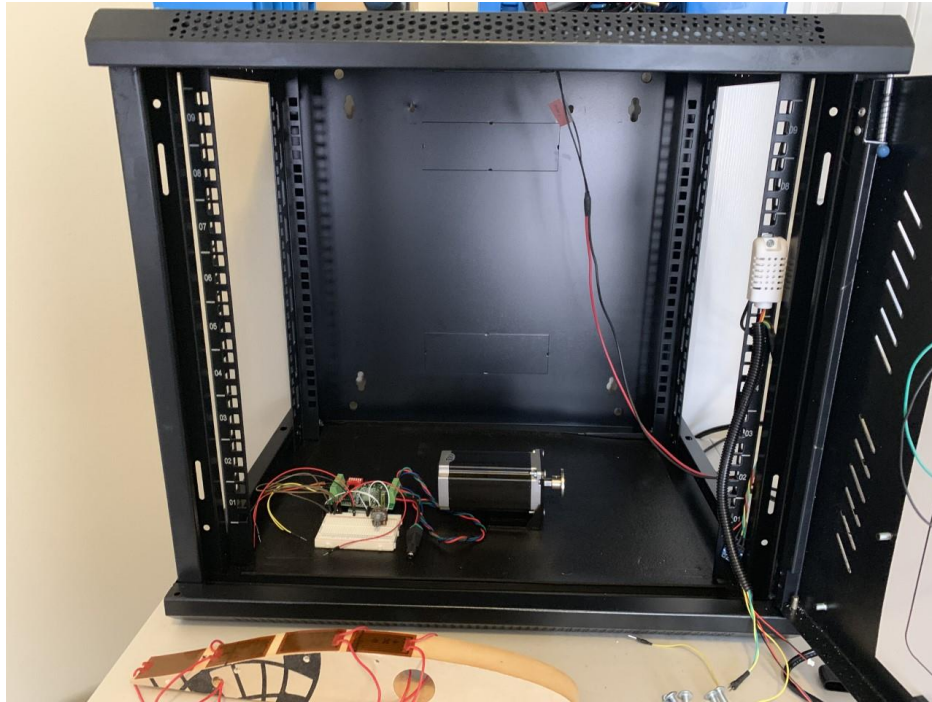


Fig. 3.3 Front image of the BBRs enclosure showing the vibration simulator testing subsystem mounted on the base.

The second constraint presented in the BBRs design was the use of a single microprocessor unit. A single unit would require robust coding that would prove difficult to maintain if specific components or sensors were interchanged to adapt to new commercially available technologies. Additionally, there were other considerations such as limited physical harness requirements, potentially slow performance due to low memory, ease of coding and familiarity with the processor integrated development environment (IDE), and interoperability concerns when changing out electrical components due to failures or requirements for increased performance. As the IDE for Arduino boards was open source, this was the ideal coding source for a processor or controller.

Both constraints established the requirement for a subsystem-based design, where the BBRs was to be built using several distinct purpose-driven systems that each had unique functions. As the microprocessor development was no longer an option, COTS microcontrollers were used instead to allow more controlled measurements to be programmed, despite requiring

more code to accomplish multiple operations. Each subsystem would utilize a specific Arduino-based microcontroller tailored to the unique requirements of that particular system; some of these boards are shown below in Fig. 3.4.



Fig. 3.4. Stacked microcontrollers (from left to right), the Teensy 3.2 board, Arduino Nano, Uno R3, and Sunfounder MEGA 328 microcontroller board. For more details, the reader is referred to [83]-[85].

These Arduino-series microcontrollers come in a variety of shapes, sizes, and capabilities, where there were three boards selected for this research effort. The first was the Arduino Uno R3 microcontroller, shown in Fig. 3.5 below, which acted as the primary test configuration board, and was used for proof of concept designs in the early prototyping stage.



Fig. 3.5. The Italian-made Arduino Uno R3 microcontroller to be used as the central processing unit (CPU) for the BBRs subsystems in prototype testing. Once the code is verified and there are no errors, the more robust ATMEGA328 will replace the R3 as the primary CPU (with the exception of the BAPCS). For more details, the reader is referred to [83].

The second board selected was the ATMEGA328 microcontroller board (i.e., the METRO328), shown in Fig. 3.6 below, which has an open source IDE compiler based on C++ language.



Fig. 3.6. The ATMEGA328 microcontroller board.

The METRO328 board [85] was selected to replace the R3 after each subsystem is complete with initial testing and ready for the next stage of fabrication. The third board selected

was the Adafruit METRO Mini 328 which is a smaller version of the METRO328 [84], shown in Fig. 3.7 below, and was selected to conserve space inside the BBRS by minimizing the subsystem electronics size for certain systems.

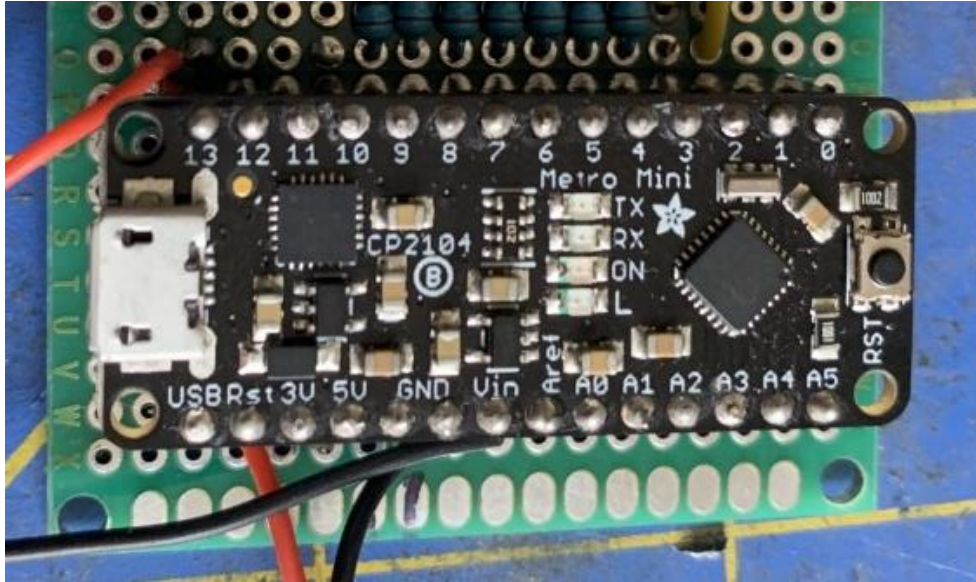


Fig. 3.7. The assembled Adafruit METRO Mini 328 microcontroller board with headers installed.

One issue with the board swap from the R3 to METRO328 was that the METRO series boards needed to be properly synched to the Arduino software package, as there would be an IDE compiler mismatch. The switch from the R3 to the METRO was recommended as the Arduino R3 board only has ~32.2 MB worth of data capacity, and it is more beneficial in the future to utilize the METRO328 board due to the larger data storage space for more advanced code. Other standard components for the research effort were the liquid crystal displays (LCD), which came in a variety of colors and sizes (i.e., limited by text capacity at 16x2 and 20x4), where the LCD acted as displays for data during testing. Multiple HD44780 LCD's were used for each subsystem, and a standard 16x2 LCD [95, 96] is shown in Fig. 3.8 below.



Fig. 3.8. Front and back image of the HD44780 LCD display, with the test pins and voltage input pins successfully soldered/connected and ready for breadboard testing.

Many of the LCDs required many digital input pins on the microcontroller, and thus limited valuable digital input availability for digital-to-analog conversion control, as well as additional measurement sensors. Therefore, to solve this issue the inter-integration circuit (I^2C) communication protocol was used for this research effort during electrical design and testing. In the case of the LCDs, an I^2C LCD shield was used to simplify the required 16-pin inputs to 4-pin inputs, with no requirement for any digital inputs as all the functions could be run on the SDA/SCL bus [97].

3.3.1.1 Inter-Integration Circuit Communication Protocol. Commonly referred to as I^2C , this is a serial protocol interface commonly used for two-wire interface connected microcontrollers within an embedded system, which is based on a master board controlling slave boards or sensors and shown in Fig. 3.9 below [8].

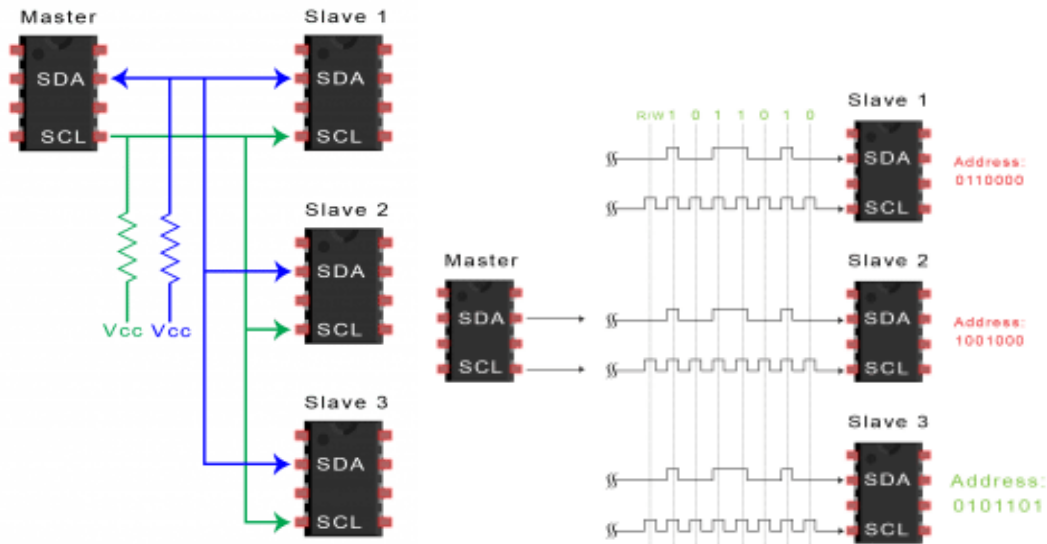


Fig. 3.9. The inter-integrated circuit communication protocol illustrated with a single master board and multiple slave boards and sensors connected using serial data (SDA) and serial clock (SCL) wiring conventions (left), and the equivalent illustration showing received signals with proper 8-bit address signals (right). This is the primary protocol used in the BBRs subsystem development. For more information, the reader is referred to [8, Fig. 4].

This was selected as it increases digital input pin availability on the microcontroller, is easy to use, and the addresses are easily mapped for slave devices using the METRO328 as the master board; pull-up resistor values ranged from 220Ω to $4.7k\Omega$ depending on the slave sensor. The upper bus speed is defined by utilizing the primary master board, and only two wires are required using this protocol with pull-up resistors connected to the main voltage bus (+3.3V and 5V) and serial data/serial clock (SDA/SCL) lines. Using this convention and assuming an 8-bit address limitation for COTS sensors, up to 8 of the same sensors can be utilized on the same I²C bus, with the capability to add a seemingly infinite variety of additional sensors and only be limited by the upper bus processing speed [8]. For this research effort, the I²C maximum clock frequency was established at approximately 400 KHz for fast-mode operations.

In terms of electrical characteristics, “I²C uses an open-drain/open-collector with an input buffer on the same line, which allows a single data line to be used for bidirectional data flow”;

the method by which the device is open drain pulling low or pulling high is shown in Fig. 3.10 below [54].

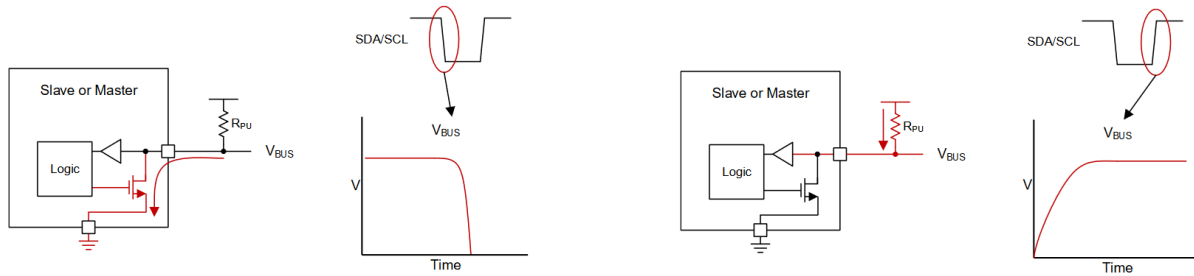


Fig. 3.10. Basic internal structure of an SDA/SCL line where (left) the bus is pulled LOW, and (right) the bus is pulled HIGH with an open-drain interface, where the flow is measured over the pull-up resistor. For more information, the reader is referred to [54, Fig. 3].

This type of electrical characteristic for the research effort is desirable because no device on the communication bus line can force a high state, and thus the bus will never have a communication issue where a short can occur [54]. Although the I²C communication protocol has a slower data transfer rate than the serial peripheral interface (SPI), and the data reference frame is only 8 bits, it is a more well-known and easier to use communication protocol [8]. This protocol is used extensively in the BBRs electrical system architecture and saved developmental time and costs in both the breadboard and fabrication stages.

3.3.2 BBRs Subsystem Design. Dividing the BBRs into subsystems was the most effective method for optimizing data rates while minimizing costs. Additionally, this allowed the research effort to divide each critically important variable discussed in Chapter 2 and individually address each with a dedicated subsystem.

3.3.2.1 Environmental Control and Monitoring Subsystem Design. The first challenge was to develop a subsystem that was responsible for monitoring and subsequently controlling the internal temperature of the STE. The subsystem requirements were to: (1) ensure that the BBRs ambient temperature, barometric pressure, relative humidity and baseplate

temperature conditions are clearly displayed, and (2) ensure that the baseplate temperature in which the solar panel/array/cell is mounted does not exceed 25°C during testing, Internal cooling was accomplished using high powered brushless DC fans, which will activate a relay when the baseplate temperature exceeds 24°C, and shuts off when temperature stabilizes below 24°C. The 1-degree difference is to ensure that the internal temperature for the BBRS does not exceed 25°C, so that the system activates early to proactively mitigate excessive heat outside the STC temperature criteria as opposed to reactively after the limit has been reached or exceeded.

Data was displayed using the HD44780 20x4 LCD [95], with sample readouts shown in Fig. 3.11 below.



Fig. 3.11. Image showing the startup menu for a sample version of the ECMS, where the code initiates the DHT22 and BMP280 sensors to tell them to start collecting data. The data is broken up into a slideshow presentation where each screen, shown in the middle and right image, stays up for 2 seconds. Setup allows user to monitor air pressure (in kPa), relative humidity (in percent), the baseplate and ambient temperatures (°C).

The primary components for the environmental control and monitoring subsystem (ECMS) are the BMP280 temperature and barometric pressure sensor [65], the DHT22 temperature and humidity sensor [66], the SONGLE SRD05-VDC relay [82], and thermal baseplate module. The BMP280 temperature and barometric pressure sensor shown in Fig. 3.12 was selected as a precision sensing solution for measuring barometric pressure with ± 1 hPa absolute accuracy, and temperature with $\pm 1.0^\circ\text{C}$ accuracy.

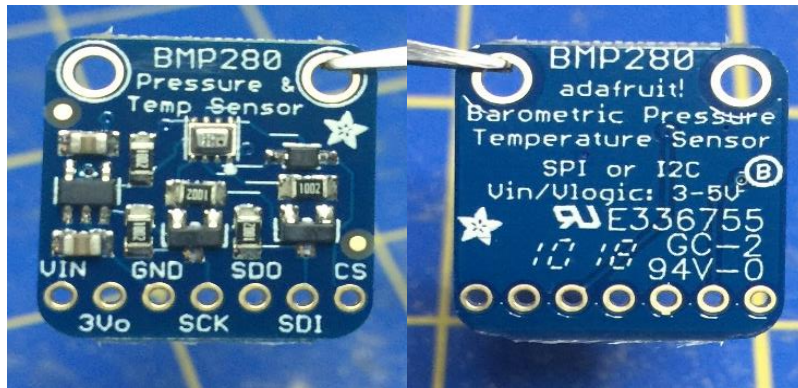


Fig. 3.12. Front image (left) and backside image (right) of the BMP280 sensor without pins or headers attached. Test headers will not be soldered onto the board, instead the board will simply have pins for ease of use in the breadboard phase.

The sensor has an internal 3.3V regulator and level shifting capability, is compatible with Uno R3/ATMEGA328 using a 3V or 5V connection and is mounted in conjunction with test solar panel baseplate (e.g., in a configuration to effectively measure flat solar cell temperature). The commercially available DHT22 wired temperature and humidity sensor shown in Fig. 3.13 below has an operating voltage range of 3V-5V, is R3/ATMEGA328 IDE compatible, and has a 2.5mA max current use during conversion.

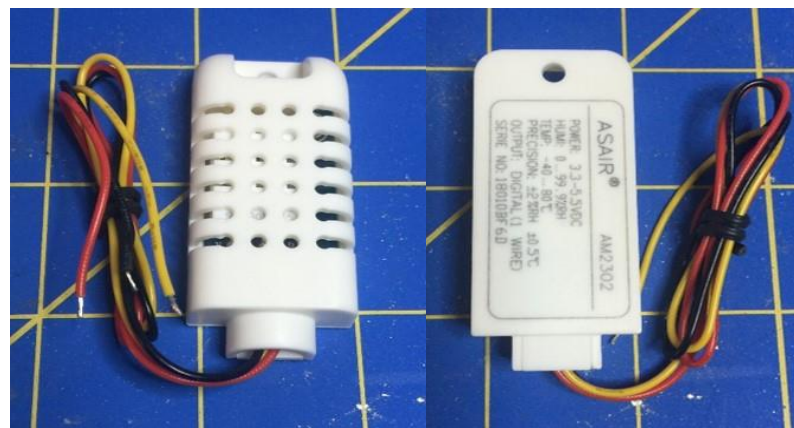


Fig. 3.13. Front (left) and back (right) image of the DHT22 wired temperature and humidity sensor.

The sensor can provide 0-100% humidity readings with 2-5% accuracy, -40 to 80°C temperature readings $\pm 0.5^\circ\text{C}$ accuracy at no more than 0.5 Hz sampling rate, which is approximately once every 2 seconds. This device is mounted to the black box simulator wall near

the main electronics box to monitor overall system enclosure temperature and humidity levels. The DHT22 senses relative humidity expressed as a percentage and calculated via (37) below which was used in generating the code algorithm for the ECMS microcontroller [66].

$$RH = \left(\frac{\rho_w}{\rho_s} \right) (100\%) \quad (37)$$

Where ρ_w is the density of water vapor and ρ_s is the density of water vapor at saturation. The DHT then measures the electrical resistance between two electrodes to detect water vapor and utilizes a single thermistor for temperature readings. The SONGLE Industries SRD-05VDC-SL-C Serial Relay Driver shown in Fig. 3.14 was incorporated for integration of 12VDC brushless fans used to regulate internal temperature, as it is well suited for external power supply high operating voltages [22, 82]. Fig. 3.15 further illustrates the relay internals using a simple circuit diagram.



Fig. 3.14. Image of the SRD-05VDC-SL-C assembled serial relay driver used in the ECMS.

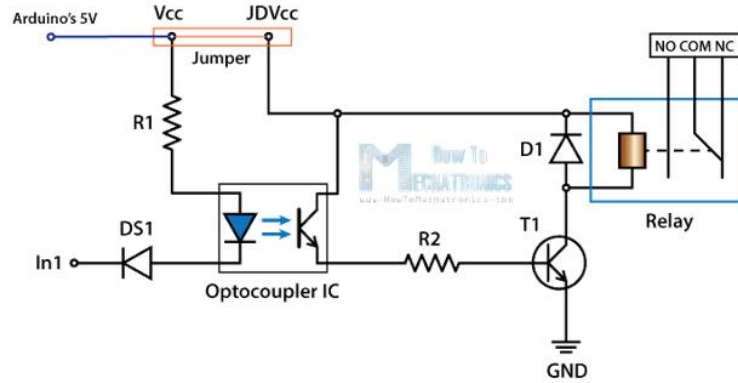


Fig. 3.15. Serial relay driver concept as described via a circuit diagram. Retrieved from Control high voltage devices: An Arduino relay tutorial. For more details, the reader is referred to [22, Fig. 2].

Prior to using the LCD and the BMP280 or DHT22 sensors, the corresponding libraries needed to be downloaded and installed on the Arduino IDE compiler so that appropriate commands and component addresses could be utilized. The custom designed ECMS thermal baseplate shown in Fig. 3.16 below is similar to the BAPCS module discussed later on in this chapter, as it allows for flexibility in different test setups and is comprised mostly of 13mm thick aluminum honeycomb panel.

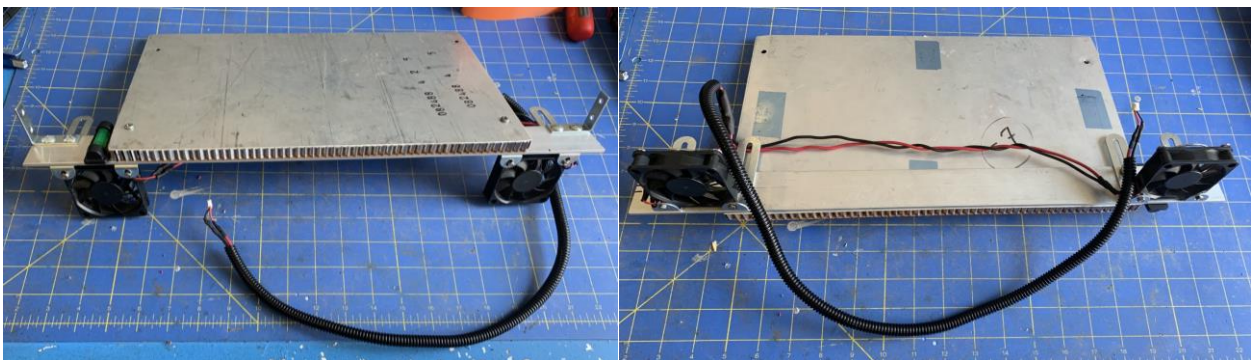


Fig. 3.16. Environmental control and monitoring subsystem (ECMS) module thermal baseplate from (left) top view and (right) bottom view.

The module is mounted on the internal BBRs rail system to help keep the module baseplate level. The module also contains an independent temperature control for a thermally regulated baseplate using polyimide heating elements, as well as a structural housing for vibration simulation using a series of different motors and rotations per minute (rpm) settings.

The thermal baseplate area is approximately 75.645 mm^2 and is where flat cells can be tested and subsequently heated or cooled depending on the desired test temperature regime. For the PV-embedded airfoil experimental setup, the baseplate is simply a structural component to physically hold the test apparatus in place and cool it as required. The PV-embedded airfoil heating component for future testing is discussed in Chapter 5.

The ECMS thermal control elements are comprised of individual 7W and 12W PTC polyimide heaters [94], that are controlled by W1209 and Bayite 12V/10A temperature controllers [93] as shown in Fig. 3.17 and Fig. 3.18 respectively.

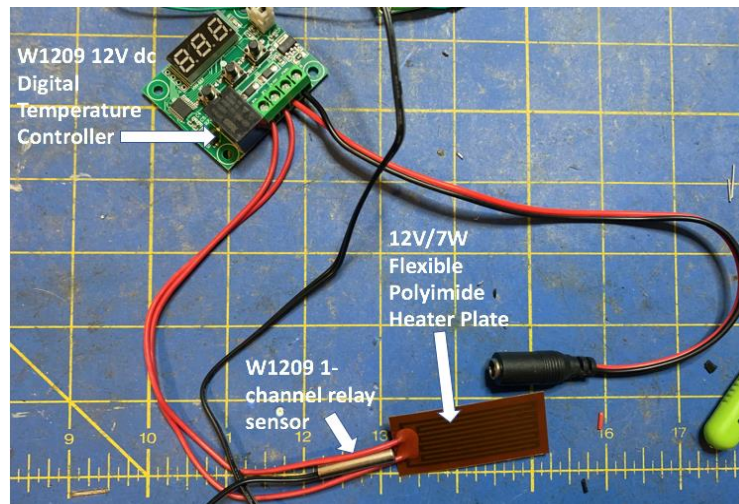


Fig. 3.17. W1209 temperature controller connected to a single polyimide heating element integrated into PV test airfoil.



Fig. 3.18. Bayite 12V/10A temperature controller.

The W1209 controllers are used for independent temperature control for the thermal baseplate to create temperature hot areas and differential heat. The temperature for both controllers is monitored through a feedback loop which is accomplished by a 1-channel relay sensor that triggers the internal relay to halt power transmission and thus halts the temperature increase. The finalized ECMS circuit schematic and code is shown in Appendix E for reference and experiment repeatability purposes.

3.3.2.2 Artificial Sun Module Subsystem Design. The next phase was to create a test module that could emit specific wavelengths within the electromagnetic spectrum, and also be light and small enough to be mounted on a moving arm to simulate the various angles of incidence a solar panel would experience, with the resultant photocurrent measured using the PCMS. The subsystem requirements were to: (1) be mountable on a stepper arm connected to the BAPCS and of a weight and shape that does not interfere with the BAPCS motor operation, (2) provide IR and UV values (in respective UV-A and UV-B spectrums), (3) measure and indicate the distance to the PV device from the ASMS source, (4) provide a method for contact-less PV surface temperature measurement, and (5) contain a spot laser for test alignment and calibration.

To accomplish this, the ASMS was divided into two different solar test array (STAR) layers. The first layer would be closest to the PV device under evaluation, with the second layer directly behind that as shown in Fig. 3.19 below.

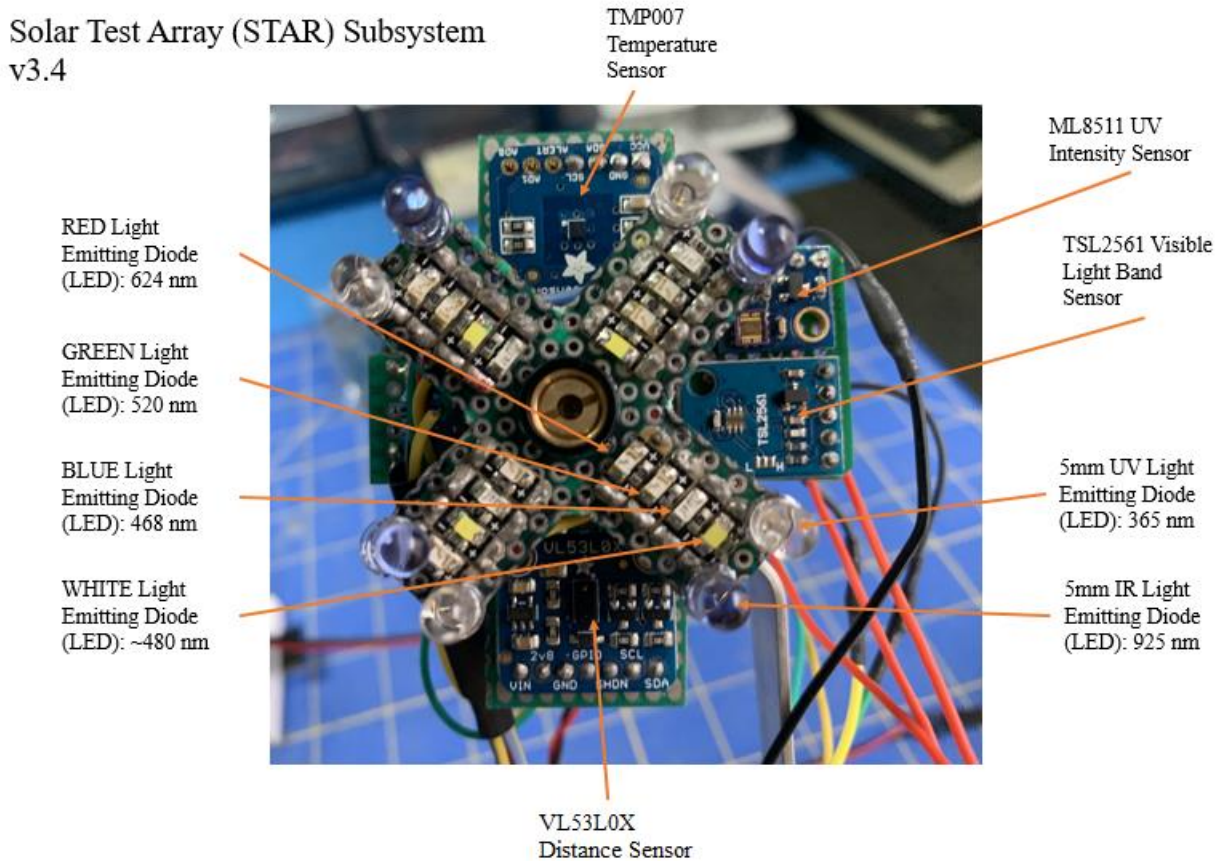


Fig. 3.19. Completed ASMS solar test array layer 1 and 2 with brief description of each component and corresponding wavelength as applicable.

3.3.2.2.1 Solar Test Array Layer 1 Subsystem Design. Some of the standard components for the STAR layer 1 include: (1) UV, IR and visible spectrum light emitting diodes, and (2) a custom fabricated LED shield. Since the visible spectrum was deduced to be the most important for the spectral response characteristic and ASMS surface area conservation was a design requirement, LED sequins [74]-[77] were used in the STAR1 design, as shown in Fig. 3.20 below.



Fig. 3.20. Front (left) and back (right) image of the LED sequins used for the artificial sun to stimulate the solar cells.

The LED sequins were intended to comprise the artificial sun under different wavelengths, namely using colors including red, green, blue, and white, with wavelengths of 624 nm, 525 nm, 470 nm, and 480 nm respectively under 100% illuminous intensity. Aside from the favorable physical size, these were ideal irradiance components due to small current draw (~5 mA at 3.3V), enabling up to 5 to be linked in parallel on a single digital microcontroller pin. The LED shield shown in Fig. 3.21 below was fabricated to control a specific illumination sequence using a programmable pushbutton, with another pushbutton used to control the 5mW calibration laser diode [80].

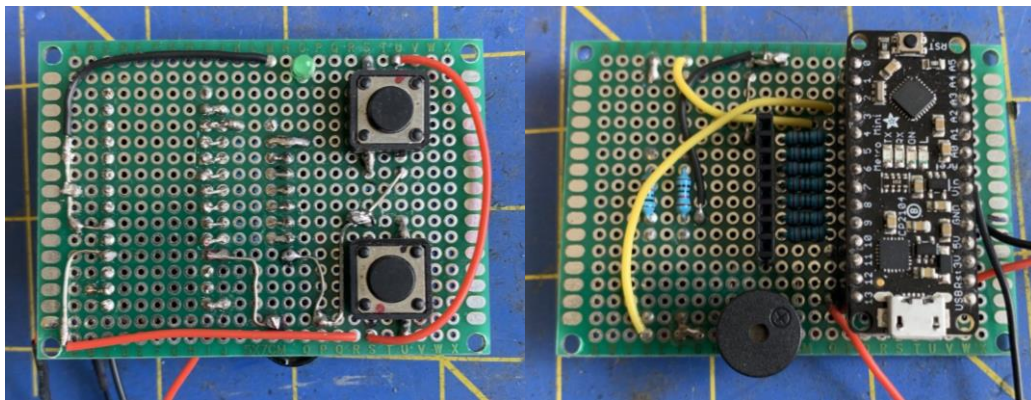


Fig. 3.21. Front (left) and back (right) image of the completed LED array shield module incorporated into the ASMS STAR1 architecture.

The LED array was used to expose the solar cell to different EMS values by using red, green, blue, white, UV, and IR LEDs, with quantified/calibrated values +/- 1% [74]-[79]. To minimize the probability of arcing, surface charge phenomenon, and any other electrical surface

conditions where a short could occur within the array, a high temperature non-conducting silicon-based epoxy was covered around all the solder points. The cure time for this epoxy requires approximately 12 hours to cure at room temperature.

3.3.2.2.2 Solar Test Array Layer 2 Subsystem Design. The second layer of the STAR assembly (i.e., STAR2) had the following requirements: (1) distance measurements to the solar cell in mm, (2) be able to measure the surface temperature within 1/100-degree Celsius accuracy $\pm 0.1^{\circ}\text{C}$, using a non-contact method, and also (3) measure any reflected energy measurements at Beta angle zero. To provide accurate distance measurements, the VL6180X time of flight (TOF) sensor [98] was used, as shown below in Fig. 3.22.



Fig. 3.22. Front (left) and back (right) image of the VL6180X TOF and lux sensor.

This sensor breakout board is comparable to the VL53L0X TOF sensor, however the VL6180X incorporates an additional lux sensor in the breakout board. This additional lux sensor was used to determine the ASMS lux level and compare to readings on the thermal baseplate and scan for any deviations. This sensor successfully met the requirement to act as a light detection and ranging (LiDAR) setup to accurately measure distances between ASMS and PV cell. It should be noted that the VL6180X is interchangeable with the VL53L0X sensor [68, 69], however the 53L0X has a narrower detection band, and has a larger operational capability; the 6180X is limited to 150-200 mm maximum distance, where the 53L0X is limited to 1200 mm

distance [69]. If the BBRS is intended to meet a larger scale requirement, then the 53L0X is recommended.

For the reflected energy measurements, the TSL2561 Light/Lux sensor breakout board [60] shown in Fig. 3.23 below was selected for this research effort.

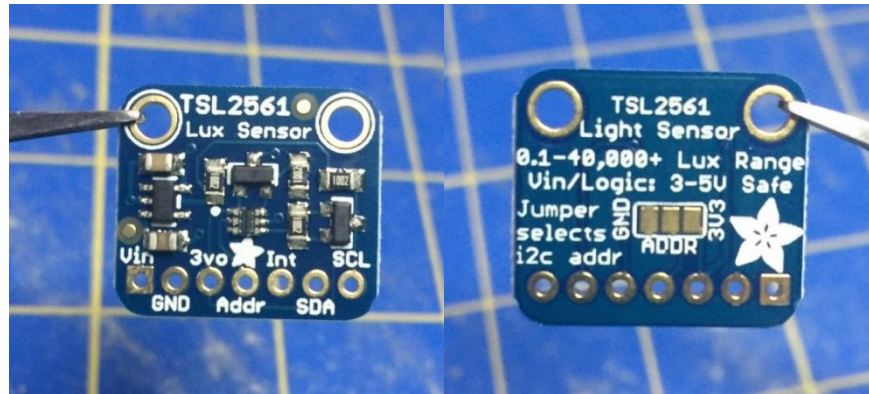


Fig. 3.23. Front (left) and back (right) image of the TSL2561 lux sensor.

The board is equipped with 3.3V regulator and level shifting circuitry, is R3/ATMEGA328 compatible, and is used to precisely measure illuminance in different lighting conditions. It has a temperature range of -30°C to 80°C a dynamic range (Lux) of 0.1 to 40,000 lux, and an operating voltage range of 2.7 to 3.6V. These conditions make it easily integrated into the existing BBRS architecture with minimal cost. It was intended to monitor lux at the solar cell baseplate (i.e., the lux receiving end), where lumens were calculated using (3) while adjusting for the area of the PV device. For UV measurements the ML8511 sensor breakout board [99] shown in Fig. 3.24 was selected and is mounted with a slight 90 degree offset from the distance sensor and temperature sensor on STAR2.

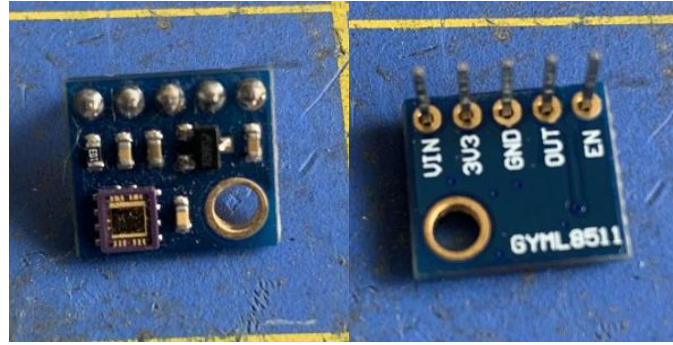


Fig. 3.24. Front (left) and back (right) image of the ML8511 UV sensor.

This sensor outputs an analog signal in relation to the amount of UV light it detects, and the output would be an analog voltage that is linearly related to the measured UV intensity level (i.e., irradiance) measured in mW/cm^2 . The ML8511 has better spectral responses in the IR range of 200-400 nm, with more accurate readings at 3.3Vref in the UVA range (315-400nm), allowing better measurements of IR intensity/irradiance than the more commonly available S12SD sensor module [100]. As mentioned previously, while utilization of these COTS sensors is more financially beneficial, however the required coding to appropriately correlate between analog output voltage and irradiance (i.e., UV intensity) was difficult; the correlation between output analog voltage and UV intensity is shown in Fig. 3.25 for the ML8511 conversion process [32, 99].

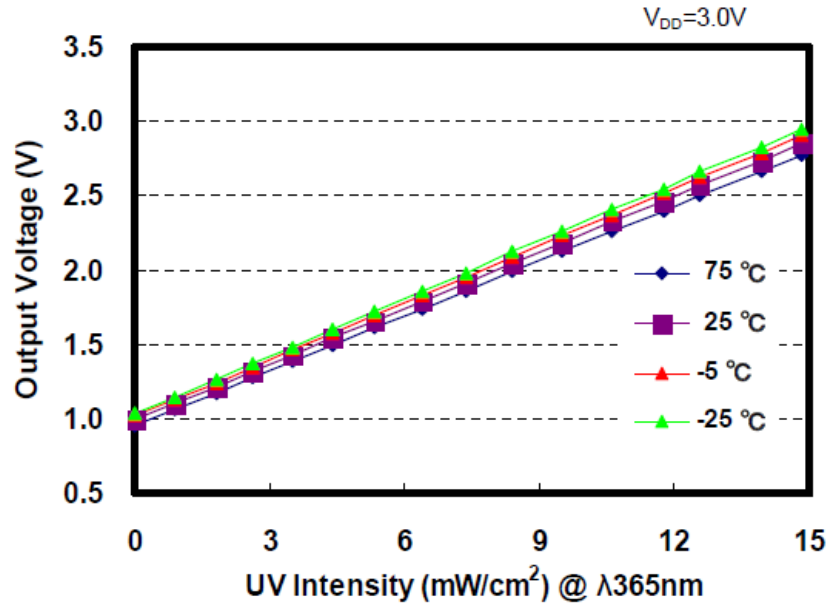


Fig. 3.25. Output voltage versus ultraviolet intensity graph for the ML8511 UV sensor under ambient temperature conditions of 25°C. The linear relationship shown above was programmed into the microcontroller for the 8511 sensors to reflect pertinent UV irradiance intensity in mW/cm² to the system user. For more details, the reader is referred to [32, Fig. 20].

To accurately measure the PV cell temperature, a contactless method was recommended as to not interfere with surface probes that could either damage the delicate cell surface, as well as to eliminate any shadowing effects caused by temperature probes during illumination testing. The Adafruit Industries TMP007 temperature sensor breakout board [64] shown in Fig. 3.26 was selected to meet this requirement, which is I²C communication protocol compatible and is mounted on the opposite side of the distance sensor on STAR2.

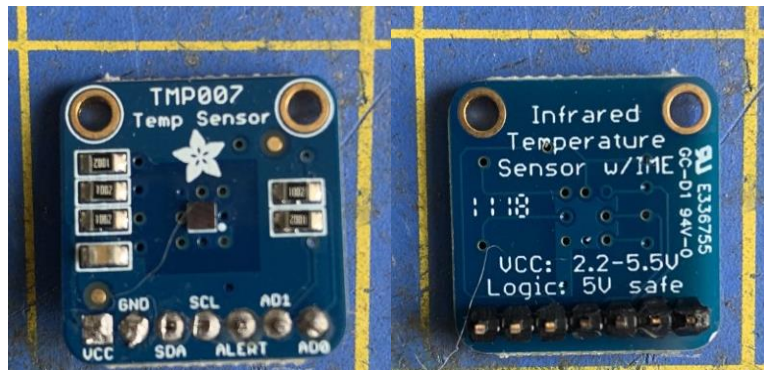


Fig. 3.26. Front and back image of the TMP007 contactless temperature sensor to detect the PV surface temperature.

The sensor detects the temperature by absorbing the emitted IR waves, with the code able to conduct an analog to digital conversion and present the surface temperature in degrees Celsius. The finalized ASMS circuit schematic and code is shown in Appendix B and C for reference and experiment repeatability purposes.

3.3.2.3 Beta Angle Position and Control Subsystem Design. The BAPCS design requirements are: (1) be able to manipulate a mechanical device (i.e., a servo motor or stepper motor) using a control device, and (2) accurately measure servo arm position relative to the PV device. The ASMS is mounted at the end of the extended servo arm manipulated by a servo/stepper motor, and the design shall provide the servo/stepper arm position in degrees relative to the PV panel. For the control device, the BAPCS operates with an easily interfaced Uxcell 4x4 membrane keypad [101] shown in Fig. 3.27 to control position, with LCD indicating AOI in degrees.

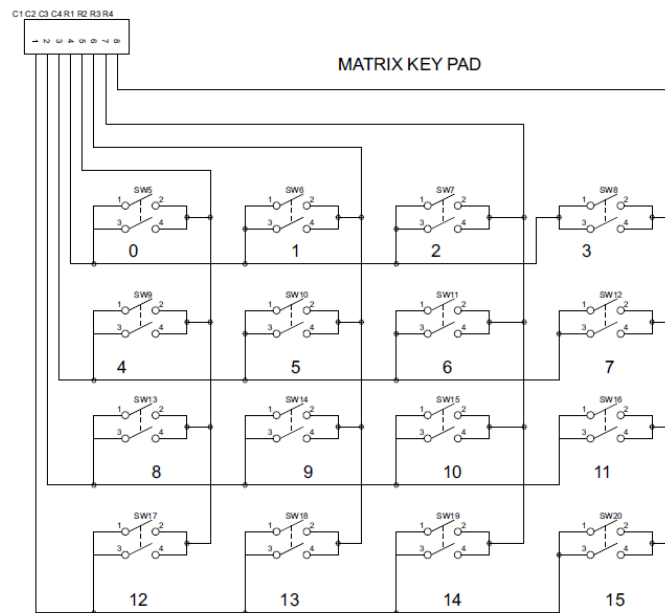


Fig. 3.27. 4x4 membrane-type keypad circuit diagram with 8-pin output for connection to microcontroller. For more details, the reader is referred to [6, Fig. 3].

The matrix keypad is easily interfaced with the METRO328 controller board, however due to the 8-pin output configuration this occupies 8 digital input pins on the microcontroller [6]. The largest obstacle when developing the BAPCS was the selection of a reliable stepper driver that had a user-friendly library compatible with the Arduino IDE compiler. For this research effort, the SparkFun A3967 [81] shown in Fig. 3.28 was selected.

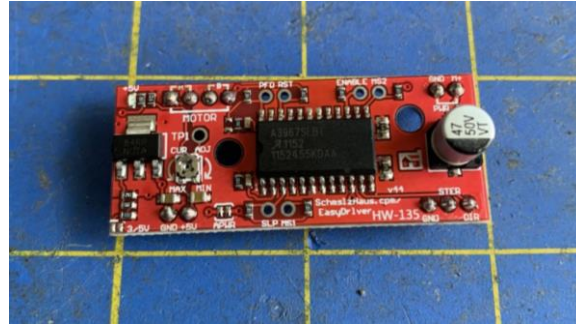


Fig. 3.28. A3967 stepper driver used in conjunction with the NEMA17 series stepper motor for the beta angle position and control subsystem (BAPCS) module.

A commonly used commercial board used for stepper motor control is the SparkFun Electronics A4988 driver, however this driver is prone to numerous shorts, excessive overheating, and poor production quality when purchased at lower costs. It is recommended that the A3967 have heat sinks installed, but it was discovered that a fan setup was also recommended to keep the board cool during continuous operations, as the operational amplifier (Op-Amp) gets very hot during continuous use under load. The board is powered directly by 12V/2A power supply and is capable of a 1.2A maximum drive current, which should yield enough torque from the bipolar stepper motor to control the ASMS.

There were several iterations of the BAPCS motor element that were experimented, but to meet the system requirements for beta angle testing the level of control for motor displacement needed to be less than 1-degree. To achieve this requirement, the NEMA17 17HS19-2004S1 Bipolar stepper [86] shown in Fig. 3.29 was utilized.

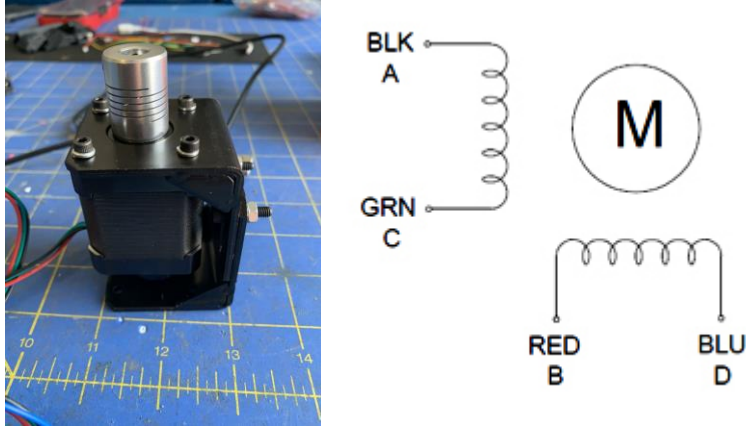


Fig. 3.29. NEMA17 series stepper motor used as the primary driver for the beta angle position and control subsystem (BAPCS) module with brackets installed (left) and basic equivalent circuit (right). For more details, the reader is referred to [86, Fig. 1].

The step angle is 1.8 degrees for this motor, where in microstep mode it would take 1600 steps to accomplish one revolution of 360 degrees, and thus refines the step angle to 0.225

degrees per step. The command logic is based on desired steps, where $steps = \left(\frac{\text{desired AOI}}{0.225 \left[\frac{\text{degree}}{\text{step}} \right]} \right)$.

The NEMA17 has a holding torque of 59 Newton centimeters (Ncm), and a rated current per phase of 2A, which matched very well with the required torque to hold and move the ASMS. To utilize the rail system for the BBRS internal structure, a BAPCS module was fabricated and is shown in Fig. 3.30 below.

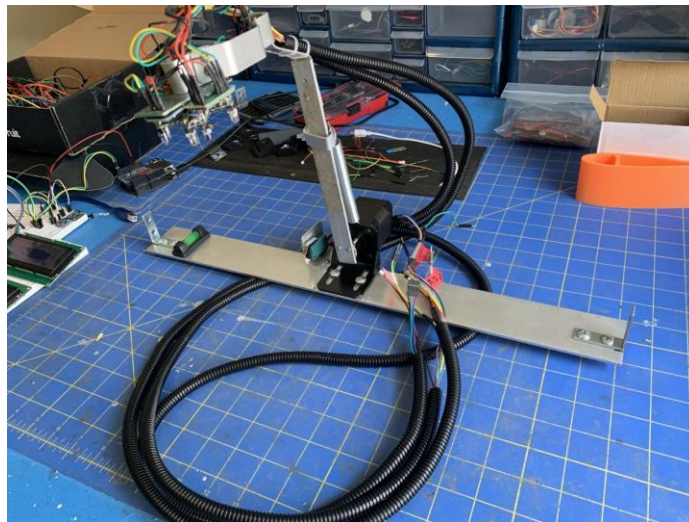


Fig. 3.30. Blackbox radiation simulator (BBRS) beta angle position and control subsystem (BAPCS) module which uses a specially designed stepper arm to house the artificial sun module subsystem solar test array layer 1 and 2.

This BAPCS module intended to be mounted on rail system within BBRS in a level condition with the ECMS thermal baseplate module and can be moved in various positions to accommodate for other test parameters. The module is comprised of a custom stepper arm, the ASMS (STAR1 and STAR2), as well as the BAPCS with the zeroize tact switch. The electrical harness created needed to be long enough to reach the main BBRS door which contains all the subsystem controllers and LCD screens. The module was also designed with component interoperability in mind and can host a variety of adjunct ASMS designs and other sensors discussed in Chapter 5. The BAPCS microcontroller code and circuit schematic are in Appendix D for reference and experiment repeatability purposes.

3.3.2.4 Spectrum Calibration and Response Subsystem Design. This subsystem was generated as a result of the additional requirement for system calibration, which did not come about until later in the research effort. Regardless, this individual system was required to ensure that the BBRS has an effective and clear standard for illuminance metrics, including: (1) a UV spectrum analysis, with resultant UV index (UVI), and corresponding UV intensity in mW/cm^2 , (2) an IR spectrum analysis, with intensity in lux, and (3) a visible spectrum analysis, with intensity in lux. The Adafruit TSL2591 sensor breakout board [67] shown in Fig. 3.31 was selected to meet this requirement which will return light in standard SI lux units, which are a result of some complex calculations based on both photo diodes on the TSL2561, with one for full spectrum and one for IR.



Fig. 3.31. Front (left) and back image (right) of the TSL2591 lux sensor.

The TSL2591 is a high dynamic range digital light sensor, with a 600,000,000:1 dynamic range, a lux range of 188 μ Lux sensitivity for up to 88,000 lux input measurements; the sensitivity of the two diodes can be seen in Fig. 3.32 below.

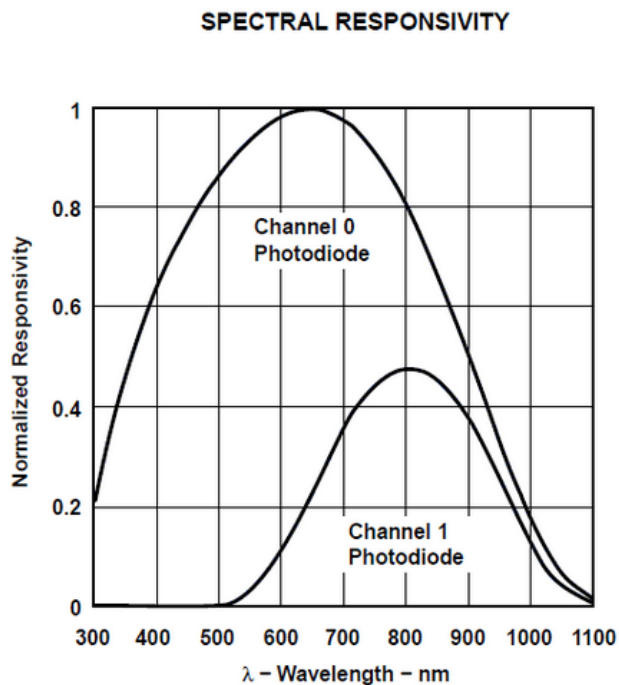


Fig. 3.32. Spectral responsivity for a channel 1 and channel 0 photodiode used in the TSL2561 that shows each diodes sensitivity. For more details, the reader is referred to [60, Fig. 7].

This sensor approximates the human eye response, with each diode intended to detect and measure analog values for the visible and IR ranges in the EMS. The VEML6075 UV-A and UV-B Sensor [70] shown in Fig. 3.33 below was selected to measure the UV intensity and record analog values for each UV spectrum. The dual band sensors and a UV index calculation

algorithm allows the measured analog voltage values to correlate to equivalent UVI. The UV, IR, and visible spectrum values were measured and datalogged using an SD card shield similar in design to the PCMS discussed in the following section. The SCARS code and circuit schematic are shown in Appendix G for reference and experiment repeatability purposes.



Fig. 3.33. Front image of the VEML6075 UVA/UVB sensor.

3.3.2.5 Photocurrent Measurement Subsystem Design. This was arguably the most important BBRS subsystem, and shall be able to provide the following information to a user: (1) current/voltage generated from the PV device, (2) display and calculate the resultant power, (3) induce variable resistance or a variable load to the PV experimental device, (4) log the data onto a serial device card for data analysis, and (5) have a harness and probe to physically connect to the PV device for data acquisition. The designed probe consisted of repurposed alligator-type clips which connected to the PV cell's installed positive and negative terminal wires. This method is beneficial for minimizing shadowing concerns and accommodates modifying the PV device series and parallel configurations for subsequent tests. The PCMS had more design iterations than any other subsystem which resulted from the fact that many new breakout boards became commercially available and provided an opportunity to simplify the complexity of a voltage measurement circuit.

The INA219 sensor breakout board [63] shown in Fig. 3.34 below was selected as the primary voltage sensor and contains an internal 0.1 ohm 1% 2W current sense resistor which is beneficial for precise low-voltage measurements.



Fig. 3.34. Front (left) and backside image (right) of the INA219 board without headers or pins soldered. The INA219 is directly connected to the positive terminal of the solar panel where the device will measure the current across the 0.1-ohm resistor (R5). For more details, the reader is referred to [63].

The sensor is capable of up to +26V target voltage, and up to $\pm 3.2\text{A}$ current measurement, with $\pm 0.8\text{mA}$ resolution which is beneficial for BBRS scalability design purposes. A Texas Instruments TS922 Op-Amp circuit was originally used for voltage measurements, but this solution was not sufficient long term due to limited physical space requirements, voltage measurement precision, and required excessive development time for careful soldering. Even though the INA219 is capable of reading both voltage and current, it was recommended to have separate sensors for each to maximize measured precision and avoid overburdening the components under high load conditions [63]. Therefore, the current measurement was accomplished using the Adafruit INA169 breakout board module [62], shown in Fig. 3.35 below.

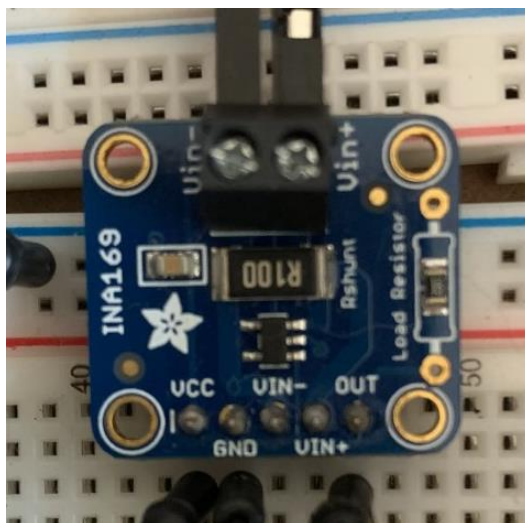


Fig. 3.35. Front image of the INA169 board with headers and pins soldered. Much like the INA219, the INA169 is directly connected to the positive terminal of the solar panel where the device will measure the current across the 0.1-ohm resistor (R5). For more details, the reader is referred to [62].

This sensor also has an internal 0.1 ohm 1% 2W current sense resistor but has a voltage capability of up to +60V target voltage, and a current limit up to +5A with $\pm 0.10\text{mA}$ resolution. Similar to the rationale for the voltage sensor upgrade, the INA169 replaced the original current sensor setup using a Texas Instruments AD623ANZ Op-Amp. For the datalogging capability, the original solution was to use a National Instruments Data Acquisition (DAQ) module, however these systems do not always offer the measurement fidelity or precision required for low-voltage systems analysis, are relatively expensive, and also require the system be paired with a software such as LabVIEW or Matlab. The intent of the BBRS was to allow users of all background to utilize this system by measuring data and logging it in a format that any researcher could understand and have access to for future analysis, such as Microsoft Excel. As a result, the Adafruit Datalogger Proshield [73] shown in Fig. 3.36 was used to gather photocurrent and other experimental data for analysis.

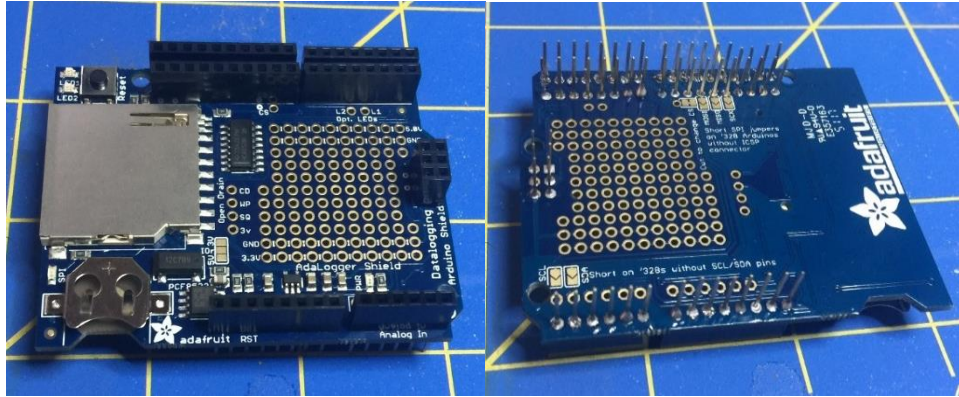


Fig. 3.36. Front (left) and backside (right) image of the datalogger after dual rail test headers were soldered for experimental test setup and breadboarding. Continuity checks passed normal using multimeter to ensure effective solder to all analog and digital pins near the real time clock (RTC). For more details, the reader is referred to [73].

The SD card interface works with FAT16 or FAT32 formatted cards and has a built in 3.3V level shifter and regulator circuitry and real time clock (RTC); the system is also Uno R3 and ATMEGA328 compatible, and provides 4 analog channels at 10-bit resolution which is beneficial for the BBRS experimental setup in continuous low-voltage low-input operations. Another advantage of this module setup is the stacking capability shown in Fig. 3.37 below, which allows for quick separation and replacement should a short or any damage occur in the PCMS.

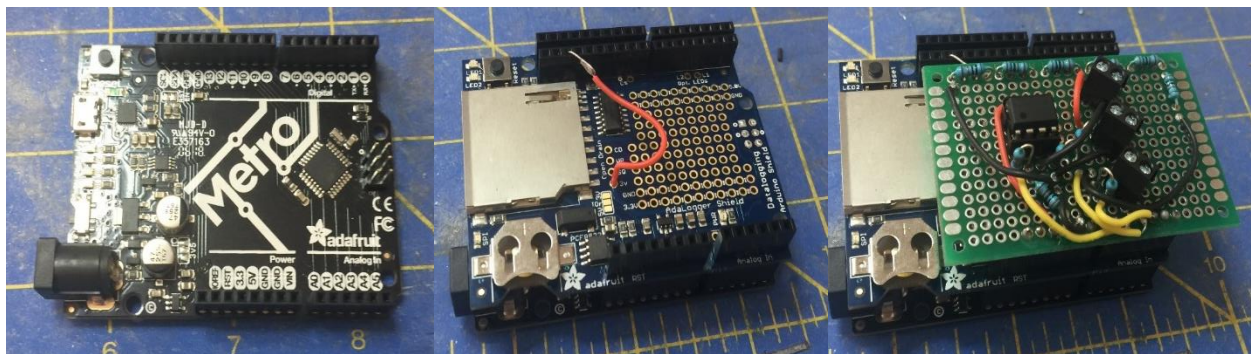


Fig. 3.37. Images of the PCMS main circuit build stackup; starting from left to right, the first image shows the standard METRO328 microcontroller board, the second image shows the SD shield mounted on top of the METRO328, with the last image showing the mounting of the legacy I-V sensor to the main PCMS circuit which has been replaced with a specially fabricated INA169 and INA219 PCB.

The simulated resistance for the PCMS was accomplished using a $10k\Omega$ potentiometer, with a commercially available buck-boost converter to serve as the variable load [89]. The potentiometer was placed on its lowest resistance for the tests; where with a minimum setting of 9.125Ω , and a maximum voltage straight from the 2P/1S PV array at an average of $3.12V$, the current over the device was 0.342 mA . The power dissipated over the device was calculated as $P = i^2 * R = (0.342)^2(9.125\Omega) = 1.066\text{ mW}$. Of note, the variable load and variable resistance test was not conducted as a part of this dissertation, with the system capability only added for future testing of other PV arrays. Once the PCMS prototype was fabricated, an initial test was executed with a 1W/6V PV cell [87] to ensure that the system was operating and logging data accurately. This test, subsequent results and analysis is discussed in Chapter 4. The PCMS circuit schematic and code is shown in Appendix F for reference and experiment repeatability purposes.

3.3.2.6 Specialized Test Equipment Bill of Materials (BOM). A comprehensive list of all the materials, components, supplies and sensors used in the fabrication of the BBRS is listed in Appendix A, with vendor references provided in [32], [60], [62]-[101]. The approximate cost of the current BBRS design does not exceed \$1800.00 USD; the entire research effort yielded a total of \$3986.17 USD and over 1200 man-hours, which includes all the time and costs associated with conceptualization, experimentation, fabrication, and component acquisition.

3.4 Design of the Experimental Photovoltaic-Embedded Airfoil

To emulate the standardized test methods used for solar devices, an experimental test solar device was fabricated for test purposes. The solar cell radiation handbook delineates the use of primary standard cells for performance verification and validation before integration into or onto a vehicle [51]. Primary standard cells are defined as the primary cells to be used for

operational purposes on the intended platform in the designated environment, and as they are considered too valuable for research and experimentation purposes in this study, secondary standard cells were used for simulator verification [51].

3.4.1 Background. Since the intent of this dissertation is to explore the use of irregularly shaped solar cells embedded on an airfoil, an adequate experimental setup will need to be custom made to ensure that sufficient sensors and solar cells can be accommodated. Initially when the BBRS was being built a stand-alone PV device was used incrementally for system verification as the design matured. To assist with proof of concept and verification of subsystem capabilities, a commonly 1-Watt, 6-Volt silicon-based PV cell encased in 6 mil coverglass with quick disconnect fittings [87] was used, as shown in Fig. 3.38 below.

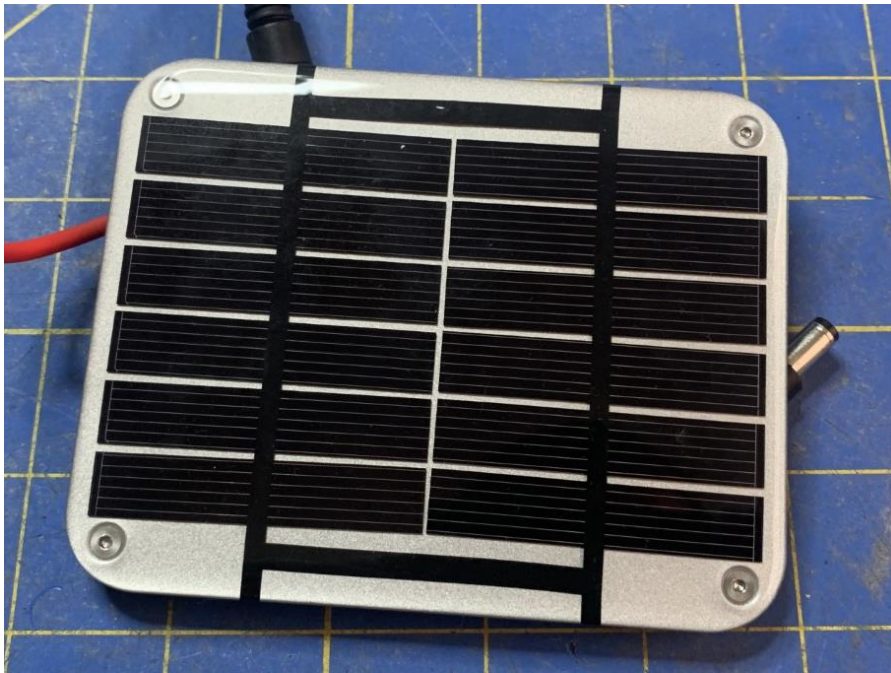


Fig. 3.38. A portable silicon-based 6V/1W solar cell used for initial verification and validation testing. For more details, the reader is referred to [87].

3.4.2 Experimental Airfoil Topology and Materials. The verification test cell is a monocrystalline cell, and is only intended for verification purposes, particularly for the SCARS and PCMS. However, this cell could not be used as an appropriate test cell for airfoil integration

as it has a rigid body that would not be able to correctly form to the contours of the airfoil without incurring damage. Therefore, a flexible solar cell option was required for sufficient testing. Since the proposed user of renewable energy technology insertion would be unmanned aerial vehicles, it is recommended to fabricate airfoils that are currently used on these HALE platforms, such as the MQ-4C Triton UAS [5].

3.4.3 Technology Limitations. Prior to designing and fabricating an experimental PV airfoil, it is pertinent to identify some technical limitations, as they impact the technical assumptions for this study.

3.4.3.1 Solar Cell Considerations. A conventional silicon monocrystalline solar cell is inherently rigid by design but is commercially available and presents a low-cost option for integration into airfoils. However, the rigidity could be an issue largely due to bending the shape to the changing slope of the airfoil surface, as well as vibrations permeating along the airfoil [15]. To help alleviate some of these problems, a possible recommendation is that a single cell be mounted at each change in slope and cover any potential “flat spots” along the airfoil. However, this still may not be able to avoid micro cracks from developing. A method to circumvent this cracking from occurring is to potentially enhance the rigidity of the solar cell under heavy vibrations by using chemically strengthened coverglass, such as those used for space-based PV devices [56]. Additionally, there may be negative impacts to mounting a series of large flat solar panels on the trailing edge of a wing, as these can negatively impact certain aerodynamic characteristics such as stall angle and maximum angle of attack [15]. Mounting an axis-tracking device by which the solar array can conduct maximum power point tracking presents even further aerodynamic concerns, therefore, it is in the best interest of the research effort to consider an airfoil that promotes maximum energy gains but also conserves aerodynamic efficiencies. To

achieve this, it is recommended that a flexible solar cell design be used and mounted away from the leading edge of the airfoil as to not alter the airfoil aerodynamic properties and mount the solar cells aft of the main vertical component emanating from the airfoil chord. An additional consideration for mounting the PV in the aft quadrant is to also preserve the integrity of the sensitive PV interconnects and coverglass resulting from potential damage resulting from icing and direct collision with foreign object debris (FOD). Through this application, assuming straight and level flight, this will force the solar array embedded on the aft section airfoil into a fixed angle configuration where maximum theoretical power gains will result from the aft quadrant of the solar array.

3.4.3.2 Experimental Airfoil Fabrication. Throughout the design process, the intent of a PV-embedded airfoil was to minimize the intrusion of the PV material to the aerodynamic shape of the airfoil. This was accomplished by contouring a flexible device to the natural slope of a 3D printed airfoil design, as well as by placing the Sundance Solar 3V/50mA flexible silicon solar cells [88] in such a manner that was conducive for flight operations. As mentioned in the previous section, for a PV-embedded airfoil to be feasible the solar cells would need to be located in an area not directly enveloping the leading edge. Each test airfoil was printed to accommodate flexible heating elements which were bonded to the airfoil surface, where the flexible PV material would be bonded overtop the heaters.

3.4.3.3 Airfoil Dimension Mapping. This mapping technique was completed using the OpenSCAD database [43] in conjunction with the AirfoilTools plotter kit, both of which are open-source programs. Using the AirfoilTools plotter, a specific airfoil design could be selected from a large database [2]. The NACA0024 symmetrical airfoil was selected as the primary case for analysis, as this type of airfoil is the most commonly used sUAS COTS design.

More specifically, the airfoil design provides the simplest and most efficient type for small scale airfoil production and is desirable for an experimental PV array design used in initial BBRS testing. An airfoil plotter tool is used to gather plot dimensions, which is then sent to OpenSCAD to take the dimensions and convert them into a usable .stl file for use in the Ultimaker Cura software [43]. The process flow is shown in Fig. 3.39 below, which illustrates the airfoil plotting tool mapping process (left), and the subsequent 3D rendering (right).

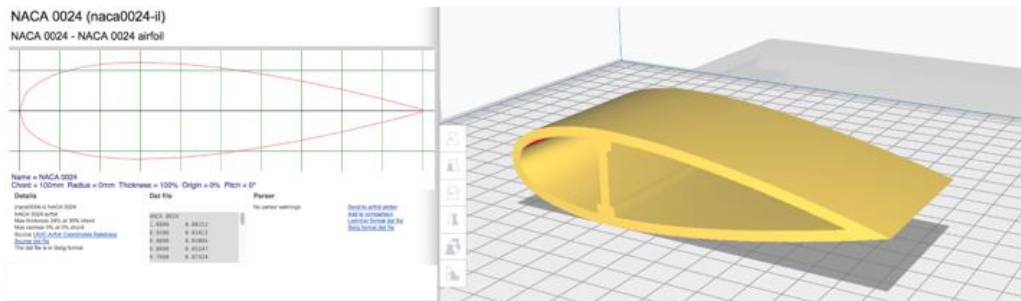


Fig. 3.39. Airfoil plotter toolkit mapping process for the NACA0024 airfoil (left), with resultant 3D rendering in Ultimaker Cura software (right) [2].

The Cura software then converts the .stl file into gcode for use in a 3D printer, where for this project the JGAurora A5S 3D printer [92] was used with a stereolithography apparatus (SLA), using Polylactic Acid (PLA) filament, with the printer shown in Fig. 3.40 below.



Fig. 3.40. JGAurora A5S 3D Printer used for experimental PV airfoils. For more details, the reader was referred to [92].

The 3D printer has a maximum printable scale of 220mm x 220mm x 305 mm (L x W x H), and airfoils can be customized to accommodate other test sensors and larger PV devices by manipulating the initial .stl file using an open source 3D rendering software package.

3.4.3.4 Integration of PV Performance Measurement Devices. 3D printing a small-scale airfoil used for different UAS platforms is critical to the experiment's success, as this will aid in making the platform for the PV devices more closely match the specific airfoil slope characteristics. However, it may become necessary to embed mounts for additional sensors and accommodate for future testing. In such a case, the NACA0024 was further modified to accommodate a GY-521 accelerometer sensor [72] to test for vibrations and MG995 servo mounts to serve for future testing, which can be seen in the final version of the experimental design. As vibration impacts to PV-embedded airfoils are not yet quantified, the research effort takes into consideration the need for future testing, as described in more detail in the future work and recommendations section. The final PV-embedded airfoil for BBRS testing is shown in Fig. 3.41 below.

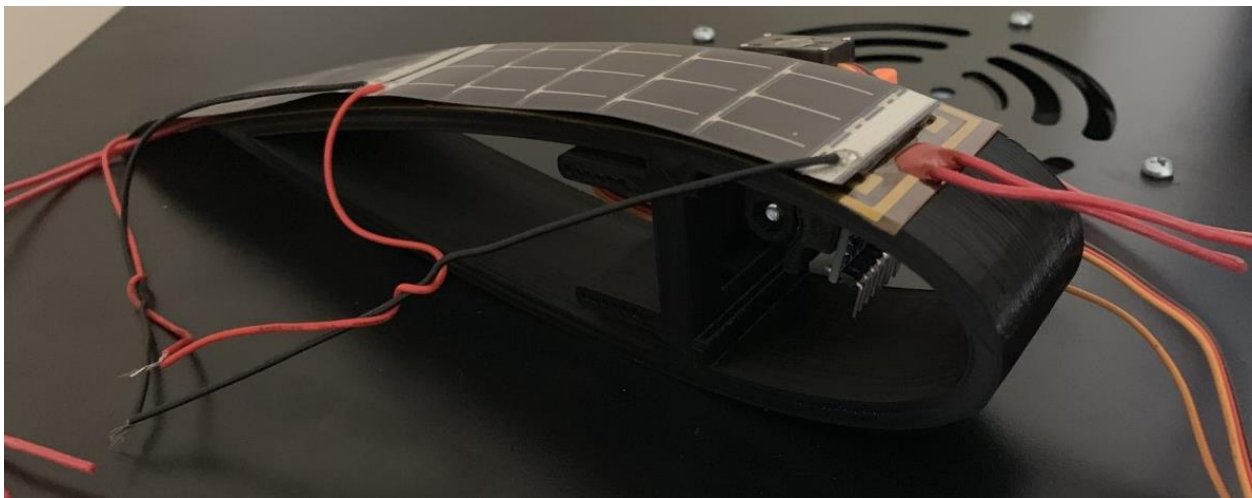


Fig. 3.41. Final version of the experimental PV-embedded NACA0024 airfoil.

CHAPTER 4

TEST METHODOLOGY AND RESULTS

4.1 Introduction

Accomplishing adequate testing for irregularly shaped PV panels was an iterative process and was separated into several phases to deal with each PV problem, measurement method, and desired output individually. The first phase dealt primarily with the fabrication of the entire BBRS, where the design of each subsystem needed to address specific and known PV device performance variables and a method to accurately measure these variables and outputs. The second phase involved the fabrication of an experimental PV-embedded airfoil. This phase also dictated the selection of different solar cell architectures (i.e., GaAs or Si), the specific array design, airfoil shape, and test airfoil fabrication using 3D printing. The intent was to later identify how cosine losses in PV output are related to the angle of incidence using different design strategies (e.g., address subproblem 1). Additionally, this phase briefly discusses qualitatively how an airfoil design can be made such that the impact to the designed aerodynamic properties are minimized, and also minimize the effects of shadowing during portions of the solar day. The objective was to see how to maximize solar exposure using a fixed position (i.e., without the use of optimized solar tracking) and still gain useful energy for other UAS operations, such as powering payloads or hybrid powertrains to supplement gas-driven systems.

The third phase formulates a basic test procedure for a PV airfoil that would describe certain behaviors based on an example operational environment. More specifically, the PV array exposure to different wavelengths and solar angle of incidence along a uniform and standard axis (i.e., assume that the cell is embedded in an airfoil, with the vehicle traveling at velocity vector V ; the incidence angle will vary semi-spherically over this plane). Each step within this phase

was comprised of sweeping 0 to 180 degrees over this axis using one wavelength of light at a time. The fourth phase involved the input of data and analysis for the BBRS analysis and subsequent statistical analyses. The fifth phase is intended to expand on the PV responses to changes in the operational environment, specifically due to thermal stresses and their impact to photocurrent output (e.g., addressing subproblem 2).

Since there were limitations and additional test parameters identified in the research effort, an additional phase is presented. This sixth phase involves preparing for future projects using lessons learned, as well as providing recommendations for alternative/additional research areas that operate outside the scope of this study. This phase is described in more detail in Chapter 5 and is comprised of considerations involving alternative cell designs, PV array shapes, alternative PV series and parallel configurations for individual cells, vibrations analysis on PV output, mean time to failure (MTTF) and failure modes for UAS components, and carbon emissions studies for gas-driven vs. renewable energy driven UAS. Other considerations as a portion of this phase were to consider if the ASMS sweep from 0 to 180 degrees is off center from the airfoil's forward velocity vector V component (e.g. analyze for deviations along the primary axis). A brief discussion on how this can influence a new PV airfoil design and what optimum beta angles can be used to yield maximum power outputs is expanded in the future work section.

4.2 Test Methodology using the BBRS

The third and fourth phases of the research effort are representative of the objective of this chapter, which is to discuss the methodology and results given different experimental test configurations and variables. To ensure that the research objectives are accomplished, the experimental tests formulated for the research effort are described in greater detail below.

4.2.1 Initial BBRB Test Procedures. The initial BBRB test procedures are applicable for all PV and SCARS initial tests and are listed and described below.

1. Remove left-side panel to examine test area. Ensure that the area within the BBRB is free of FOD. Examine condition of thermal baseplate and ensure that no exposed electrical harnesses connectors are contacting the thermal baseplate. NOTE: Intermittent contact with aluminum thermal baseplate and open connectors can result in an electrical short condition and negatively impact test conditions and resultant data.
2. Place test apparatus, sensor(s), or PV device in desired orientation and position relative to the ASMS 90-degree position. For the SCARS and PCMS, ensure that the test connectors are connected and secured for each respective harness as required. For test repeatability purposes, it is recommended to mark the area of the apparatus on the thermal baseplate with a grease pen to accurately position the apparatus each time a test is conducted.
3. Ensure that all toggle switches are in the OFF position. Reinstall left-side panel. Open main BBRB door, remove electrical systems shroud cover, and insert SD card for SCARS and PCMS as required.
4. Plug in the BBRB to the nearest 120-V/60-Hz power outlet. NOTE: This system is intended to be operated using a standard 120-V/60-Hz system. Switch the main BBRB +5V power distribution unit located on the inside of the right-side panel to the ON position.
5. Upon system power up, ensure that each subsystem is loading properly and that each sensor suite does not show any faults or failures as indicated on each screen on the main BBRB door. Troubleshoot system(s) as required.

6. The BAPCS will automatically begin its calibration process by executing a “homing” feature and calibrating at a position of 0 degrees relative to the thermal baseplate. Ensure that the homing feature is not obstructed by FOD and that the system zeroizes at 0 degrees relative. Test the BAPCS by executing a sweep from 0 degrees (0 steps) to 180 degrees (800 steps) by entering “800” using the CNC keypad and “ENTER”. Ensure that the BAPCS arm is unobstructed as it moves from 0 to 180 degrees. Once the system reaches the 180-degree position, enter “0” on the CNC keypad and “ENTER”. The system will return to the 0-degree (i.e., home position) position, and the process will be complete as indicated on the BAPCS LCD screen.
7. Test the ASMS to ensure that each wavelength of the ASMS changes with each button press. Test the calibration laser with the other pushbutton, line up the test apparatus to the desired position, remark the orientation with a grease pen as applicable, and turn off laser with the same pushbutton.
8. Ensure there are no faults or failures, and then proceed with follow-on specific experimental test procedure.
9. Execute desired experimental test.
10. When testing is complete, return the ASMS to the 90-degree position by entering 400 on the CNC keypad and ENTER. Once ASMS is in the 90-degree position, open the main BBRS door and switch the main BBRS +5V power distribution unit located on the inside of the right-side panel to the OFF position.
11. Open main BBRS door, remove electrical systems shroud cover, and remove SD card for SCARS and PCMS as applicable. Reinstall shroud cover.

12. Switch all external power indicator switches to the OFF position and unplug the BBRS from the 120-V/60-Hz power outlet.

13. Upload the SD card(s) to any computer that is SD-card compatible, open the respective .txt file as applicable, and copy/paste the data into the main BBRS data analysis spreadsheet or separate excel file as desired. NOTE: For ease of operation in multiple tests, it is recommended to erase all data from the SD card(s) and reformat each card every time a new test is conducted.

14. Clear thermal baseplate of apparatus, sensor(s), or PV devices, as required.

4.2.2 Energy Flux Initial Test. An initial calibration and measurement test for the energy flux present in the BBRS is essential when evaluating a PV's spectrum response for different wavelengths of light. Using the SCARS, it is possible to capture the intensities of each wavelength as a function of angle of incidence. The specific test procedure is described below.

1. Execute test procedures as per section 4.2.1, steps 1-8. NOTE: For step 2, ensure that SCARS sensor suite is connected and the PCMS harness is not connected as there is no PV device in the BBRS for this test. For step 3, insert a formatted SD card in the SCARS.

2. For step 7, ensure that the laser is pointed to the SCARS sensor suite center of mass, as shown in Fig. 4.1 below.

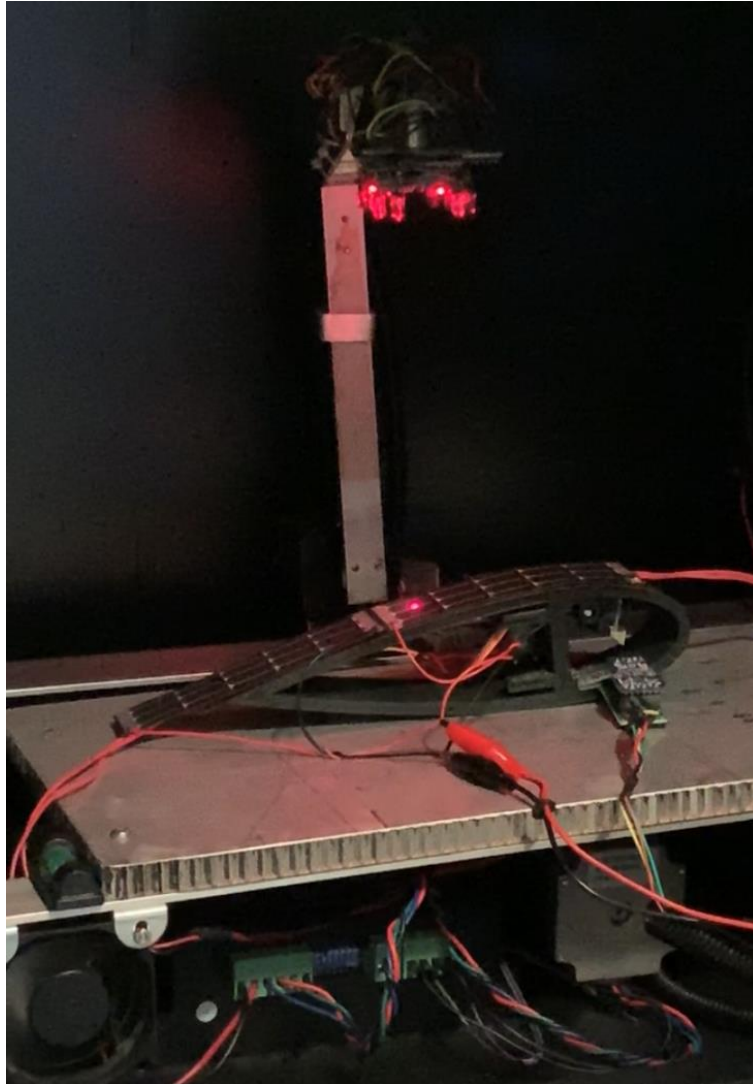


Fig. 4.1. Inside of the BBRs using the calibration laser to determine ASMS positioning over the PV-embedded airfoil for testing.

3. Upon completion of section 4.2.1, step 8, return the ASMS to the home position (i.e., 0 degrees relative) by entering “0” on the CNC keypad and ENTER, or by simply hitting ENTER on the keypad. Once the ASMS has reached the initial condition, press the LED pushbutton once to ensure a green light for “SYSTEM READY” illuminates on the BBRs main door. Begin testing the spectrum energies for each wavelength. Each pushbutton press following power-up will change the wavelength in the following sequence: SYSTEM READY, RED, GREEN, BLUE, WHITE, UV, IR, OFF.

4. Press the LED pushbutton once for RED. After 5 seconds, enter “800” on the CNC keypad to sweep the ASMS 180 degrees. NOTE: The BAPCS will move the ASMS at ~13.84 deg/sec.
5. Move the ASMS back to the 0-degree position by hitting “ENTER” on the CNC keypad.
6. Once this is complete, repeat steps 4-5 for each wavelength until all wavelengths have been tested, as indicated by the SYSTEM READY green light on the BBRs main door.
7. Execute test procedures as per section 4.2.1, steps 9-14.

The results for the SCARS initial experimental procedure are described and shown in section 4.4.1.

4.2.3 PV Array Beta Angle Spectral Response Experiment. To sufficiently address subproblem 1, each wavelength of light was used to stimulate the PV array under varying angles of incidence for two different configurations.

4.2.3.1 Flat Cell Configuration Testing. To provide the highest current values and scan for variances, both cells were connected in parallel yielding the 2-parallel/1-series configuration (i.e., 2P/1S). The specific test procedure is described below.

1. Execute test procedures as per section 4.2.1, steps 1-8. NOTE: For step 2, ensure that the test solar cell is connected to the PCMS harness, and leave the thermal heater cables disconnected. For step 3, insert a formatted SD card in the PCMS.
2. For step 7, ensure that the laser is pointed to the solar cell array center of mass.
3. Upon completion of section 4.2.1, step 8, return the ASMS to the home position (i.e., 0 degrees relative) by entering “0” on the CNC keypad and ENTER, or by simply hitting ENTER on the keypad. Once the ASMS has reached the initial condition, press the LED pushbutton once to ensure a green light for “SYSTEM READY” illuminates on the BBRs main door. Begin

testing the spectrum energies for each wavelength. Each pushbutton press following power-up will change the wavelength in the following sequence: SYSTEM READY, RED, GREEN, BLUE, WHITE, UV, IR, OFF.

4. Press the LED pushbutton once for RED. After 5 seconds, enter “800” on the CNC keypad to sweep the ASMS 180 degrees. NOTE: The BAPCS will move the ASMS at ~13.84 deg/sec.
5. Move the ASMS back to the 0-degree position by hitting “ENTER” on the CNC keypad.
6. Once this is complete, repeat steps 4-5 for each wavelength until all wavelengths have been tested, as indicated by the SYSTEM READY green light on the BBRs main door.
7. Execute test procedures as per section 4.2.1, steps 9-14.

The results for the flat cell configuration test experimental procedure are described and shown in section 4.4.2.

4.2.3.2 Airfoil Cell Configuration Testing. Similar to the flat cell configuration, the PV-embedded airfoil solar cells were also put in a 2P/1S electrical wiring configuration. The specific test procedure is described below.

1. Execute test procedures as per section 4.2.1, steps 1-8. NOTE: For step 2, ensure that the experimental PV-embedded airfoil is connected to the PCMS harness, and leave the thermal heater cables disconnected. For step 3, insert a formatted SD card in the PCMS.
2. For step 7, ensure that the laser is pointed to the PV-embedded airfoil center of mass.
3. Upon completion of section 4.2.1, step 8, return the ASMS to the home position (i.e., 0 degrees relative) by entering “0” on the CNC keypad and ENTER, or by simply hitting ENTER on the keypad. Once the ASMS has reached the initial condition, press the LED pushbutton once to ensure a green light for “SYSTEM READY” illuminates on the BBRs main door. Begin

testing the spectrum energies for each wavelength. Each pushbutton press following power-up will change the wavelength in the following sequence: SYSTEM READY, RED, GREEN, BLUE, WHITE, UV, IR, OFF.

4. Press the LED pushbutton once for RED. After 5 seconds, enter “800” on the CNC keypad to sweep the ASMS 180 degrees. NOTE: The BAPCS will move the ASMS at ~13.84 deg/sec.
5. Move the ASMS back to the 0-degree position by hitting “ENTER” on the CNC keypad.
6. Once this is complete, repeat steps 4-5 for each wavelength until all wavelengths have been tested, as indicated by the SYSTEM READY green light on the BBRs main door.
7. Execute test procedures as per section 4.2.1, steps 9-14.

The results for the flat cell configuration test experimental procedure are described and shown in section 4.4.2.

4.2.4 Thermal Stress Experiment. To sufficiently address subproblem 2, the PV array in both the flat and airfoil configuration were tested to examine for thermal stress impacts to electrical output during each configuration’s maximum power point angle. Additionally, this experiment will serve as a means to test the PV device for survivability in specific temperature profiles. The specific test procedure is described below.

1. Execute test procedures as per section 4.2.1, steps 1-8. NOTE: For step 2, ensure that the flat solar cell or experimental PV-embedded airfoil (whichever is desired to test) connected to the PCMS harness, and ensure that the thermal heater cables are connected as well. For step 3, insert a formatted SD card in the PCMS.
2. For step 7, ensure that the laser is pointed to the flat solar cell or PV-embedded airfoil center of mass.

3. Upon completion of section 4.2.1, step 8, send the ASMS to the maximum power point position (i.e., 90 degrees relative for flat cell configuration, and 140 degrees relative for the PV-embedded airfoil configuration) by entering “400” or “622” on the CNC keypad and ENTER, or by simply hitting ENTER on the keypad. Once the ASMS has reached the initial condition, press the LED pushbutton once to ensure a green light for “SYSTEM READY” illuminates on the BBRs main door. Begin testing the spectrum energies using the WHITE LED.
4. Ensure that the thermal regulator is powered on and operational by plugging in a 10A power supply. Press the “SET” key, and when prompted enter the desired temperature in degrees Fahrenheit ($^{\circ}\text{F}$). The actual temperature ramp rate using a 10A power supply and Bayite temperature controller is shown in Fig. 4.2 below.

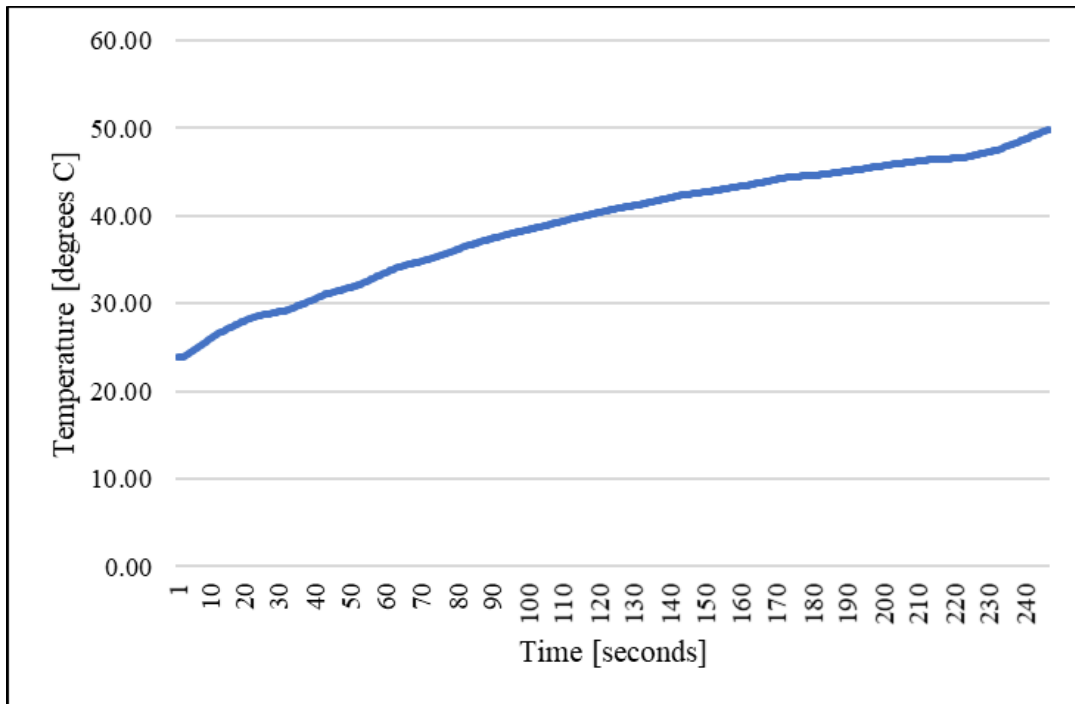


Fig. 4.2. Temperature ramp rate used for both flat and curved PV array configurations. The slope illustrates the measured temperature increase over time using the Bayite temperature controller coupled with a 10A power supply. The measured temperature ramp rate is approximately 6.857°C per minute.

5. Observe the PV electrical characteristics on the PCMS display and look for rapid decreases in voltage and/or current. Once a condition occurs where a zero voltage is quickly attained, then readjust the temperature threshold by using the “SET” button and decrease the temperature to the desired limit. NOTE: The PV device will be very hot, be careful when handling. To prevent further damage to the PV array from occurring, be prepared to quickly decrease the temperature or remove power to turn the temperature controller off.
6. Adjust the ASMS to the desired degree position by entering the number of steps and hitting “ENTER” on the CNC keypad.
7. Replace the experimental apparatus (as required) for the second portion of the thermal stress test, and repeat steps 3-6 as required.
8. Execute test procedures as per section 4.2.1, steps 9-14.

The results for the thermal stress test experimental procedure are described and shown in section 4.4.3.

4.3 Statistical Test Methodology

To analyze the spectral response for a PV array in two different configurations (i.e., flat and airfoil/curved), a statistical test was performed based on the data retrieved from each experiment. This statistical test will compare the two sets of data to determine any significance impacts to PV performance output by evaluating both electromagnetic spectrum wavelength and beta angle. According to the Leedy and Ormrod textbook description [33], a mixed-methods study that uses the multiphase iterative design may be the best design for this research effort. The goal of the research effort is to show that different treatments have different effects for a single group or individual, and to “show that change occurs following a particular treatment” [33]. In

the case of solar cell testing, it would be more cost and time effective to have one string of solar cells subjected to thermal oscillations, radiation, and both as a means of determining overall cell deterioration. Each sample group was made up of a predetermined number of solar cells using *a priori* to determine sufficient sample size based on desired statistical power. Ideally, the number of cells per group should be the number required to form a cell string that resemble that of a small satellite solar panel in either a one-in-parallel, two-in-series, or two-in-parallel, one-in-series (1P/2S or 2P/1S) configuration.

4.3.1 Choosing the Appropriate Statistical Test. In this test, quantitative data is used as a type of outcome measure, which falls under the Interval/Ratio category, where the test seeks to analyze the relationship between variables (i.e. wavelength of light effect on electrical energy yield). There are no paired observations, and there is only one independent variable (i.e. the type of solar cell – monocrystalline), and more than one group; these considerations for the test deduce that a one-way analysis of variance (ANOVA) test is most appropriate.

4.3.2 Statistical Hypothesis. Currently, there is no standardized test method for irregularly shaped PV arrays to quantify cosine losses. The BBRS is intended to address testing for PV-embedded airfoils under various conditions. If solar cell technology becomes more resilient and can yield larger power margins and become more cost efficient, then it may be possible to enhance PV utilization for unmanned aerial vehicle applications. As a result, it can potentially increase UAS user's confidence in renewable energy alternatives for unmanned power systems and reduce the existing carbon footprint for conventional gas-driven UAVs. For this study, the null hypothesis for test 1 (H_0) is stated as: white, red, green, and blue wavelengths in the visible EM spectrum will have a similar average photovoltaic impact on silicon-based solar cell output voltage, but with each spectrum wavelength (represented by color) will yield

different voltages. It is expected that based on available EM energies that white will yield the highest voltage, followed by green, blue, and red. This is represented by $H_0: V_W > V_G > V_B > V_R$, where V_x denotes the voltage generated based on a specific color. The alternative hypothesis (H_A) is stated as the mean effect of a given wavelength yield different trends and the voltage will differ in magnitude. For this study, a confidence interval (α) of 95% is assumed, with a minimum p-value corresponding to 0.05, where if the value is less than 0.05 the null hypothesis will be rejected. Only the visible spectrum with values between 365nm and 650nm were utilized. The null hypothesis (H_0) for the second statistical test is that the wavelength is not as important in the determination of output power for the curved panel as input beam radiation, where the alternative hypothesis (H_A) is that the wavelength is more important in the determination of output power than input beam radiation.

4.3.2.1 Determination of *a priori* and Statistical Power. The intent for this section is to address statistical sampling size based on the connection to a desired statistical power for the experiment. For this test, two low voltage silicon flexible solar cells were used for the experiment. However, it is important to evaluate the sample size in an effort to conserve time, resources, and minimize costs for test and research. Using the GPower software, statistical power can be tested in addition to estimating an appropriate sample size based on a desired statistical power. In this case, the sample would be each “run” covering angle changes from 0 to 180 degrees under a single wavelength; thus, simulating the solar day. To save time with the PV studies, and assuming the same large effect size, Fig. 4.3 below demonstrates how *a priori* can help determine the required sample size in this test for a desired statistical power of 95%.

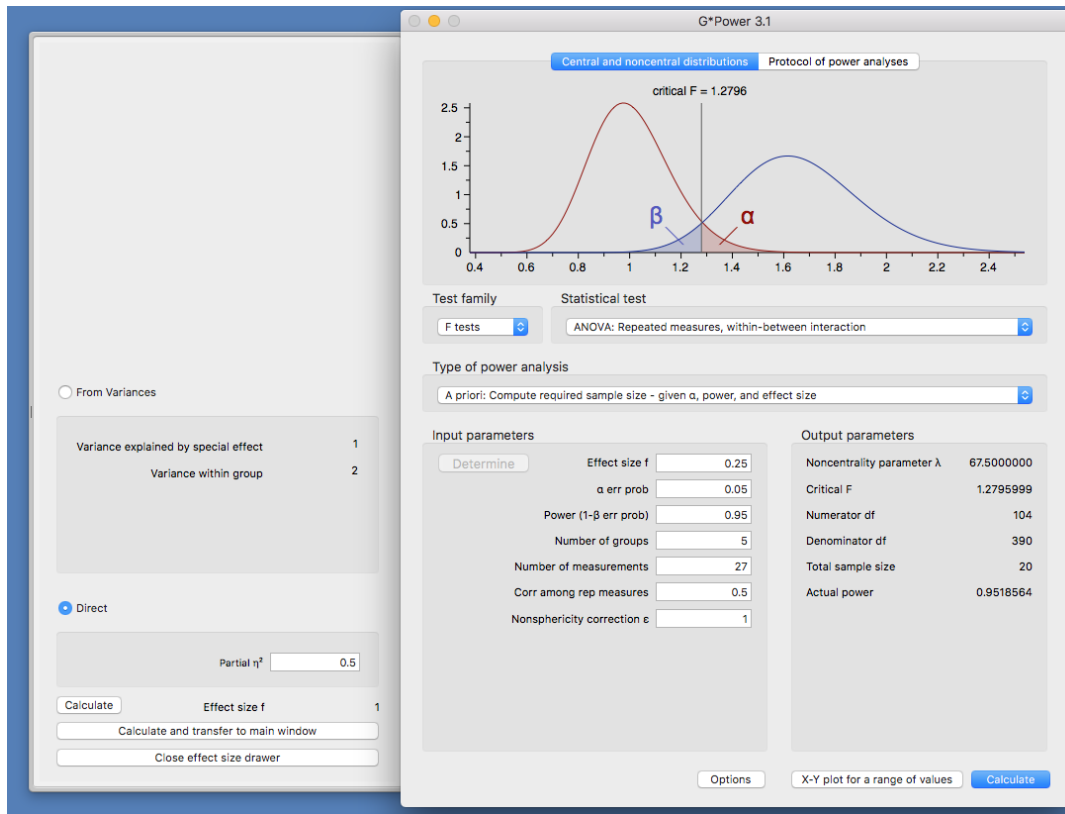


Fig. 4.3. GPower-generated *a priori* metrics for the ANOVA statistical test indicating a sample size of 20 with 27 measurements to achieve a statistical power of 95%.

This *a priori* metric was used for all experimental procedures, as each test run for the energy flux initial test and spectral response experiment was repeated 20 times, with the averages used in the BBRs data analysis Excel file for final calculations. However, for the thermal stress experiments, since the PV devices were tested to the point of complete failure and plastic deformation, the test was only completed 3 times due to the number of cells available for testing.

4.4 Results

The results for the experiments discussed in sections 4.2.2 through 4.2.4 are shown and described in the following subsections.

4.4.1 Energy Flux Initial Test. Prior to making any conclusions about PV electrical output based on spectral response, each wavelength needed to be measured for intensity and

luminous flux density. To accomplish this, an initial test was conducted to ensure that each wavelength could be mapped to a corresponding energy level. The test showed that each wavelength emitted by the ASMS yielded different intensities under varying AOIs, as shown by the trends in Fig. 4.4a through Fig. 4.4f below. From (a) to (f), each spectrum was mapped in the order of red, green, blue, white, UV, and IR with the resultant distributions broken down by the UV, visible, and IR energy components.

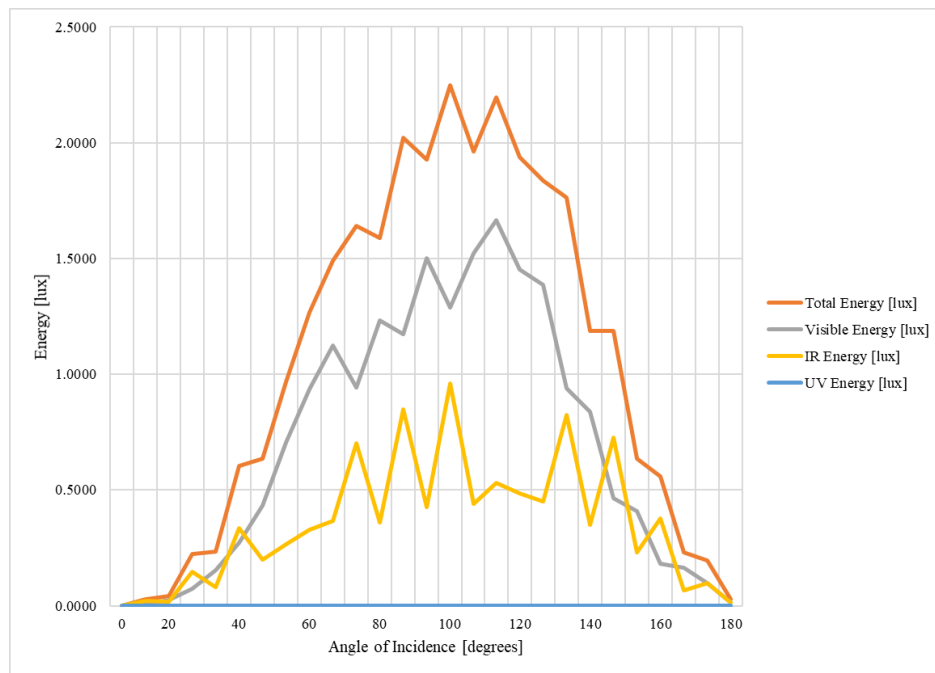


Fig. 4.4a. Total energy gathered from the energy flux initial test in the red EMS region (624 nm) using the SCARS. Where the spectrum energy distributions are gathered under the following environmental conditions: 22.21°C ambient, 101.47 kPa ambient pressure, 89.10% relative humidity, 235mm from sensor to irradiance source, 21.53°C sensor temperature, and an emission source temperature of 22.09°C.

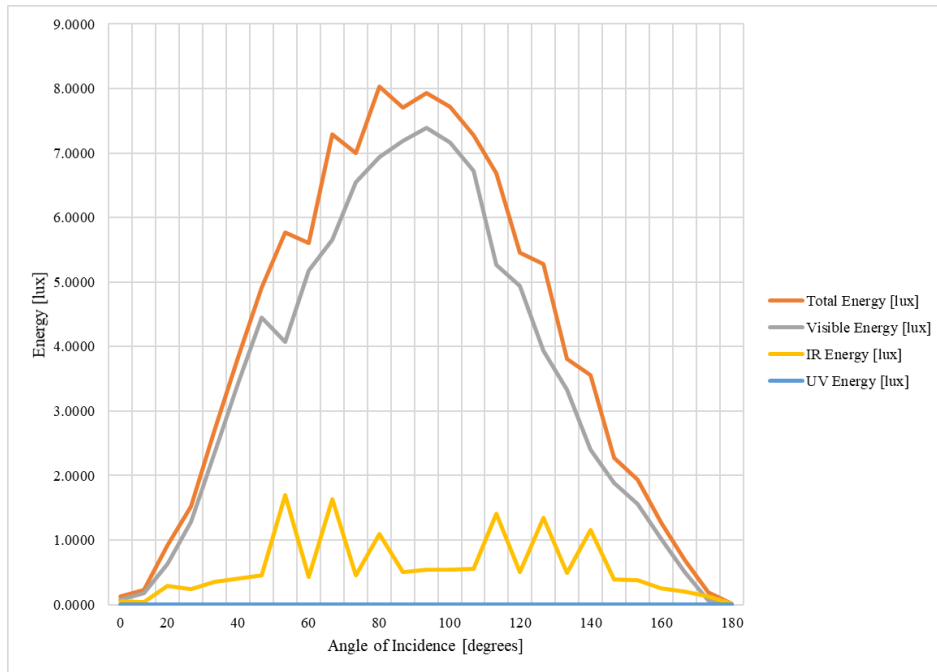


Fig. 4.4b. Total energy gathered from the energy flux initial test in the green EMS region (520 nm) using the SCARS. Environmental data remains the same as described in Fig. 4.4a.

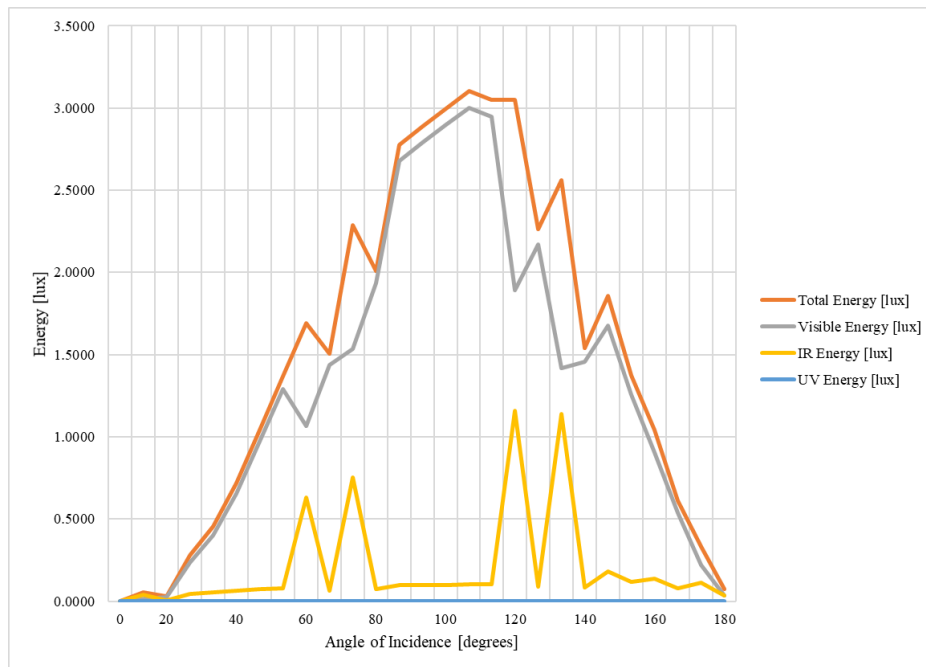


Fig. 4.4c. Total energy gathered from the energy flux initial test in the blue EMS region (468 nm) using the SCARS. Environmental data remains the same as described in Fig. 4.4a.

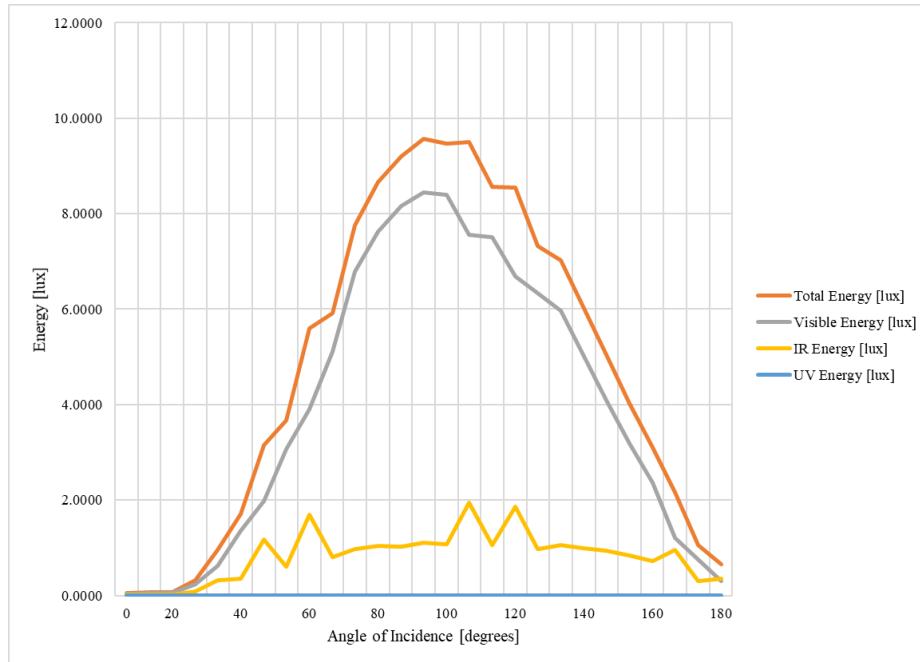


Fig. 4.4d. Total energy gathered from the energy flux initial test in the white EMS region (480 nm) using the SCARS. Environmental data remains the same as described in Fig. 4.4a.

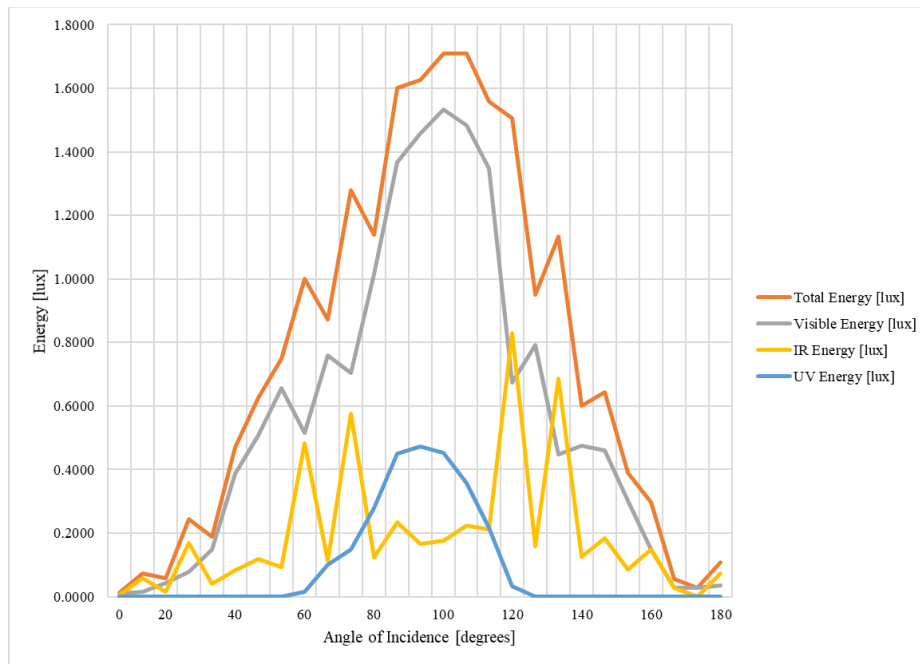


Fig. 4.4e. Total energy gathered from the energy flux initial test in the UV EMS region (365 nm) using the SCARS. Environmental data remains the same as described in Fig. 4.4a.

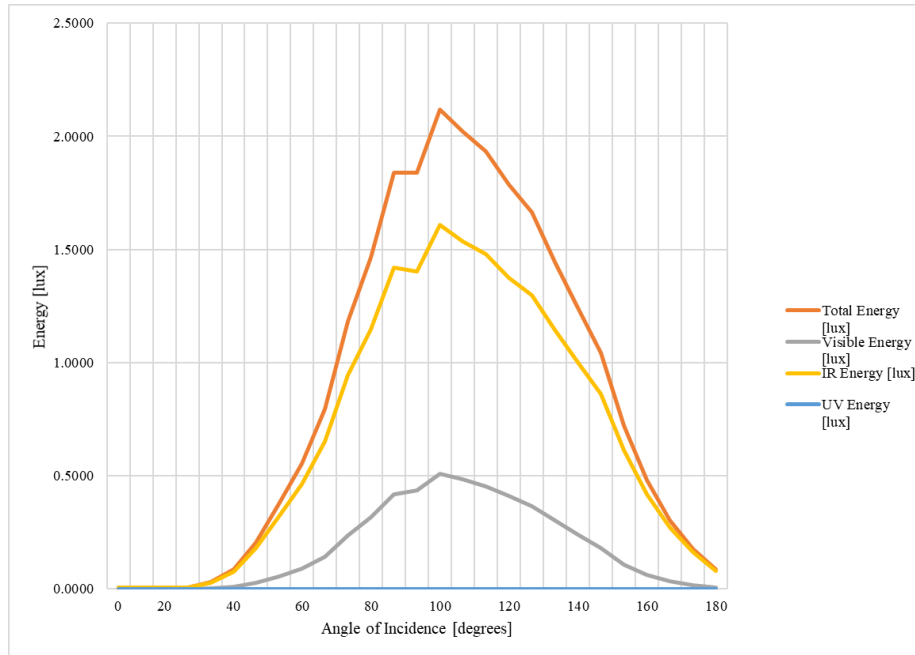


Fig. 4.4f. Total energy gathered from the energy flux initial test in the IR EMS region (925 nm) using the SCARS. Environmental data remains the same as described in Fig. 4.4a.

The biggest takeaway from Fig. 4.4a – 4.4f is that the green and white spectrum energies yielded the largest amounts of luminous flux intensities, and each wavelength yielded maximum total energy at approximately 90 degrees relative to the sensor. For the red, green, blue, white and UV wavelengths the visible component of luminous flux encompasses the highest component of the total energy, and for IR the visible energy component is the most lacking. This data makes sense based on the advertised wavelength calibrations from the technical data sheets for each LED, as well as matches reality for how the sensors in the SCARS are intended to detect portions of the UV, visible and IR spectrum.

4.4.2 PV Array Beta Angle Spectral Response Experiment. Now that the spectrum energies from the irradiance source are effectively “mapped”, the system was successfully deemed calibrated and ready to begin the next phase of testing. The first portion was to analyze the voltage profile and get a rough estimate of differences in performance for the spectrum energies in the same fashion as the energy flux initial test. Similar to the distribution trends

shown in Fig. 4.4a – 4.4f, Fig. 4.5 below shares a similar trend only this time with a noticeable right skew to each of the wavelength distributions as a function of AOI when comparing the results of a flat panel to curved panel configuration.

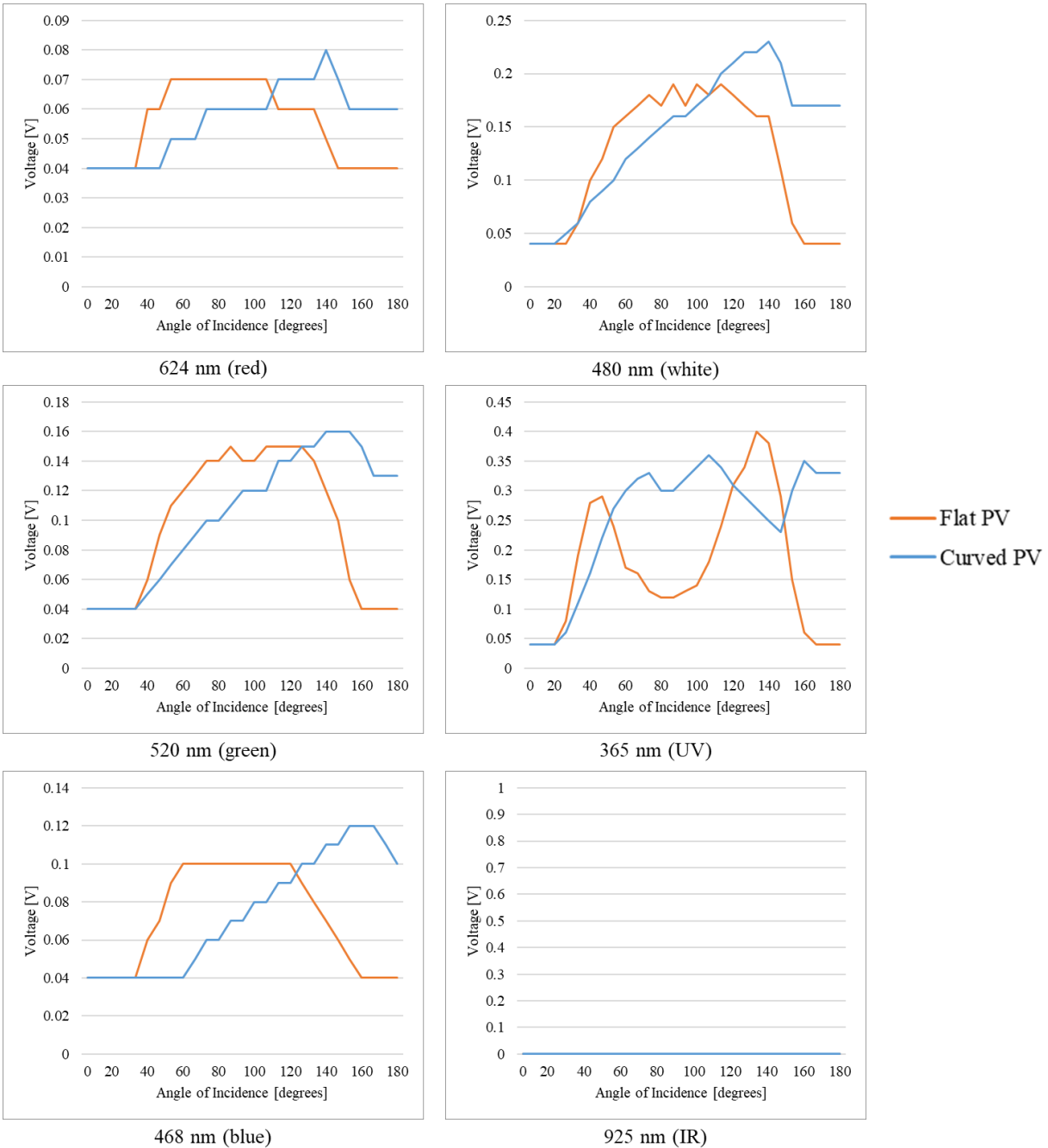


Fig. 4.5. Voltage profile for different wavelengths of light for both flat and airfoil (curved) configured PV arrays. Data was gathered using the PCMS.

Upon further inspection similar to the initial energy flux test, the flat cell configuration illustrates a maximum power point of approximately 90 degrees relative. However, for the PV airfoil configuration (i.e., curved PV setup) the distributions are skewed in the direction where the average slope is focused on more of a quarter perspective relative to the PV array (i.e., the back half of the airfoil). It should also be noted that repeated tests under these identical conditions yield the same skewed trends. This makes sense as the airfoil configuration is essentially in a fixed slope position but is somehow in an angular position such that it has more solar collections capability and is able to translate that directly into electrical energy. The information in Table 3 below shows the average total voltage gathered over 180-degree ASMS sweeps for the flat and curved PV configurations.

TABLE 3
CUMULATIVE VOLTAGE GAINS FOR 180-DEGREE ASMS SWINGS OVER 20
DIFFERENT TESTS BASED ON WAVELENGTH OF LIGHT

<i>Wavelength (λ) [nm]</i>	<i>Color</i>	<i>Total Voltage Gained, Flat PV Configuration [V]</i>	<i>Total Voltage Gained, Curved PV Configuration [V]</i>	<i>Delta [V]</i>
624	Red	1.48	1.52	0.04
520	Green	2.60	2.82	0.22
468	Blue	1.93	2.00	0.07
480	White	3.19	3.85	0.66
365	UV	4.64	6.84	2.20
925	IR	0.00	0.00	0.00

Note. Voltages shown are the average of 20 different tests for each corresponding wavelength, where the ASMS was used to stimulate each PV array in the flat and curved (airfoil) configuration. The total voltage gathered for the flat configuration was 13.84 V, as opposed to the curved configuration which yielded 17.03 V. This delta of 3.19 V reflects an 18.73% increase in total solar day performance for curved over flat configuration PV arrays. Even after removing the UV spectrum results from the analysis yields a delta of 0.99 V in favor of the curved PV configuration, reflecting a 9.72% increase in performance.

For the UV spectrum, a large dip is noticeable which is believed to be the result of undesired reflections from the PV array. The UV LEDs at maximum power point angles (i.e., 90 degrees relative) in the flat panel configuration are mostly over the cell interconnects. Therefore, for each test following this one a large dip is noted at these angles for both the flat and airfoil configurations. Including the UV data when determining a correction factor may unintentionally yield inconsistent and unreliable results. Based on this discovery, only the visible spectrum is used for the spectral response characteristic and subsequently derived correction factor. Additionally, the IR spectrum is not yielding a photovoltaic response, and will also be disregarded from the analysis. Considering the results in Table 3 above, there was a total delta of 0.99 V when only evaluating the voltages generated using the visible wavelengths and reflects a 9.72% increase in total performance when exposed to an artificial solar day (i.e., 180-degree ASMS sweep).

Analyzing Fig. 4.6 below, the dip for the UV region is still apparent, but there are two key observations to make. One is that the visible spectrum data shows similar skewed distribution sets that were present in the initial energy test and the initial voltage response test. The second is that while the UV spectrum energy magnitude shown in Fig. 4.4 is small compared to the other wavelengths; the photovoltaic response based on that region yields a significantly higher electrical power output. This indicates that the Si-based PV array chosen for this experiment is more efficient at converting UV energy into electrical energy than the visible spectrum.

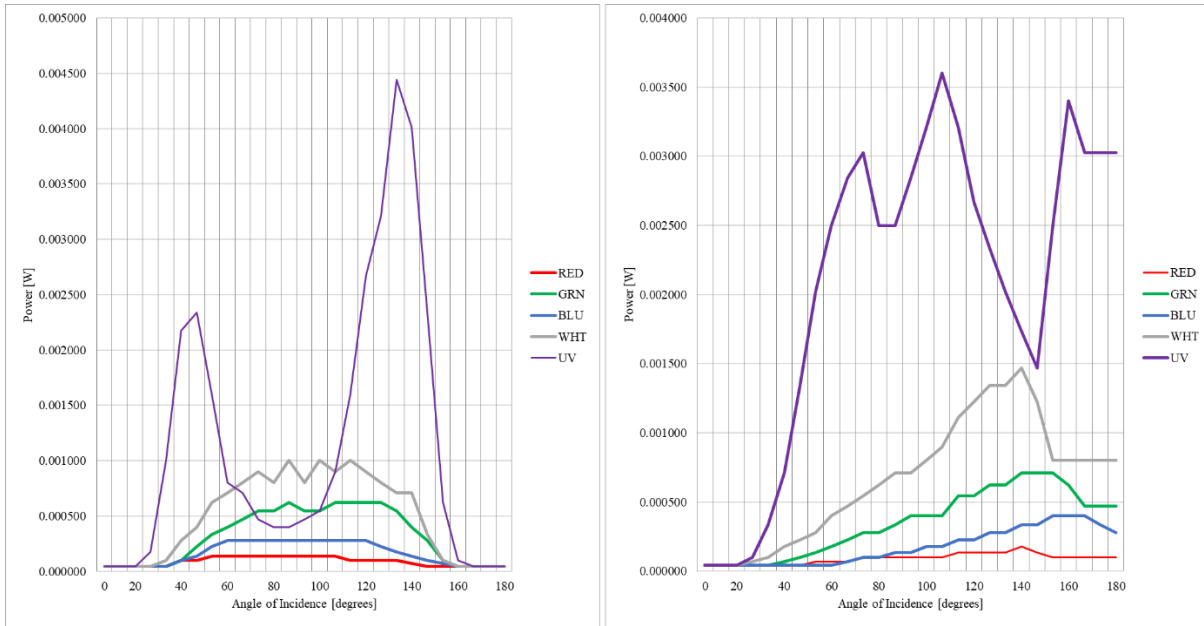


Fig. 4.6. PV panel power vs. AOI for both flat and airfoil panel configurations. The total power is illustrated using different wavelengths of light for both flat (left) and airfoil (right) configured PV arrays. Data was gathered using the PCMS.

The tests described in section 4.2.3 were repeated 20 times, with the average spectrum response for all the tests over all the wavelengths graphically represented in Fig. 4.7 and 4.8 below.

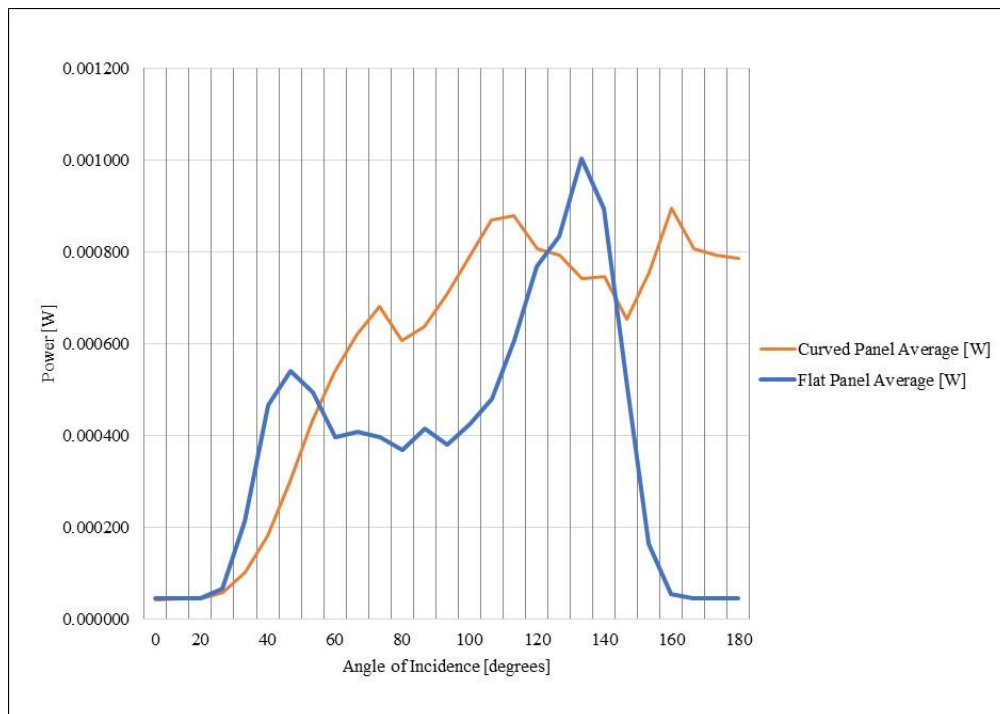


Fig. 4.7. Average total power generated accounting for multiple wavelengths of light for both flat and airfoil configured PV arrays as a function of angle of incidence. Data was gathered using the PCMS, and ASMS emission values ranging from 325nm to 925nm. Many of the losses for the airfoil panel occur within the first 55 degrees, but the losses are limited to approximately 24%.

The difference between Fig. 4.7 and Fig. 4.8 is that the above figure accounts for all the spectrum energies and wavelengths within the range of 325nm to 925nm. This is intended to show the difference in how the UV spectrum “dips” due to the reflections on the interconnect can further impact the cumulative data trends over repeated test events. Looking at Fig. 4.8 below, the trends between the flat and curved panel have been once again made evident where the skewed distribution is still present after 20 independent tests even while including the average outputs of all the visible spectrum wavelengths.

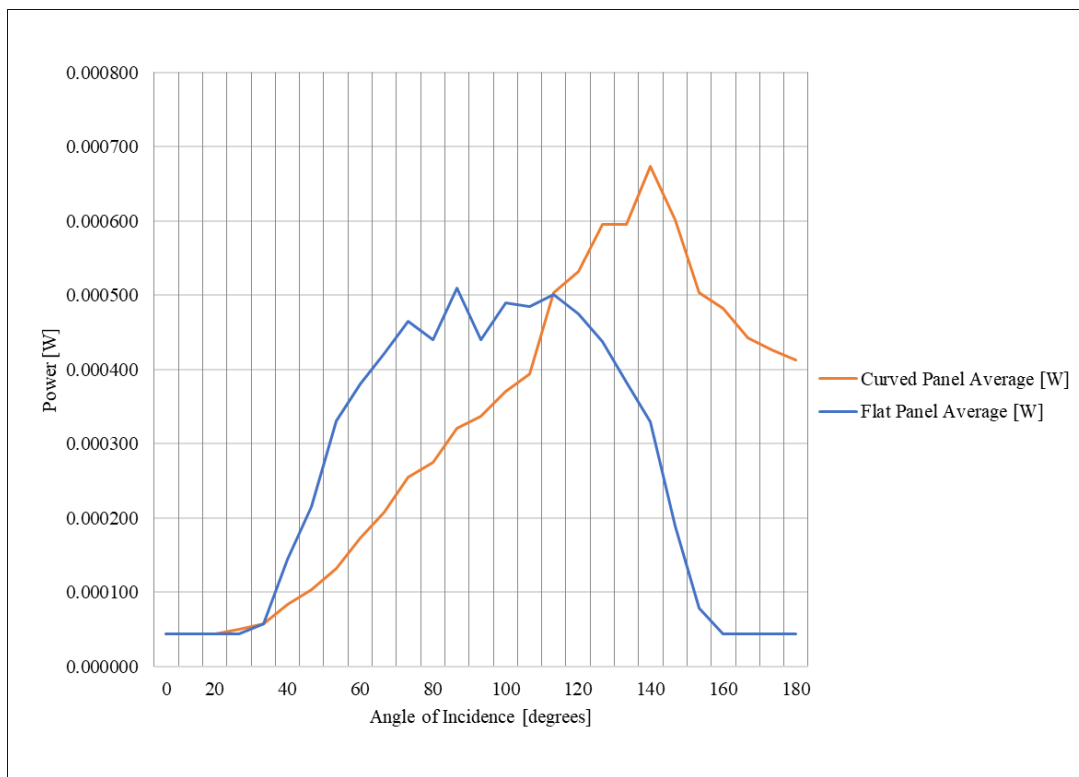


Fig. 4.8. Average total power generated accounting for multiple wavelengths of light for both flat and airfoil configured PV arrays as a function of angle of incidence. Data was gathered using the PCMS, and ASMS emission values ranging from 365nm to 650nm. Many of the losses for the airfoil panel occur within the first 110 degrees, but the losses are limited to approximately 24%.

The information in Fig. 4.8 indicates that the maximum power point for the curved panel configuration (i.e., the PV airfoil configuration) is approximately 140 degrees relative to the panel. Additionally, at ~112 degrees AOI relative the electrical performance of the flat panel decreases rapidly while the curved panel increases. At 180 degrees relative the curved panel output is substantially higher than the flat panel, which indicates that a UAV using this system could gain more energy at lower solar angles (i.e., sunrise and sunset) than if a flat configuration was used.

4.4.3 Thermal Stress Experiment. A critical portion of every solar cell study is how the system performs or deteriorates as a function of heat. This test was run using identified maximum power points for each configuration and analyzing the trends in electrical output. It was originally predicted that each of the arrays would have a negative trend in electrical output for voltage and current regardless of panel configuration. As observed in the graphs of Fig. 4.9 below, it is apparent that not only are the negative trends are present, but that the trends are almost identical when comparing the two configurations.

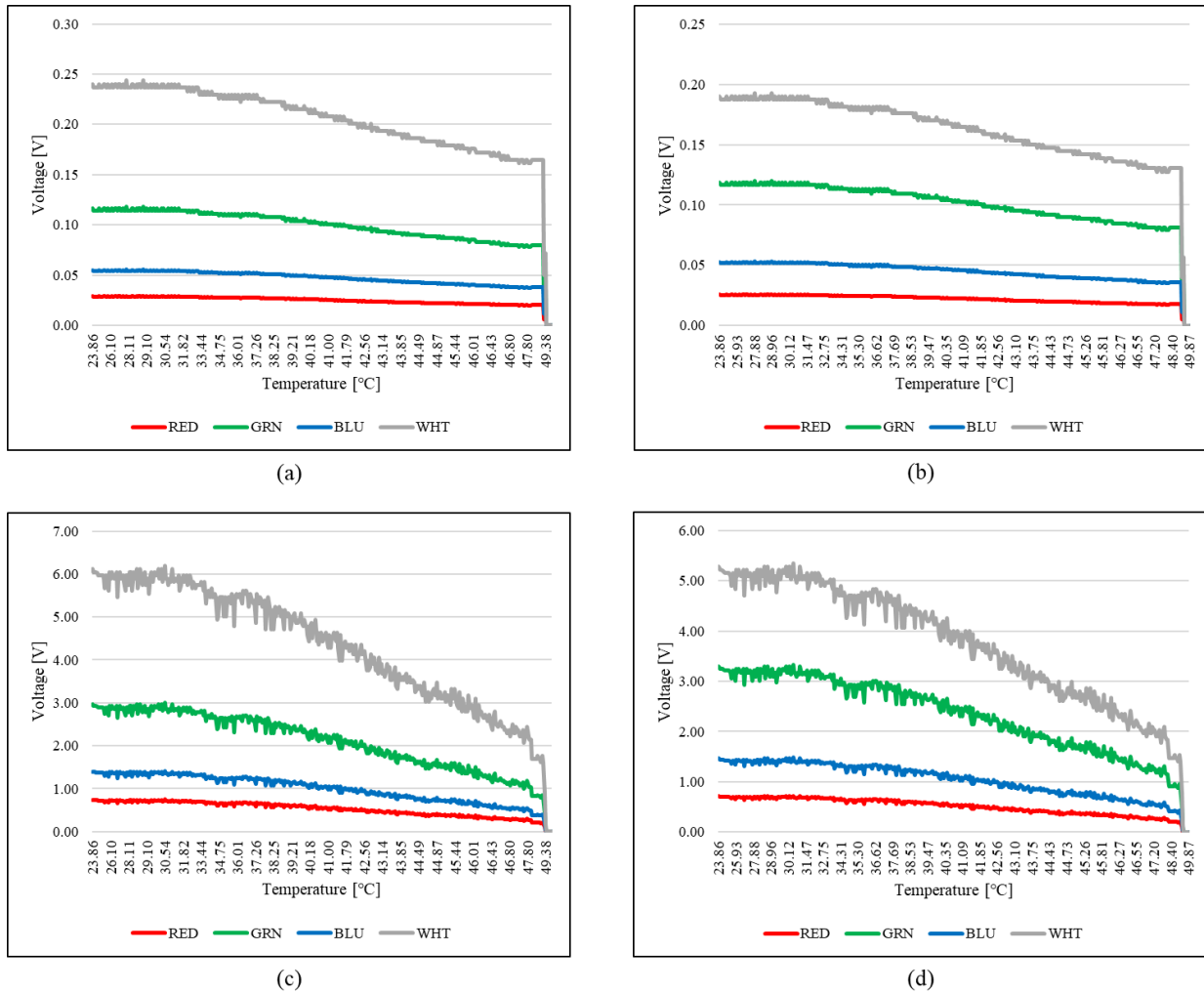


Fig. 4.9. Temperature impacts on flat and PV airfoil configured arrays broken down by spectral response for current and voltage. Graph (a) illustrates temperature impacts to spectral response in terms of voltage for the PV airfoil configuration, with (c) showing the impacts to current. Graph (b) illustrates temperature impacts to spectral response in terms of voltage for the PV flat configuration, with (d) showing the impacts to current. Data was gathered using the PCMS while executing the thermal stress experiment.

This experiment was vital in understanding how to conceptualize a WCA for PV-embedded airfoils, as the trends may not always be similar and that material conditions of the coverglass, and specular reflections based on the AOI need to be accounted for. The reflections and shadowing a UAV can experience based on beta angle can vary based on orientation and operational environment, where the temperature ramp rates may not be as uniform as those conducted in a controlled environment within the BBRs. Such a dynamic thermal environment

may have more peaks and valleys when presented graphically and may yield shorter or higher failure rates for individual solar cells.

4.4.4 ANOVA Test Results. The null hypothesis (H_0) was that white, red, green, and blue wavelengths in the visible EM spectrum will have a similar photovoltaic impact on silicon-based solar cell voltage output, but will generate different voltage levels with white being the highest, green, blue, then red. This is proven true prior to the statistical test even being conducted, so therefore the null would be accepted. However, the second hypothesis pertaining to the wavelength's impact on voltage output determination for a curved cell was not so obvious. For this test, the MiniTab software program was utilized where pertinent data such as flat and curved panel power, angle of incidence, wavelength, and input beam radiation were evaluated. Fig. 4.10 below illustrates a small portion of the MiniTab inputs, where the averages of the 25 tests were entered.

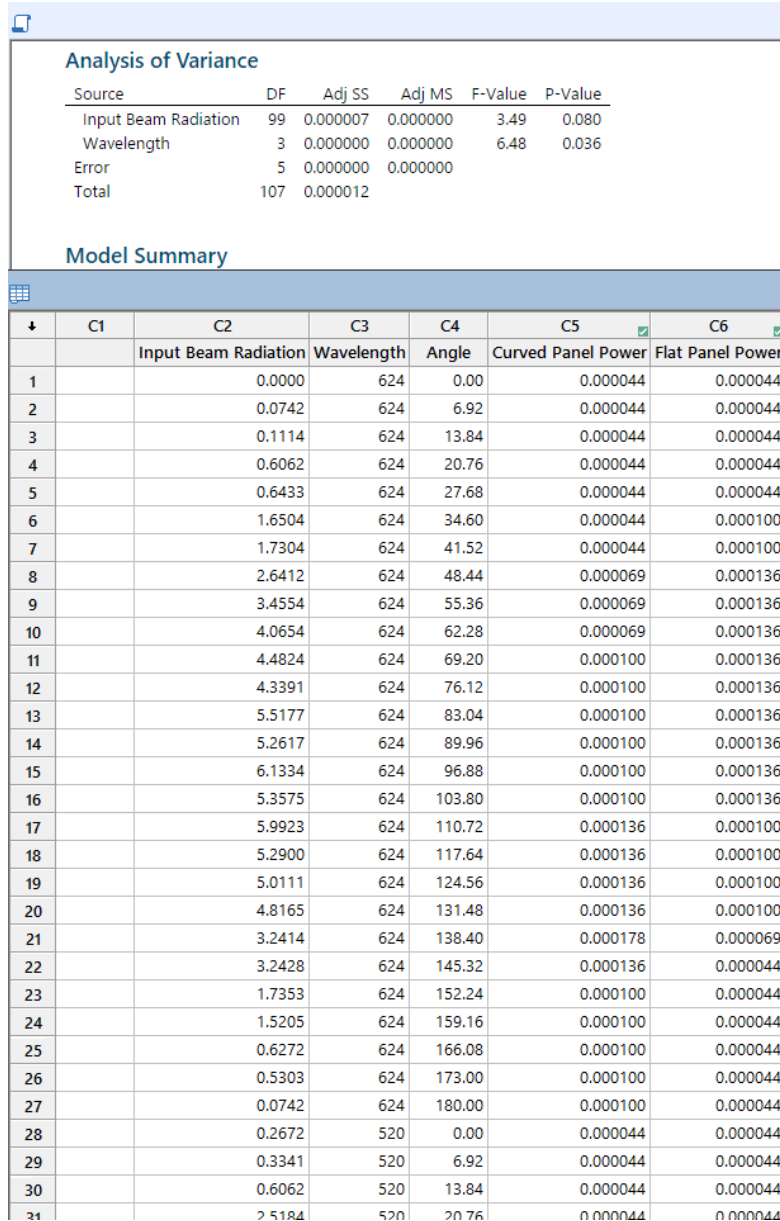


Fig. 4.10. Analysis of variance (ANOVA) sample of inputs to MiniTab software for average power yielded from flat and airfoil configuration PV arrays.

As an ANOVA was executed, the table on the top left of Figures 4.10 and 4.11 showed interesting P-values for the input beam radiation and wavelength as the two categories of evaluation. The null hypothesis (H_0) for the second statistical test is that the wavelength is not as important in the determination of output power for the curved panel as input beam radiation,

where the alternative hypothesis (H_A) is that the wavelength is more important in the determination of output power than input beam radiation.

The P-value for the input beam radiation was 0.080, whereas the wavelength was 0.036, which indicates that while both factors were significant in influencing the electrical output for both the flat panel and curved panel configuration, the null hypothesis would be rejected. Therefore, based on the results the wavelength of light is more significant than input beam radiation for PV array voltage output.

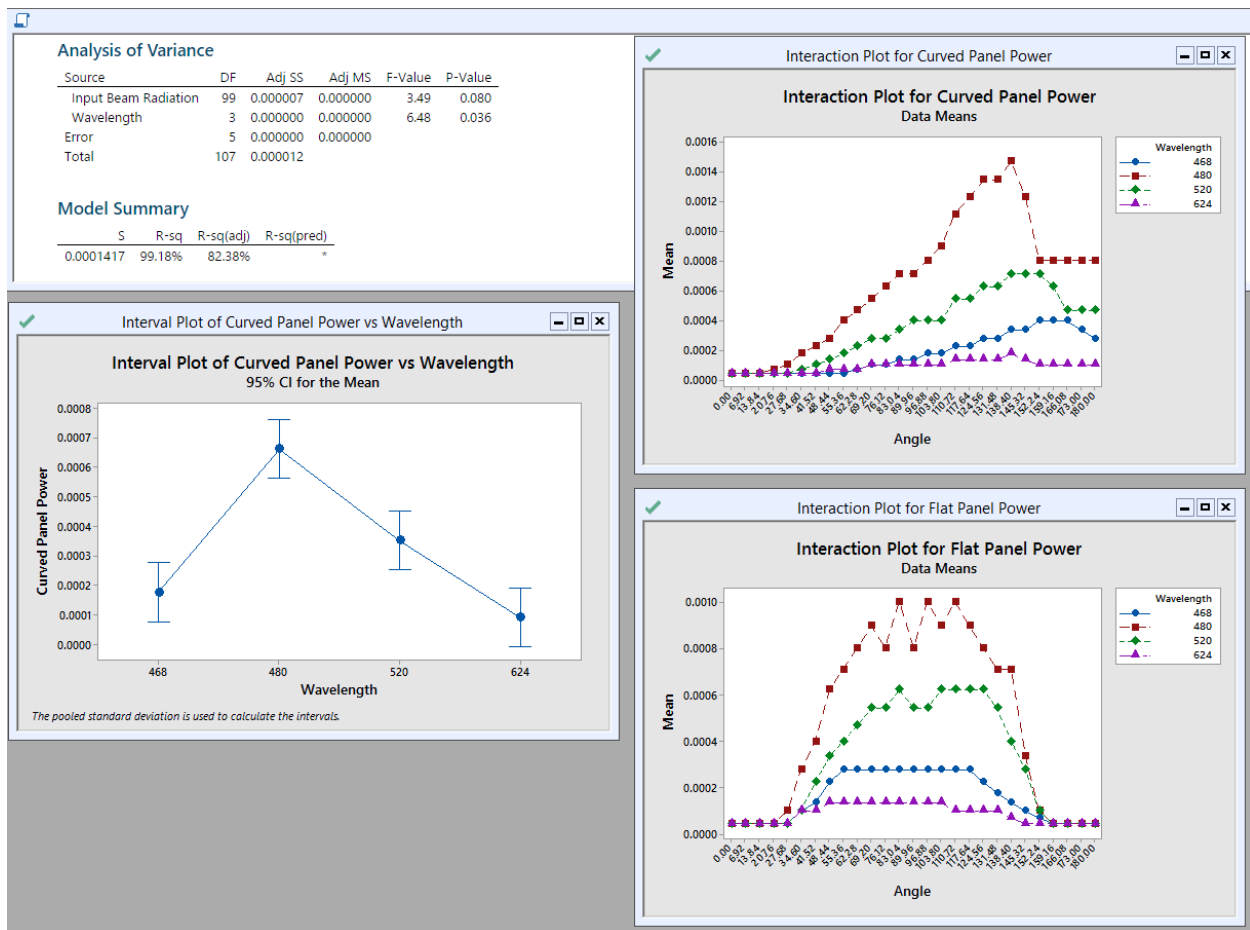


Fig. 4.11. Minitab analysis of variance for the BBRs test data comparing the flat panel and PV-embedded airfoil (curved) panel configuration.

In addition to the significance of each contributing variable and which is more significant, the flat and curved cell distribution trends are still apparent even in the interaction plots for the ANOVA.

4.5 Data Collection and Analysis Procedures

Solar cells used in this experiment were exposed to each wavelength of light with a corresponding current measurement output for every cell. Red has a corresponding wavelength to 625-780 nm, 495-575 nm for green, 455-495 nm for blue, and approximately 480 nm for white [61]. It should be noted that for this test, measured electrical outputs are voltage and current, and are the only electrical outputs used to evaluate the relationship between wavelengths effect on solar cell performance. Data collected from the experiment was done through the PCMS and SCARS datalogging feature. Data was subsequently tabulated in an excel file for later processing, with further analyses executed using the MiniTab program. For all intents and purposes when discussing the analysis results, the term “array” is considered synonymous with “panel”, and “device” where two cells were combined to form an array in a 1S/2P configuration; the term “cell” is avoided as multiple solar cells constitute an array.

The specific procedure for data extraction was accomplished by simply powering down the BBRS, opening the main door, removing the electrical system shroud, and removing each SD card from the PCMS and/or SCARS as required. The SD card was then inserted into a computer where each data set is labeled under a .txt file structure, and each data set needed to be copied and pasted into an excel file. To assist with data compilation, a custom BBRS excel spreadsheet was created with specific portions for data entry. The equations discussed in the mathematical framework in section 4.6.1 are embedded in this spreadsheet to avoid repeating calculations for

each data set; a sample of this spreadsheet is shown in Appendix H to predict PV airfoil power, and in Appendix J to determine the appropriate correction factor.

4.6 Solar Cell Correction Factor for Irregularly Shaped Arrays

Conventional flat PV devices were used during the initial BBRS experiments, where no correction factor for performance was required. Flat PV cells form large arrays that can be steered towards normalized illumination vectors to promote maximum unobstructed sunlight capture which is known as maximum power point tracking. In a system where multiple axis tracking cannot be used to continuously manipulate the array to face the sun, some power output losses are expected for such designs. In this case, a correction factor needs to be developed to predict the maximum cosine losses for an irregularly shaped PV array structure. This is accomplished by first analyzing the mathematical differences in PV system power output for flat panels and curved surfaces, and second by accounting for the spectral geometries present for the flat and curved surfaces in a fixed configuration [35].

An irregularly shaped photovoltaic array performance correction factor (PAPCF) is a valuable tool for UAS system designers to analyze for potential cosine losses when applying PV devices to fixed flight control surfaces or other available flight surface areas that do not interfere with inflight performance characteristics. For a particular UAS to collect power in a specific operational environment, a PAPCF predicting cosine losses can allow better concept of operations (CONOPS) to be built for optimized flight paths at multiple altitudes and other mission flight profiles. Most importantly, a prediction metric to determine the UAS adjunct PV system power output profiles can influence what type of electrical loads the main system bus can withstand. For example, if a BAMS UAS is intending to embark with a new payload that requires 25W, then the PV system would need to ideally continuously provide at least 25W, and

maneuver in such a manner that makes sense to meet operational flight needs as well as optimized solar collections.

Therefore, since operational needs out-prioritize solar collections it would likely be recommended to assume a worst-case analysis for the cosine losses where the PAPCF lowest value would be considered in this design. Alternatively, the performance correction factor should also be taken into consideration when excess energy is anticipated, and PAPCF values exceed 1.0. In such a case excess energy would need to (1) be properly radiated via electrical shunting to the environment as heat, (2) the energy would need to be redirected to other payloads or battery charging operations, and/or (3) exceed a desired amount where the PV system would enter standby mode and cease collection operations.

4.6.1 Mathematical Framework and Rationale. Through utilization of the BBRS and comparing values of interest for a flat panel and curved panel (i.e., irregularly shaped PV panel), a correction factor can be applied to assist engineers design a PV-embedded airfoil that meets electrical power requirements.

4.6.1.1 Initial Calculations. The initial calculations begin with an expression for overall photovoltaic efficiency, as shown in (38) [48].

$$\eta_{PV} = \frac{V_{OC} * I_{SC}}{P_{in}} FF \quad (38)$$

Since the fill factor is fundamentally a quantitative measurement of the panel quality, it can be characterized as the ratio of the maximum and theoretical total power output produced as represented by (39) [18].

$$FF = \frac{P_{MAX}}{P_{total}} = \frac{I_{MP} V_{MP}}{V_{OC} * I_{SC}} \quad (39)$$

If the input power is expressed as the product of the incident sunlight intensity and surface area of the solar panel, then the equation is represented simply by (40.1).

$$P_{input} = I_b * A \quad (40.1)$$

Considering the discussed information, one can assume a simplified equation for predicted PV power output, as shown by (40.2).

$$P_{total}[W] = I_b \left[\frac{W}{m^2} \right] * A_{PV}[m^2] * \eta_{PV}[\%] \quad (40.2)$$

The input power is measured using the SCARS subsystem, where the PV efficiency is now expressed as a ratio between power out and power in. For input power, the TSL2591 and TSL2561 measure incident radiation in lux, and to convert the lux measurement to watts is accomplished by using Equation 40.3.

$$P_{in}[W] = \frac{E_V[lx] * A_{PV}[m^2]}{\eta_{LED} \left[\frac{lm}{W} \right]} \quad (40.3)$$

Where for an LED the typical luminous efficacy (η_{LED}) value is approximately 90 lumens per watt [26]. The simple PV total power equation now becomes (40.4).

$$P_{total} = I_b * A_{PV} * \left(\frac{P_{out}}{P_{in}} \right) = I_b * A_{PV} * \left[\frac{\left(\frac{E_V[lx] * A_{PV}[m^2]}{\eta_{LED} \left[\frac{lm}{W} \right]} \right)}{P_{out}} \right] \quad (40.4)$$

The spectral response of the cell must also be considered and is described as a physical property of the PV cell and is represented by ratio of the current generated by the solar cell to the power incident on the solar cell, which is shown by (41.1) [48].

$$SR_{flat} = \frac{I_{out}}{P_{in}} = \frac{q\lambda_i}{hc} \quad (41.1)$$

Where λ_i is indicative for each wavelength (i) in nanometers (nm) of light used to generate an incident radiation (i.e., emission of luminous flux density) to the solar panel, h is Planck's constant ($6.626 \times 10^{-34} \text{ J} \cdot \text{s}$), and c is the speed of light constant ($299792458 \frac{\text{m}}{\text{s}}$). This will assist in making a coefficient of wavelength as part of the correction factor based on spectral response (i.e., the SRC) to the simplified PV equation, shown in Equation 42.4. This is accomplished by analyzing the spectral response for a flat and curved panel, which when included into the final equation for a curved panel will account for the observed differences in voltage output based on a single wavelength weighted by radiation intensity as described by Equation 41.2.

$$SRC = \frac{SR_{\beta}}{SR_b} = \frac{SR_{curve}}{SR_{flat}} \quad (41.2)$$

Once this is accomplished for a single wavelength, the average is taken accounting for all wavelengths used to stimulate the cell in both flat and curved configurations for all the 25 test runs (i.e., the average of the 25 samples) and is shown by (41.3).

$$SRC = \frac{\left(\frac{SR_{curve,\lambda}}{\sum SR_{curve}} \right)}{\left(\frac{SR_{flat,\lambda}}{\sum SR_{flat}} \right)} \quad (41.3)$$

The spectral response characteristic (SRC) is a ratio, where $\overline{SR_{curve,\lambda}}$ is the average spectral response (by analyzing the power output) for a specified wavelength, $\overline{\sum SR_{curve,\lambda}}$ is the average of the sum of power output based on all wavelengths for curved (airfoil) configuration PV array testing, $\overline{SR_{flat,\lambda}}$ is the average spectral response, and $\overline{\sum SR_{flat,\lambda}}$ is the average of the sum of power output based on all wavelengths for flat configuration PV array testing.

4.6.1.2 Corrections for a Curved Airfoil Array. All of the assumptions stated to this point assume a beam radiation incidence angle of directly normal to the panel surface, characterized in this dissertation as beta angle of zero, and that this beam accounts only for the relation of a flat panel to a curved panel. To accurately predict PV performance for an irregularly shaped panel, assume the following relationships occur when comparing a flat panel to curved panel. A comparison of beam radiation incident to a flat panel versus a tilted panel is made, provided that a curved panel is a series of tilted panels over unit distance. This series of panels can be solved over an integrated distance, but for the consideration of this prediction tool (e.g., a correction factor for predicting power for irregularly shaped PV panels), an average slope using symmetrical airfoil such as the NACA0024 is considered. Using Fig. 4.12, the geometries of the incident radiation in relation to the PV panel geometry is provided in the following coordinate plane.

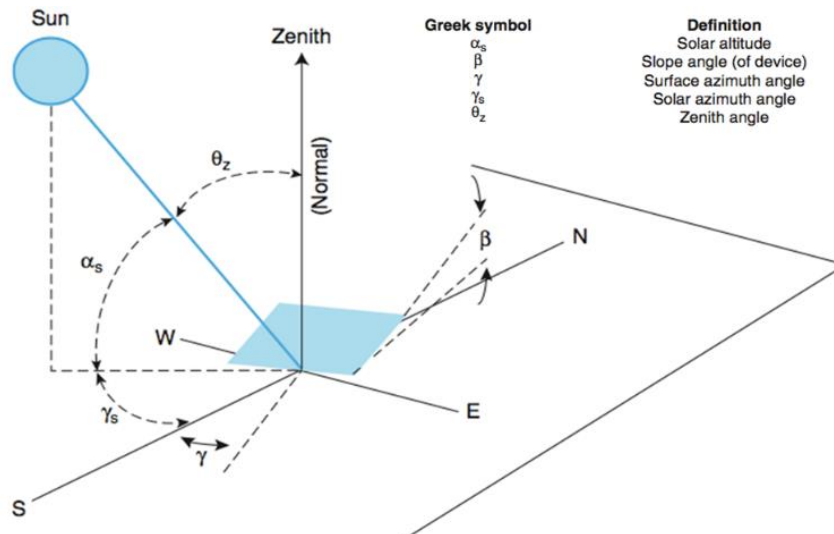


Fig. 4.12. View of the geometric relationship between the solar irradiance source's position, orientation of a raised solar device, and compass directions, showing the solar source striking the PV panel at an oblique angle. This diagram is shown for the northern hemisphere, in the southern hemisphere the orientation would be reversed with the solar source positioned to the north of the East West line. For more details, the reader is referred to [55, Fig. 16].

Under these assumptions, the beam radiation ratio can be expressed as (42.1).

$$\overline{R}_b = \frac{I_{\beta,b}}{I_b} = \frac{I_{n,b} \cos(\theta_i)}{I_{n,b} \cos(\theta_z)} \quad (42.1)$$

Where \overline{R}_b is a ratio of the beam insolation on a tilted surface to that on an equivalent horizontal surface, $I_{\beta,b}$ is the beam insolation on a tilted surface (in Wm^{-2}), I_b is the component normal to the horizontal surface, and $I_{n,b}$ is the component of global solar radiation that arrives directly to the Earth's surface. θ_i is the incidence angle and using the geometries illustrated in Fig. 4.12, it is represented by (42.2).

$$\theta_i = \cos^{-1}[\sin(\alpha) \cos(\beta) + \cos(\alpha) \sin(\beta) \cos(\gamma - \gamma_s)] \quad (42.2)$$

Since the incidence angle (θ_i) is with respect to normal light source angles on tilted panels, an airfoil-specific beam radiation ratio must be developed and is shown by (42.3).

$$\overline{R}_b = \frac{I_{n,b} \cos(\theta_i)}{I_{n,b} \cos(\theta_z)} = \frac{I_{\beta,b} \sin(\alpha_s) \cos(\beta) + \cos(\alpha_s) \sin(\beta) \cos(\gamma - \gamma_s)}{I_b \cos(\theta_z)} \quad (42.3)$$

As a result, the final equation for predicted PV performance using an irregularly shaped panel structure is shown by (42.4).

$$P_{total} = \left[\left[\left(\frac{SR_{\beta,i}}{\sum_{n=1}^i SR_{\beta}} \right) \right] \left[\frac{I_{\beta,b} \sin(\alpha_s) \cos(\beta) + \cos(\alpha_s) \sin(\beta) \cos(\gamma - \gamma_s)}{I_b \cos(\theta_z)} \right] I_b \right] A_{PV} * \left[\frac{\left(\frac{E_V [lx] * A_{PV} [m^2]}{\eta_{LED} \left[\frac{lm}{W} \right]} \right)}{P_{out}} \right] \quad (42.4)$$

Resulting in a final correction factor applied to the predicted total power equation shown by (42.5).

$$P_{T,\beta} = [SRC * \overline{R}_b] * I_b * A_{PV} * \eta_{PV} \quad (42.5)$$

Where the spectral response characteristic (SRC) determination assists in computing the average power output for a specified wavelength, where it is divided by the sum of the average power outputs for the entire spectrum ranges used. This is shown in a condensed Microsoft Excel table showing the steps necessary to compute the PAPCF and is located in Appendix H.

4.6.2 Proposed Performance Correction Factor. Based on the experimental airfoil spectral response, the PAPCF formulated, using the rationale shown in section 5.2, is formed using variables and information that can be obtained from the BBRS tests, where the PAPCF is subsequently generated for a given airfoil design. In this case, a NACA0024 symmetrical airfoil was used as the experimental design for the research effort. Using the airfoil plotter dimensions, an average slope was determined and calculated to be 8.825 degrees. The BBRS test information was collected and tabulated using Microsoft Excel, where a PAPCF for the NACA0024 airfoil embedded with single junction silicon-based PV is shown in Fig. 4.13.

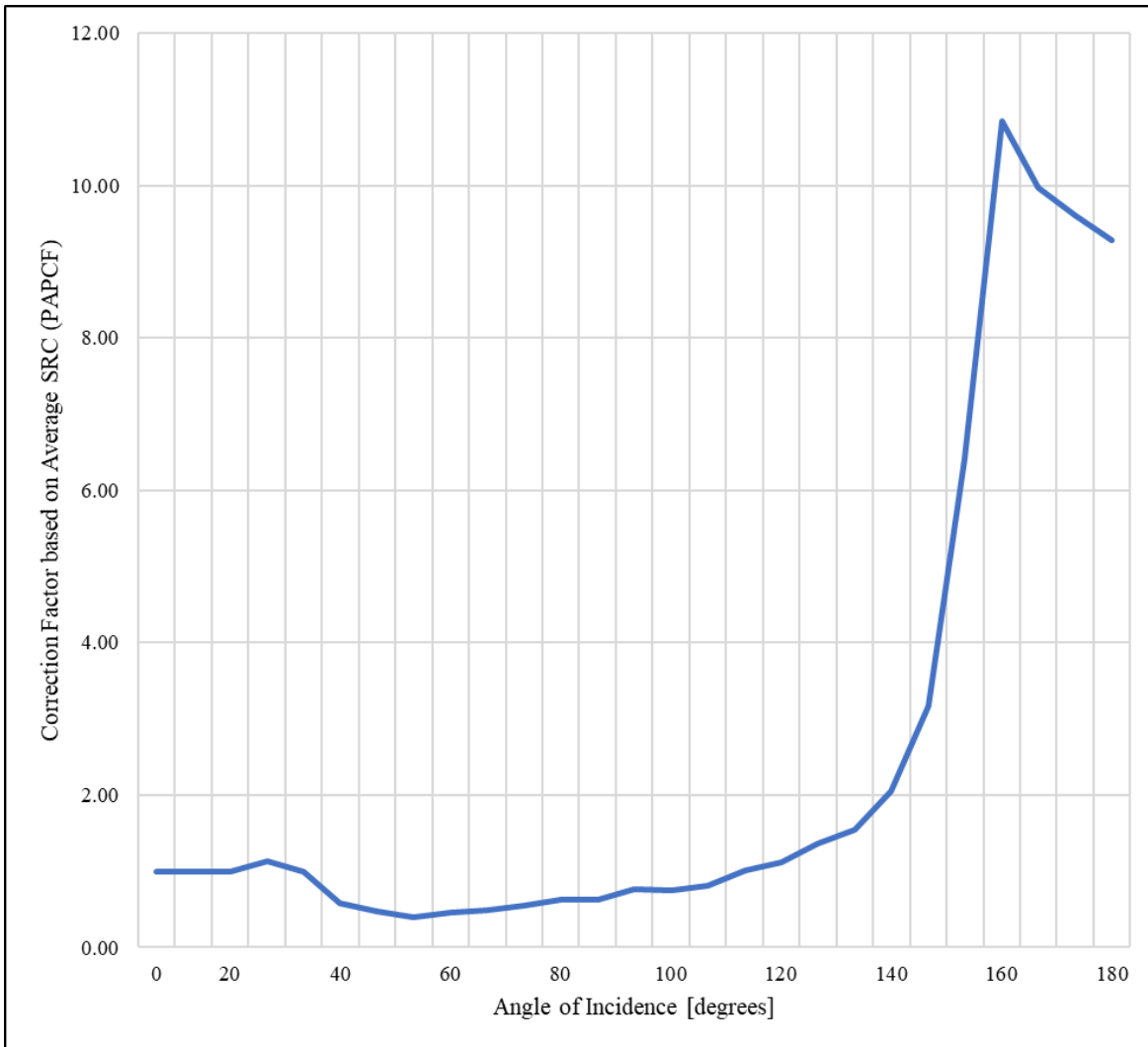


Fig. 4.13. The photovoltaic array performance correction factor for the NACA0024 airfoil. The correction factor is a sliding scale to compare the performance of a flat PV panel to a NACA0024 PV airfoil panel, where the factor is determined by angle of incidence and accounts for only the visible EMS region.

As can be expected, the amount of solar energy that can be collected for both the flat cell and curved cell with small beta angles is very low, and the resultant PAPCF for both flat and curved conditions is 1.0. However, as the beta angle increases (i.e., as the sun is rising over the leading edge of the airfoil), the collection efficiency of the flat cell is higher than that of the curved cell, and therefore the PAPCF is approximately 0.3. Beta angles between 27 and 110 degrees yield favorable results towards the flat PV configuration, until the beta angle regime of 112 to 180 degrees where the curved cell configuration performs significantly better than the flat

cell. From this data and resultant PAPCF it is recommended that the UAS utilize a flight pattern CONOPS where the sun is in the rear quadrant facing the airfoil trailing edge in order to maximize solar collections to accommodate payload power requirements.

4.7 Validity and Triangulation Concerns

According to Zohrabi [59], it is the responsibility of the “researcher and research participants to build validity into the different phases of the research from data collection through data analysis and interpretation. Using the most precise measurement tools available, gathering the most accurate information through valid methods is essential for generating quality, acceptable and credible research [59]. Ensuring accurate voltage and current measurements are taken, carefully organizing the data, and executing the appropriate statistical method to evaluate quantitative data will all aid in drawing reliable conclusions. Presenting the research findings without valid data or evaluation methods will negatively impact the credibility of the study. When determining the proposed correction factor, confirmation bias was taken into account to ensure that the data was strictly analyzed without considering what “common sense” and reality would dictate. The data analysis was executed without the undue influence of proving the null hypothesis, and the observed data was able to prove the rationale of the mathematical framework.

4.8 Ethical Issues and IRB Considerations

Ethical considerations were accounted for as applicable for this type of research as per regulations set forth by the institutional review board (IRB) review and the US Department of Health and Human Services (HHS) [53]. According to the Federal Policy for the Protection of Human Subjects, human subjects are defined as “a living individual about whom an investigator (whether professional or student) conducting research obtains (1) data through intervention or

interaction with the individual, or (2) identifiable private information” [53]. Additional IRB requirements for review and forms still need to be completed, as required by federal regulation codes under the National Science Foundation (45 CFR 690.101) and Department of Energy (10 CFR Part 745) [53]. Most importantly it should be noted that no human subjects were used in the research project.

4.9 Reliability and Reproducibility

Due consideration in this dissertation was given to both reliability of data and reproducibility. The specificity of the test parameters, standard assumptions, component capabilities, and BBRS design and fabrication was provided to promote maximum reproducibility or repeatability for independent researchers intending to further the dissertation research. This was accomplished to ensure that the dissertation experiments gave due attention to the process of experimental design and the scientific method, to provide an effective and reliable methodology and analysis [49].

CHAPTER 5

CONCLUSIONS, CONTRIBUTIONS, AND FUTURE WORK

5.1 Research Conclusions

5.1.1 Subsystem Design Challenges. During the BBRS fabrication process described in Chapter 3, there were several distinct challenges that arose during the design and prototyping phases. Some initial observations were that the METRO328 board needed to be properly synched to the Arduino software package, as an IDE compiler mismatch can occur; this was fixed by downloading and installing multiple libraries into the IDE. Controller memory was also a challenge, where during microcontroller selection the Arduino UNO board was observed to only have ~32.2 MB worth of data capacity. It became more beneficial to utilize the METRO328 board due to the larger data storage space for more advanced code. Additionally, the original system design was to operate off of one controller, however this changed to a subsystem setup based on the limited allocation for code space on each board, and to also make the troubleshooting process easier while maximizing system processing speed. As the boards got bigger physical space and interchangeability became an issue, therefore it was recommended to use a stacked configuration for the microcontroller boards so that the programming port is available on the outside of the simulator.

For the BAPCS, finding the best control mechanism was difficult that promoted the highest level of control and degree accuracy. Initially the 28BYJ-48 stepper motor coupled with the ULN2003 motor driver was used and provided accurate angle measurements within 1.25 degrees, however several issues were discovered. When a rotary encoder was used as the control, the stepper motor demonstrated consistent power when positive displacement is executed, but during negative displacement (i.e., turning the rotary encoder the opposite direction) generated motor jitter. To solve this issue an Uxcell 4x4 membrane keypad [101] was used to accurately

control the number of steps. Additionally, there was an issue with the motor torque to reliably manipulate the ASMS. Other drivers such as the ULN2003 had overall quality that proved questionable due to performance and failures during testing, therefore the stepper motor driver and stepper motor were upgraded to allow maximum torque at $\sim 1.2\text{A}$. Arguably one of the largest obstacles was the datalogging capability, where a USB Data Acquisition (DAQ) Module was considered for use. However, models such as the National Instruments USB-1208LS required a dedicated data acquisition software suite to log and read data. The intent was to have the BBRS capable of logging data independently of any software suite, log to a portable card and display data real time to a user. Additionally, while the DAQ modules had high sampling rates and decent resolution, the amount of analog inputs was limited, better modules were more expensive, and the system would not be interoperable with the rest of the BBRS infrastructure.

5.1.2 Limitations. An apparent material limitation was discovered during the thermal stress experiment, where the material properties of a flexible silicon PV device behave differently when exposed to high temperatures than a conventional rigid PV device. When the flexible PV array was used in both the flat and airfoil configurations, there was noticeable decay in electrical output as a function of temperature to the point where the array completely failed as noted in Chapter 4. When the experiment was completed, it was presented that the thermal stresses had a near identical impact in both configurations to the resultant electrical output using the same temperature ramp rate, as the failure point was within 1.5°C . Similarly performing silicon PV cells that are rigid have better survivability in higher temperatures and higher temperature ramp rates [52]. Therefore, an important variable for flexible arrays in airfoil integration has been noted, as these deformations in the surface material can render the PV-embedded airfoils effectively worthless when temperatures over 49°C is encountered. For the

purposes of this dissertation however, a limitation was discovered for the PV devices selected.

Once they had exceeded the temperature threshold, apparent plastic deformations had occurred at the surface junctions shown in Fig. 5.1 below, which rendered the cells unusable for future use.

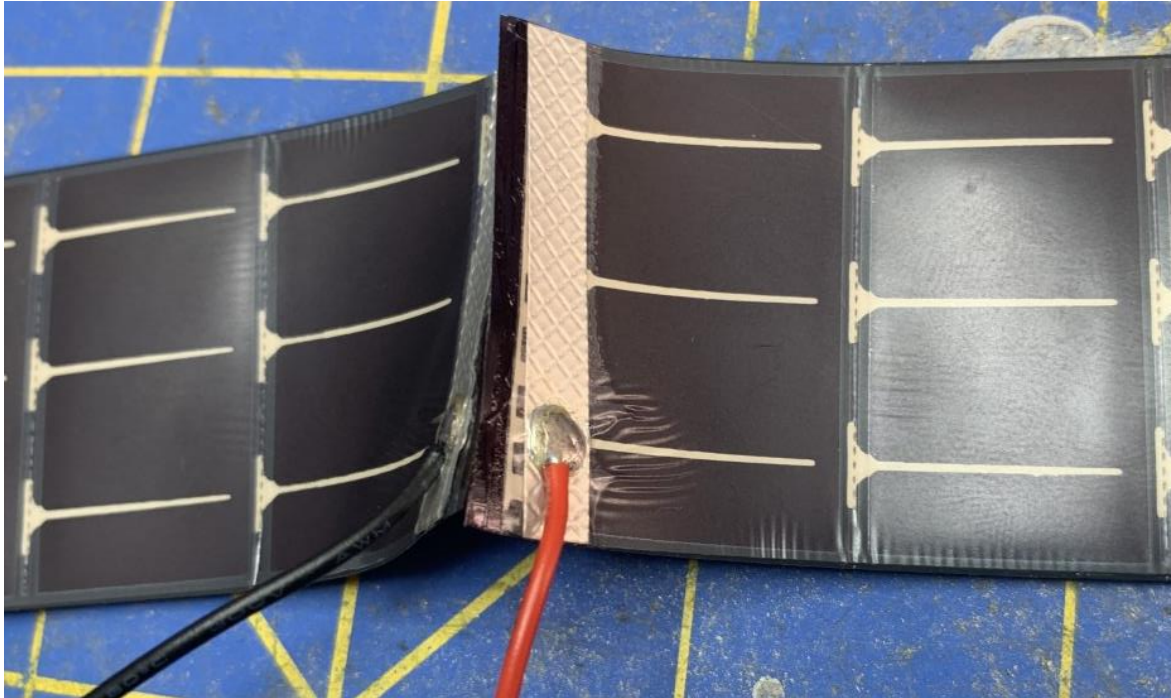


Fig. 5.1. Flexible PV cell after thermal stress experiment for both airfoil and flat cell configuration. Multiple plastic deformations were noted along the cell surface, as well as at the junctions.

Additionally, some wavelength calibrated lasers were used to initially stimulate the cells as they are commonly used for solar test applications. However, it was noted that for the original test setup that the Si-based PV cells used would get overly saturated using 5mW lasers in the 532nm spectrum which would yield unreliable PV electrical output measurements.

5.1.3 Comparison of Flat Panel to Airfoil Array Performance. Through the dissertation experiments performed in Chapter 4, it was shown that lower irradiance angles of incidence (AOI) directed towards the leading edge of an airfoil the PV-embedded system has worse performance than a flat configuration. However, when exposed to irradiance angles in the

rear quadrant relative to the leading edge (i.e., more irradiance toward the trailing edge) the electrical output is significantly greater than the flat cell configuration.

5.1.4 Significance of the Study. This dissertation can assist UAS developers for both large and small-scale UAV design that intends to utilize PV devices for supplemental power. For small UAS, use of a flexible array demonstrates clear temperature limitations and performance decay at increased temperatures but adaptability as it can be embedded easily to irregular shapes and the CONOPS can be refined to optimize solar collections. For large UAS, the flexible PV device may be replaced with multiple rigid cells in different angled configurations that make up a larger curved array that bends to an airfoil shape. However, vibrations may hinder electrical output and long-term performance, which can be studied in a different experiment. Utilizing renewable energy systems on UAS can enhance total system performance and increase on-station time by supplying alternative power to electrically driven propellers for propulsion on UAVs [5].

Studies such as this are vital for providing lessons learned to future UAV design enhancements, where solar panel size is limited, and electrical power requirements are high to support sophisticated payloads [23]. Identifying the potential risk areas and research to show effective mitigations can allow a program to save time, resources and cost when developing new UAS for various missions (Huasgen & Carpenter, 2015). Additionally, considering the deterioration of available fossil fuels and rising acquisition and maintenance costs, providing fossil-fuel dependent research areas the opportunity to transition to renewable energy solutions can save on energy costs and reduce geographic pollution levels [28].

5.1.4.1 Contributions. From a much larger perspective, this dissertation provides a unique piece of specialized test equipment to analyze a PV array or individual solar cell under consistent and controlled environmental conditions. While the current BBR iteration has a

maximum dimension capacity of 220mm x 220mm x 300mm, the system is scalable to meet larger PV requirements and dimensions through use of the subsystem design structure. There is high confidence that the BBRS will provide a cost-effective solution for providing standardized and repeatable tests for different PV arrays. This dissertation contributes a means to enhance test methodology for renewable energy systems in both terrestrial and space-based applications for unmanned systems.

5.2 Future Work

This section is intended to address all identified future work areas and recommendations to continue on with the research effort.

5.2.1 Different Airfoil Configurations. The current BBRS stimulates a flat 8.142 mm^2 experimental flexible solar cell array mounted on a NACA0024 symmetrical airfoil using varying wavelengths of light under various environmental conditions, and subsequently measures the photovoltaic response. In future testing, the BBRS could be used to measure other irregularly shaped structures such as the NASA LRN1015, or FX67K-150 airfoil that is currently used for the MQ-4C Triton BAMS UAS or other HALE platforms [5]. Additionally, other surface areas such as the fuselage can be 3D printed and embedded with PV arrays to examine for cosine losses and optimized solar collection angles. An important consideration of this dissertation was to provide a minimally intrusive renewable energy payload design so that the aerodynamic properties of an unmanned or manned system is relatively unaffected by the PV system's presence. For future iterations of the research, a study of aerodynamic impacts caused by PV array integration would be beneficial, as the lift-curve slope, maximum angle of attack, and lift and drag coefficients may change.

5.2.2 Spectrum Emitter Sources. The ASMS currently uses light emitting diodes (LED) calibrated to yield a specific wavelength given a driving voltage of +5V, with variations in luminous flux densities not exceeding +/- 10 nm. Since the LEDs emit energy in an omnidirectional manner, analyzing how the PV cell responds to a more focal directional energy emission could be of benefit. Therefore, it is considered as an additional path for experimentation to use lasers with low intensities suitable for BBR fabrication. Some benefits of using lower power (5-10mW) lasers would be more favorable/lighter weight, more commercial availability, and lower cost while achieving smaller deviation in luminous flux wavelength (i.e., +/- 0.15nm). For immediate consideration, lasers in the RGB visible spectrum can be fabricated, calibrated, tested, and integrated into the existing BBR architecture. Oversaturation of the PV device would need to be considered however, as directional high energy lasers intended for use with low voltage yield PV devices can not only cause unreliable photocurrent readings but also damage the PV cell material when exposed for long periods [31].

5.2.2.1 Quality Control Methods. During the early experimentation with the BBRs, specifically for the ASMS stimulating the PV-embedded airfoils and flat cells, it was observed that the UV spectrum reflections and PCMS readings were impacted by cell interconnect location(s). More specifically, the UV spectrum readings were skewed due to reflections from the interconnect material and indicating less photocurrent generation at certain beta angles where otherwise higher currents would be noted. This “dip” in the electrical energy generated is noted during the PV airfoil and flat cell power output graphs, such as in Figures 4.6 and 4.7 for the UV spectrum portion. This observation yielded two paths forward for the research effort, where (1) the UV spectrum analysis can be used for quality control to determine areas of a PV array that have surface discrepancies (i.e., scratches, deformations in the monocrystalline

layer, issues with electrical interconnects) which can hinder optimized solar collections when present, and (2) the UV spectrum skews the data for total electrical energy generation. Therefore, the BBRS experiments were tailored to focus solely on the visible portion of the EMS. As observed from Fig. 5.2 below, only a small portion of energy in the EMS is available for PV solar collections and subsequent conversion to electrical energy.

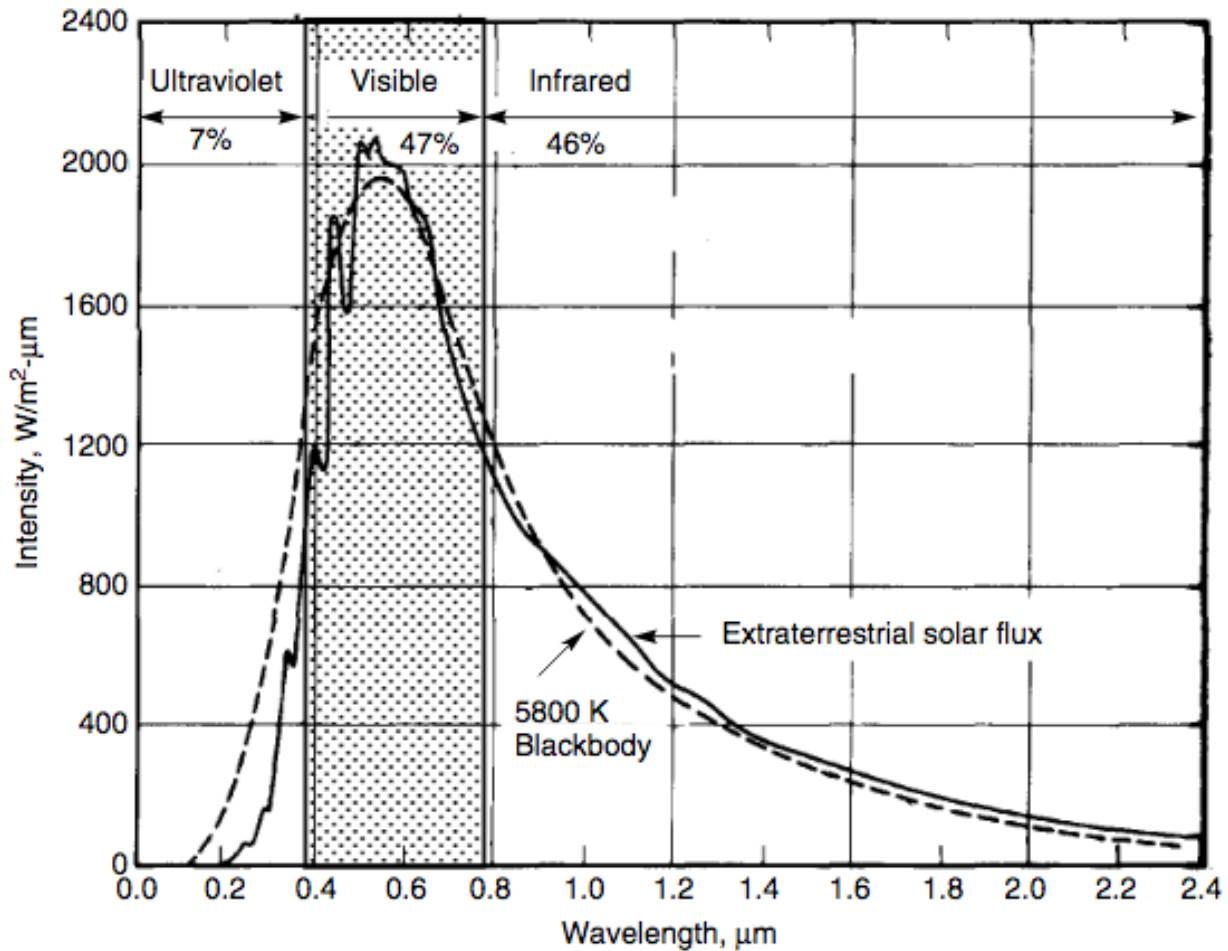


Fig. 5.2. Electromagnetic spectrum energies for a blackbody broken down by ultraviolet, visible, and infrared spectrums. Note that the ultraviolet spectrum accounts for only 7% of the total electromagnetic spectrum energy in a 5800K blackbody. For more details, the reader is referred to [28, Fig. 10].

Similar to what was discussed in Chapter 2 and Chapter 6, a limitation was placed on the BBRS experiment using only the visible spectrum. Future iterations of this research effort will

involve additionally considering the IR spectrum using different solar cell types, as the flexible PV material used for flat cell and airfoil configurations was not responsive in that EMS region.

5.2.3 Emissivity Impacts. The next path would be to account for emissivity impacts from atmospheric interference, with varying concentrations of chemicals in the atmospheric layer. The initial intent was to calculate any atmospheric impacts to PV yield using ex post facto calculations (e.g., use of the ASHRAE clear sky radiation model with varying k clearness index factors), however there is benefit to future iterations of the research project to utilize filtering for the UV, IR, and visible bands [11]. This can be used to simulate atmospheric impacts to solar source emissivity; accounting for these factors will help increase the confidence level for accuracy in PV measurements in specific PV configurations, as well as add variation to the ASMS luminous flux density.

5.2.4 GaN Comparison to Si PV Technologies. As mentioned previously in Chapter 2, there is value in exploring the differences for PV-embedded technologies using Si and GaN semiconductor materials. Based on the literature review pertaining to bandgap energies, it is hypothesized that if there are limitations to how free electrons can move between the forbidden band to the conduction band (e.g., band gap energy), then there is a correlation between PV output and band gap energy. However, there may be additional work to be conducted as part of this study to first understand the emission process for direct and indirect bandgap processes as GaN and GaAs are direct, whereas Si is indirect. Direct band gap allows absorption to occur at shorter wavelengths where the emission occurs with photon energies closer to the band gap, and the valence band maximum aligns with the conduction band minimum, as illustrated in Fig. 5.3 below [46].

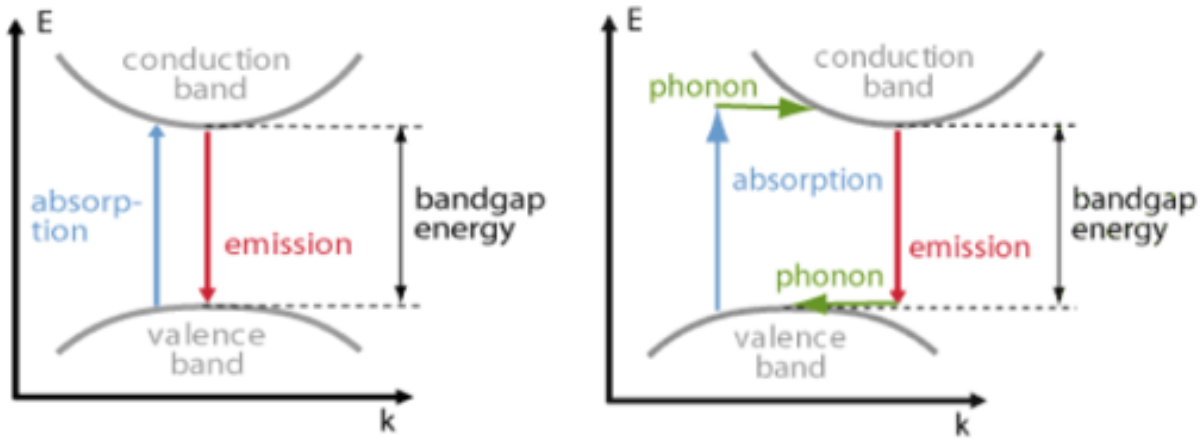


Fig. 5.3. Direct (left) and indirect (right) bandgap processes for a theoretically ideal semiconductor. For more details, the reader is referred to [46, Fig. 3-4].

Conversely for the indirect bandgap, additional photons would be needed in absorption and emission processes in order “to provide the required momentum change of electrons” [46]. Since there is a difference in how the emission process works in direct and indirect processes, the impacts to theoretical photovoltaic output need to be specifically addressed in order to successfully compare the two materials. Si when compared to GaN has a distinctly lower absorption coefficient where more Si layers in a PV device need to be present to yield more energy, where different semiconductor materials and their corresponding energies and wavelengths are shown in Table 4 below.

TABLE 4
TYPE AND ENERGY FOR SOME COMMON SEMICONDUCTOR MATERIALS

<i>Material</i>	<i>Abbrev.</i>	<i>Bandgap Type</i>	<i>Bandgap Energy [eV]</i>	<i>Bandgap Wavelength [μm]</i>
Lead Selenide	PbSe	Direct	0.27	4.57
Lead Telluride	PbTe	Direct	0.32	3.86
Indium Arsenide	InAs	Direct	0.36	3.43
Lead Sulfide	PbS	Direct	0.37	3.34
Germanium	Ge	Indirect	0.67	1.84
Gallium Antimonide	GaSb	Direct	0.726	1.70

Silicon	Si	Indirect	1.12	1.10
Indium Phosphide	InP	Direct	1.35	915
Gallium Arsenide	GaAs	Direct	1.441	857
Cadmium Tellurite	CdTe	Direct	1.5	823
Cadmium Selenide	CdSe	Direct	1.74	710
Aluminum Arsenide	AlAs	Indirect	2.12	583
Gallium Phosphide	GaP	Indirect	2.24	551
Cadmium Sulfide	CdS	Direct	2.42	510
Gallium Nitride	GaN	Direct	3.4	363
Cubic Zinc Sulfide	ZnS	Direct	3.54	349
Hexagonal Zinc Sulfide	ZnS	Direct	3.91	316
Aluminum Nitride	AlN	Direct	6.015	205

Note. Data reprinted from [46].

Since PV devices can only use photon energies above the semiconductor material band gap, a problem is posed with sunlight that yields long wavelengths. If the wavelength is too long, then the photonic energy being presented to the Si-based or GaN-based PV will not produce a current, and simply generate heat. Utilizing a cell that can take advantage of the shorter and longer wavelengths to generate higher voltages more effectively is desirable for a renewable energy system. Establishing a balance between absorption capabilities based on available sunlight spectrums (e.g., a local solar analysis of wavelengths present based on geographic position) and desired voltage output will be accomplished by tailoring the PV material and resultant band gap energy to meet voltage requirements.

A shorter photon wavelength will yield a higher photon flux, and if a small band gap energy semiconductor is used then more hole-electron pairs opportunities exist, thus providing higher currents but lower voltages. For a larger band gap energy semiconductor, such as GaN, there is more displacement for higher energy in the available hole-electron pairs, thus yielding

higher voltages but lower currents. Standard data can be generated for initial analysis using Microsoft Excel to compare incident photon wavelength to electron energy gain and electron frequency for Si, GaN and GaAs semiconductor materials as shown in Fig. 5.4 below.

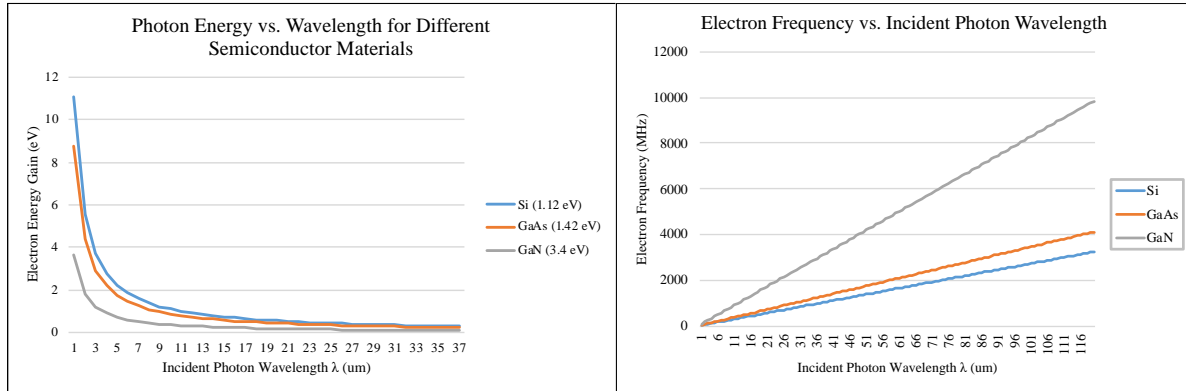


Fig. 5.4. A comparison of Si, GaN, and GaAs semiconductor materials by resultant photon energy as a function of incident photon wavelength (left) and electron frequency as a function of incident photon wavelength (right). There are noticeable differences in the photon energy capabilities when comparing Si to GaN for electron energy gain and electron frequency, however this could lead to fewer ranges of light wavelengths being used for solar energy conversion processes. This brief analysis assumes a bandgap energy for Si at 1.12 eV, GaAs at 1.42 eV, and GaN at 3.4 eV under ambient temperatures of 25°C.

However, more detailed models can be generated using Matlab and Simulink similar to the one shown in Chapter 2 to account for these differences in bandgap energies, and potentially predict the changes in PV performance based on different semiconductor materials.

5.2.5 Vibration Testing. To address future testing for the BBRS, the ECMS is equipped with vibration testing elements which consist of several SW-420C vibration sensors with breakout board assembly, and a GY-521 accelerometer, as shown in Fig. 5.5 and Fig. 5.6 respectively.

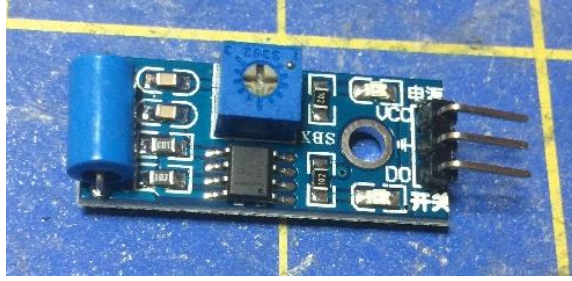


Fig. 5.5. Front image of the SW-420NC vibration sensor that can be paired with the ECMS thermal baseplate to detect vibration intensities. For more details, the reader is referred to [71].



Fig. 5.6. Front image of the GY-521 3-axis accelerometer to be used for precise vibration sensing when paired with a 3D printed PV-embedded airfoil. For more details, the reader is referred to [72].

Fig. 5.7 below shows the adjunct vibration simulation setup mounted underneath the ECMS thermal baseplate, which is currently in the breadboard phase, and is intended for future PV-embedded airfoil testing.

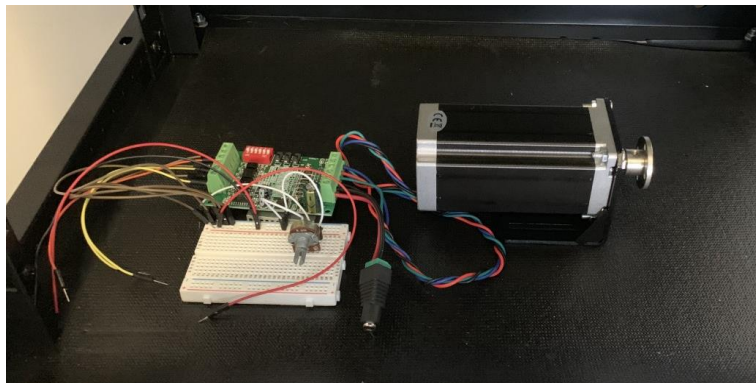


Fig. 5.7. Front image of the vibration simulation subsystem using the NEMA23 motor, TP6560 driver, and UNO R3 controller board. System setup is intended to be used for simulating UAV propulsion system vibrations under various rpm conditions while a PV-embedded airfoil is subjected to various wavelengths of light and irradiance levels.

Various UAS vibrations are simulated using the NEMA23 bipolar motor, and TP6560 stepper driver where a $10k\Omega$ potentiometer is used to control the motor rpm. The GY-521 3-axis accelerometer can be mounted inside the PV-embedded airfoil as discussed in Chapter 3, and the raw data can be modified using KST open source software which executes a fast Fourier transform (FFT) to translate 3-axis analog data into vibration frequencies [20]. The SW-420NC vibration sensor [71] does not provide accelerometer data, and only provides the magnitude of various vibrations throughout a system based on a predetermined threshold in the code. These sensors are helpful to determine if vibrations are present at all in different spots of a dedicated vibration test setup, but for more accurate analog data acquisition the GY-521 is recommended. A large design consideration for this future testing is determination of optimal sensor placement, and therefore a study for analog sensor mounting will be required.

5.2.6 Other Design Improvements and Research Efforts. During the course of completing the dissertation, there were several other areas for future work noted for both the test apparatus and the BBRs. For the test cells, exploring other options for flexible semiconductor materials would be beneficial to analyze for performance differences resulting from the future GaN and Si comparison experiments, as many other semiconductor materials such as Dilute Nitride are being compared to conventional solar cell technology [38]. Regarding the BBRs, it would be beneficial to add more datalogging capability for each subsystem, but there were constraints due to the microcontroller's limited dynamic memory. For future iterations of the BBRs subsystem controllers, it would be recommended to explore new and more robust commercially available microcontrollers as technology improves. Additionally, it would be valuable to test a sample PV array or PV-embedded airfoil under more complex electrical loads using a buck-boost converter instead of simply testing under different resistances using a

potentiometer. More specifically within the BBRS, it would be advantageous in future testing with different illumination sources to be able to adjust the sensitivity or gain for the spectral response sensors in the SCARS without having to modify the source code. One particular area of concern when scaling the system to accommodate larger airfoils and PV arrays would be the BAPCS current limit on the stepper driver. The driver is the primary interface between the power supply, motor, and microcontroller, and is very sensitive to current fluctuations. Therefore, a consistent and reliable power supply is recommended, as well as a suitable stepper driver such as the MA850H driver to handle higher current loads. This is pertinent as torque loads may increase if a heavier ASMS is required in BBRS scalability, where a higher operating current will be required to achieve higher generated torque from the stepper motor [9].

Other areas of potential research would be the specific reduction of greenhouse gas emissions resulting from a HALE UAS equipped with a PV system for adjunct payload and/or propulsion power, and subsequent failure modes and service life for UAS components. If a new HALE UAS is intended to use unique solar collection equipment, then it would be of value to determine what types of failures could be presented in the system and when they might occur using mean time to failure (MTTF) and Markovian chain analytics. This type of analysis would be beneficial to determine overall system reliability and maintainability. For a basic example, consider two GaN PV devices are operating in parallel, and have an individual failure rate of 0.1 per year where if one fails, the other can still provide some power. However, suppose the increased electrical demand could triple the failure rate of the remaining solar cell. Assuming the use of a load-sharing state-dependent system and the application of Markov analysis for this analysis, the system reliability can be determined using (43.1) and its treatment as shown below in (43.2) [12].

$$R(t) = e^{-2\lambda t} + \frac{2\lambda}{2\lambda + \lambda^+} [e^{-\lambda^+ t} - e^{-2\lambda t}] \quad (43.1)$$

$$R(t) = e^{-2(0.1)t} + \frac{2(0.1)}{2(0.1) + (0.1*3)} [e^{-(0.1*3)t} - e^{-2(0.1)t}] \quad (43.2)$$

Where the above equation can be used for the following t (in years) to determine the total system reliability decrease over the course of several years, as well as the system MTTF; this is shown by the resultant computations below in (43.3) - (43.5).

$$R(1 \text{ year}) = e^{-(0.2)(1)} + \frac{0.2}{(0.2) + (0.3)} [e^{-(0.3)(1)} - e^{-(0.2)(1)}] = 0.9745 \quad (43.3)$$

$$\begin{aligned} R(2 \text{ years}) &= 0.9133 \\ R(3 \text{ years}) &= 0.8333 \\ R(4 \text{ years}) &= 0.7456 \\ R(5 \text{ years}) &= 0.6574 \end{aligned} \quad (43.4)$$

$$MTTF = \frac{1}{2(0.1)} + \frac{2(0.1)}{-0.1} \left[\frac{1}{(0.1*3)} - \frac{1}{2(0.1)} \right] = 8.333 \text{ years} \quad (43.5)$$

This type of analysis is beneficial to UAS engineers and operators to determine a WCA should components begin to break upon extended use where depot-level maintenance windows may not be met due to operational flight requirements. Based on this specific example, given a basic reliability function, the MTTF for delicate PV UAS components can be modeled to show deterioration in reliability over a course of 5 years from ~97% to ~66%. This can assist in developing appropriate maintenance windows for PV-embedded UAV systems, and even contribute to mission readiness/capability metrics using component material condition as a driving factor.

5.3 Conclusion Statement

The objectives of this dissertation were to fabricate a simulation device to test irregularly shaped PV arrays embedded into airfoil technology, where the user has the ability to take

observed data and determine a correction factor to accommodate for cosine losses. This dissertation has completed those objectives and identified additional research areas for future work as well as recommendations to improve the existing research effort. The BBRS can be a valuable tool for solar technology researchers looking for cost-efficient methods to test unique PV arrays. Additionally, the BBRS can be scaled to meet larger experimental models and test for other factors to PV array performance such as thermal stresses. For the data analysis, mapping the spectral response and using the methods described in Chapter 4 allow UAS designers to determine a correction factor when compared to flat panel performance to predict PV system output based on AOI. These quantitative metrics can allow UAS operators to determine the most favorable flight profiles to maximize solar collections while considering other operational mission requirements. A similar analysis using the BBRS can be conducted to accommodate for other irregularly shaped PV arrays that may be mounted on other UAS surfaces such as the fuselage. Once the appropriate spectral geometries for the array orientation is calculated then a subsequent correction factor can once again be applied allowing for PV power output estimation.

The dissertation also highlights some survivability aspects of a unique PV-embedded airfoil system where performance risks due to thermal stresses and vibrations would need to be effectively mitigated. More specifically, there was an identified tradeoff condition where flexible PV material can be used to potentially overcome vibration concerns but may also lack the ability to effectively radiate heat.

In an effort to gain a stronger understanding of the basics of solar cell technology, realizing the impacts the different wavelengths in the EM spectrum can have on solar cell performance is crucial to determining the optimum conditions for each type of solar cell and airfoil type unique to that particular UAV. In the future, evaluating different cell types such as

Si-polycrystalline, GaN/GaAs, quad-junction, inverted metamorphic (IMM) and other chemical compositions and configurations will aid in UAS electrical power research.

The paper from Imamura & Khoshaim shows there is a relationship between photocurrent yield and average cell size for silicon-based cells, where the size of a cell is directly proportional to production of electrical current [24]. There may be an additional benefit to rerunning the test under similar conditions but introducing cell size in relation to wavelength implications would be interesting to evaluate. In addition, the Yurong study indicated very strong evidence to support that higher growth temperatures in the epitaxy process and altering the chemical composition can yield higher electrical energy outputs under higher external temperatures [1, 57].

In conclusion, this dissertation is beneficial to the world of renewable energy for terrestrial solar energy applications, and for unmanned vehicle enhancements. Increasing solar cell efficiency through optimizing solar absorption during the limited window for solar exposure and increasing resiliencies to temperature while minimizing weight will allow for greater energy PV adaptation in multiple areas.

REFERENCES

- [1] N. J. Tro, “Periodic properties of the elements,” in *Chemistry: A molecular approach*, 1st ed. Upper Saddle River, NJ, USA: Prentice Hall, 2008, ch. 8, sec. 8, pp. 355-357.
- [2] AirfoilTools.com, *Airfoil plotter: NACA0024 airfoil*. Airfoil Tools Database, Jun. 2019. [Online]. Available: <http://airfoiltools.com/plotter/index?airfoil=naca0024-il>
- [3] AZO CleanTech, *Sustainability in the Aerospace Industry*, Jul. 2015. [Online]. Available: <http://www.azocleantech.com/article.aspx?ArticleID=565>
- [4] Y. Baghzouz, *Lecture 1: Photovoltaic devices*, University of Las Vegas, EE446/646, 2018. [Online]. Available: <http://www.egr.unlv.edu/~eebag/Photovoltaic%20Devices%20I.pdf>
- [5] M. Brizon, *Solar energy generation model for high altitude long endurance platforms*. M.S. thesis, Department of Physics, Royal Institute of Technology, Stockholm, SE, 2015.
- [6] S. Chandrasekaran, *Interface 4x4 matrix keypad with microcontroller*, Aug. 2013. [Online]. Available: <https://embedjournal.com/interface-4x4-matrix-keypad-with-microcontroller/>
- [7] S. S. Choi, and H. S. Lim, *Factors that affect cycle-life and possible degradation mechanisms of a Li-Ion cell based on LiCoO₂*, *Journal of Power Sources*, vol. 111, no. 1, pp. 133-136.
- [8] Circuit Basics, *Basics of the I2C communication protocol*, Circuitbasics.com. [Online]. Available: <http://www.circuitbasics.com/basics-of-the-i2c-communication-protocol/>
- [9] DroneBot Workshop, *Using big stepper motors with Arduino*, Aug. 2019. [Online]. Available: <https://dronebotworkshop.com/big-stepper-motors/>
- [10] O. Dupre, R. Vaillon, and M. A. Green, “Temperature coefficients of photovoltaic devices”, in *Thermal behavior of photovoltaic devices: Physics and engineering*, 1st ed., New York, NY, USA: Springer International Publishing, 2017, pp. 37-130.
- [11] D. Dusabe, J. Munda, and A. Jimoh, *Modelling of cloudless solar radiation for PV module performance analysis*, *Journal of Electrical Engineering*, vol. 60, no. 4, pp. 192-197, 2009.
- [12] C. Ebeling, “State dependent systems”, in *An introduction to reliability and maintainability engineering*, 2nd ed., Waveland Press: Long Grove, IL, USA: 2010, pp. 113-119.
- [13] A. El Hammoumi, S. Motahhir, A. Chalh, A. El Ghzizal, and A. Derouich, *Low-cost virtual instrumentation of PV panel characteristics using excel and Arduino in comparison with traditional instrumentation*, *Renewables: Wind, Water and Solar*, vol. 5, no. 3, Mar. 2018, doi: <https://doi.org/10.1186/s40807-018-0049-0>
- [14] K. Emery, D. Myers, and S. Rummel, *Solar simulation – Problems and solutions*, 20th IEEE PV Specialists Conference, vol. 1087, 1988.
- [15] Federal Aviation Administration, “Aircraft performance: Atmospheric pressure”, in *FAA Handbook of Aeronautical Knowledge*, 2015. [Online]. Available: https://catsr.vse.gmu.edu/SYST460/FAAHandBookAero_Chap10_AircraftPerformance_Atmosphere.pdf

- [16] Georgia State University HyperPhysics, *Physics: Light and vision*, 2016. [Online]. Available: <http://hyperphysics.phy-astr.gsu.edu/hbase/vision/efficacy.html>
- [17] E. T. Hashim and A. A. Abbood, *Temperature Effect on Power Drop of Different Photovoltaic Modules*, *Journal of Engineering*, vol. 22, no. 5, pp. 129-143, May 2016.
- [18] D. Hart, "Power computations", in *Power Electronics*, 1st ed., New York, NY, USA: McGraw Hill, 2011, ch. 4, pp. 67-100.
- [19] P. E. Hausgen and B. Carpenter, *Value of solar array technology advancement*, *Journal of Spacecraft and Rockets*, vol. 52, no. 5, pp. 1388-1394, Oct. 2015, doi:10.2514/1.A33324
- [20] A. Hjort and M. Holmberg, *FREIA report 2015/4: Measuring mechanical vibrations using an Arduino as a slave I/O to an EPICS control system*, Department of Physics and Astronomy, Uppsala University, Uppsala, SE, Jun. 2015. [Online]. Available: <https://www.diva-portal.org/smash/get/diva2:839696/FULLTEXT01.pdf>
- [21] R. Hoheisel, F. Dimroth, A. W. Bett, S. R. Messenger, P. P. Jenkins, and R. J. Walters, *Electroluminescence analysis of irradiated GaInP/GaInAs/Ge space solar cells*, *Solar Energy Materials and Solar Cells*, no. 108, pp. 235-240, Jan. 2013, doi: 10.1016/2012.06.015.
- [22] How To Mechatronics, *Control high voltage devices: An Arduino relay tutorial*, 2018. [Online]. Available: <https://howtomechatronics.com/tutorials/arduino/control-high-voltage-devices-arduino-relay-tutorial/>
- [23] P. A. Iles, *Evolution of space solar cells*, *Solar Energy Materials and Solar Cells*, vol. 68, no. 1, pp. 1-13, 2001, doi:10.1016/S0927-0248(00)00341.
- [24] M. S. Imamura and B. H. Khoshaim, *A New Approach to Optimum Sizing and In-Orbit Utilization of Spacecraft Photovoltaic Power Systems*, *Acta Astronautica*, vol. 15, no. 12, pp. 1019-1028, ISSN 0094-5765, Feb. 2003, doi: 10.1016/0094-5765(87)90027-0. [Online]. Available: <http://www.sciencedirect.com/science/article/pii/0094576587900270>
- [25] International Organization for Standardization, "ISO 9288:1989: Thermal insulation, Heat transfer by radiation: Physical quantities and definitions", ISO, USA, Rep. 9288, 1989. [Online]. Available: <https://www.iso.org/standard/16943.html>
- [26] K. Jager, O. Isabella, A. H. Smets, R. van Swaaij, R. and M. Zeman, "Chapter 9: Solar cell parameters and equivalent circuit", in *Solar Energy*, 1st ed., Delft University of Technology, Stockholm, SE: pp. 101-109, 2014.
- [27] B. Jamil and M. M. Khan, *Estimation of clear-sky radiation using ASHRAE model for Aligarh, India*, *International Journal of Engineering Research and Technology*, vol. 7, no. 3, pp. 227-236, 2014.
- [28] G. M. Masters, "Chapter 8: Photovoltaic materials and characteristics", in *Renewable and Efficient Electric Power Systems*, 3rd ed., New York, NY, USA: Wiley & Sons, 2014.
- [29] M. Kalloniatis and C. Luu, "Psychophysics of vision", in *Measurement of Light*, 2018. [Online]. Available: <http://retina.umh.es/webvision/psych1.html>
- [30] H. K. Kim and C. Y. Han, *Analytical and numerical approaches of a solar array thermal analysis in a low-earth orbit satellite*, *Advances in Space Research*, vol. 46, no. 11, pp. 1427-1439, Aug. 2010, doi: 10.1016/j.asr.2010.08.023

- [31] M. N. Kumar, H. S. Saini, K. S. Anjaneyulu, and K. Singh, *Solar power analysis based on light intensity*, The International Journal of Engineering and Science, vol. 1, no. 2, pp. 1-5, 2014.
- [32] Lapis Semiconductor, *ML8511 UV sensor with voltage output*, Mar. 2013. [Online]. Available: https://cdn.sparkfun.com/datasheets/Sensors/LightImaging/ML8511_3-8-13.pdf
- [33] P. D. Leedy and J. E. Ormrod, *Practical Research Planning and Design*, 11th ed., Boston, MA, USA: Pearson Education Inc., 2016.
- [34] Lucky Light Electronics, *1.10mm height 1206 package hyper red chip LED technical data sheet*, Dec. 2005. [Online]. Available: <https://cdn-shop.adafruit.com/datasheets/LL-S150VC-V1-2B.pdf>
- [35] S. M. Lurwan, N. Mariun, H. Hizam, M. A. M. Radzi and A. Zakaria, *Predicting power output of photovoltaic systems with solar radiation model*, IEEE International Conference for Power and Energy, pp. 304-308, 2014.
- [36] G. M. Masters, "Chapter 7: The solar resource", in *Renewable and Efficient Electric Power Systems*, 3rd ed., New York, NY, USA: Wiley & Sons, 2014.
- [37] L. Ming, W. Rong, Y. Kui and Y. Tiancheng, *Photoluminescence analysis of electron irradiation-induced defect in GaAs/Ge space solar cells*, Nuclear Instruments and Methods in Physics Research, vol. 312, pp. 137-140, Oct. 2013, doi: 10.1016/2013.07.006
- [38] N. Miyashita, N. Ahsan and Y. Okada, *Generation and collection of photocarriers in dilute nitride GaInNAsSb solar cells*, Progress in Photovoltaics: Research and Applications, vol. 24, pp. 28-37, Jun. 2015, doi: 10.1002/pip.2641
- [39] M. Muselli, P. Poggi, G. Notton and A. Louche, *Improved Procedure for Stand-Alone Photovoltaic Systems Sizing using METEOSAT Satellite Images*, Solar Energy, vol. 62, no. 6, pp. 429-444, Mar. 1997, doi: 10.1016/S0038-092X(98)00030-9.
- [40] M. Myers, D. Wolford, D. Snyder and M. Piszczor, *ER-2 high altitude solar cell calibration flights*, 2015 IEEE 42nd Photovoltaic Specialist Conference, New Orleans, LA, USA, Paper no. 15664201, Jun. 2015.
- [41] National Renewable Energy Laboratory, *Measurement and instrumentation data center solar radiation historical data*, 2019. [Online]. Available: <https://midcdmz.nrel.gov/apps/sitehome.pl?site=BMS>
- [42] National Renewable Energy Laboratory, *National solar radiation database: Archives*, 2019. [Online]. Available: <https://nsrdb.nrel.gov/>
- [43] OpenSCAD Technologies, *OpenSCAD databases: Airfoils*, 2019. [Online]. Available: http://spolearninglab.com/curriculum/lessonPlans/hacking/resources/software/3d/openscad/openscad_databases.html
- [44] Operations Technology, Inc., *Webinar: Design, analyze & operate photovoltaic power systems with ETAP*, Irvine, CA, USA, Nov. 2018.
- [45] C. Riordan and R. Hulstron, *What is an air mass 1.5 spectrum*, Photovoltaic Specialists Conference, Kissimmee, FL, May 1990, doi: 10.1109/PVSC.1990.111784

- [46] R. Paschotta, “Band gap energy”, in *RP Photonics Encyclopedia*, 2019. [Online]. Available: https://www.rp-photonics.com/band_gap.html
- [47] A. D. Ryer, “Measurement geometries”, in *Light Measurement Handbook*. Newburyport, MA, USA: International Light, Inc., 1997. [Online]. Available: <http://apps.usd.edu/coglab/schieber/pdf/handbook.pdf>
- [48] A. Sehti and G. Gyaneshwaran, *Extended essay: Efficiency and spectral response analysis of solar panel for different incident frequencies*, Dec. 2016. [Online]. Available: https://www.academia.edu/31143248/Efficiency_and_spectral_response_analysis_of_solar_panel_for_different_incident_frequencies
- [49] M. Shuttleworth, (2009, June 14). *Reproducibility*, Jun. 2009. [Online]. Available: <https://explorable.com/reproducibility>
- [50] K. Soga and H. Akasaka, *Influences of solar incident angle on power generation efficiency of PV modules under field conditions*, *Journal of Asian Architecture and Building Engineering*, vol. 2, no. 2, pp. 43-48, Nov. 2003.
- [51] H. Y. Tada, J. R. Carter, B. E. Anspaugh and R. G. Downing, R. G., *JPL publications 82-69: Solar cell radiation handbook*, 3rd ed., Jet Propulsion Laboratory, Pasadena, CA, USA: National Aeronautics and Space Administration, 1982.
- [52] University of Toledo, “Fundamental properties of solar cells”, in *Principles and Varieties of Solar Energy*, 2012. [Online]. Available: http://astro1.panet.utoledo.edu/~relling2/teach/archives/6980.4400.2012/20120131_PHYS_6980_4400_FundamentalProperties.pdf
- [53] US Department of Health and Human Services, *Office for Human Research Protections: Federal Policy for the Protection of Human Subjects ('Common Rule')*, Mar. 2016. [Online]. Available: <https://www.hhs.gov/ohrp/regulations-and-policy/regulations/common-rule/index.html>
- [54] J. Valdez and J. Becker, (2015). *Understanding the I2C bus*, Texas Instruments Application Rep. SLVA704, 2015. [Online]. Available: <http://www.ti.com/lit/an/slva704/slva704.pdf>
- [55] F. M. Vanek, L. D. Albright and L. T. Angenent, (2016). “Chapter 9: The solar resource”, in *Energy Systems Engineering*, 3rd ed., McGraw-Hill, ch. 9, pp. 293-319, 2016.
- [56] H. F. Wang, G. Z. Xing, X. Y. Wang, L. L. Zhang, L. Zhang and S. Li, *Chemically strengthened protection glasses for the applications of space solar cells*, *American Institute of Physics*, vol. 4, no. 4, pp. 1-7, Jan. 3, 2014, doi: 10.1063/1.4873538
- [57] N. L. Yurong, K. H. Tan, W. K. Loke, S. Wicaksono, D. Li, S. F. Yoon, P. Sharma, T. Milakovich, M. T. Bulsara and E. A. Fitzgerald, *Performance of 1 eV GaNAsSb-based photovoltaic cell on Si substrate at Different Growth Temperatures*, *Prog. Photovolt: Res. Appl.*, vol. 25, pp. 327–332, Feb. 2017, doi: 10.1002/pip.2870.
- [58] S. Zhang, S. Lin, X. Li, X. Liu, H. Wu, P. Wang, Z. Wu, H. Zhong, H. Xu, and Z. Xu, *Opening the band gap of graphene through silicon doping for improved performance of graphene/GaAs heterojunction solar cells*. College of Information Science and Electronic Engineering, Zhejiang University, Hangzhou, CN, Jul. 2015, doi: 10.1039/c5nr06345k

- [59] M. Zohrabi, *Mixed method research: instruments, validity, reliability and reporting findings*, Theory and Practice in Language Studies, vol. 3, no. 2, pp. 254-262, Feb. 2013, doi:10.4304/tpls.3.2.254-262
- [60] Texas Advanced Optoelectric Solutions, “TSL-2560/TSL2561 light-to-digital converter datasheet”, TAOS, Plano, TX, USA, Rep. TAOS059N, Mar. 2009. [Online]. Available: <https://cdn-shop.adafruit.com/datasheets/TSL2561.pdf>
- [61] K. Sudhakar, J. Noopur and B. Shivani, *Effect of Color Filter on the Performance of Solar Photovoltaic Module*. 2013 International Conference on Power, Energy and Control, pp. 35-38, 2013, doi: 10.1109/PVSC.1990.111784.
- [62] Adafruit Industries, “INA139/INA169 High-Side measurement current shunt monitor datasheet”, Rep. SBOS181D, Texas Instruments, Dallas, TX, USA, Nov. 2005. [Online]. Available: <https://cdn-shop.adafruit.com/datasheets/ina169.pdf>
- [63] Adafruit Industries, “INA219 zero-drift, bi-directional current/power monitor with i2c interface datasheet”, Rep. SBOS448F, Texas Instruments, Dallas, TX, USA, Sep. 2011. [Online]. Available: <https://cdn-shop.adafruit.com/datasheets/ina219.pdf>
- [64] Adafruit Industries, “TMP007 Infrared Thermopile Sensor with Integrated Math Engine datasheet”, Rep. SBOS685B, Texas Instruments, Dallas, TX, USA, May 2014. [Online]. Available: <https://cdn-shop.adafruit.com/datasheets/tmp007.pdf>
- [65] Adafruit Industries, “BMP280 digital pressure sensor datasheet”, Rep. BST-BMP280-DS001-11, Bosch Sensortec, Gerlingen, DE, May 2015. [Online]. Available: <https://cdn-shop.adafruit.com/datasheets/BST-BMP280-DS001-11.pdf>
- [66] Adafruit Industries, “Digital-output relative humidity & temperature sensor/module AM2303 datasheet”, Aosong Guangzhou Electronics Co., Baiyun District, Guangzhou, CN, 2016. [Online]. Available: <https://cdn-shop.adafruit.com/datasheets/DHT22.pdf>
- [67] AMS Electronics, “TSL2591 light-to-digital converter datasheet”, AMS, Premstaetten, AT, Rep. v2-04, Jun. 2018. [Online]. Available: https://cdn-learn.adafruit.com/assets/assets/000/078/658/original/TSL2591_DS000338_6-00.pdf?1564168468
- [68] Adafruit Industries, “Adafruit VL53L0X Time of Flight Micro-LIDAR Distance Sensor Breakout”, Nov. 2016. [Online]. Available: <https://learn.adafruit.com/adafruit-vl53l0x-micro-lidar-distance-sensor-breakout/downloads>
- [69] ST Microelectronics, “VL53L0X: World smallest Time-of-Flight ranging and gesture detection sensor”, Rep. DocID029104 Rev 1, May 2016. [Online]. Available: <https://www.st.com/resource/en/datasheet/vl53l0x.pdf>
- [70] Adafruit Industries, “Adafruit VEML6075 UVA UVB and UV Index Sensor Breakout”, 2018. [Online]. Available: <https://www.adafruit.com/product/3964#technical-details>
- [71] Wingoneer Electronics, “WINGONEER SW-420 NC Type Vibration Sensor Module Vibration Switch for Arduino Smart Car”, 2018. [Online]. Available: https://www.amazon.com/gp/product/B06XHFFPL6/ref=ppx_yo_dt_b_asin_title_o04_s01?ie=UTF8&psc=1

- [72] HiLetgo Electronics, “GY-521 MPU-6050 MPU6050 3 Axis Accelerometer Gyroscope Module 6 DOF 6-axis Accelerometer Gyroscope Sensor Module 16 Bit AD Converter Data Output IIC I2C for Arduino”, 2019. [Online]. Available: <https://www.amazon.com/HiLetgo-MPU-6050-Accelerometer-Gyroscope-Converter/dp/B01DK83ZYQ>
- [73] Adafruit Industries, “Adafruit assembled data logging shield for Arduino”, 2019. [Online]. Available: <https://www.adafruit.com/product/1141#technical-details>
- [74] Adafruit Industries, “1.10mm height 1206 package hyper red chip LED technical data sheet”, Rep. LL-S150VC-V1-2B, Lucky Light Electronics Co., Dec. 2005. [Online]. Available: <https://cdn-shop.adafruit.com/datasheets/LL-S150VC-V1-2B.pdf>
- [75] Adafruit Industries, “1.10mm height 1206 package pure green chip LED technical data sheet”, Rep. S150PGC-G5-1B, Lucky Light Electronics Co., Jul. 2006. [Online]. Available: <https://cdn-shop.adafruit.com/datasheets/S150PGC-G5-1B.pdf>
- [76] Adafruit Industries, “1.10mm height 1206 package blue chip LED technical data sheet”, Rep. LL-S150BC-B4-1B, Lucky Light Electronics Co., May 2006. [Online]. Available: <https://cdn-shop.adafruit.com/datasheets/LL-S150BC-B4-1B.pdf>
- [77] Adafruit Industries, “1.10mm height 1206 package white chip LED technical data sheet”, Rep. LL-S150W-W2-1C, Lucky Light Electronics Co., Dec. 2005. [Online]. Available: <https://cdn-shop.adafruit.com/datasheets/LL-S150W-W2-1C.pdf>
- [78] Adafruit Industries, “Technical data sheet 5mm infrared LED, T-1 3/4”, Rep. DIR-033-004, Everlight Electronics, Tucheng, Taipei, Taiwan, Jul. 2005. [Online]. Available: https://cdn-shop.adafruit.com/datasheets/IR333_A_datasheet.pdf
- [79] SparkFun Electronics, “Model No.: YSL-R547P4C-E3: 5mm UV LED 365nm data sheet”, Rep. 518109, Longhua Town, Shenzhen, CN, 2019. [Online]. Available: <https://www.sparkfun.com/datasheets/Components/LED/YSL-R547P4C-E3.pdf>
- [80] Adafruit Industries, “Laser diode: 5mw 650nm Red”, 2018. [Online]. Available: <https://www.adafruit.com/product/1054#technical-details>
- [81] SparkFun Electronics, “A3967 microstepping driver with translator”, Allegro Microsystems, LLC, Worcester, MA, USA, Rep. 26184.24H, 2013. [Online]. Available: <https://cdn.sparkfun.com/datasheets/Robotics/A3967-Datasheet.pdf>
- [82] SONGLE Electronics, “Serial relay driver data sheet”, Rep. ISO9002, 2015. [Online]. Available: <https://www.circuitbasics.com/wp-content/uploads/2015/11/SRD-05VDC-SL-C-Datasheet.pdf>
- [83] Arduino Electronics, “Arduino Uno Rev3”, 2018. [Online]. Available: <https://store.arduino.cc/usa/arduino-uno-rev3>
- [84] Adafruit Industries, “Adafruit Metro Mini 328 - Arduino-Compatible - 5V 16MHz”, 2018. [Online]. Available: <https://www.adafruit.com/product/2590#technical-details>
- [85] Adafruit Industries, “Adafruit METRO 328 - Arduino Compatible - with Headers - ATmega328”, 2016. [Online]. Available: <https://www.adafruit.com/product/2488#technical-details>

- [86] Stepper Online, “Nema 17 Bipolar 59Ncm (84oz.in) 2A 42x48mm 4 Wires w/ 1m Cable & Connector”, 2016. [Online]. Available: <https://www.omc-stepperonline.com/nema-17-bipolar-59ncm-84oz-in-2a-42x48mm-4-wires-w-1m-cable-and-connector.html>
- [87] Adafruit Industries, “Small 6V/1W solar panel – silver”, 2019. [Online]. Available: <https://www.adafruit.com/product/3809#technical-details>
- [88] Sundance Solar, “Powerfilm 3V 50mA flexible solar panel MP3-37”, 2020. [Online]. Available: <https://store.sundancesolar.com/powerfilm-3v-50ma-flexible-solar-panel-mp3-37/>
- [89] MCIGICM Electronics, “MCIGICM 10k Potentiometer knob Linear Potentiometer WH148 3Pin 15mm Shaft with Nut and Washer”, 2018. [Online]. Available: <https://www.amazon.com/gp/product/B07CZXS1R>
- [90] CenryKay Electronics, “CenryKay DC-DC Buck Boost Converter Display 5V-30V to 0.5 – 30V 3A LCD Digital Voltmeter Ammeter Adjustable Boost Drop (Buck Boost Converter)”, 2019. [Online]. Available: <https://www.amazon.com/gp/product/B07RTY3TFH>
- [91] Makom Industries, “Makom 12U Wall Mount Network Equipment Server Data Cabinet Enclosure Wallmount Rack Glass Door Locking with Keys (Black)”, 2019. [Online]. Available: <https://www.amazon.com/gp/product/B0775LK7RN>
- [92] JG Maker, “JGMAKER 3D Printer A5S DIY Kit Aluminum Color Touch Screen Upgrade Desktop 3D Printing Machine PLA Filament Large Build Size 305x305x320mm”, 2019. [Online]. Available: <https://www.amazon.com/gp/product/B07PMNCNFS>
- [93] Bayite Thermal, “DC 12V Fahrenheit Digital Temperature Controller 10A 1 Relay with Sensor”, 2018. [Online]. Available: <https://www.amazon.com/gp/product/B011VGAPOC>
- [94] Icstation Thermal Technologies, “Icstation 24V 30W Flexible Polyimide Heater Plate Adhesive PI Heating Film 45mmx100mm”, 2019. [Online]. Available: <https://www.amazon.com/gp/product/B074SXKPZL>
- [95] Ardest Electronics, “1602 LCD 2004 20x4 i2c LCD Display Adapter IIC//TWI/SPI/I2C Serial Interface Module Shield for Arduino UNO R3 MEGA2560”, 2017. [Online]. Available: <https://www.amazon.com/gp/product/B07D3YPK3H>
- [96] Hitachi Electronics, “HD44780U (LCD-II): Dot Matrix Liquid Crystal Display Controller/Driver”, Rep. ADE-207-272(Z), HE Co., Tokyo, Japan, 2018. [Online]. Available: <https://cdn-shop.adafruit.com/datasheets/HD44780.pdf>
- [97] Riorand Electronics, “LCD Module For Arduino 20 X 4, White On Blue”, 2018. [Online]. Available: <http://www.riorand.com/riorandtm-lcd-module-for-arduino-20-x-4-white-on-blue.html>
- [98] Adafruit Industries, “Adafruit VL6180X Time of Flight Micro-LIDAR Distance Sensor Breakout”, 2016. [Online]. Available: <https://learn.adafruit.com/adafruit-vl6180x-time-of-flight-micro-lidar-distance-sensor-breakout>
- [99] KNACRO Electronics, “KNACRO GY-ML8511 UV sensor module Photodiode sensitive to UV-A and UV-B Embedded operational amplifier”, 2018. [Online]. Available: <https://www.amazon.com/KNACRO-GY-ML8511-Photodiode-sensitive-operational/dp/B07KZLRBL2/>

- [100] Roithner Laser Technik, “GUVA-S12SD Technical data UV sensor”, Vienna, Austria, Jul. 2011. [Online]. Available: <https://cdn-shop.adafruit.com/datasheets/1918guva.pdf>
- [101] Uxcell Electronics, “4x4 16 Key Matrix Membrane Switch Keypad Keyboard 76x69x0.8mm”, 2018. [Online]. Available: <https://www.amazon.com/gp/product/B0087ZEGUA>
- [102] F. M. Vanek, L. D. Albright and L. T. Angenent, (2016). “Chapter 10: Solar photovoltaic technologies”, in *Energy Systems Engineering*, 3rd ed., New York, NY, USA: McGraw-Hill, ch. 10, pp. 321-364, 2016.

APPENDIX A

Blackbody Radiation Simulator (BRRS) Master Equipment List (MEL)

Date	Item	Cost	Project Type	Notes	Vendor	Order Number
24-Sep-18	UXCELL Axial lead 1% tolerance metal film resistors 0.1 Ohms	\$6.08	Blackbody Radiation Simulator (BRRS)		Amazon	113-7306189-854906
24-Sep-18	MakeFocus Guard Stepper Motor Model#28VJ-48 with ULN2003 Stepper Drivers	\$10.99	Blackbody Radiation Simulator (BRRS)		Amazon	113-7306189-854906
25-Sep-18	ThermATronics BC10 Solder Tip cleaning wire	\$7.95	Blackbody Radiation Simulator (BRRS)		Amazon	113-0279145-512702
25-Sep-18	Soldering Iron Tip, Model# 990M-T-B	\$10.99	Blackbody Radiation Simulator (BRRS)		Amazon	113-0279145-512702
25-Sep-18	Tin Lead Resin Core Solder wire Model# WYCTIN 60-40	\$7.59	Blackbody Radiation Simulator (BRRS)		Amazon	113-0279145-512702
27-Sep-18	Micro XH Connectors for harnessing	\$8.99	Blackbody Radiation Simulator (BRRS)		Amazon	113-3140982-9817016
30-Sep-18	NEMA 17 Bipolar 2A Stepper Motor	\$13.99	Blackbody Radiation Simulator (BRRS)		Amazon	113-08011402-6635447
30-Sep-18	Ogura Plastic Dnsuprom Junction Box Model# IP65	\$12.99	Blackbody Radiation Simulator (BRRS)		Amazon	113-08011402-6635447
30-Sep-18	WINOMO NEMA 17 Stepper Motor Mounting Brackets	\$8.29	Blackbody Radiation Simulator (BRRS)		Amazon	113-1163360-9886625
3-Oct-18	inSharePlus 12V LED Strip Power Supply 2A	\$7.79	Blackbody Radiation Simulator (BRRS)		Amazon	113-4125826-6765834
3-Oct-18	MagickShell 5mm Flange Shaft coupling for stepper motor	\$10.99	Blackbody Radiation Simulator (BRRS)	Pack of 2	Amazon	113-2084008-5454555
3-Oct-18	KNACRO Stepstick Stepper Motor Driver Module, Model# A4988	\$6.80	Blackbody Radiation Simulator (BRRS)		Amazon	111-1247867-979787
5-Oct-18	Male and Female Pin Prototyping Headers for Electronic Circuit Boards	\$8.99	Blackbody Radiation Simulator (BRRS)	Pack of 60	Amazon	113-0761444-1354602
5-Oct-18	Adafruit Metro Mini 328-SV 16 MHz Microcontroller	\$13.29	Blackbody Radiation Simulator (BRRS)		Amazon	113-0761444-1354602
5-Oct-18	Adafruit Metro Mini 328-SV 16 MHz Microcontroller	\$13.29	Blackbody Radiation Simulator (BRRS)		Amazon	113-0761444-1354602
5-Oct-18	RioRand LCD Display Module	\$7.99	Blackbody Radiation Simulator (BRRS)		Amazon	113-0761444-1354602
11-Oct-18	ELEGOO Stepstick Stepper Motor Driver, Model# A4988	\$9.99	Blackbody Radiation Simulator (BRRS)	Pack of 5	Amazon	113-7448965-4605014
13-Oct-18	Adafruit Contactless Infrared Thermopile Sensor, Model# TMP007	\$14.99	Blackbody Radiation Simulator (BRRS)	\$1.00 S&H	Amazon	113-7471085-773458
13-Oct-18	FBAPyIPA AC 6A 2 Solder Lug On/Off momentary switch	\$6.50	Blackbody Radiation Simulator (BRRS)	Pack of 15	Amazon	113-4549579-9762652
13-Oct-18	Adafruit Analog Light Sensor ALS-PT19, Model# ADA2748	\$6.99	Blackbody Radiation Simulator (BRRS)		Amazon	113-4549579-9762652
13-Oct-18	Adafruit Time of Flight Distance Laser Measurement Circuit, Model# VL53L0X	\$18.07	Blackbody Radiation Simulator (BRRS)		Amazon	113-4509992-9749844
13-Oct-18	R-Tech 12V DC 1A Power Supply Adapter for Stepper Motor Power	\$12.85	Blackbody Radiation Simulator (BRRS)		Amazon	113-2673770-6292313
13-Oct-18	GrFun EasyDriver Shield Motor Driver V4L, Model# A3967	\$5.98	Blackbody Radiation Simulator (BRRS)		Amazon	111-4372747-7989656
18-Oct-18	4x4 16-Key Matrix Membrane Switch keypad	\$13.46	Blackbody Radiation Simulator (BRRS)		Amazon	113-2591164-2615444
27-Oct-18	Esupport 12mm Black Round Toggle Switch	\$7.29	Blackbody Radiation Simulator (BRRS)	Pack of 10	Amazon	113-6867984-3430224
27-Oct-18	Esupport 12mm Red Round Toggle Switch	\$7.29	Blackbody Radiation Simulator (BRRS)	Pack of 10	Amazon	113-6867984-3430224
27-Oct-18	Heat shrink tubing for electrical wire soldering and insulation	\$7.99	Blackbody Radiation Simulator (BRRS)	Variety pack of 532 pieces	Amazon	113-6867984-3430224
27-Oct-18	Eloho Plastic Waterproof Electrical Junction Boxes	\$12.69	Blackbody Radiation Simulator (BRRS)	Pack of 10	Amazon	113-6867984-3430224
27-Oct-18	Adafruit LED Sequencer (White), Model# ADA1757	\$7.47	Blackbody Radiation Simulator (BRRS)	Pack of 5	Amazon	113-0964608-5338189
29-Oct-18	KNACRO GY-ML8511 Ultraviolet sensor Photodiode	\$12.96	Blackbody Radiation Simulator (BRRS)		Amazon	113-3421580-1179077
31-Oct-18	KY-039 IR Measurement Device	\$4.61	Blackbody Radiation Simulator (BRRS)	Pre-corporation expenses	Ebay	26371433771
31-Oct-18	Adafruit 5mm Infrared LED	\$11.07	Blackbody Radiation Simulator (BRRS)	Pack of 25	Amazon	113-7638106-4799037
31-Oct-18	TOOGOO Ultraviolet LED, 20A, 5mm	\$5.82	Blackbody Radiation Simulator (BRRS)	Pack of 6	Amazon	113-6697232-4338189
31-Oct-18	Adafruit Contactless Infrared Thermopile Sensor, Model# TMP007	\$19.43	Blackbody Radiation Simulator (BRRS)		Amazon	113-0819266-6744233
1-Nov-18	Hammond ABS Plastic Electronics Project Box, Model# 1591ESBK	\$7.99	Blackbody Radiation Simulator (BRRS)		Amazon	113-8451324-3104219
3-Nov-18	Adafruit Digital Luminosity/Lux Light Sensor, Model# TSL2561	\$8.68	Blackbody Radiation Simulator (BRRS)		Amazon	113-5208282-8539416
3-Nov-18	KNACRO GY-2561 Luminosity Sensor, Model# TSL2561	\$5.50	Blackbody Radiation Simulator (BRRS)		Amazon	113-5208282-8539416
3-Nov-18	DC Power Female Pigtail connector 5-5mm	\$6.30	Blackbody Radiation Simulator (BRRS)	Pack of 10	Amazon	113-7319699-8337850
3-Nov-18	DC Power Female Jack Panel Mount 5mm	\$7.99	Blackbody Radiation Simulator (BRRS)	Pack of 20	Amazon	113-7319699-8337850
3-Nov-18	Uxcell 2 pin 3.5mm Screw Terminal Block for Printed Circuit Board	\$10.20	Blackbody Radiation Simulator (BRRS)	Pack of 50	Amazon	113-7319699-8337850
3-Nov-18	KNACRO GY-ML8511 Ultraviolet sensor Photodiode	\$12.96	Blackbody Radiation Simulator (BRRS)		Amazon	113-4235831-1511415
3-Nov-18	KeyesStudio GY-ML8511 UV Sensor Module	\$10.99	Blackbody Radiation Simulator (BRRS)		Amazon	113-3405395-1419463
3-Nov-18	Adafruit Metro Mini 328-SV 16 MHz Microcontroller	\$13.38	Blackbody Radiation Simulator (BRRS)		Amazon	113-0161034-8829834
20-Nov-18	Sunfounder 16-channel 12-bit PWM Servo Motor Driver, Model# PCA9685	\$11.99	Blackbody Radiation Simulator (BRRS)		Amazon	113-0161034-8829834
4-Dec-18	Geat Mini Laser Diode, 650nm, 6mm 5mW	\$6.29	Blackbody Radiation Simulator (BRRS)	Pack of 10	Amazon	113-5333907-3835442
13-Dec-18	Power Electronics (1st Ed.)	\$10.20	Blackbody Radiation Simulator (BRRS)	Used for electrical circuit modeling/PSPICE examples	Amazon	113-4820687-9876234
20-Dec-18	An Introduction to Reliability and Maintainability Engineering (with modeling software)	\$105.45	Blackbody Radiation Simulator (BRRS)	Purchased for reliability modeling software	Amazon	113-4820687-9876234
17-Jan-19	Aluminum housing for MOSFET integrated circuit (100mm x 25mm x 10mm)	\$8.99	Blackbody Radiation Simulator (BRRS)		Amazon	113-8769580-6476230
17-Jan-19	Aluminum housing for integrated circuits (50mm x 50mm x 20mm)	\$10.99	Blackbody Radiation Simulator (BRRS)	Pack of 4	Amazon	113-8769580-6476230
3-Feb-19	650nm Red 5mW Laser Diode Module	\$6.99	Blackbody Radiation Simulator (BRRS)	Pack of 2	Amazon	113-3985296-2609827
3-Feb-19	532nm Green 5mW Laser Diode Module	\$12.89	Blackbody Radiation Simulator (BRRS)		Amazon	113-3985296-2609827
3-Feb-19	405nm Violet/Blue 5mW Laser Diode Module	\$8.99	Blackbody Radiation Simulator (BRRS)		Amazon	113-3985296-2609827
4-Mar-19	Statistical Models in Engineering, Hahn & Shapiro, 1967	\$7.73	Blackbody Radiation Simulator (BRRS)		Ebay	263661922013
12-Mar-19	Thermal Behavior of Photovoltaic Devices: Physics and Engineering	\$63.49	Blackbody Radiation Simulator (BRRS)	Pre-corporation expenses	Amazon	111-1405609-0847400
16-Mar-19	Powerflex 3V 50mA Flexible Solar Panel, Model# MP3-17	\$14.95	Blackbody Radiation Simulator (BRRS)	Pack of 2, \$3.81 USD S&H	Amazon	113-4485499-1138623
16-Mar-19	UCTRONICS 0.96 inch OLED Module 128x64, Model# SSD1306	\$6.99	Blackbody Radiation Simulator (BRRS)		Amazon	113-4256495-1546663
16-Mar-19	GrFun EasyDriver Shield Motor Driver V4L, Model# A3967	\$5.98	Blackbody Radiation Simulator (BRRS)		Amazon	113-7821209-3519416
16-Mar-19	NEMA 17 Bipolar 2A Stepper Motor	\$13.99	Blackbody Radiation Simulator (BRRS)		Amazon	113-7821209-3519416
16-Mar-19	MagickShell 5mm Flange Shaft coupling for stepper motor	\$10.99	Blackbody Radiation Simulator (BRRS)	Pack of 2	Amazon	113-7821209-3519416
16-Mar-19	High current Stepper Motor Driver Carrier, Model# DRV8825	\$13.83	Blackbody Radiation Simulator (BRRS)		Amazon	113-7821209-3519416
19-Mar-19	Adafruit Contactless Infrared Thermopile Sensor, Model# TMP007	\$19.41	Blackbody Radiation Simulator (BRRS)		Amazon	113-3872290-3728265
19-Mar-19	Adafruit Assembled Data Logging Shield	\$14.25	Blackbody Radiation Simulator (BRRS)		Amazon	113-7851712-6776256
19-Mar-19	Energyzer CR 1220 3V Lithium Batteries for SD shield	\$5.49	Blackbody Radiation Simulator (BRRS)	Pack of 4	Amazon	113-7851712-6776256
14-Apr-19	SenMod Micro SD Card SDHC TF Card Adapter Bracket board	\$8.29	Blackbody Radiation Simulator (BRRS)	Pack of 5	Amazon	113-4073568-9141056
29-Jun-19	10N6 TO-220 10A 60V G Channel Power Metal Oxide Semiconductor Field Effect Transistor (MOSFET)	\$7.99	Blackbody Radiation Simulator (BRRS)	Pack of 5	Amazon	113-1010161-6918625
29-Jun-19	Uxcell Current Current Axial Lead 5W 1 Ohm Power Resistor, Model# 105-100K0852	\$7.95	Blackbody Radiation Simulator (BRRS)	Pack of 15	Amazon	113-1010161-6918625
29-Jun-19	EZOKEE 0.96" DC BC 12864 128x64 OLED LCD Display Shield Board Module SSD1306	\$14.99	Blackbody Radiation Simulator (BRRS)	Pack of 3	Amazon	113-1010161-6918625
10-Jul-19	100 Ohm 2M Ohm Variable Resistor Trimmer Potentiometer Assorted Kit	\$9.99	Blackbody Radiation Simulator (BRRS)	Pack of 150 for 15 different values	Amazon	113-5629964-7987836
10-Jul-19	Adafruit USB Micro-B Breakout Board (ADA1813)	\$4.74	Blackbody Radiation Simulator (BRRS)		Amazon	113-9185041-7469069
10-Jul-19	Adafruit USB Micro-B Breakout Board (ADA1813)	\$4.74	Blackbody Radiation Simulator (BRRS)		Amazon	113-9185041-7469069
10-Jul-19	HOODDEAL Photo Light Sensitive Resistor Photoresistor Opotensistor 5mm CDS GM5516 5528 GL5639 5537 5539 5549	\$5.99	Blackbody Radiation Simulator (BRRS)	Pack of 20	Amazon	113-9185041-7469069
10-Jul-19	Dymall Voltage Sensor dc 0-25 V for Arduino with Code	\$5.99	Blackbody Radiation Simulator (BRRS)	Pack of 2	Amazon	113-9185041-7469069
12-Jul-19	X-Tronic Model #3020-XTS Digital Display Soldering Iron Station	\$59.80	Blackbody Radiation Simulator (BRRS)	Old soldering station broke, needed new one	Amazon	113-0234348-3821857
12-Jul-19	Adafruit VEM-L675 (VIA UV) Infrared Sensor (Breakout)	\$13.36	Blackbody Radiation Simulator (BRRS)		Amazon	113-2529923-2592221
18-Jul-19	Makem JUI Server Data Cabinet Glass Door Locking with Key Enclosure Wall Mount Network Rack	\$60.97	Blackbody Radiation Simulator (BRRS)	Containment unit for BRRS	Amazon	113-1667378-1049034
19-Jul-19	Isolation 12V 7W Flexible Polyimide Heater Plate Adhesive PI Heating Film 25mmx50mm	\$12.50	Blackbody Radiation Simulator (BRRS)	Pack of 4	Amazon	113-1790546-7216226
19-Jul-19	HELGO W1209 12V DC Digital Temperature Controller Board Micro Digital Thermistor -50-110°C Electronic Temperature Temp Control Module Switch with I/OA One-channel Relay	\$7.49	Blackbody Radiation Simulator (BRRS)	Pack of 2	Amazon	113-4234886-1629855
19-Jul-19	Vtech 27mm Piezoelectric Discs with Leads (Trigger Acoustic Pickup)	\$6.99	Blackbody Radiation Simulator (BRRS)	Pack of 12	Amazon	113-0364594-3039450
26-Jul-19	Centra DC-DC Buck Boost Converter (5V-30V to 0.5 - 30V) 3A LCD Digital Voltmeter Ammeter	\$13.99	Blackbody Radiation Simulator (BRRS)	Variable load	Amazon	113-9604853-4057860
26-Jul-19	GY-521 MPY-6060 MP6050 Module 3-Axis Analog GYRO Sensor and 3-Axis Accelerometer Module	\$5.88	Blackbody Radiation Simulator (BRRS)	Vibration sensor	Amazon	113-2426819-5979408
15-Aug-19	FORMAKER ASS DYE Kit Aluminum PLA Filament 3D Printing Machine (105g,305x20mm)	\$399.00	Blackbody Radiation Simulator (BRRS)	Making enclosure and servo components for BRRS	Amazon	113-9749606-4292210
15-Aug-19	HATCHBOX PLA 3D Printer Filament, Dimensional Accuracy +/- 0.03 mm, 1 kg Spool, 1.75 mm, Black	\$19.99	Blackbody Radiation Simulator (BRRS)	3D printer filament	Amazon	113-9749606-4292210
15-Aug-19	AmononBasics 60W 10-Port Multi USB Wall Charger, Black	\$29.99	Blackbody Radiation Simulator (BRRS)	USB hub for multiple microcontroller power	Amazon	113-9749606-4292210
15-Aug-19	Adafruit Metro Mini 328-SV 16 MHz Microcontroller	\$18.48	Blackbody Radiation Simulator (BRRS)		Amazon	113-9749606-4292210
15-Aug-19	WayinTop 20x4 2004 LCD Display Module with DC Serial Interface Adapter	\$31.76	Blackbody Radiation Simulator (BRRS)		Amazon	113-9749606-4292210
16-Aug-19	High Torque Nema 23 CNC Stepper Motor 14mm 425oz-in/3Nm	\$36.99	Blackbody Radiation Simulator (BRRS)	Upgraded BAPCS motor	Amazon	113-7188156-8118629
16-Aug-19	ALITOVE AC 100-240V to DC 24V 5A Power Supply with 5.5x2.1mm DC Output Jack	\$17.99	Blackbody Radiation Simulator (BRRS)	Motor power supply	Amazon	113-7188156-8118629
16-Aug-19	MAR600 Stepper Motor Module Driver 18-30V for 2-Phase Stepper Motor	\$40.30	Blackbody Radiation Simulator (BRRS)	High torque motor driver	Ebay	02-037556-0429
17-Aug-19	TB6560 Single 1.6A 2A Stepper Motor Driver	\$8.98	Blackbody Radiation Simulator (BRRS)		Amazon	113-1881243-4762620
18-Aug-19	Nema 23 Stepper Motor Steel Mounting Bracket with Mounting Screws	\$11.99	Blackbody Radiation Simulator (BRRS)	NEMA 23 motor mounting bracket for BAPCS, set of 4	Amazon	113-4267937-5481839
18-Aug-19	Nema 23 CNC Stepper Motor 2.8A 178.5oz-in/126Nm	\$26.00	Blackbody Radiation Simulator (BRRS)	Secondary low profile motor for BAPCS	Amazon	113-4267937-5481839
30-Aug-19	Bayite 10A/12VDC Digital Temperature Controller Relay with Sensor	\$17.98	Blackbody Radiation Simulator (BRRS)		Amazon	113-7706558-9061844
31-Aug-19	ARCTIC MX-4 Carbon Based Thermal Compound Paste (10 oz)	\$7.67	Blackbody Radiation Simulator (BRRS)		Amazon	113-5698687-6453834
2-Sep-19	SunFounder Uno R3 Arduino ATMEGA328P Microcontroller Board	\$10.98	Blackbody Radiation Simulator (BRRS)		Amazon	113-2430837-0116262
2-Sep-19	Electronics Silicon Circuit Prototyping Board - Overlay for Arduino R3 board	\$14.00	Blackbody Radiation Simulator (BRRS)	Pack of 10	Amazon	113-2430837-0116262
2-Sep-19	Hitec 110pcs 6/8/10 Double Row 3-Pin 2.54mm Arduino Stackable Shield Header Assortment Kit	\$13.99	Blackbody Radiation Simulator (BRRS)	Pack of 110	Amazon	113-2430837-0116262
2-Sep-19	USB 2.0 Cable A-Male to B-Male Cable (3.3 Feet, 1 Meter)	\$7.99	Blackbody Radiation Simulator (BRRS)		Amazon	113-2430837-0116262
2-Sep-19	USB 2.0 Micro-USB Cable	\$6.99	Blackbody Radiation Simulator (BRRS)		Amazon	113-2430837-0116262
2-Sep-19	Isolation 12V 7W Flexible Polyimide Heater Plate Adhesive PI Heating Film 25mmx50mm	\$12.50	Blackbody Radiation Simulator (BRRS)	Pack of 4	Amazon	113-7807616-6747432
2-Sep-19	Isolation 24V 30W Flexible Polyimide Heater Plate Adhesive PI Heating Film 45mmx100mm	\$10.99	Blackbody Radiation Simulator (BRRS)	Pack of 4	Amazon	113-2502293-3555409
2-Sep-19	12V 0.10A Brushless DC Cooling Fan, Model# AV-F410MB, 40mm x 40mm x 10mm	\$12.98	Blackbody Radiation Simulator (BRRS)	Pack of 2	Amazon	113-9125250-5142640
2-Sep-19	ANSANE 16x2 1602 LCD Arduino Display Screen Blue + DC-Module Interface Adapter	\$9.99	Blackbody Radiation Simulator (BRRS)	Pack of 2	Amazon	113-0877283-0752566
1-Sep-19	BANTECHGO 30 Gauge Silicone Wire Spool Ultra Flexible High Temp 200 deg/C 600V 30 AWG Silicone Wire, 50 feet (Red)	\$7.98	Blackbody Radiation Simulator (BRRS)		Amazon	113-8329580-4637805
1-Sep-19	BANTECHGO 30 Gauge Silicone Wire Spool Ultra Flexible High Temp 200 deg/C 600V 30 AWG Silicone Wire, 50 feet (Black)	\$7.98	Blackbody Radiation Simulator (BRRS)		Amazon	113-8329580-4637805
18-Sep-19	5V USB LED Strip Light 5M SMD 3528 with 3M Tape for TV Computer Backlighting (5M 3528, Non-waterproof, Green)	\$39.98	Blackbody Radiation Simulator (BRRS)	Pack of 2	Amazon	113-6845283-5694610

APPENDIX B

Appendix B.1 Artificial Sun Module Subsystem (ASMS) Solar Test Array Layer 1 (STAR1)

Code

```
/*
Artificial Sun Module Subsystem (ASMS)
Solar Test Array Layer 1 (STAR1) v4.1.1
Last Update: 07 OCT 2019
Created using Arduino IDE 1.8.8
*/
#include <Wire.h> // Initialize I2C comm protocol
#include <LiquidCrystal_I2C.h>
LiquidCrystal_I2C lcd(0x27, 20, 4);
const int buttonPin = 2; // the number of the pushbutton pin
const int ledPin1 = 3; // the number of the LED pin (System
Ready)
const int ledPin2 = 4; // the number of the LED pin (RED)
624nm
const int ledPin3 = 5; // the number of the LED pin (GRN)
525nm
const int ledPin4 = 6; // the number of the LED pin (BLU)
480nm?
const int ledPin5 = 7; // the number of the LED pin (WHT)
???nm
const int ledPin6 = 8; // the number of the LED pin (UV)
365nm
const int ledPin7 = 9; // the number of the LED pin (IR)
940nm
const int pinBuzz = 10; // buzzer hooked up to digital pin 10
// variables will change:
int buttonState = 0; // variable for reading the pushbutton
status
int buttonPressCount = 0;
//int numberOfLED = 5;
int numberOfLED = 7;
```

```

void setup() {
    // initialize the LED pin as an output:
    pinMode(ledPin1, OUTPUT);
    pinMode(ledPin2, OUTPUT);
    pinMode(ledPin3, OUTPUT);
    pinMode(ledPin4, OUTPUT);
    pinMode(ledPin5, OUTPUT);
    pinMode(ledPin6, OUTPUT);
    pinMode(ledPin7, OUTPUT);

    // initialize the pushbutton pin as an input:
    pinMode(buttonPin, INPUT);
    //initialize buzzer as an output
    pinMode(pinBuzz, OUTPUT);
}

void loop() {
    // read the state of the pushbutton value:
    buttonState = digitalRead(buttonPin);
    int botao; // saves the last logic state of the button
    if (botao ==1){
        digitalWrite(pinBuzz, 1);
    } else
    { digitalWrite(pinBuzz, 0);
    }
    delay(10);
    // check if the pushbutton is pressed.
    // if it is, the buttonState is HIGH:
    if (buttonState == HIGH)
        if (buttonPressCount % numberOfLED == 0)
            digitalWrite(ledPin1, HIGH); // turn LED1 on:
            lcd.setCursor(17, 3);
            lcd.print("RDY");
        else

```

```

    digitalWrite(ledPin1, LOW);
if (buttonPressCount % numberOfLED == 1)
    digitalWrite(ledPin2, HIGH); // turn LED2 on:
    lcd.setCursor(17, 3);
    lcd.print("RED");
else
    digitalWrite(ledPin2, LOW);
if (buttonPressCount % numberOfLED == 2)
    digitalWrite(ledPin3, HIGH); // turn LED3 on:
    lcd.setCursor(17, 3);
    lcd.print("GRN");
else
    digitalWrite(ledPin3, LOW);
if (buttonPressCount % numberOfLED == 3)
    digitalWrite(ledPin4, HIGH); // turn LED4 on:
    lcd.setCursor(17, 3);
    lcd.print("BLU");
else
    digitalWrite(ledPin4, LOW);
if (buttonPressCount % numberOfLED == 4)
    digitalWrite(ledPin5, HIGH); // turn LED5 on:
    lcd.setCursor(17, 3);
    lcd.print("WHT");
else
    digitalWrite(ledPin5, LOW);
if (buttonPressCount % numberOfLED == 5)
    digitalWrite(ledPin6, HIGH); // turn LED6 on:
    lcd.setCursor(17, 3);
    lcd.print("UV");
else if
    digitalWrite(ledPin6, LOW);
if (buttonPressCount % numberOfLED == 6)
    digitalWrite(ledPin7, HIGH); // turn LED7 on:

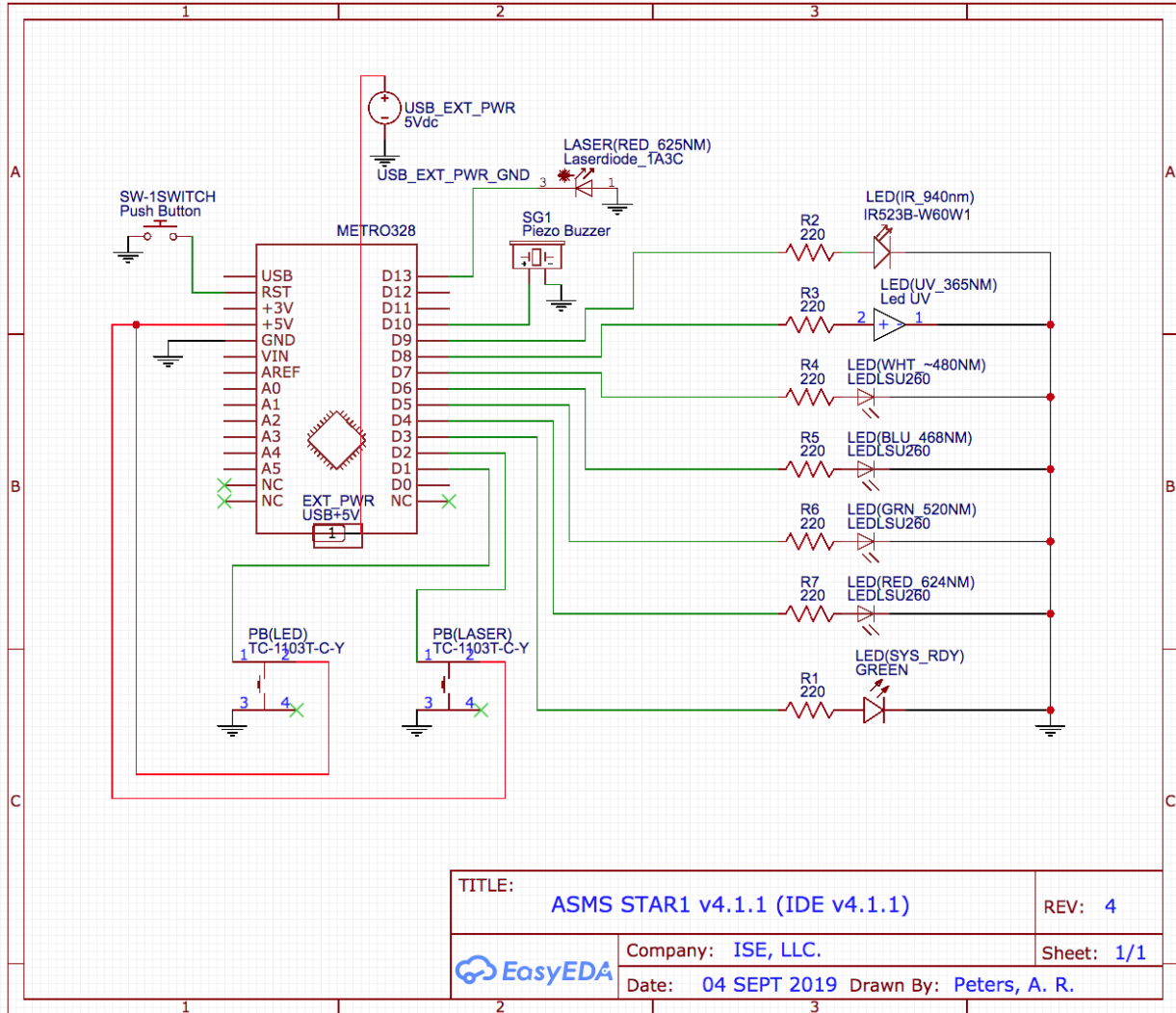
```

```
    lcd.setCursor(17, 3);  
    lcd.print("IR");  
else if  
    digitalWrite(ledPin7, LOW);  
buttonPressCount++;  
delay(300);  
}  
}
```

APPENDIX B

Appendix B.2 Artificial Sun Module Subsystem (ASMS) Solar Test Array Layer 1 (STAR1)

Circuit Schematic



APPENDIX C

Appendix C.1 Artificial Sun Module Subsystem (ASMS) Solar Test Array Layer 2 (STAR2)

Code

```
/*
Artificial Sun Module Subsystem Version (ASMS)
Solar Test Array Layer 2 (STAR2) v4.1.1
Last Update: 07 OCT 2019
Created using Arduino IDE 1.8.8
*/
#include <Wire.h>
#include <Adafruit_Sensor.h>
#include <Adafruit_TSL2561_U.h>
#include "Adafruit_VL53L0X.h"
#include "Adafruit_TMP007.h"
#include <SPI.h>
#include <LiquidCrystal_I2C.h>
LiquidCrystal_I2C lcd(0x27, 20, 4);
Adafruit_VL53L0X lox = Adafruit_VL53L0X();
Adafruit_TMP007 tmp007(0x40); // component replaced
Adafruit_TSL2561_Unified tsl =
Adafruit_TSL2561_Unified(TSL2561_ADDR_FLOAT, 12345);
//ML8511 setup
int UVOUT = A0; // set OUT pin from ML8511 to analog pin 0
int REF_3V3 = A1; // set analog pin as a reference voltage of
3.3V for the ML8511
void setup(){
  pinMode(UVOUT, INPUT); // establish input for UV sensor
  pinMode(REF_3V3, INPUT); // establish ref voltage input for UV
sensor
  Wire.begin();
  lox.begin(0x29);
  lcd.begin(20,4);
  lcd.init();
```



```

lcd.backlight();
lcd.setCursor(0, 0);
lcd.print("ASMS v4.1.1");    // bootup text
delay(1000);
lcd.setCursor(0, 1);
lcd.print("Initializing VL53L0X");
delay(500);
lcd.setCursor(0, 2);
lcd.print("Initializing TMP007");
delay(500);
lcd.setCursor(0, 3);
lcd.print("Initializing ML8511");
delay(500);
lcd.clear();
lcd.setCursor(0, 0);
lcd.print("Initializing TSL2561");
delay(500);
lcd.clear();
if (!lox.begin(0x29)) {
    Serial.println(F("Failed to boot VL53L0X"));
    lcd.print("VL53L0X error");
    while(1);
}
if (!tmp007.begin(0x40)) {
    Serial.println("Failed to boot TMP007");
    lcd.print("TMP007 error");
    while (1);
}
if(!tsl.begin()){    // need to determine I2C address for new
component
    lcd.print("TSL2561 Error");
    while(1);
}

```

```

}
//TSL2561 configuration void setups
void configureSensor(){ // Setup the sensor gain and integration
time; set up for 402ms
//Set the gain for the TSL2561:
    // tsl.setGain(TSL2561_GAIN_1X);          // No gain ... use in
bright light to avoid sensor saturation
    // tsl.setGain(TSL2561_GAIN_16X);        // 16x gain ... use in
low light to boost sensitivity
    // tsl.enableAutoRange(true);            // Auto-gain ...
switches automatically between 1x and 16x
    tsl.setGain(TSL2561_GAIN_16X);
//Set the integration time for the TSL2561: (to yield better
sensor resolution (402ms = 16-bit data))
    // tsl.setIntegrationTime(TSL2561_INTEGRATIONTIME_13MS);
// fast but low resolution
    // tsl.setIntegrationTime(TSL2561_INTEGRATIONTIME_101MS); //
medium resolution and speed
    // tsl.setIntegrationTime(TSL2561_INTEGRATIONTIME_402MS); //
16-bit data but slowest conversions
    tsl.setIntegrationTime(TSL2561_INTEGRATIONTIME_402MS);
//since there is time between each angle measurement, its best
to have better accuracy
}
void displaySensorDetails(){
    sensor_t sensor;
    tsl.getSensor(&sensor);
}
//ML8511 command loop analog to digital conversion; takes an
average of readings on a given pin and returns the average
int averageAnalogRead(int pinToRead)
{
byte numberOfReadings = 8;
unsigned int runningValue = 0;
for(int x = 0 ; x < numberOfReadings ; x++)
runningValue += analogRead(pinToRead);
}

```

```

runningValue /= numberOfReadings;
return(runningValue);
}
// utilize the arduino map function for floats to run the UV
input
/* page 2 of the S12SD datasheet shows photocurrent along UV
power, so we need to make sure
to model this in order to adequately reflect the
photocurrent/power relationship, and
accurately show UV-A power in mW/cm2
*/
float mapfloat(float x, float in_min, float in_max, float
out_min, float out_max)
{
return (x - in_min) * (out_max - out_min) / (in_max - in_min) +
out_min;
}

void loop(){
// VL53L0X range measurement command loop
VL53L0X_RangingMeasurementData_t measure;
lox.rangingTest(&measure, false); // pass in 'true' to get
debug data printout!
if (measure.RangeStatus != 4) { // phase failures have
incorrect data
    lcd.clear();
    lcd.setCursor(0, 0);
    lcd.print("Range: ");
    lcd.print(measure.RangeMilliMeter);
    lcd.print(" mm");
} else {
    lcd.setCursor(0, 0);
    lcd.print("VL53L0X Error");
    return;
}
}

```

```

// TMP007 contactless temperature reading command loop
float objt = tmp007.readObjTempC();
float diet = tmp007.readDieTempC();
lcd.setCursor(0, 1);
lcd.print("PV: ");
lcd.print(objt);
lcd.print((char)223);
lcd.print("C");
lcd.setCursor(0, 2);
lcd.print("ASMS: ");
lcd.print(diet);
lcd.print((char)223);
lcd.print("C");
//delay(1500);
//lcd.clear();

// ML8511 UV sensor command loop (replacing the S12SD) - code
will be moved to SCARS v2.0.1
/*
  UV sensor will detect typical wavelengths of 200-400 nm (at Ta
= 25C), and outputs a calibrated analog
  voltage which varies with UV light intensity; this will impact
how the mapfloat will calculate output
  voltage to irradiance
*/
int uvLevel = averageAnalogRead(UVOUT);
int refLevel = averageAnalogRead(REF_3V3);
float outputVoltage = 3.3 / refLevel * uvLevel;
float uvIntensity = mapfloat(outputVoltage, 0.99, 2.8, 0.0,
15.0); // convert the voltage to a UV intensity level
  lcd.setCursor(0, 3);
  lcd.print("UV: ");
  lcd.print(uvIntensity);
//TSL2561 command loop
  sensors_event_t event;

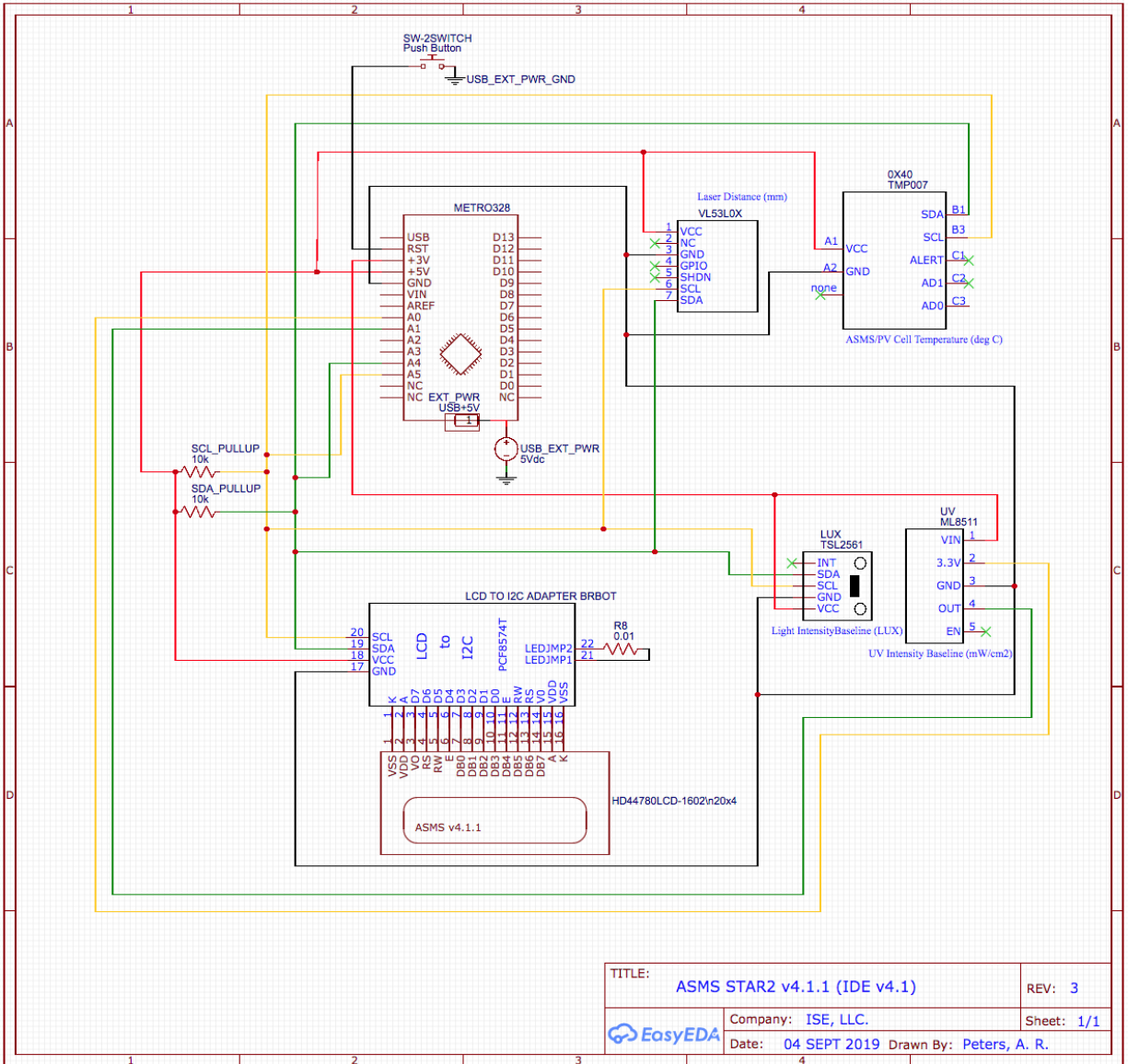
```

```
    tsl.getEvent(&event);
    if (event.light){
        lcd.setCursor(9, 3);
        lcd.print("VIS: ");
        lcd.print(event.light);    // if I want to calculate and
show lumens then just add equation (3) here
        //lcd.print(" lux");
        delay(1000);
        //lcd.clear();
    }
    else{
        lcd.setCursor(14, 3);
        lcd.print("0 lux"); // If event.light = 0 lux the sensor is
probably saturated and no reliable data could be generated!
        delay(1000);
    }
}
```

APPENDIX C

Appendix C.2 Artificial Sun Module Subsystem (ASMS) Solar Test Array Layer 2 (STAR2)

Circuit Schematic



APPENDIX D

Appendix D.1 Beta Angle Position and Control Subsystem (BAPCS) Code

```
/*
Beta Angle Position and Control Subsystem (BAPCS) v4.7.1
Last update: 03 OCT 2019
Created using Arduino IDE 1.8.8
Comments: Must be used with UNO R3. METRO328 board incompatible.
*/
#include <Wire.h> // Initialize I2C comm protocol
#include <SPI.h>
#include <LiquidCrystal_I2C.h>
LiquidCrystal_I2C lcd(0x27, 16, 2);
#include <AccelStepper.h>
#define zeroswitch 13 // Microswitch connected to digital pin 13
#include <Keypad.h>
// 4x4 keypad setup
byte index = 0;
char numbers[16]; // may be used to store float later on
long num; // this may need to be changed depending on the
situation
const byte ROWS = 4;
const byte COLS = 4;
char keys[ROWS][COLS] = {
  {'1', '2', '3', 'A'},
  {'4', '5', '6', 'B'},
  {'7', '8', '9', 'C'},
  {'*', '0', '#', 'D'}, // * = start, # = stop, program the
A (F1) button to set HOME function
};
```

```

byte rowPins[ROWS] = { 11, 10, 9, 8 };
byte colPins[COLS] = { 7, 6, 5, 4 };

Keypad keypad = Keypad( makeKeymap(keys), rowPins, colPins,
ROWS, COLS );

// AccelStepper Setup
AccelStepper stepperNEMA(1, 2, 3); // Number 1 used to
establish A3687 driver interface

// STEP pin A3687 to
digital pin 2

// DIR pin A3687 to digital
pin 3

long solarangle_step; // Used to store the X value entered in
the Serial Monitor

int move_finished = 1; // Used to check if move is completed

long initial_zeroize = -1; // Used to zeroize stepper at
startup

float solarangle_degrees;

static char outstr[3]; // limits the decimal places for the
steps (i.e., 400 not 400.000 steps)

//char entryStr[8];

//int = 0;

//const int pinBuzz = 12; // buzzer hooked up to digital pin 12

void setup() {
    Wire.begin();

    Serial.begin(9600); // Start the serial monitor to control
the motor

    //displayCodeEntryScreen();

    //keypad.addEventListener(keypadEvent); //add an event
listener for this keypad

    //float solarangle_step = 000.000;

```



```

float len = 000.000; // float variable for the keypad stored
input
pinMode(zeroswitch, INPUT_PULLUP);
//pinMode(zeroswitch, INPUT);
// pinMode(pinBuzz, OUTPUT);
lcd.begin(16,2); // startup menu
lcd.backlight();
lcd.setCursor(0, 0);
lcd.print("BAPCS v4.7.1");
delay(1000);
lcd.setCursor(0, 1);
lcd.print("Initializing");
delay(1000);
lcd.clear();

// Set Max Speed and Acceleration of each Steppers at startup
for homing

stepperNEMA.setMaxSpeed(100.0); // Set Max Speed of
Stepper (Slower to get better accuracy)

stepperNEMA.setAcceleration(100.0); // Set Acceleration of
Stepper

// Start Zeroizing procedure of Stepper Motor at startup
Serial.print("Zeroizing ASMS . . . . . ");
while (digitalRead(zeroswitch)) { // Make the Stepper move
CCW until the switch is activated

stepperNEMA.moveTo(initial_zeroize); // Set the position to
move to

initial_zeroize--; // Decrease by 1 for next move if needed
stepperNEMA.run(); // Start moving the stepper

lcd.setCursor(0, 0);
lcd.print("ASMS Zeroize");
lcd.setCursor(0, 1);

```

```

    lcd.print("In Progress");
    delay(5);
}

stepperNEMA.setCurrentPosition(0); // Set the current
position as zero for now

stepperNEMA.setMaxSpeed(100.0); // Set Max Speed of
Stepper (Slower to get better accuracy)

stepperNEMA.setAcceleration(100.0); // Set Acceleration of
Stepper

initial_zeroize = 1;

while (!digitalRead(zeroswitch)) { // Make the Stepper move CW
until the switch is deactivated

    stepperNEMA.moveTo(initial_zeroize);

    stepperNEMA.run();

    initial_zeroize++;

    delay(5);

}

stepperNEMA.setCurrentPosition(0);

stepperNEMA.setMaxSpeed(400.0); // Set Max Speed of
Stepper (Faster for regular movements)

stepperNEMA.setAcceleration(400.0); // Set Acceleration of
Stepper

Serial.println("Zeroize Completed");
Serial.println("");
lcd.clear();
lcd.setCursor(0, 0);
lcd.print("ASMS Zeroize");
lcd.setCursor(0, 1);
lcd.print("Complete");
delay(750);

// Print out Instructions on the Serial Monitor at Start

```

```

    Serial.println("Enter Solar Angle (Positive = CW / Negative =
CCW / Zero = Home):");

    lcd.clear();

    lcd.setCursor(0, 0);

    lcd.print("Angle:");

    lcd.setCursor(0, 1);

    lcd.print("0.00"); // use this line for displaying the solar
angle (angle = steps*0.225)

    lcd.print((char)223);
}
/*
Used for future iterations of the BAPCS CNC interface
// Display function to show the steps as they are being entered
void displayCodeEntryScreen() {
    keypad.getKey();

    lcd.setCursor(8,1);

    keypad.addEventListener(keypadEvent); //add an event listener
for this keypad
}

void keypadEvent(KeypadEvent eKey) {
    switch (keypad.getState()) {
        case PRESSED:
            lcd.setCursor(8, 1);
            lcd.print(eKey);
        }
    }
}
*/
void loop() {

```

```

    int solarangleDefault_step = 800;    // if a value more than
    800 is given in the keypad, then the default position for the
    ASMS will be 180 degrees

    solarangle_degrees = (solarangle_step*0.225);

// This displays the steps input on the right side of the LCD
    lcd.setCursor(8, 0);
    lcd.print("Steps:");
    lcd.setCursor(8, 1);
    lcd.print(outstr);
// 4x4 keypad command loop
    char key = keypad.getKey();
    if(key != NO_KEY)
    {
        if(key == 'C')
        {
            index = 0;
            numbers[index] = '\0';
        }
        else if (key == '#'){    // this is to cancel the current
key entry
            memset(outstr, 0, sizeof(outstr));
            index = 0;
            key = 0;
        }
        else if(key == '.')
        {
            numbers[index++] = '.';
            numbers[index] = '\0';
        }
        else if(key >= '0' && key <= '9')

```

```

    {
        numbers[index++] = key;
        numbers[index] = '\0';
    }
else if(key == '*')
{
    float solarangle_step = atof(numbers);
    dtostrf(solarangle_step, 7, 3, outstr);
    stepperNEMA.moveTo(solarangle_step);
    lcd.clear();
    lcd.setCursor(0, 0);
    lcd.print("Angle:");
    lcd.setCursor(0, 1);
    lcd.print(solarangle_step*0.225);
    lcd.print((char)223);

    index = 0;
    numbers[index] = '\0';
    if(solarangle_step < 0 || solarangle_step > 800) {
        lcd.setCursor(0, 1);
        lcd.print("Error");
        memset(outstr, 0, sizeof(outstr));
        index = 0;
        stepperNEMA.moveTo(solarangleDefault_step);
    }
}
}

// Insert updated CNC interface here if desired
// NEMA17 command loop

```

```

while (Serial.available()>0){ // Check if values are
available in the Serial Buffer

    move_finished = 0; // Set variable for checking move of the
Stepper

    solarangle_step = Serial.parseInt(); // Put numeric value
from buffer in solarangle_step variable

    if (solarangle_step < 0 || solarangle_step > 800) { // Make
sure the position entered is not beyond the HOME or MAX position

        Serial.println("");

        Serial.println("Please enter a value greater than zero and
smaller or equal to 800.....");

        Serial.println("");

        //lcd.setCursor(0, 1);

        //lcd.print("Error"); // feedback on LCD saying that the
desired angle is out of limits

    }

    else {

        Serial.print("Moving stepper into position: ");
        Serial.println(solarangle_step);

        lcd.clear();

        lcd.setCursor(0, 0);

        lcd.print("Setting Angle");

        lcd.setCursor(0, 1);

        lcd.print("Please wait...");

        stepperNEMA.moveTo(solarangle_step); // Set new moveto
position of Stepper

        delay(250); // Wait 0.25 seconds before moving ASMS

    }

}

if (solarangle_step >= 0 && solarangle_step <= 800) {

```

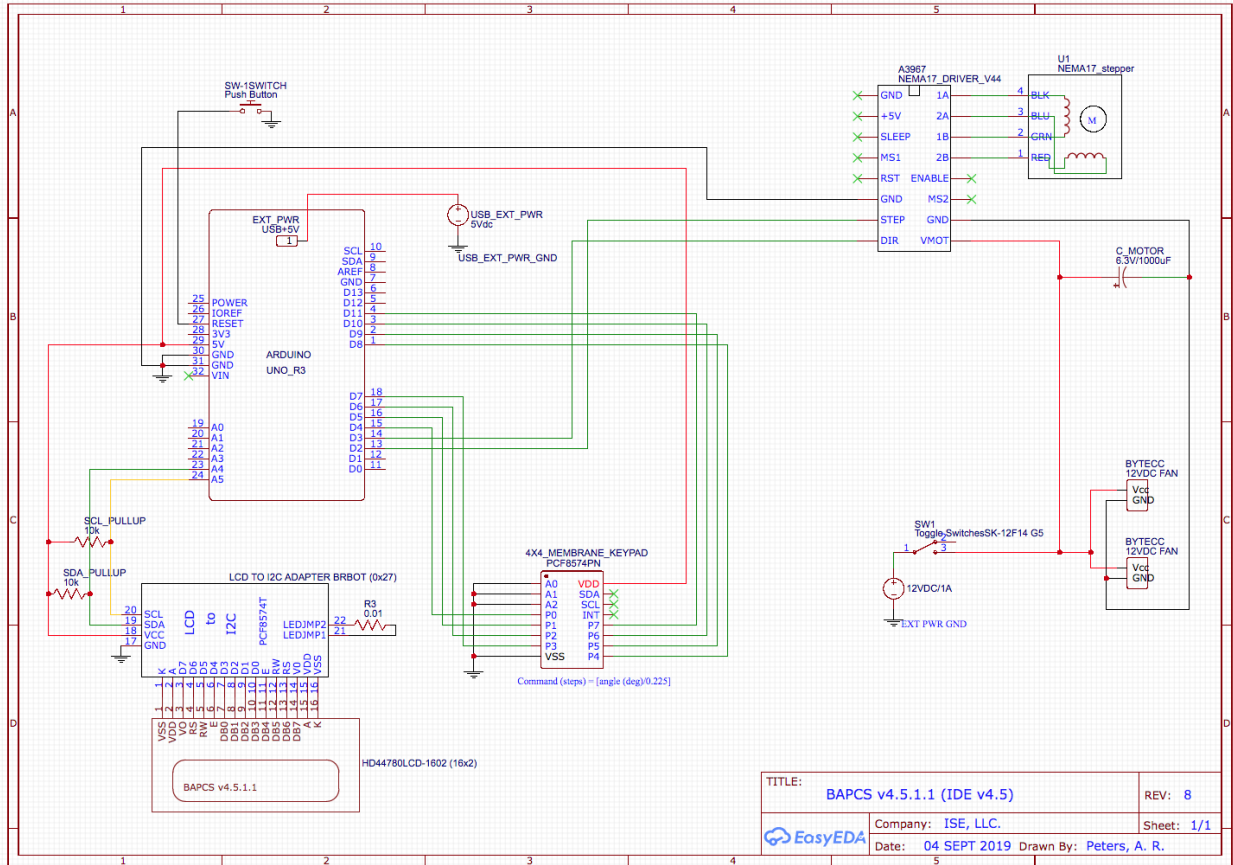
```

//if (solarangle_degrees >= 0 && solarangle_degrees <= 180){
// command line for degrees instead of steps
// Check if the Stepper has reached desired position
  if ((stepperNEMA.distanceToGo() != 0)) {
    stepperNEMA.run(); // Move Stepper into position
  }
// If move is completed display message on Serial Monitor
  if ((move_finished == 0) && (stepperNEMA.distanceToGo() == 0))
{
  Serial.println("COMPLETED!");
  Serial.println("");
  lcd.clear();
  lcd.setCursor(0, 0);
  lcd.print("Solar Angle:");
  lcd.setCursor(0, 1);
  lcd.print(solarangle_degrees); // use this line for
displaying the solar angle (angle = steps*0.225)
  lcd.print((char)223); // character for degrees symbol
  Serial.println("Enter Solar Angle (Positive = CW / Negative
= CCW / Zero = Home):");
  move_finished = 1; // Reset move variable
}
}
}

```

APPENDIX D

Appendix D.2 Beta Angle Position and Control Subsystem (BAPCS) Circuit Schematic



APPENDIX E

Appendix E.1 Environmental Control and Monitoring Subsystem (ECMS) Code

```
/*
Environmental Control and Monitoring Subsystem Version (ECMS)
v3.4.2
Last Update: 26 SEP 2019
Created using Arduino IDE 1.8.8
*/
#include <Wire.h>
#include <SPI.h>
#include <Adafruit_Sensor.h>
#include "Adafruit_BMP280.h"
#include "DHT.h"
#include "LiquidCrystal_I2C.h"
LiquidCrystal_I2C lcd1(0x27, 20, 4); // ECMS LCD 20x4
#define DHTPIN 8
#define DHTTYPE DHT22 // DHT22 sensor is used
DHT dht(DHTPIN, DHTTYPE); // Initialize DHT library
Adafruit_BMP280 bmp280;
int relaypin = 13; //relay driver control pin set to
controller digital pin 13
unsigned long previousMillis = 0;
unsigned long interval = 100;
const int chipSelect = 10;
void setup(){
// LCD Screen configuration
Wire.begin();
lcd1.begin(20, 4);
lcd1.init();
lcd1.backlight();
lcd1.setCursor(0, 0);
lcd1.print("ECMS v3.4"); //bootup text, only displayed for
3 seconds
```

```

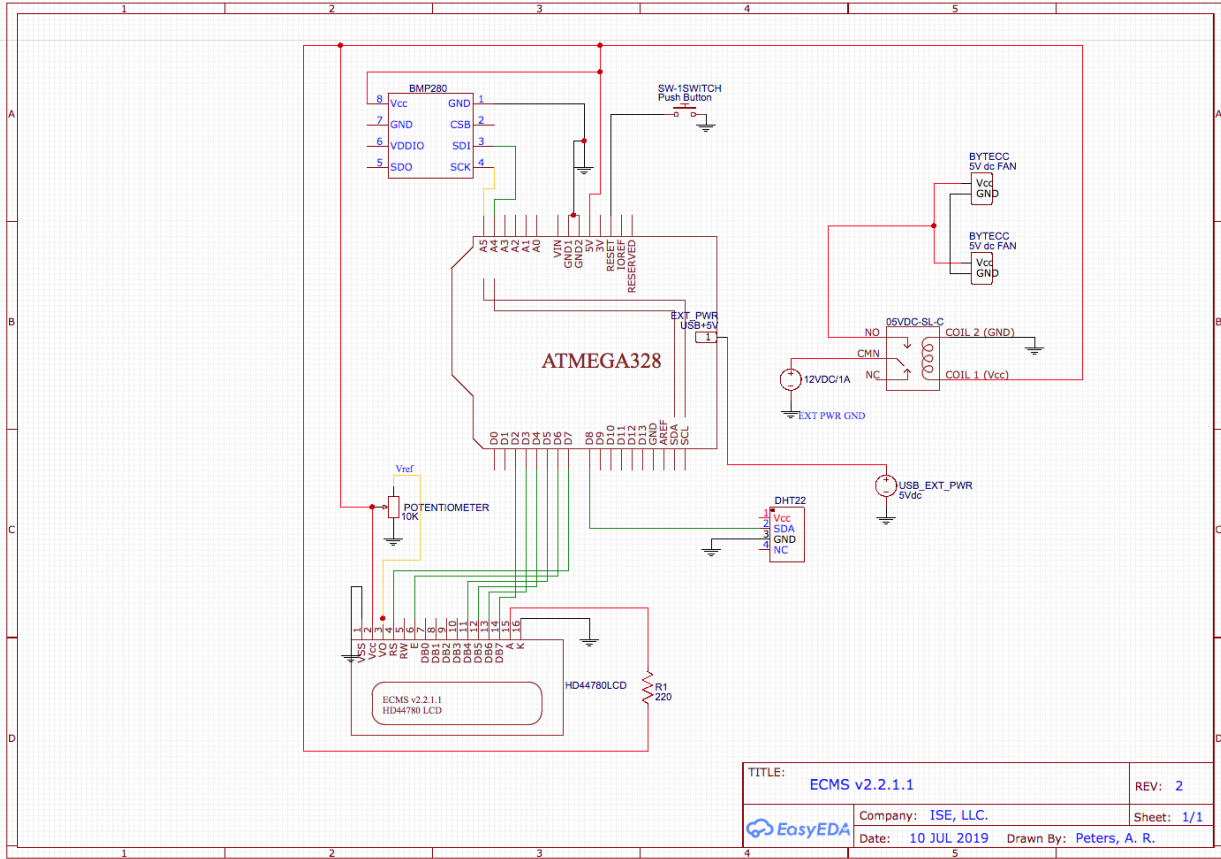
delay(500);
lcd1.setCursor(1, 1);
lcd1.print("Initializing DHT22");
delay(500);
lcd1.setCursor(1, 2);
lcd1.print("Initializing BMP280");
delay(500);
lcd1.clear();
// Sensors setup
dht.begin();
bmp280.begin();
pinMode(relaypin, OUTPUT); // this line added for 5VDC
relay
digitalWrite(relaypin, LOW); // this line added for 5VDC relay
}
void loop(){
// BMP280 temperature command loop
float basetemp = bmp280.readTemperature();
if(basetemp <=25){// 24C is the set temperature threshold
digitalWrite(9, LOW);
}
else if(basetemp >24){
digitalWrite(9, HIGH);
}
// LCD1 display loop
lcd1.setCursor(0, 0); // read the baseplate
temperature
lcd1.print("Base Temp:");
lcd1.setCursor(11, 0);
lcd1.print(bmp280.readTemperature());
lcd1.print((char)223); // custom character added for
degree symbol
lcd1.print("C");
lcd1.setCursor(0, 1); // read the ambient temperature

```

```
    lcd1.print("Amb Temp:");
    lcd1.setCursor(10, 1);
    lcd1.print(dht.readTemperature());
    lcd1.print((char)223);          // custom character added for
degree symbol
    lcd1.print("C");
    lcd1.setCursor(0, 2);          // read the pressure
    lcd1.print("Pressure:");
    lcd1.setCursor(10, 2);
    lcd1.print(bmp280.readPressure()/1000);
    lcd1.print(" kPa");
    lcd1.setCursor(0, 3);          // read the humidity
    lcd1.print("Humidity:");
    lcd1.setCursor(10, 3);
    lcd1.print(dht.readHumidity());
    lcd1.print("%");
    delay(500);
}
```

APPENDIX E

Appendix E.2 Environmental Control and Monitoring Subsystem (ECMS) Circuit Schematic



APPENDIX F

Appendix F.1 Photocurrent Measurement Subsystem (PCMS) Code

```
/*
Photocurrent Measurement Subsystem (PCMS) v5.1
Last Update: 25 SEPT 2019
Created using Arduino IDE 1.8.8
*/
#include <Wire.h>
//#include <Adafruit_Sensor.h>
#include <Adafruit_INA219.h>
#include <LiquidCrystal_I2C.h>
LiquidCrystal_I2C lcd(0x27, 20, 4);
#include <SPI.h>
#include "SdFat.h"
SdFat SD;
Adafruit_INA219 ina219;
unsigned long previousMillis = 0;
unsigned long interval = 100;
const int chipSelect = 10;
float shuntvoltage = 0;
float busvoltage = 0;
float current_mA = 0;
float loadvoltage = 0;
float energy = 0;
float current;
File TimeFile;
File VoltFile;
File CurFile;
```

```

void setup() {
  Wire.begin();
  lcd.init();
  lcd.backlight();
  lcd.setCursor(0, 0);
  lcd.print("PCMS v5.1");    // bootup text
  delay(1000);
  lcd.setCursor(0, 1);
  lcd.print("Inititalizing INA169");
  delay(500);
  lcd.setCursor(0, 2);
  lcd.print("Initializing INA219");
  delay(500);
  lcd.setCursor(0, 3);
  lcd.print("Initializing FAT32");
  delay(500);
  lcd.clear();
  ina219.begin();
  ina219.setCalibration_16V_400mA();
  SD.begin(chipSelect);
  uint32_t currentFrequency;
}

void loop() {
  float current = (analogRead(A1) * 5.0 / 1023.0)*1000;
  unsigned long currentMillis = millis();
  if (currentMillis - previousMillis >= interval)
  {
    previousMillis = currentMillis;

```

```

    ina219values();

    TimeFile = SD.open("TIME.txt", FILE_WRITE);
    if (TimeFile) {
        TimeFile.println(currentMillis);
        TimeFile.close();
    }
    VoltFile = SD.open("VOLT.txt", FILE_WRITE);
    if (VoltFile) {
        VoltFile.println(loadvoltage);
        VoltFile.close();
    }
    CurFile = SD.open("CUR.txt", FILE_WRITE);
    if (CurFile) {
        CurFile.println(current);
        CurFile.close();
    }
}

lcd.clear();
lcd.setCursor(0, 0);
lcd.print("Voltage: ");
lcd.print(loadvoltage);
lcd.print(" V");
lcd.setCursor(0, 1);
lcd.print("Current: ");
lcd.print(current, 3);
lcd.print(" mA");
lcd.setCursor(0, 2);

```

```

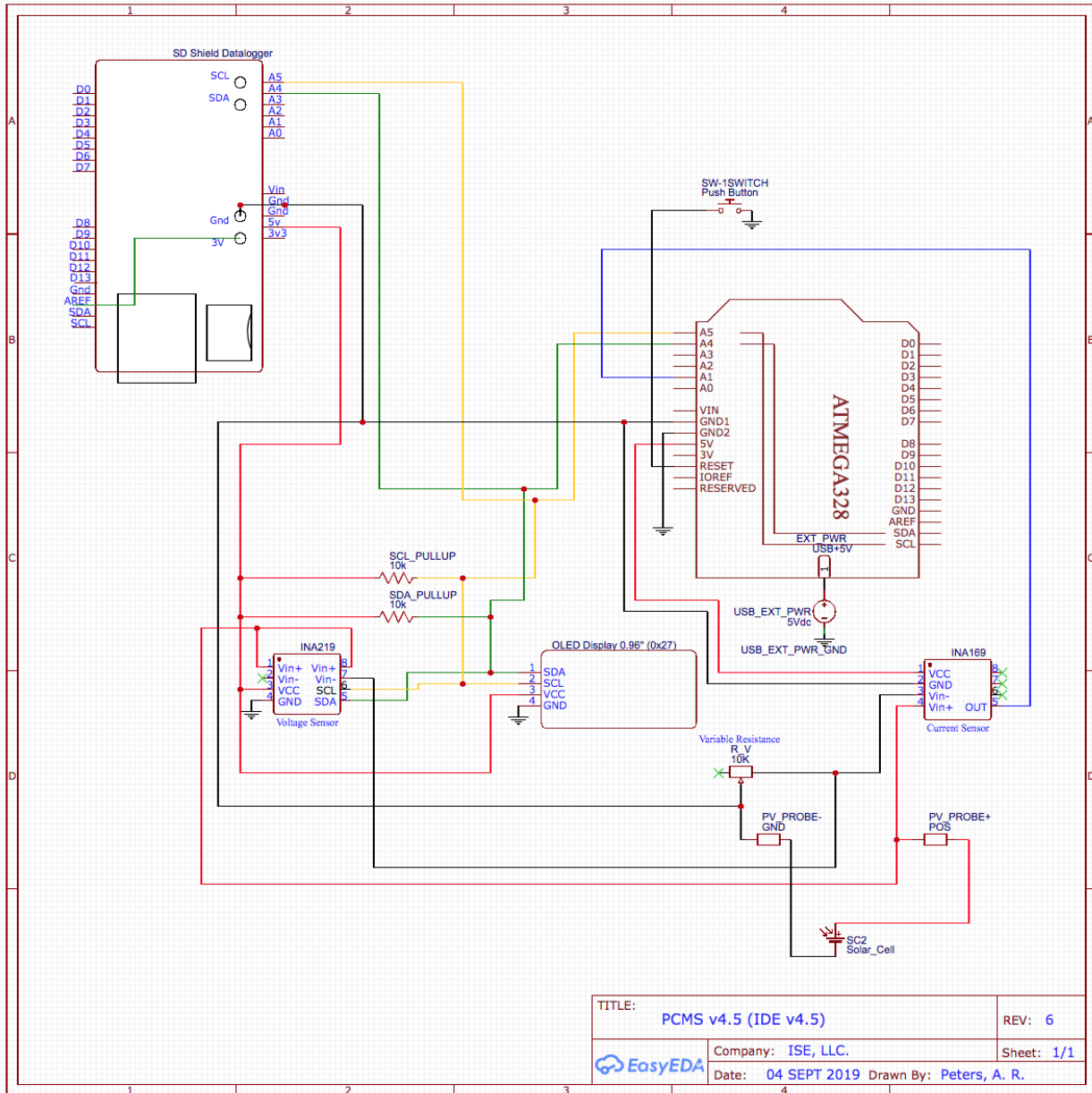
lcd.print("Power: ");
lcd.print(loadvoltage * current);
lcd.print(" mW");

//lcd.setCursor(0, 3);
//lcd.print("Energy: ");
//lcd.print(energy);
//lcd.print(" mWh");
delay(500);
}
void ina219values() {
  shuntvoltage = ina219.getShuntVoltage_mV();
  busvoltage = ina219.getBusVoltage_V();
  current_mA = ina219.getCurrent_mA();
  loadvoltage = busvoltage + (shuntvoltage / 1000);
  energy = energy + loadvoltage * current_mA / 3600;
}

```


APPENDIX F

Appendix F.2 Photocurrent Measurement Subsystem (PCMS) Circuit Schematic



APPENDIX G

Appendix G.1 Spectrum Calibration and Response Subsystem (SCARS) Code

```
/* Spectrum Calibration Analysis and Response Systems (SCARS)
v4.3
```

```
Last Update: 26 SEP 2019
```

```
Created using Arduino IDE 1.8.8
```

```
*/
```

```
#include <Wire.h>
```

```
#include <SPI.h>
```

```
#include <Adafruit_Sensor.h>
```

```
#include "Adafruit_TSL2591.h"
```

```
#include "Adafruit_VEML6075.h"
```

```
#include "LiquidCrystal_I2C.h"
```

```
LiquidCrystal_I2C lcd(0x25, 20, 4);
```

```
#include "SdFat.h"
```

```
SdFat SD;
```

```
Adafruit_TSL2591 tsl = Adafruit_TSL2591(2591); // pass in a
number for the sensor identifier
```

```
Adafruit_VEML6075 uv = Adafruit_VEML6075();
```

```
unsigned long previousMillis = 0;
```

```
unsigned long interval = 100;
```

```
const int chipSelect = 10;
```

```
File UVAFfile;
```

```
File UVBfile;
```

```
File UVIfile;
```

```
File VISIRLuxFile;
File IRAnalogFile;
File VISAnalogFile;
void setup(){
    SD.begin(chipSelect);
    displaySensorDetails();
    configureSensor();
    Wire.begin();
    lcd.begin(20, 4);
    lcd.backlight();
    lcd.setCursor(0, 0);
    lcd.print("SCARS v4.3");    // bootup text
    delay(500);
    lcd.setCursor(1, 1);
    lcd.print("Init TSL2591");
    delay(500);
    lcd.setCursor(1, 2);
    lcd.print("Init VEML6075");
    delay(500);
    lcd.setCursor(1, 3);
    lcd.print("Init FAT32");
    delay(500);
    lcd.clear();
}
```

```

// TSL2591 troubleshooting just in case there is an error
    if(!tsl.begin()){
        lcd.print("TSL2591 Error");
        while(1);
    }
// VEML6075 troubleshooting just in case there is an error
    if (! uv.begin()) {
        lcd.println("VEML6075 Error");
    }

        // Set the integration constant
uv.setIntegrationTime(VEML6075_100MS);

        // Set the high dynamic mode
uv.setHighDynamic(true);

        // Set the mode
uv.setForcedMode(false);

        // Set the calibration coefficients
uv.setCoefficients(2.22, 1.33, // UVA_A and UVA_B
coefficients
                    2.95, 1.74, // UVB_C and UVB_D
coefficients
                    0.001461, 0.002591); // UVA and UVB
responses
}

//TSL2591 configuration void setups

void configureSensor(){ // Setup the sensor gain and integration
time; set up for 402ms

```

```

    // You can change the gain on the fly, to adapt to
    brighter/dimmer light situations

    //tsl.setGain(TSL2591_GAIN_LOW);    // 1x gain (bright light)

    tsl.setGain(TSL2591_GAIN_MED);      // 25x gain

    //tsl.setGain(TSL2591_GAIN_HIGH);   // 428x gain

    // Changing the integration time gives you a longer time over
    which to sense light

    // longer timelines are slower, but perform better in very low
    light situations

    //tsl.setTiming(TSL2591_INTEGRATIONTIME_100MS); // shortest
    integration time (bright light)

    // tsl.setTiming(TSL2591_INTEGRATIONTIME_200MS);

    tsl.setTiming(TSL2591_INTEGRATIONTIME_300MS);

    // tsl.setTiming(TSL2591_INTEGRATIONTIME_400MS);

    // tsl.setTiming(TSL2591_INTEGRATIONTIME_500MS);

    // tsl.setTiming(TSL2591_INTEGRATIONTIME_600MS); // longest
    integration time (dim light)

}

void displaySensorDetails(){

    sensor_t sensor;

    tsl.getSensor(&sensor);

}

// TSL2591 simple read task to read the IR and full spectrum
simultaneously and convert to lux

//void advancedRead(void) //, or select the simpleRead by doing
the following:

void advancedRead(void)

```

```

{
    //uint16_t x1 = tsl.getLuminosity(TSL2591_INFRARED);

    //uint16_t x2 = tsl.getLuminosity(TSL2591_VISIBLE);

    // More advanced data read example. Read 32 bits with top 16
    bits IR, bottom 16 bits full spectrum

    // That way you can do whatever math and comparisons you
    want!

    uint32_t lum = tsl.getFullLuminosity();

    uint16_t ir, full;

    ir = lum >> 16;

    full = lum & 0xFFFF;

    lcd.setCursor(0, 0);

    lcd.print("VIS+IR: ");

    lcd.print(tsl.calculateLux(full, ir), 4);

    lcd.print(" lux");

    lcd.setCursor(0, 1);

    lcd.print("IR Analog: ");

    lcd.print(ir);

    lcd.setCursor(0, 2);

    lcd.print("VIS Analog: ");

    lcd.print(full - ir);

    lcd.setCursor(0, 3);

    //lcd.print("Full Analog: ");

    //lcd.print(full);

    lcd.print("UV: ");

```

```

    lcd.print(uv.readUVA());

    lcd.print(" "); lcd.print(uv.readUVB()); lcd.print(" ");
    lcd.print(uv.readUVI());

    // SD Card Datalogger

unsigned long currentMillis = millis();

    if (currentMillis - previousMillis >= interval)
    {

        previousMillis = currentMillis;

        UVAFfile = SD.open("UVA Data.txt", FILE_WRITE);

        if (UVAFfile) {

            UVAFfile.println(uv.readUVA()); // log UV data, may need
to rework this just in case it doesnt log correctly

            UVAFfile.close();

        }

        UVBFile = SD.open("UVB Data.txt", FILE_WRITE);

        if (UVBFile) {

            UVBFile.println(uv.readUVB()); // log UV data, may need
to rework this just in case it doesnt log correctly

            UVBFile.close();

        }

        UVIFfile = SD.open("UVI Data.txt", FILE_WRITE);

        if (UVIFfile) {

            UVIFfile.println(uv.readUVI()); // log UV data, may need
to rework this just in case it doesnt log correctly

            UVIFfile.close();

        }
    }

```

```

VISIRLuxFile = SD.open("VIS+IR Lux Data.txt", FILE_WRITE);

if (VISIRLuxFile) {

    VISIRLuxFile.println(tsl.calculateLux(full, ir), 4); //
log visible and IR (e.g. total) lux data

    VISIRLuxFile.close();

}

IRAnalogFile = SD.open("IR Analog Data.txt", FILE_WRITE);

if (IRAnalogFile) {

    IRAnalogFile.println(ir); // log analog IR values

    IRAnalogFile.close();

}

VISAnalogFile = SD.open("VIS Analog Data.txt", FILE_WRITE);

if (VISAnalogFile) {

    VISAnalogFile.println(full - ir); // log visible analog
values

    VISAnalogFile.close();

}

}

void loop(){

//TSL2591 command loop

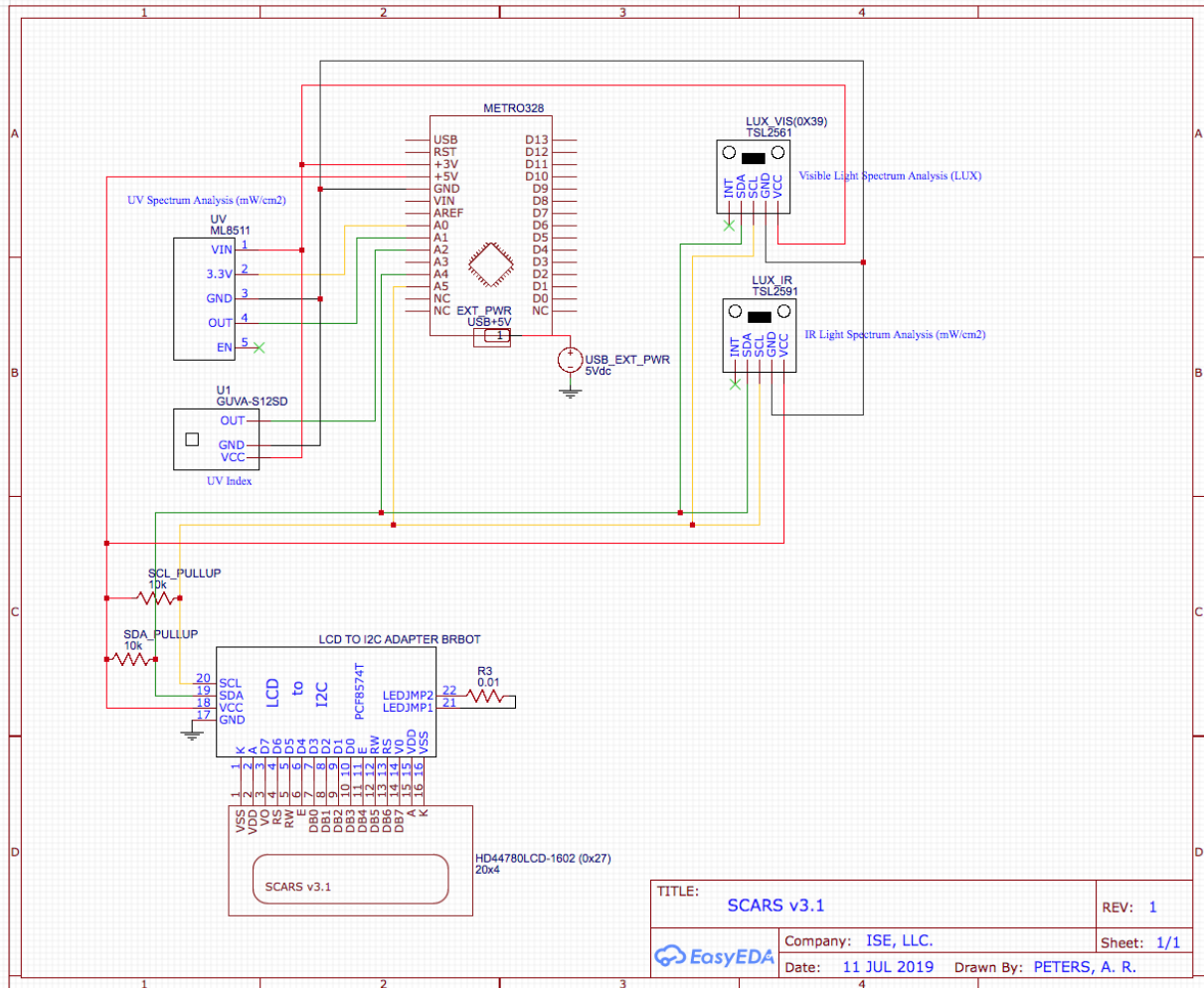
advancedRead();

}

```


APPENDIX G

Appendix G.2 Spectrum Calibration and Response Subsystem (SCARS) Circuit Schematic



APPENDIX H

BBRS PV Array Predicted Power Output Computation Table

$P_{T,\beta} = \overline{P_{T,\lambda,\beta}}$		$SRC = \frac{P_{out,\beta}}{P_{out,b}}$	$P_T = SRC * \overline{P_{T,\lambda,\beta}}$	
Average Total Power, based on individual angle [W], curved	Average Total Power, based on individual angle [W], flat*	SRC Correction Factor [Unitless]	Predicted Power for PV Airfoil [W]	
0.000103	0.000044	1.000000	4.44444E-05	
0.000560	0.000044	1.000000	4.44444E-05	
0.000675	0.000044	1.000000	4.44444E-05	
0.000973	0.000044	1.140625	5.06944E-05	
0.001462	0.000100	1.000000	0.0001	
0.001548	0.000278	0.581731	0.000161592	
0.000495	0.000400	0.480645	0.000192258	
0.001069	0.000625	0.399160	0.000249475	
0.001125	0.000711	0.453552	0.000322526	
0.001056	0.000803	0.494234	0.00039676	
0.001232	0.000900	0.550075	0.000495067	
0.000435	0.000803	0.626183	0.000502686	
0.000734	0.001003	0.628571	0.000630317	
0.000765	0.000803	0.764984	0.000614112	
0.000663	0.001003	0.754958	0.000757055	
0.000422	0.000900	0.813754	0.000732378	
0.000737	0.001003	1.005540	0.001008333	
0.000513	0.000900	1.119708	0.001007737	
0.000370	0.000803	1.359746	0.001091574	
0.000300	0.000711	1.554348	0.001105314	
0.000129	0.000711	2.046414	0.001455227	
0.000289	0.000336	3.175824	0.00106743	
0.000185	0.000100	6.415929	0.000641593	
0.000140	0.000044	10.843750	0.000481944	
0.000092	0.000044	9.968750	0.000443056	
0.000034	0.000044	9.609375	0.000427083	
0.000049	0.000044	9.281250	0.0004125	

Predicted Power Output for PV Airfoil from Flat Panel

*Measured power from a baseline flat cell in the identical configuration, and surface area. Only change would be the mounting on the NACA0024 airfoil with a beta of 8.826 deg.

APPENDIX I

Average Daily Insolation Matlab Code

```
clc; clear all;
N = 279;           % day number of year
lat = 45;         % latitude (degrees)
tilt = 40;        % panel tilt angle (degrees)
optTilt = lat + 3; % optimum tilt angle for this month, degrees

% reflectivity of ground surface for solar based on N
rho = 0.13;

% meteorological data based on N
KT = 0.55;
Hbar = 12/3.6;
tAir = 18;
tRated = 20;
alphaTau = 0.85;
UL = 0.02;

% the rated solar cell efficiency at STC
efficRated = 0.15;

% calculate the average daily insolation based on N
% determine solar declination (degrees)
delta = 23.45*sind((360/365)*(284 + N));

% Using equation 9-22 from Vanek, 2016
% assumes isotropic sky conditions
HdOverH = 1.39 - 4.03*KT + 5.53*(KT^2) - 3.11*(KT^3);

% Using equation 9-27 from Vanek, 2016
% computes the sunset hour angle (rads)
omegaRad = min(acos(-tand(lat)*tand(delta)), ...
               acos(-tand(lat-tilt)*tand(delta)));

Rb = (cosd(lat-tilt)*cosd(delta)*sin(omegaRad)+ ...
      omegaRad*sind(lat-tilt)*sind(delta))/...
      (cosd(lat)*cosd(delta)*sin(omegaRad) + ...
      omegaRad*sind(lat)*sind(delta));

% Using equation 9-28 from Vanek, 2016
% determine the direct component of Rbar
direct = (1 - HdOverH)*Rb;

% determine the diffuse component of Rbar
```

```

diffuse = HdOverH*(1 + cosd(tilt))/2;

% determine the reflection component of Rbar
reflected = rho*(1-cosd(tilt))/2;

% determine the average daily direct insolation
Hdirect = Hbar * direct;
% determine the average daily diffuse insolation
Hdiffuse = Hbar * diffuse;

% determine the average daily reflected insolation
Hreflected = Hbar * reflected;

% determine the average total daily insolation on tilted panel
based on N (kWh/m^2)
Htilt = Hdirect + Hdiffuse + Hreflected;

% graph the output as a function of cell temperature coefficient
% establish the range of cell temperature coefficient values to
% graph
beta = 0.001:0.001:0.01;

% assumed conditions here
Ta_TM = 3;

TM_Tr = tAir - tRated;

% Using equation 10-24 from Vanek, 2016
Cf = 1.0 - 0.000117*(lat - optTilt)^2;

% Using equation 10-22 and 10-23 from Vanek, 2016
Tc_Ta = Cf*(0.219+0.832*KT)*alphaTau/UL;

% Using equation 10-18 from Vanek, 2016
effic = efficRated*(1.0 - beta*(Tc_Ta + Ta_TM + TM_Tr));
output = Htilt*effic;

% create subplot 1
subplot(2, 1, 1)
plot(beta, effic)
axis([0.001, 0.01, 0.10, 0.16])
xlabel('Cell Temperature Coefficient, /K', 'FontSize', 11)
ylabel('Cell efficiency, decimal', 'FontSize', 11)
title('Average Daily Insolation Example', 'FontSize', 14)
grid on

% create subplot 2

```

```
subplot(2, 1, 2)
plot(beta, output)
axis([0.001, 0.01, 0.4, 0.8])
xlabel('Cell Temperature Coefficient, /K', 'FontSize', 11)
ylabel('Average Daily Panel Output, kWh', 'FontSize', 11)
grid on
```

